SUBHARMONIC VENTURE

Telli Faez

2012

The financial support for the publication of this thesis was kindly provided by:

- Bracco Research S.A. (Geneve, CH)
- Erasmus MC

Subharmonic Venture

Subharmonische avontuur

Thesis

to obtain the degree of doctor from the
Erasmus University Rotterdam
by command of the Rector Magnificus

Prof. dr. H.G. Schmidt,

and according to the decision of the Doctoral Board.

The public defense shall be held on
Thursday the 18th of October 2012 at 13.30 hours
by

Telli Ebrahimi Poorfaez
born in Tehran, Iran

ERASMUS UNIVERSITEIT ROTTERDAM

Doctoral Committee

Promotors:	Prof. dr. ir N. de Jong
	Prof. dr. ir. A. F. W. van der Steen
Co-promotor:	Dr. A. M. Versluis
Other members:	Prof. dr. W. J. Niessen
	Prof. dr. A. van der Lugt
	Dr. L. Bridal

روز هجران و شب فرقت یار آخر شد   زدم این فال و گذشت اختر و کار آخر شد

آن همه ناز و تنعم که خزان میفرمود   عاقبت در قدم باد بهار آخر شد

سکر ایزد که باقبال کله گوشه گل   نخوت باد دی و شوکت خار آخر شد

صبح امید که بد معتکف پرده غیب   گو برون آی که کار شب تار آخر شد

آن پریشانی شبهای دراز و غم دل   همه در سایه گیسوی نگار آخر شد

باورم نیست ز بد عهدی ایام هنوز   قصه غصه که در دولت یار آخر شد

ساقیا لطف نمودی قدحت پر می باد   که بتدبیر تو تشویش خمار آخر شد

در شمار ارچه نیاورد کسی حافظ را   سکر کان محنت بیحد و شمار آخر شد

SUBHARMONIC VENTURE

List of content

Chapter I

Introduction

Preface

As a person, always fascinated with the presence of physics in the daily life challenges, let me share this joy with you! But before leaving you with complicated medical terms, allow me to tell you a story. My grandmother passed away when I was nine years old. She was the sweetest person I have ever known. She died on a hospital bed due to heart attack. Few minutes before her death, she had asked my uncle for a slice of watermelon. Her son, happy for the signs of fast recovery of his mom from the earlier heart attack she had just survived few days before, leaves her bedside to fulfill her wish. Within those couple of minutes he was away, my grandmother had a second heart attack and this time she never recovered from it. Unfortunate stories of this type are not unique. Many may have similar experiences or have heard similar ones from friends and acquaintances. What strikes me most is that these stories mostly have one thing in common: abruptness and unexpectation.

It should be noted that a heart attack is not only reserved for aged fellows or those who do not follow a healthy diet or lifestyle. Many cases have been observed among young people and athletes who have never had any sign of heart trouble in their lives.

What is causing a heart attack? Myocardial infarction known as heart attack is a result of interruption of blood supply to a part of the heart and the death of heart cells. This is most commonly due to blockage of a coronary artery due to thickening of the arterial wall caused by the accumulation of lipids (cholesterol and fatty acids) in the wall of an artery. This thickening of the artery wall, also called plaque is a recognized vascular disease known as atherosclerosis. Atherosclerotic plaques are generally divided in two types: stable and unstable (vulnerable). Unstable or vulnerable plaques are usually weak and prone to rupture. When a vulnerable atherosclerotic plaque in the coronary artery ruptures, it can cause the formation of a blood clot known as thrombus that will rapidly slow or stop blood flow leading to death of the tissues fed by the artery in less than 5 minutes. When a vulnerable plaque in the carotid artery ruptures, atherosclerotic plaque or thrombus moves into the blood circulation and might occlude cerebral arteries. If this catastrophic event takes place in the coronary artery it causes a heart attack. If it is in an artery to the brain it is called stroke.

Now you may ask: you call this catastrophe a joy? Where did the physics go? You are absolutely right! All this drama was to explain that the key to prevent a heart attack or stroke is in the early detection of the vulnerable atherosclerotic plaque. Atherosclerosis affects the entire artery tree, but mostly larger, high-pressure vessels such as the coronary, renal, femoral, cerebral, and carotid arteries.

One of the diagnostic methods to detect and monitor an atherosclerotic plaque is medical ultrasonography. Diagnostic sonography is a fast, painless and easy non-invasive imaging technique used for visualizing subcutaneous body structures including vessels and internal organs. It is widely recognized by the public for its application during pregnancy (see figure 1). Ultrasound images which are produced by exposing part of the body to high frequency sound waves are captured in real-time. Therefore they can indicate the structure and movement of the body's internal organs, as well as blood vessels and the blood flowing through them.

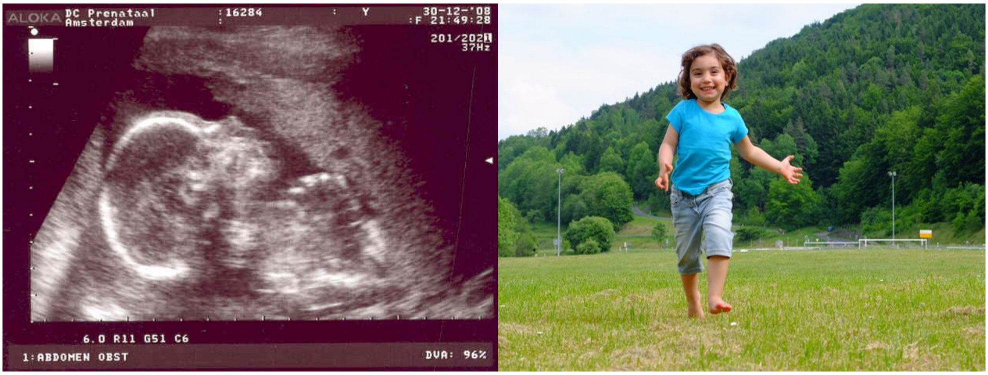

Fig 1. Soline Faez 20 weeks pre-birth (left) and three years after (right).

The human body has two carotid arteries which are located on each side of the neck and carry blood to the brain from the heart. The carotid artery is located superficially under the skin and is easily accessible for performing an ultrasound. Carotid ultrasound imaging is most frequently performed to screen a possible blockage or narrowing of the carotid arteries by atherosclerosis.

One of the markers of vulnerable atherosclerotic plaque is "vasa vasorum" neovascularization both in the adventitial layer and in the atherosclerotic plaque. These two microvascular networks are thought to have a central role in the early process of plaque progression and vulnerability, and may also be involved in plaque inflammation (Moreno et al 2006, Fleiner et al 2004).

Vasa vasorum

They are networks of small blood vessels which are formed on the surface of larger arteries and veins. They generally connect with a branch of the same or a neighboring vessel (Ritman and Lerman 2007). In humans, vessels with walls less than 29-cell layers thick (Wolinsky and Glagov 1967) normally do not have vasa (Okuyama *et al* 1988) and, in general, vessels less than 0.5 mm lumen diameter, e.g. normal vessels in mice and intramyocardial vessels in humans, do not have vasa vasorum (Geiringer 1951). Figure 2 presents microscopic images of the vasa vasorum network in cats, rats, dogs and human arteries.

The function of vasa vasorum is both to supply nutrients and oxygen to the tissues within the arterial and venous walls and to remove waste products, either produced by cells in the wall or introduced by diffusional transport through the endothelium of the artery or vein. The venous blood in the main lumen of veins provides little, if any, oxygen to the wall via transendothelial diffusion from the main lumen and for this reason a high density of vasa vasorum is required in vein walls.

Vasa vasorum can be dynamically compressed by the surrounding arterial wall and increase in number. The pressure distribution within the arterial wall compresses most of the vasa vasorum (Gössl *et al* 2003). Since the radii of the vasa vasorum are much smaller than the parent vessel lumen, the vascular resistance to flow in the vasa vasorum is high. The pressure within the distal vasa vasorum close to the media is lower than the coronary arterial lumen pressure. Hence in this region the compressive pressure within the wall can exceed the blood pressure within the vasa vasorum at the same location.

For more than two decades extensive studies have found a strong correlation between the vasa vasorum neovascularization and atherosclerosis progression in human coronary arteries (Herrmann *et al* 2001, Wilens and Plair 1965, O'Brien *et al* 1994, Barger *et al* 1984, Virmani *et al* 2000 and 2005, Kolodgie *et al* 2004). Studies have shown that the vasa vasorum were associated with arteriosclerotic disease, but were not present in nondiseased vessels. Since then, the vasa vasorum is considered responsible for atherogenesis (Nakata and Shionoya 1966, Mann 1978, Barger *et al* 1984 and 1990, Barker *et al* 1993 and 1994), coronary interventions (Cragg *et al* 1983, Kwon *et al* 1998, Sanada *et al* 1998), hypercholesterolemia (Kwon *et al* 1998, Herrmann *et al* 2001 and 2002, Wilson *et al* 2001, Cheema *et al* 2006) and hypertension (Marcus *et al* 1985, Kai *et al* 2002, Kuwahara *et al* 2002) which are the risk factors for atherosclerosis.

Veins generally do not develop atherosclerosis except when they are exposed to increased lumen pressure. Angiogenesis and inflammation are major contributors to the diseased vessel wall and the adventitial vasa vasorum facilitate both processes (Mulligan 2010). Altogether, studies conducted in human tissue clearly indicate that the combination of the presence of vasa vasorum and high intra-vascular blood pressure (Watelet *et al* 1997, Dashwood *et al* 2004), elevated plasma lipid concentrations (Steinberg 1983, Tarbell 2003) and coronary artery luminal endothelium damage are the key elements for developing the atherosclerotic plaques (Fuster *et al* 1992, Busse and Fleming 1996).

Imaging techniques of vasa vasorum

Atherosclerotic cardiovascular disease is the main cause of mortality in Europe (Lloyd-Jones *et al* 2010). Therefore, identifying "at-risk" cases, known as "vulnerable" patients is extremely important (Naghavi *et al* 2006). For this purpose, direct visualization of arterial vasa vasorum and intraplaque neovascularization can assist in the early detection of vulnerable atherosclerotic disease (Naghavi *et al* 2006, Feinstein 2008).

Noninvasive imaging is the prefered method for early detection of unstable or vulnerable plaques. It is safe and reliable. Current noninvasive imaging methods include carotid ultrasound, cardiovascular computed tomography (CT), single photon emission CT, cardiac magnetic resonance (CMR), positron emission tomography and hybrid technologies along with molecular imaging techniques (Naghavi *et al* 2006, Redberg *et al* 2003, Sanz and Fayad 2008, Choudhury and Fisher 2009, Piedra *et al* 2009, Raman *et al* 2008). Moreover, the use of ultrasound contrast agents (UCA) as a complementary tool to enhance vascular ultrasound imaging is emerging as a potentially important method in facilitating the detection and characterisation of atherosclerotic disease (Feinstein *et al* 2010).

Real time contrast-enhanced ultrasound (CEUS) can visualize vasa vasorum both in the adventitial layer and in the atherosclerotic plaque (Feinstein 2006, Granada and Feinstein 2008, Magnoni *et al* 2009, Shah *et al* 2007, Coli *et al* 2008, Staub *et al* 2010).

UCAs are gas-filled microbubbles that function as intravascular tracers which can be visualized using ultrasound as they circulate in the vasa vasorum (Granada and Feinstein 2008). Detailed information about their physical and chemical properties and their functionality is provided in chapter II. Contrast agent microbubbles behave as nonlinear resonators in an ultrasound field, whereas tissue scatters linearly. Considering the complex and variable morphology of plaques, limited resolution and associated motion artifact, precise quantification of plaque using linear ultrasound imaging (B-mode) is problematic mainly due to the low contrast to tissue ratio for vasa vasorum coronary imaging. One solution is to benefit from the nonlinear behavior of microbubbles- in contrast to linear tissue response- in vascular ultrasound imaging. Nonlinear behavior translates into the leakage of energy to harmonic multiples of the transmitting frequency. Therefore different techniques focused on harmonic imaging such as pulse inversion (Burns *et al* 2000) and power modulation (Brock-Fisher *et al* 1996) were developed.

Linear ultrasound transducers typically utilize frequencies between 7.5 and 10 MHz (Coll and Feinstein 2008). However, for carotid, intravascular coronary vasa vasorum imaging and small animal imaging which a higher spatial resolution is required, transmitting frequencies of 10 to 50 MHz are favored. (Feinstein 2004, Goertz *et al* 2006, Goertz *et al* 2007, Needles *et al* 2010). It is known that microbubbles perform best when they are insonified at or near their resonance frequencies (Vos *et al* 2011). The resonance frequencies of conventional UCA microbubbles range generally between 1 MHz and 8 MHz (Gorce *et al* 2000, Shi *et al* 2002, Feinstein 2004, and Sarkar *et al* 2005). Under these circumstances the performance of nonlinear imaging techniques is degraded because the driving frequency is higher than the resonance frequency (Needles *et al* 2010). In addition second harmonic imaging techniques are hampered because of the increase in the amplitude of harmonics produced by tissue as a result of nonlinear propagation of ultrasound (Tang *et al* 2010).

Why study subharmonics?

As an alternative harmonic imaging technique, the use of subharmonic emission (half the transmitting frequency) from the contrast agents was proposed as a new imaging modality (Shankar *et al* 1999, Forsberg *et al* 2000, Dayton *et al* 2002, Shi *et al* 2002). Tissue does not generate subharmonic energy and subharmonic imaging does not suffer from nonlinear propagation artifacts (Tang *et al* 2010). The subharmonic signal has a greater penetration distance since its attenuation is lower than the fundamental frequency, offering a potentially powerful diagnostic tool for clinical examinations (Lotsberg *et al* 1996, Krishna *et al* 1999, Shankar *et al* 1999, Shi *et al* 1999a, Chomas *et al* 2002, Bhagavatheeshwaran *et al* 2004, Goertz *et al* 2005, Forsberg *et al* 2007). The feasibility of using subharmonic energy to detect microvascularity has been shown in mice (Goertz *et al* 2005), in rabbit aortas (Goertz *et al* 2007, Needles *et al* 2010), in canines and patients with suspected portal hypertension (Eisenbrey *et al* 2011).

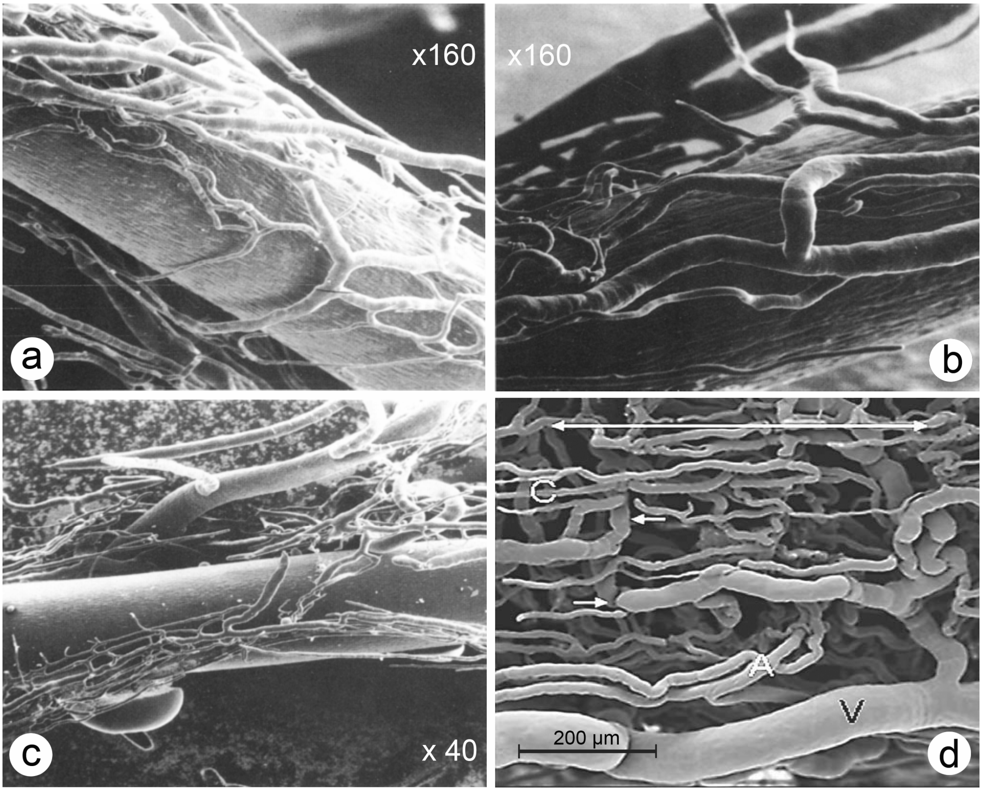

Fig 2. Vasa vasorum network on the surface of a) the ulnar artery of a cat, b) a facial artery of a rat, c) a radial artery of a dog and d) the human great saphenous vein. V= vein, A= Artery, C= capillary network. Reproduced with permission from Clower *et al* 1984 and Kachlik *et al* 2007.

Unlike the second and higher harmonic amplitudes that increase monotonically with the amplitude of the incident wave for moderate acoustic pressures (Leighton 1994, Chang *et al* 1995), a thresholding pressure exists for the generation of the subharmonic energy (Eller *et al* 1969, Shankar *et al* 1999). This threshold has two minima, one close to the resonance frequency of the microbubbles and another one close to twice that frequency (Katiyar *et al* 2011). Therefore, the insonation frequency, applied acoustic pressure and the size distribution of the contrast agent microbubbles including their physical properties are the important parameters in achieving an optimal subharmonic response suitable for imaging.

Another advantage of subharmonic emission is the possibility of combining it with other conventional imaging modalities such as pulse inversion and amplitude modulation. Subharmonic imaging can be easily implemented in commercial ultrasound scanners and optimize the performance of the system by cancelling the scattered signal from the tissue (Needles *et al* 2010). Figure 3 depicts the image taken from a chicken embryo with a commercial scanner (VisualSonics Inc. Toronto, Canada). The driving frequency is 18 MHz and an acoustic pressure of 200 kPa was applied. In this figure the B-mode image (a) and the subharmonic image combined with pulse inversion (b) are shown. As can be seen the distinction between the tissue and the contrast agent microbubbles is impossible in the B-mode image, while in the subharmonic image the scattered signal from the tissue is perfectly cancelled.

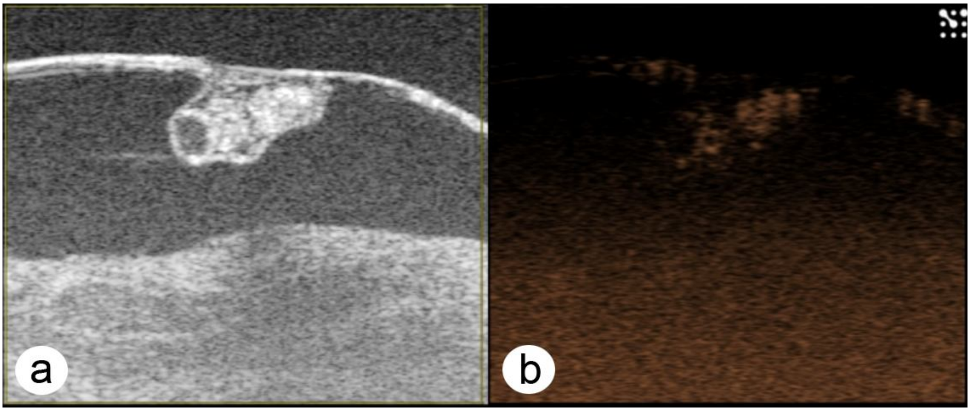

Fig 3. a) B-mode and b) subharmonic-pulse inversion images of a chicken embryo insonified at 18 MHz. Credits: Verya Daeichin (Erasmus MC).

Outline of this dissertation

The primary goal of this journey was to win the title of “The Pioneer of Subharmonic Carotid Imaging” in the future! This has not been achieved. Instead, this book takes you through all the author’s efforts to experimentally observe and understand the subharmonic behavior of contrast agent microbubbles which are the beginning steps towards the ultimate goal. This adventure uncovered many unseen new facets, bridged many barriers which had not been crossed since, and formed valuable collaborations.

This thesis is divided into two main parts. After presenting a review on the contrast agent modeling in chapter II, the next four chapters are dedicated to the characterization of different microbubbles by means of acoustical measurements (chapter III) or optical ultra-high speed imaging (chapters IV-VI). The second part of this book is focused on the methods to manipulate and enhance the subharmonic response of contrast agent microbubbles for carotid imaging purposes (chapters VII and VIII). In chapter IX, an alternative harmonic imaging method known as “second harmonic inversion” is explored. At last, the outcome of this study and the future perspectives are discussed and concluded in chapter X.

References

Barger AC, Beeuwkes R III, Lainey LL, Silverman KJ. 1984 Hypothesis: vasa vasorum and neovascularization of human coronary arteries. A possible role in the pathophysiology of atherosclerosis. N Engl J Med;310:175–7.

Barger AC, Beeuwkes R III. 1990 Rupture of coronary vasa vasorum as a trigger of acute myocardial infarction. Am J Cardiol;66:41G–43G.

Barker SG, Talbert A, Cottam S, Baskerville PA, Martin JF. 1993 Arterial intimal hyperplasia after occlusion of the adventitial vasa vasorum in the pig. Arterioscler Thromb;13:70–77.

Barker SG, Tilling LC, Miller GC, Beesley JE, Fleetwood G, Stavri GT, *et al* 1994 The adventitia and atherogenesis: removal initiates intimal proliferation in the rabbit which regresses on generation of a ‘neoadventitia’. Atherosclerosis;105:131–144.

Bhagavatheeshwaran G, Shi W T, Forsberg F and Shankar P M 2004 Sub-harmonic signal generation from contrast agents in simulated neovessels. Ultrasound Med Biol 30 199-203.

Busse R, Fleming I. 1996 Endothelial dysfunction in atherosclerosis. J Vasc Res;33:181–94.

Chang PH, Shung KK, Wu S and Levene HB 1995 Second harmonic imaging and harmonic doppler measurements with albunex IEEE transactions on ultrasonics, ferroelectrics, and frequency control 42 1020-1027.

Cheema AN, Hong T, Nili N, Segev A, Moffat JG, Lipson KE, *et al* 2006 Adventitial microvessel formation after coronary stenting and the effects of SU11218, a tyrosine kinase inhibitor. J Am Coll Cardiol;47:1067–75.

Chomas J, Dayton P, May D and Ferrara K 2002 Nondestructive subharmonic imaging IEEE Trans. Ultrason. Ferroelectr. Freq. Control 49 883-92.

Choudhury RP, Fisher EA. Molecular imaging in atherosclerosis, thrombosis, and vascular inflammation. 2009 Arterioscler Thromb Vasc Biol;29: 983–91.

Coli S, Magnoni M, Sangiorgi G, *et al* 2008 Contrast-enhanced ultrasound imaging of intraplaque neovascularization in carotid arteries: correlation with histology and plaque echogenicity. J Am Coll Cardiol;52:223–30.

Coll B, Feinstein SB. 2008 Carotid intimamedia thickness measurements: techniques and clinical relevance. Curr Atheroscler Rep;10:444 –450.

Clower BR., Sullivan DM., Smith RR., 1984 Intracranial vessels lack vasa vasorum, J Neurosurg 61:44-48.

Cragg AH, Einzig S, Rysavy JA, Castaneda-Zuniga WR, Borgwardt B, Amplatz K. 1983 The vasa vasorum and angioplasty. Radiology;148:75–80.

Dashwood MR, Anand R, Loesch A, Souza DS. 2004 Hypothesis: a potential role for the vasa vasorum in the maintenance of vein graft patency. Angiology;55:385–95.

Dayton PA and Ferrara KW 2002 Targeted imaging using ultrasound J Magn Reson Imaging 16 362-77.

Eisenbrey JR, Dave JK, Halldorsdottir VG, Merton DA, Machado P, Liu JB, Miller C, Gonzalez JM, Park S, Dianis S, Chalek CL, Thomenius KE, Brown DB, Navarro V, Forsberg F 2011 Simultaneous grayscale and subharmonic ultrasound imaging on a modified commercial scanner Ultrasonics 51 890-897.

Eller A and Flynn HG 1969 Generation of Subharmonics of Order One-Half by Bubbles in a Sound Field J Acoust Soc Am 46 722-727.

Feinstein SB 2004 The powerful microbubble: from bench to bedside, from intravascular indicator to therapeutic delivery system, and beyond American journal of physiology 287 450-457.

Feinstein SB. 2006 Contrast ultrasound imaging of the carotid artery vasa vasorum and atherosclerotic plaque neovascularization. J Am Coll Cardiol;48:236–43.

Feinstein SB. 2008 Non-invasive Surrogate Markers of Atherosclerosis. London, UK: Informa Healthcare;85–96.

Feinstein SB, Coll B, Staub D, *et al* 2010 Contrast enhanced ultrasound imaging. J Nucl Cardiol;17:106 –115.

Fleiner M, Kummer M, Mirlacher M, *et al* 2004 Arterial neovascularization and inflammation in vulnerable patients: early and late signs of symptomatic atherosclerosis. Circulation;110: 2843–50.

Forsberg F, Shi WT and Goldberg BB 2000 Subharmonic imaging of contrast agents Ultrasonics 38 93-8

Forsberg F, Catherine WP, Daniel AM, Juan JP and Anne LH 2007 Breast Lesions: Imaging with Contrast-enhanced Subharmonic US—Initial Experience Radiology 244 718-724.

Fuster V, Badimon L, Badimon JJ, Chesebro JH. 1992 The pathogenesis of coronary artery disease and the acute coronary syndromes (1 & 2). New England J Med;326:242–250.

Geiringer E. 1951 Intimal vascularization and atherosclerosis. J Pathol Bact 63:201–211.

Goertz DE, Frijlink ME, Tempel D, van Damme LC, Krams R, Schaar JA, Ten Cate FJ, Serruys PW, de Jong N and van der Steen AFW 2006 Contrast harmonic intravascular ultrasound: a feasibility study for vasa vasorum imaging Investigative radiology 41 631-638.

Goertz DE, Frijlink ME, Tempel D, Bhagwandas V, Gisolf A, Krams R, de Jong N and van der Steen AFW 2007 Subharmonic Contrast Intravascular Ultrasound for Vasa Vasorum Imaging Ultrasound Med. Biol. 33 1859-1872.

Gorce JM, Arditi M and Schneider M 2000 Influence of bubble size distribution on the echogenicity of ultrasound contrast agents: a study of SonoVue Investigative radiology 35 661-671.

Gössl M, Malyar NM, Rosol M, Beighley PE, Ritman EL. 2003 Impact of coronary vasa vasorum functional structure on coronary vessel wall perfusion distribution. Am J Physiol (Heart Circ Physiol) 285:H2019–26.

Granada JF, Feinstein SB. 2008 Imaging of the vasa vasorum. Nat Clin Pract Cardiovasc Med;5 Suppl 2:S18 –25.

Herrmann J, Lerman LO, Rodriguez-Porcel MG, Holmes DR Richardson DM, Ritman EL, *et al* 2001 Coronary vasa vasorum neovascularization precedes epicardial endothelial dysfunction in experimental hypercholesterolemia. Cardiovasc Res;51:762–766.

Herrmann J, Best PJ, Ritman EL, Holmes DR, Lerman LO, Lerman A, *et al* 2002 Chronic endothelin receptor antagonism prevents coronary vasa vasorum neovascularization in experimental hypercholesterolemia. J Am Coll Cardiol;39:1555–1561.

Kachlik D, Baca V, Stingl J, Sosna B, Lametschwandtner A, Minnich B, Setina M, 2007 Architectonic Arrangement of the Vasa Vasorum of the Human Great Saphenous Vein, J Vasc Res;44:157–166.

Kai H, Kuwahara F, Tokuda K, Shibata R, Kusaba K, Niiyama H, *et al* 2002 Coexistence of hypercholesterolemia and hypertension impairs adventitial vascularization. Hypertension;39:455–9.

Katiyar A and Sarkar K 2011 Excitation thresholds for subharmonic response of ultrasound contrast microbubbles POMA 11 020003.

Kolodgie FD, Virmani R, Burke AP, Farb A, Weber DK, Kutys R, Finn AV, Gold HK. 2004 Pathologic assessment of the vulnerable human coronary plaque. Heart 90: 1385–1391.

Krishna PD, Shankar PM and Newhouse VL 1999 Subharmonic generation from ultrasonic contrast agents Physics in medicine and biology 44 681-94.

Kuwahara F, Kai H, Tokuda K, Shibata R, Kusaba K, Tahara N, *et al* 2002 Hypoxia-inducible factor-1alpha/vascular endothelial growth factor pathway for adventitial vasa vasorum formation in hypertensive rat aorta. Hypertension;39:46–50.

Kwon HM, Sangiorgi G, Ritman EL, Lerman A, McKenna C, Virmani R, *et al* 1998 Adventitial vasa vasorum in balloon injured coronary arteries: visualization and quantitation by a microscopic threedimensional computed tomography technique. J Am Coll Cardiol 32:2072–2079.

Leighton T G 1994 The Acoustic Bubble (London: Academic Press Ltd.)

Lloyd-Jones D, Adams RJ, Brown TM, *et al* 2010 Heart disease and stroke statistics—2010 update. A report from the American Heart Association. Circulation 121:948 –54.

Lotsberg O, Hovem JM and Aksum B 1996 Experimental observation of subharmonic oscillations in infoson bubbles J. Acoust. Soc. Am. 99 1366-1369.

Magnoni M, Coli S, Marrocco-Trischitta M, *et al* 2009 Contrast-enhanced ultrasound imaging of periadventitial vasa vasorum in human carotid arteries. Eur J Echocardiogr 10:260–264.

Mann FD. 1978 Vasa vasorum and coronary atherosclerosis. Lancet;1:1319–20.

Marcus ML, Heistad DD, Armstrong ML, Abboud FM. 1985 Effects of chronic hypertension on vasa vasorum in the thoracic aorta. Cardiovasc Res;19:777–81.

Moreno PR, Purushothaman KR, Sirol M, Levy AP, Fuster V. 2006 Neovascularization in human atherosclerosis. Circulation 113:2245–2252.

Mulligan-Kehoe M.J. 2010 The vasa vasorum in diseased and nondiseased arteries, Am j Physiol Heart Circ Physiol 298 H295-H305.

Naghavi M, Falk E, Hecht HS, *et al* 2006 From vulnerable plaque to vulnerable patient—Part III: Executive summary of the Screening for Heart Attack Prevention and Education (SHAPE) Task Force report. Am J Cardiol;98:2H–15H.

Nakata Y, Shionoya S. 1966 Vascular lesion due to obstruction of the vasa vasorum. Nature;212:1258–1259.

Needles A, Arditi M, Rognin NG, Mehi J, Coulthard T, Bilan-Tracey C, *et al* 2010 Nonlinear contrast imaging with an array based micro-ultrasound system Ultrasound Med. Biol. 36 2097-2106.

O'Brien ER, Garvin MR, Dev R, Stewart DK, Hinohara T, Simpson JB, Schwartz SM. 1994 Angiogenesis in human coronary atherosclerotic plaques. Am J Pathol 145: 883–894.

Okuyama K, Yagimuna G, Takahashi T, Sasaki H, Mori S. 1988 The development of vasa vasorum of the human aorta in various conditions. A morphometric study. Archives of Pathol and Lab Medicine;112:721–5.

Piedra M, Allroggen A, Lindner JR. 2009 Molecular imaging with targeted contrast ultrasound. Cerebrovasc Dis;27 Suppl 2:66 –74.

Raman SV, Winner MW 3rd, Tran T, *et al* 2008 In vivo atherosclerotic plaque characterization using magnetic susceptibility distinguishes symptomproducing plaques. J Am Coll Cardiol Img 1:49 –57.

Redberg RF, Vogel RA, Criqui MH, Herrington DM, Lima JA, Roman MJ. 2003 34th Bethesda Conference: Task force #3-What is the spectrum of current and emerging techniques for the noninvasive measurement of atherosclerosis? J Am Coll Cardiol; 41:1886 –1898.

Ritman E.L. Lerman A. 2007 The dynamic vasa vasorum. Cardiovascular research 75 649-658.

Sanada JI, Matsui O, Yoshikawa J, Matsuoka T. 1998 An experimental study of endovascular stenting with special reference to the effects on the aortic vasa vasorum. Cardiovasc Intervent Radiol 21:45– 9.

Sanz J, Fayad ZA. 2008 Imaging of atherosclerotic cardiovascular disease. Nature 451:953–7.

Sarkar K, Shi WT, Chatterjee D and Forsberg F 2005 Characterization of ultrasound contrast microbubbles using in vitro experiments and viscous and viscoelastic interface models for encapsulation J Acoust Soc Am 118 539-550.

Shah F, Balan P, Weinberg M, *et al* 2007 Contrast-enhanced ultrasound imaging of atherosclerotic carotid plaque neovascularization: a new surrogate marker of atherosclerosis? Vasc Med 12:291–297.

Shankar PM, Krishna PD and Newhouse VL 1999 Subharmonic backscattering from ultrasound contrast agents J. Acoust. Soc. Am. 106 2104-10.

Shi WT, Forsberg F, Hall AL, Chiao RY, Liu JB, Miller S, Thomenius KE, Wheatley MA, Goldberg BB 1999 Subharmonic imaging with microbubble contrast agents: initial results Ultrason. Imaging 21 79-94.

Shi WT, Hoff L and Forsberg F 2002 Subharmonic performance of contrast microbubbles: an experimental and numerical investigation Ultrasonics Symposium Proceedings 2 1957-60

Staub D, Patel MB, Tibrewala A, *et al* 2010 Vasa vasorum and plaque neovascularization on contrast-enhanced carotid ultrasound imaging correlates with cardiovascular disease and past cardiovascular events. Stroke 41: 41–47.

Steinberg D. 1983 Lipoprotein and atherosclerosis. A look back and a look ahead. Arteriosclerosis;3:283–301.

Tang MX, Kamiyama N, Eckersley RJ 2010 Effects of Nonlinear Propagation in Ultrasound Contrast Agent Imaging Ultrasound Med. Biol. 36 459-466.

Tarbell JM. 2003 Mass transport in arteries and the localization of atherosclerosis. Ann Rev Biomed Eng 5:79–118.

Virmani R, Kolodgie FD, Burke AP, Farb A, Schwartz SM. 2000 Lessons from sudden coronary death: a comprehensive morphological classification scheme for atherosclerotic lesions. Arterioscler Thromb Vasc Biol 20: 1262–1275.

Virmani R, Kolodgie FD, Burke AP, Finn AV, Gold HK, Tulenko TN, Wrenn SP, Narula J. 2005 Atherosclerotic plaque progression and vulnerability to rupture: angiogenesis as a source of intraplaque hemorrhage. Arterioscler Thromb Vasc Biol 25: 2054–2061.

Vos HJ, Goertz DE, van der Steen AFW, de Jong N 2011 Parametric array technique for microbubble excitation IEEE transactions on ultrasonics, ferroelectrics, and frequency control 58 924-934.

Watelet J, Soury P, Menard JF, Plissonnier D, Peillon C, Lestrat JP, *et al* 1997 Femoropopliteal Bypass: In situ or reversed vein grafts? Ten-year results of a randomized prospective study. Am Vasc Surg 11:510–519.

Wilens SL, Plair CM. 1965 Blood cholesterol, nutrition, atherosclerosis. A necropsy study. Arch Intern Med 116: 373–380.

Wilson SH, Simari RD, Best PJ, Peterson TE, Lerman LO, Aviram M, *et al* 2001 Simvastatin preserves coronary endothelial function in hypercholesterolemia in the absence of lipid lowering. Arterioscler Thromb Vasc Biol 21:122–8.

Wolinsky H, Glagov S. 1967 Nature of species differences in the medial distribution of aortic vasa vasorum in mammals. Cir Res 20:409–421.

Chapter II

20 years of ultrasound contrast agent modeling

Telli Faez, Marcia Emmer, Klazina Kooiman, Michel Versluis, Antonius F W van der Steen, Nico de Jong

In Press, IEEE Trans Ultrason Ferroelectr Freq Control July 30, 2012

Abstract

The merit of UCAs was already discovered in the 1960s. It was however not before the 1990s that UCA were clinically approved and marketed. In these years it was realized that the UCA are not just efficient ultrasound scatterers, but that their main constituent, the coated gas microbubble, acts as a nonlinear resonator and as such is capable of generating harmonic energy. Subharmonic, ultraharmonic and higher harmonic frequencies of the transmitted ultrasound frequency have been reported. This opened up new prospects for their use and several detection strategies have been developed to exploit this harmonic energy to discriminate the contrast bubbles from surrounding tissue. This insight created a need for tools to study coated bubble behavior in an ultrasound field and the first models were developed. Since then 20 years have elapsed which resulted in broad range of UCA and UCA models. Where the models have helped in understanding the responses of coated bubbles, the influence of the coating has to date not been fully elucidated and UCA models are still being improved. The aim of this review is to offer an overview in these developments and indicate future directions.

INTRODUCTION

In 1968, it was reported that the injection of agitated saline in the aortic root resulted in “a cloud of echoes between the undulating margins of the aortic root" (Gramiak and Shah 1968). It appeared that gas `mini bubbles' in the agitated saline acted as great contrast enhancers. Normally blood is a poor ultrasound scatterer and it remains dark in an echo image. The addition of gas bubbles to the blood pool by Gramiak and Shah (Gramiak and Shah 1968) greatly increased the backscattered ultrasound, and resulted in an enhanced contrast between the aortic root wall and the blood. Nowadays, agitated saline is still used for the detection of right-to-left shunts in the heart (Soliman *et al* 2007).

Before gas bubbles could be widely applied as UCA, some improvements were necessary. Bubbles produced by agitation are both large and unstable. A gas bubble is unstable due to the surface tension between the gas core and the surrounding liquid, which forces the bubble to decrease in size. The rate can be calculated using the equation by Epstein and Plesset (1950) and the parameter values given by Chen *et al* (2002) that an air bubble with a diameter of 5 µm in air-saturated water disappears in approximately 125 ms and an air bubble with a diameter of 3 µm disappears in approximately 32 ms at room temperature and ambient pressure.

Moreover, the gas bubbles are effectively removed by the lungs. Unless administered by intracoronary or aortic root injection, the bubbles are unable to traverse the pulmonary circulation to opacify the left cardiac chambers. It takes at least 12 seconds for a contrast agent to pass from a peripheral vein (i.e. the site of injection) to the end-organ (Goldberg *et al* 2001). Thus to be useful in an echography study, the bubbles should persist in solution for several minutes and have a size smaller than 10 µm in diameter to be able to enter into the systemic circulation after an intravenous injection.

Coated microbubbles

It was found empirically that a small admixture of the patient's blood to the saline improves the stability and effectiveness of the agitated saline as a contrast agent (Blomley *et al* 2007). Surfactants from the blood form a coating around the gas core and promote the lifetime of the microbubble by greatly reducing the surface tension at the interface. Although this was known for many years, it was not before the end of 1980s that sufficiently stable microbubbles were marketed. In 1994 the first commercially available contrast agent, approved for human use in the USA, Albunex (Molecular Biosystems, San Diego, CA, USA), was up for sale. Albunex has a coating made of human serum albumin. The albumin coating forms an elastic solid shell around the gas core and is relatively stiff. It enhances the bubble's stability by supporting a strain to counter the effect of the surface tension, which is different compared to the nowadays more commonly used lipid coatings which act as surfactants.

The second commercial contrast agent, Levovist, was available soon after Albunex in Europe and Japan in 1996. Levovist (Bayer Schering Pharma AG, Berlin, Germany) consists of galactose microcrystals whose surfaces provide absorption sites on which air bubbles form when suspended in water. A trace amount of palmitic acid further stabilizes Levovist microbubbles. Since 1997 contrast agents are further stabilized by replacing the air core with high-molecular-weight inert gases such as perfluorocarbon, which have a lower solubility and diffusivity compared to air in aqueous liquids (Goldberg *et al* 2001). The perfluorocarbons are exhaled after several passes through the lungs. Examples of these kinds of agents are Optison (GE Healthcare, Chalfont St Giles, UK) that contains octafluoropropane and an albumin shell and SonoVue (Bracco, Milan, Italy) that has a sulfur hexafluoride core and a phospholipid coating. In the latter case the bubbles are not only efficient scatterers due to the stable gas core (Nand *et al* 2002), but also the relative flexibility of the lipid coating allows large bubble vibrations at low acoustic pressures without immediate bubble destruction (Chomas *et al* 2001, Bouakaz *et al* 2007). A summary of currently clinically available contrast agents is given in Table I and Figure 1.

Function of a contrast bubble

The contrast agent microbubbles owe their functionality to their highly compressible gas core in comparison with the surrounding liquid and tissue. This results in a high backscattering of the ultrasound wave. Moreover, the microbubbles can act as resonant systems with resonant frequencies within the same range as medical ultrasound frequencies. A resonant microbubble has a strong increase in scattering cross-section compared to nonresonant microbubbles, e.g. a free gas microbubble has a resonant scattering cross-section that is an order of a thousand times larger than its geometrical cross-section (Pace *et al* 1997).

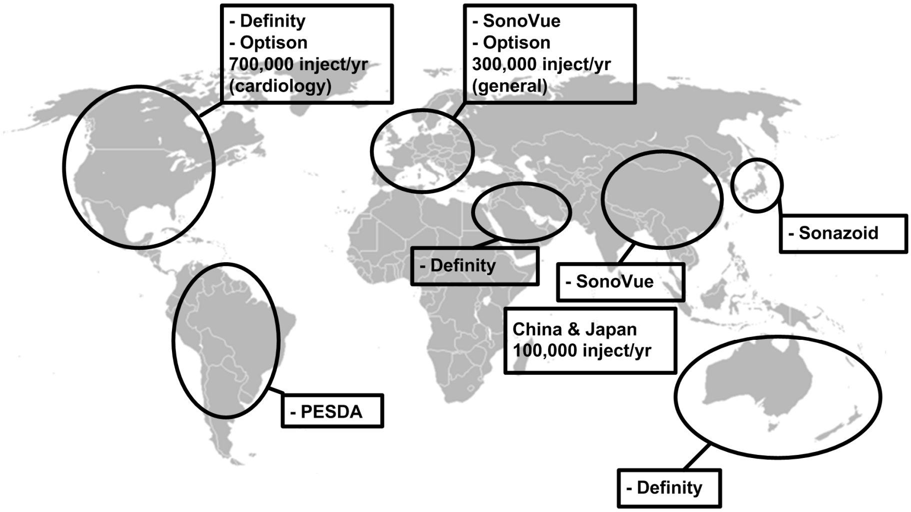

Fig 1. Estimated sales figures and availability of UCAs in 2010.

For a long time the backscattered ultrasound intensity from the microbubbles was considered to have small amplitudes, meaning linear oscillations only (Medvin 1977). In the search for methods to detect emboli in the blood circulation as a result of decompression sickness, researchers already investigated nonlinear bubble oscillations (Eatock *et al* 1985), but it was only realized in the mid-nineties that contrast agent microbubbles also produce harmonic energy, which can be used for imaging (Uhlendorf *et al* 1990, de Jong *et al* 1991, Schrope *et al* 1992).

The backscattered harmonic energy by the microbubbles may contain higher harmonic, subharmonic or even ultraharmonic energies (Schrope *et al* 1992, Shi and Forsberg 2000, Chomas *et al* 2002), while backscattered energy from tissue contains less or no harmonics. Therefore, harmonics can be used to differentiate the microbubbles from the tissue and further enhance the contrast between bubbles (in the blood vessels) and the surrounding tissue in an echo image. A few examples of imaging techniques that are based on the nonlinear response of the microbubbles are second harmonic imaging (Schrope and Newhouse 1993), pulse inversion imaging (Hope Simpson *et al* 1999), power modulation imaging (Brock-Fisher *et al* 1996), and combinations of these imaging techniques. Nowadays, these techniques have been implemented in commercial ultrasound systems and are widely used in the clinic.

The vast majority of contrast examinations worldwide are used for endocardial border delineation (van Camp *et al* 2007). In addition contrast enhanced ultrasound aids visualizing perfusion defects in the myocardium (Kaufmann *et al* 2007, Kaul 2008) and it increases the intensity of Doppler signals for the detection of blood flow. Radiology applications focus on cancer and peripheral vascular disease, where the estimation of microvascular density and flow rate is particularly important (Cosgrove 2006).

Table 1. Commercially available UCAs.

Name	Manufacturer	Year	Gas	Coating	Approved	Available
Echovist	Bayer Schering Pharma AG	1991	air	galactose	EU, Japan, Canada	-
Albunex	Molecular Biosystems	1994	air	human albumin	EU, USA, Canada	-
Levovist	Bayer Schering Pharma AG	1996	air	galactose, trace palmitin	Worldwide[1]	[2]
Optison	GE Healthcare AS	1997	C_3F_8	human albumin	EU, USA	EU, USA[3]
Definity	Lantheus Medical imaging	2001	C_3F_8	phospholipids	Worldwide[4]	Worldwide
SonoVue	Bracco SpA	2001	SF_6	phospholipids	Europe, China, S Korea, India, Hong Kong, Singapore	Europe, China, S Korea, India, Hong Kong, Singapore
Imagent	Alliance Pharmaceutical Corp	2002	C_6F_{14}	phospholipids	USA	-
Sonazoid	Amersham Health	2006	C_4F_{10}	phospholipids	Japan	Japan
BR38[5]	Bracco SpA	-	C_4F_{10} / N_2	phospholipids	-	-

[1]: Approved in 65 countries, but not in the USA
[2]: Expected to finish in 2010
[3]: Temporary not available 2006-2010
[4]: Approved in USA, Canada, Mexico, Israel, Europe, India, Australia, Korea, Singapore, UAE and New Zealand
[5]: In clinical development

Molecular imaging and therapeutic applications

Apart from the diagnostic application of coated microbubbles, in the past years, there has been great interest on the molecular imaging and therapeutic application of these bubbles (Hernot and Klibanov 2008, Bohmer *et al* 2009, Linder 2009, Gessner and Dayton 2009). The first therapeutic applications were based on fast microbubble collapses, which generated strong flows that were applied to induce cell damage, vascular injury (Skyba *et al* 1998) and the lysis of thrombus (Tachibana and Tachibana 1995). Oscillating microbubbles can also be used to locally trigger a transient increase in endothelial cell membrane permeability or opening of tight junctions between endothelial cells to allow delivery of therapeutics such as drugs or genes that normally cannot enter these cells or the underlying tissue (van Wamel *et al* 2006, Sheikov *et al* 2008, Juffermans *et al* 2009, Meijering *et al* 2009, Kooiman *et al* 2010). In addition, microbubbles can act as a drug delivery system and carry therapeutics to the affected location in the human body. Therapeutics can be attached to or incorporated into microbubbles and ultrasound is used to locally trigger their release (Bohmer *et al* 2009, Kooiman *et al* 2009). While the drugs may enter the endothelial cells or the underlying tissue, the microbubbles themselves will stay in the blood vessel.

Molecular imaging is a new discipline that unites molecular changes associated with diseases and *in vivo* imaging. For this purpose, microbubbles are composed such that they carry ligands on their surface (Ferrara *et al* 2009, Klibanov 2009). These ligands bind to specific sites on the vessel wall, such as receptors that are upregulated on endothelial cells within tumors or atherosclerotic plaques. The microbubbles indicate these sites by reflecting the ultrasound wave. The ligands are connected to the shell via a lipid, polymer or protein anchor. The strongest effective association and also the most widely used non-covalent specific interaction in biotechnology is (strept)avidin binding to biotin. Biotin is easily anchored to the microbubble shell components and there is a wide range of biotinylated ligands available. Subsequently, (strept)avidin acts as a bridge between the biotinylated bubble and the biotinylated ligand. This procedure has resulted in a large variety of available targeted bubbles. The disadvantage of this method is however that streptavidin is a foreign protein for the human body and that these agents will not be applicable in a clinical setting (Klibanov 2009). Covalent coupling methods to attach ligands to the microbubble shell have been developed for translation to human use (Wijkstra *et al* 2012).

MicroMarker (Bracco and VisualSonics, Toronto, Canada) is a hybrid form with a covalent bond between streptavidin and a lipid, and a non-covalent bond between streptavidin and the antibody. Visistar Integrin (Targeson, Inc, San Diego, CA, USA) is the first commercially available covalent targeted bubble. It is intended for pre-clinical use and consists of a standard lipid-perfluorocarbon microbubble with a peptide ligand bound to PEG-lipid. The principle target for this bubble is $\alpha_v\beta_3$ integrin, expressed in angiogenesis. BR55 (Bracco, Geneva, Switzerland) is the first targeted contrast agent tested in the clinic (Wijkstra *et al* 2012). This agent is functionalized with a heterodimer peptide targeting the vascular endothelial growth factor receptor 2 (VEGFR2) (Pochon *et al* 2010), which is upregulated in tumor vessels. The group of Lindner (Oregon Health & Science University, Portland, OR, USA) will develop their lipid coated decafluorobutane bubble (YSPSL-MB) for commercial use (Davidson *et al* 2010a, 2010b). This agent bears a recombinant dimeric human PSGL-1 binding moiety on its surface. It will bind to both P- and E-selectin to monitor ischemic injury over time as well as possible transplant rejection.

A special case of a targeted agent is Sonazoid. It is developed as a UCA to detect blood perfusion, but it can also be used as a targeted bubble. The phosphatidylserine in the coating functions as a marker of apoptosis on cell membranes. Macrophages and Kupffer cells will phagocytose cells expressing this marker. Hence Sonazoid is taken up by the macrophages and Kupffer cells and can be used to detect foci that lack active phagocytic capability, such as tumor nodes in the liver (Nakano *et al* 2008). Table II presents a summary of available UCA for molecular imaging.

Outline bubble models

Over the past few years a handful of reviews have been published with the aim of summarizing the physical principles and engineering of contrast agent microbubbles as well as their progressing applications in imaging and therapy (Bloch *et al* 2004, Qin *et al* 2009, Klibanov 2006, Kaul 2008). Recently Doinikov and Bouakaz (2011) have presented an exhaustive study on the existing contrast agent models. They compared the principle behind the derivation of each model and specifically the different formulations introduced for the shell parameters of the microbubbles.

The purpose of this chapter is to give an overview of contrast agent modeling developments over the past 20 years based on their applicability to the various developed contrast agents. For more insight into the mathematical derivation of each model the readers are referred to the complementary review of Doinikov and Bouakaz (2011). The contrast agent models discussed here are based on the Rayleigh-Plesset equation, which describes the motion of a gas bubble in a pressure field. We present the Rayleigh-Plesset equation in a fundamental form and briefly explain the role of damping in this equation. Furthermore we describe how in the limit of small-amplitude oscillations the Rayleigh-Plesset equation can be linearized to a form equivalent to that of a forced linear oscillator, which is often used to map out the parameter space from analytical modeling. The next step in the derivation of a contrast agent model is the implementation of the bubble coating. Where theory concerning the uncoated bubble is considered to be known, the influence of the coating is not fully understood yet. Over the last 20 years different models have been deduced and tested. These developments are driven by both the introduction of new UCA and insight in bubble behavior; see also the timeline in Fig. 2. To show the steps in the development of the coated bubble models, we arranged them according to the coating material and oscillation amplitude of the bubble.

Table II. Commercially available targeted contrast agents.

Name	**Manufacturer**	**Linker**	**Ligand**	**Target**	**Possible application**
Sonazoid	Amersham Health	NA[1]	NA[1]	Kupffer cells and macrophages	Liver tumors, ischemia / reperfusion injury
Micromarker	Bracco SpA	streptavidin	Biotinylated ligand of choice	biomarker of choice	depends on ligand
Targestar	Targeson, Inc.	streptavidin	Biotinylated ligand of choice	biomarker of choice	depends on ligand
Visistar Integrin	Targeson, Inc.	covalent to PEG-lipid	cyclic RGD peptide	$\alpha_v\beta_3$ integrin	angiogenesis
Visistar VEGFR2[2]	Targeson, Inc.	covalent to PEG-lipid		VEGF-like protein	angiogenesis
YSPSL-MB[2]	Oregon H&S University	covalent to PEG-lipid	PSGL-1	P and E selectin	ischemia / reperfusion injury transplant rejection
BR55[3]	Bracco SpA	covalent to PEG-lipid	Heterodimer peptide	VEGFR2	angiogenesis
Selectin agent[2]	Bracco SpA	streptavidin	biotinilated PSGL-1 analogue	P and E selectin	Inflammatory disease

[1]: “Passive” targeting, phagocytic uptake of the bubbles by cells

[2]: In development

[3]: In clinical development

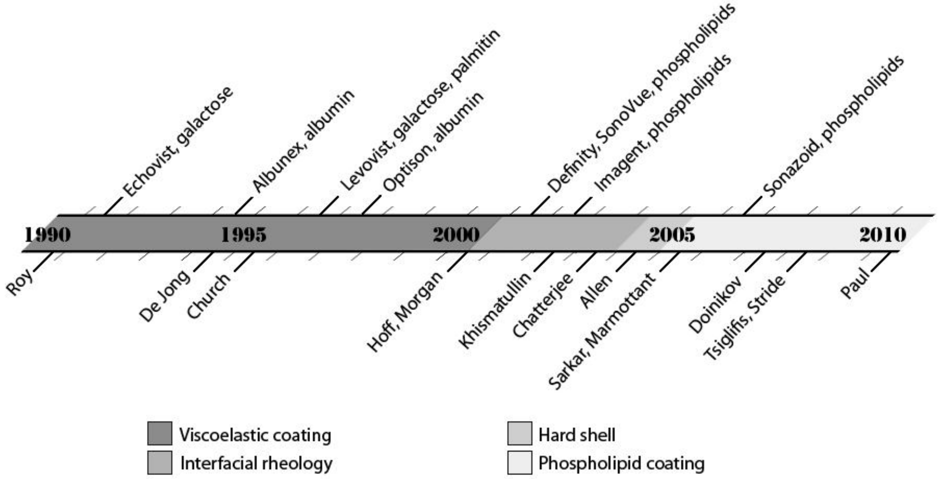

Fig 2. Timeline displaying contrast agent modeling developments. Top) approval date for clinical use of contrast agents. Bottom) Publication date of model indicated by first author.

FREE GAS BUBBLE MODEL

The Rayleigh-Plesset equation

Lord Rayleigh pioneered the research on the motion of bubbles by studying the inertial cavitation, nearly 60 years after the earliest studies done by Besant on the collapse and growth of a spherical cavity within a continuous liquid medium (Besant 1859). Inertial cavitation intrigued many when it became apparent that during the collapse of a gas cavity significant amounts of energy are released, high enough to seriously damage screw-propellers of ships. In 1917 Rayleigh considered the collapse of an empty cavity in a liquid (Rayleigh 1917). This cavity remained spherical at all times and was located in an incompressible liquid.

The main step from cavitation towards bubble dynamics was the introduction of a variable external driving pressure and the influence of surface tension by Plesset (1949). Plesset described the dynamics of vapor-filled bubbles and Noltingk and Neppiras (1950) did the same for gas-filled bubbles. The effect of viscosity on the equation of motion of a bubble in an incompressible liquid was considered by Poritsky. These contributions led together to the Rayleigh-Plesset-Noltingk-Neppiras-Poritsky (RPNNP) equation (Lauterborn 1976). Starting from the Navier-Stokes equations assuming liquid incompressibility and including viscous effects in the boundary conditions we arrive at this equation, which is nowadays known as the ‘Rayleigh-Plesset’ equation (Leighton 1994):

$$\begin{aligned}\rho_l\left(R\ddot{R}+\frac{3}{2}\dot{R}^2\right)&=\left(p_0+\frac{2\sigma}{R_0}-p_\upsilon\right)\left(\frac{R_0}{R}\right)^{3\kappa}\\&\quad+p_\upsilon-\frac{2\sigma}{R}-\frac{4\mu\dot{R}}{R}-p_0-P(t)\end{aligned} \qquad (1)$$

Modified Rayleigh-Plesset equations

In the first coated bubble models, the liquid surrounding the bubble was considered incompressible and the `standard' Rayleigh-Plesset (RP) equation (Eq. 1) was applied. More recent models include liquid compressibility and they are based on modified versions of the RP equation. In an incompressible liquid, the speed of sound would be infinite. When the bubble wall has a speed much lower than the speed of sound $\dot{R} << c$, this is a valid assumption. Therefore for large bubble oscillations ($R_{max} / R_0 > 2$, $\dot{R} > 0.01 \cdot c$), an extended version of the RP equation should be used, such as formulations from the Herring-Keller/Keller-Miksis or Gilmore-Akulichev families (Vokurka 1986). These equations incorporate radiation damping. For low acoustic pressures it is not necessary to include radiation damping to describe the motion of the bubble accurately, but for higher acoustic pressures bubble vibrations with larger amplitudes are expected and a more robust and accurate equation may serve as a basis for the coated bubble model, such as the following modified version of the Rayleigh-Plesset equation, which is popular in the field of sonoluminescence (Brenner *et al* 2002):

$$\begin{aligned}\rho_l\left(R\ddot{R}+\frac{3}{2}\dot{R}^2\right)&=\left(p_0+\frac{2\sigma}{R}\right)\left(\frac{R_0}{R}\right)^{3\kappa}\left(1-\frac{3\kappa}{c}\dot{R}\right)\\&-\frac{2\sigma}{R}-\frac{4\mu_l\dot{R}}{R}-p_0-P(t)\end{aligned} \quad (2)$$

Harmonic oscillator

Assuming that the bubble oscillates in the small-amplitude limit, it is possible to linearize the RP equation using $R = R_0(1+x(t))$ and arrive to the equation for a forced harmonic oscillator (Leighton 1994, Hilgenfeldt *et al* 1998):

$$\ddot{x}+\omega_0\delta\dot{x}+\omega_0^2x=F(t) \quad (3)$$

Where χ is the relative radial excursion, $F(t) = F_0 \sin(\omega t)$ is the acoustic forcing term, $\omega_0 = 2\pi f_0$, δ is the dimensionless damping coefficient and f_0 is the resonance frequency.

Damping in the equation of motion

Damping reduces the amplitude of oscillations of the bubble. For an uncoated gas bubble energy losses by damping occur through three mechanisms (Leighton 1994)

- **Radiation damping:** Energy is radiated away from the bubble as acoustic waves.
- **Viscous damping:** Work is done against viscous forces.
- **Thermal damping:** Energy is lost through thermal conduction between the gas and the surrounding liquid.

Viscous damping is independent of the insonation frequency in a Newtonian fluid. It is the dominant source of damping for microbubbles with a resting diameter of 2 µm, but its influence diminishes as the size of the bubble increases. Typically the radiation damping is neglected at low frequencies, while thermal damping is neglected at high frequencies. The physical background of the transition from low to high frequency is related to resonance and highly depends on the bubble size. It is in the order of 1 MHz for bubbles with resting diameter of 10 µm and 10 MHz for bubbles of 1 µm diameter (Leighton 1994).

Thermal damping is often neglected in the RP equation (Leighton and Dumbrell 2004). For the time-dependent nonlinear oscillations of bubbles thermal damping requires rigorous treatments that are not easily incorporated (e.g. Nigmatulin *et al* 1981, Prosperetti 1991, Preston *et al* 2002), which is therefore one of the reasons it is often neglected or it is replaced by a `thermal viscosity' (e.g. van der Meer *et al* 2007). However it should be noted that this might not always be valid. Moreover, all else being equal, thermal damping is generally less for a bubble of perfluorocarbon or other fluorine-containing gas relative to an air bubble due to the differences in the thermal properties of the gases. For gas bubbles with a size of 10 µm diameter that are insonified below 0.6 MHz, thermal damping is the dominant source of damping at almost 100 % of the total damping (Leighton 1994).

For a coated bubble energy is lost through a fourth source of damping, which is viscous energy dissipation in the viscoelastic coating material. It has been shown that the coating is the major source of damping for coated bubbles. Based on optical observations, van der Meer *et al* (2007) reported a 70% contribution of the shell on the total damping of SonoVue lipid-coated bubbles. Where the damping mechanisms of an uncoated bubble are fully understood, the influence of the coating is still an open subject of study and coated bubble modeling in this direction is still evolving.

Damping reduces the amplitude of the bubble oscillations and it widens the resonance curve of the bubble. The linear analytical solution for the resonance frequency (or resonance curve) can therefore be used to compare the experimental resonance curve of the coated bubbles with simulated data of the free gas bubble as to estimate the values for the viscous damping parameters (van der Meer *et al* 2007, chapter V). In the frequency domain the contribution of damping is relatively small and the resonance frequency is very close to the undriven natural frequency of the bubble.

SOFT SHELL BUBBLE MODELS

UCA models can generally be divided into two categories: UCA models for bubbles with soft coating materials such as albumin or phospholipids and those for hard coatings like polymers. UCA available in the early 1990s were mainly composed of materials such as galactose and albumin, which are less flexible than the phospholipid coatings that are currently more frequently used (see Table I) and softer than polymers.

An albumin shell consists of denatured albumin, approximately 15 nm thick (Church 1995, Chomas *et al* 2001a). The albumin forms a relatively stiff structure around the gas core. The coating of phospholipid bubbles consists of a monolayer of phospholipids and is much thinner (1-2 nm) than the albumin shells. The flexible nature of a lipid monolayer and the smaller shell thickness allow larger oscillation amplitudes compared to an albumin coating. Hit by a relatively high acoustic pressure (>150 kPa) the lipid coated bubble may loose gas and lipids due to gas diffusion and lipid shedding, but the bubble may persist albeit with a smaller diameter (Borden *et al* 2005). Guidi *et al* (2010) show that deflation of lipid-coated bubbles is an interesting phenomenon, which can be useful for bubble characterization. Acoustic driven deflation of lipid-coated bubbles is different from the destruction mechanism of albumin-coated bubbles. The albumin coating cracks when the bubble is insonified with a significant acoustic pressure. The cracked bubble exhibits static diffusion with a dissolution rate comparable to that of an uncoated bubble (Chomas *et al* 2001b).

Early models considered the albumin coating as a solid elastic layer. Therefore they all modeled the UCA coating with constant properties. To current standards this seems only valid when the contrast agent bubble oscillates with very small amplitude. However in those early years of UCA modeling not much was known about the oscillation of individual contrast bubbles. Available data consisted mainly of acoustic measurements such as scatter and attenuation measurements (de Jong *et al* 2009). The application of high-speed imaging provided more insight in the oscillations of individual bubbles and initiated the development of models suitable to predict larger oscillations of soft shell (phospholipid-coated) bubbles, which will be further discussed in the following sections. Figure 3 shows a few examples of optical techniques from which input for modeling was obtained.

Viscoelastic shell models

With the arrival of the first commercially available contrast agent Albunex, a need for tools to study UCA behavior was created and the first models for coated bubbles were formulated. In these early days the starting point for modeling was not the bubble as a harmonic oscillator, on the contrary, the bubbles were supposed to be detected by transient cavitation. Roy *et al* (1990) defined a model that predicted transient cavitation thresholds for Albunex. A generalized form of the RP equation was obtained including a surface layer and boundary conditions for the interfaces between the gas, the surface layer and the liquid. The surface layer was considered to be a simple viscous liquid.

In the early 1990s also the first publications describing the generation of second harmonic energy by the bubbles appeared (Uhlendorf *et al* 1990, de Jong *et al* 1991, Schrope *et al* 1992). It was realized that at low acoustic pressures the contrast bubbles are also capable of `stable cavitation'. The bubbles are able to radiate ultrasound over a prolonged time. Moreover it appeared that the backscattered ultrasound contained higher harmonics in addition to the fundamental frequency, which was soon found extremely useful for contrast agent detection.

In search of methods to detect emboli in the blood circulation as a result of decompression sickness, Eatock *et al* (1985) already used a RP model in 1985. They used this model to study the magnitude of the nonlinear effect in the scattering of ultrasound by nitrogen bubbles in water in the medical diagnostic frequency and acoustic pressure range. In 1994 de Jong *et al* extended the RP equation with pressure terms modeling the coating of an Albunex contrast bubble and demonstrated that the nonlinear behavior of the contrast bubbles can be used to discriminate them from surrounding water or tissue. Two shell parameters were implemented in the equation of motion to capture the influence of the relatively stiff Albunex coating. It was assumed to behave as a viscoelastic solid and was described by the shell elasticity S_p and shell friction S_f. Their values were determined under linear conditions for Albunex microbubbles by fitting calculated acoustic transmission and scattering values to measurements (de Jong and Hoff 1993, de Jong *et al* 2009).

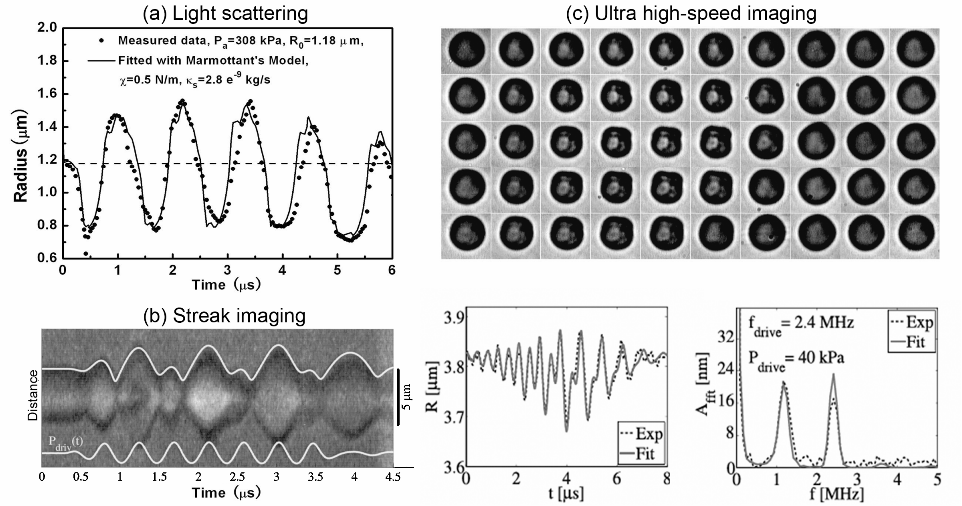

Fig 3. Experimental techniques from which input is obtained for modeling. a) Light scattering; radius-time curve of a Definity microbubble driven at 1 MHz with an acoustic pressure of 308 kPa, reproduced with permission from Tu *et al* (2011), b) streak imaging of a 2.6 μm radius bubble excited at 2.4 MHz with a seven-cycle pulse at an acoustic pressure of 360 kPa, reproduced with permission from Morgan *et al* (2000) and c) Optical images of a 3 μm radius BR14 microbubble recorded by ultra high-speed imaging, driven at 2.4 MHz and an acoustic pressure of 40 kPa. The two plots below indicate the radius-time curve (left) and the corresponding power spectrum (right) of a 3.8 μm radius bubble, reproduced with permission from Sijl *et al* (2010).

De Jong and coworkers added the coating in an ad hoc way to the RP equation. Church was already involved in the formulation of the model by Roy *et al* (1990) and extended this model with the Kelvin-Voigt constitutive law to describe the Albunex coating in 1995 (Church 1995). He accounted for the thickness and viscoelastic properties of the shell by applying essentially Hooke's law for an incompressible material predicting the stresses developing on the shell for small displacements. The model became one of the most frequently used models, especially after Hoff reformulated it in the limit of small shell thickness in comparison with the bubble radius (Hoff *et al* 2000). This approach has a more rigorous theoretical basis compared to the model by de Jong *et al*. However both models assume that the bubble is surrounded by an incompressible Newtonian liquid and the encapsulation is a viscoelastic solid.

Khismatullin and Nadim (2002) derived a model applying the Kelvin-Voigt constitutive equation to investigate the effect of a compressible and viscoelastic liquid to the coated bubble dynamics. The Newtonian liquid was simulated using a 4-constant Oldroyd model. They found that the effect of the compressibility and viscosity of the liquid was outweighed by the influence of the coating. More recently developed models such as the ones by Morgan *et al* (2000); Marmottant *et al* (2005); Tsiglifis and Pelekasis (2008) include a slightly compressible liquid, which is less complicated compared to the 4-constant Oldroyd model. However, these studies do not quantify how much the assumption of slightly compressible liquid contributes to the accuracy of the prediction of the bubble response.

Surfactant coated models

Small amplitude oscillations

More insight in the nature of the albumin shell and the development of phospholipid-coated bubbles resulted in the next generation of UCA models. Where the first UCA models treated the albumin coating as a solid elastic layer, these models consider the coating both albumin and phospholipid as a surfactant.

Morgan *et al* (2000) investigated the experimental contrast agent MP1950 (Mallinckrodt ,Inc., St. Louis, MO) composed of a decafluorobutane core coated with a flexible monolayer of phospholipid molecules. To account for the higher bubble wall speeds as a result of the higher flexibility of the phospholipid coating, they used the modified Herring equation (Vokurka 1986), which includes radiation damping. The coating is described as a surfactant, which influences the implementation of the coating elasticity. For this term Morgan *et al* (2000) applied the derivation by Glazman (1983). The coating viscosity was implemented following the formulation of Church (1995).

Morgan *et al* (2000) were the first who used optical data of individual bubbles to determine the values of the shell parameters, see Fig. 3b. Theoretical predictions were fitted to radius-time curves derived from images acquired with a streak camera. The accuracy of the shell parameters determined from individual bubble experiments is higher than parameters acquired in the more common bulk measurements (de Jong *et al* 2009). On the other hand studies have shown that equally sized bubbles can respond very differently to the same ultrasound field (Emmer *et al* 2009, chapter IV). This indicates that there is a large variation in the properties of individual bubbles. Kooiman *et al* (2010) have recently investigated the distribution of lipids over the coating surface in fluorescence confocal microscopy studies. For each contrast bubble different lipid distributions were observed which may be the cause of individual coating properties.

The study by Morgan *et al* (2000) pioneered in the use of high-speed imaging to investigate coating properties of individual bubbles and modeling phospholipid coated bubbles treated as surfactants. However, after a few years it was demonstrated by Marmottant *et al* (2005) that the pressure contribution derived for the elasticity in Morgan *et al*'s model leads to unrealistic high surface tension values and a modification was necessary.

Although an albumin coating has a larger thickness compared to a phospholipid coating, Chatterjee and Sarkar (2003) argue that also the albumin shell should not be considered as a solid layer since this coating is only a few molecules thick. They apply a Newtonian interfacial rheological model to simulate the behavior of Optison, which is the successor of Albunex. The coatings of both agents are similar, but the gas core has been replaced by C_3F_8. In this model only viscous interfacial stresses are taken into account. As a result also this model predicted unrealistic values for the surface tension of the albumin coating.

To solve this problem Sarkar *et al* (2005) extended the model by Chatterjee and Sarkar (2003) with an elasticity term. They compared the outcome of the model by Chatterjee and Sarkar (2003) 'the Newtonian interface model', their new model 'the viscoelastic interface model' and the model by Hoff *et al* (2000) with the experimental data on their merit of predicting subharmonics. It was found that the Newtonian model, predicting the unrealistic high surface tension values, was superior compared to the other two models. They concluded that a new model predicting subharmonics without the unrealistic surface tension values should contain a 'softening' of the encapsulation by assuming a surface dilatational elasticity constant that decreases with an increasing fractional area. More recent models dedicated to large amplitude oscillations of surfactant-coated agents follow this trend and include coating parameters that vary with the bubble surface area (Paul *et al* 2010).

The last model assuming small bubble oscillations described here is the model by Doinikov and Dayton (2007). They developed a theoretical description of lipid-coated microbubbles whereby instead of the Kelvin-Voigt constitutive law, the linear Maxwell constitutive law was applied. For a finite-thickness shell, this model contains six parameters (relaxation time λ, shear viscosity η_s, surface tension coefficients σ_1 and σ_2, density ρ_s and thickness of the shell R_2 - R_1) to describe the coating. For a zero-thickness shell model these parameters reduce to viscosity and relaxation time instead of shell elasticity and viscosity, the two shell parameters used in the Kelvin-Voigt equation. This Maxwell model was used to investigate the influence of these different shell properties on the resonant behavior of coated bubbles.

Large amplitude oscillations

The contrast agent bubble models described so far all include the coating as a material with constant properties. The responses of different types of agents are simulated using the same model. The values of the coating parameters are simply adapted for the different shell compositions. However, with the expanding clinical use of phospholipid coated bubbles it became clear that the previous models simulating small amplitude oscillations do not suffice. To predict the responses of lipid-coated agents more sophisticated models are necessary.

Phospholipid UCA detection strategies are mainly based on imaging at low acoustic pressures. At these pressures the backscattered ultrasound by these bubbles is already significant due to the flexibility of the phospholipid coating. Although a low acoustic pressure suggests that the bubbles oscillate with small amplitude and thus exhibit linear responses, recent studies have shown that this assumption cannot be sustained. The term 'linear response' refers to a response that relates to the transmit frequency only and has an amplitude that is linearly proportional to the amplitude of the acoustic pressure. As a consequence of the latter condition any acoustic pressure should lead to a bubble vibration. All small amplitude models fulfill this condition. However experimental data shows differently. Optical high-speed recordings of individual bubbles revealed that the onset of bubble vibration of some lipid bubbles is suppressed by what is termed as 'thresholding' behavior (Emmer *et al* 2007). No bubble oscillations were observed below a certain acoustic pressure threshold (order of 10-100 kPa). It was not excluded that these bubbles did respond at acoustic pressures below the threshold value, but it was apparent that these responses are very small and even though at first sight it can be argued whether they are relevant for clinical use, the fact that these bubbles have a strong response at a slightly higher pressure makes them extremely useful for clinical use, e.g. for power modulation imaging (Brock-Fisher *et al* 1996).

In addition to thresholding behavior, high-speed recordings displayed “compression-only” behavior of the lipid-coated bubbles (de Jong *et al* 2007). Bubbles exhibiting this behavior showed no or little expansion phase, but only compression in response to a symmetric ultrasound pressure field. This type of response is highly nonlinear and the backscattered ultrasound by the bubble contains significant amounts of harmonic energy including subharmonic energy (Sijl *et al* 2007), see Figure 3c. To predict thresholding and compression-only behavior, models with constant coating properties developed for small amplitude (i.e. linear) oscillations do not suffice.

The first model dedicated to the nonlinear behavior of lipid coated bubbles was proposed by Marmottant *et al* (2005). Surface tension measurements on phospholipid monolayers in Langmuir-Blodgett balances showed the dependence of the surface tension on the surface concentration of the phospholipid molecules. Inspired by this effect, Marmottant *et al* incorporated in their model an ad hoc effective surface tension, which accounts for the coating elasticity. Depending on the bubble radius (and thus the concentration of phospholipid molecules) the coating can be in three different regimes: buckled, elastic, and ruptured. When the bubble is compressed, the coating material is condensed which leads to buckling, and with the bubble coating in such a tensionless state, the resulting surface tension is zero. When the bubble is expanded the coating may be ruptured and the gas core will be exposed to the surrounding liquid, leading to a surface tension of that of the gas-liquid interface. In the intermediate elastic regime, the coating is assumed to behave elastically and the model is similar to that of de Jong *et al* (1994).

Where the papers by Emmer *et al* (2007) and de Jong *et al* (2007) already speculated on the influence of the shell on the thresholding and compression-only behavior, the effective surface tension in the Marmottant model appeared to be the key to simulate the observed phenomena. More importantly, Overvelde *et al* (2010) showed that the surface tension of the bubble at rest, which is directly related to the ambient phospholipids concentration, is crucial in determining the bubble response. Typically the bubble starts off in the elastic regime, where it is relatively stiff. Its resonance frequency is high and driven below resonance it will not easily oscillate. An increasing acoustic pressure can modify the concentration of lipid molecules on the bubble's surface, forcing the bubble into the buckling regime, which suddenly reduces its stiffness, resulting in a much lower frequency of maximum response. Consequently, its oscillation amplitude will sharply rise, as the bubble is tuned more into resonance, in very good agreement with the thresholding behavior observed previously. Sijl and coworkers showed through a weakly nonlinear analysis that the rapid change of the bubble stiffness leads to a boost of the nonlinear behavior of the bubbles. Bubbles with a resting surface tension near the buckling regime show compression-only behavior (Sijl *et al* 2011) and were observed to oscillate in subharmonic modes at acoustic pressures down to 5 kPa. The change of shell elasticity upon insonation reduces the subharmonic threshold pressure to values far below those of the free gas bubbles (5 vs. 50-80 kPa) (Sijl *et al* 2010). It should also be noted that the shell has its main influence when the bubble is insonified at driving frequencies below its resonance frequency (Sijl *et al* 2008). Above resonance inertia dominates.

Marmottant *et al* (2005) did not investigate the influence of the coating viscosity on the bubble responses. Recent studies have revealed that the shell viscosity is dilatation rate dependent and it shows shear thinning behavior (Morgan *et al* 2000, van der Meer *et al* 2007, and chapter IV). Doinikov *et al* (2009) showed that by using the Church model (1995) as a basis and expanding the coating viscosity from a constant to $\kappa\left(\dot{R}/R\right)=\kappa_0+\kappa_1\,\dot{R}/R$, one can also predict compression-only behavior. This may serve as a beginning for further investigation on the influence of shell viscosity on the bubble behavior.

Recent studies focused on replacing the ad hoc surface tension law in the Marmottant model by a more accurate definition to avoid unphysical transitions from one regime into the other (Sijl *et al* 2011). Paul *et al* (2010) argue that the boundaries of the different regimes of the surface tension are not easily established and propose extensions to the linear Hooke law instead. They test a quadratic elasticity model (interfacial elasticity varying linearly with area fraction) and an exponential elasticity model (elasticity varying exponentially) on their merit predicting subharmonic responses. They found that these models predict lower subharmonic threshold values and therefore match better with their experimental values than the Marmottant model.

Tsiglifis and Pelekasis (2008) chose a more extensive and rigorous approach to model nonlinear lipid coated bubble behavior such as threshold behavior. In their paper, the Keller-Miksis equation was chosen to model the bubble dynamics. The coating is regarded as a continuum and is described by an elasticity G and viscosity μ_s. The elasticity is however not a constant, but varies with bubble deformation, which is defined by a strain softening Mooney-Rivlin or a strain hardening Skalak law. In case of strain hardening this means that the stress-strain relationship of the coating exhibits a larger slope when the bubble deformations increase. This essentially amounts to an increased apparent elasticity modulus in the bubble model. The opposite holds for the strain softening law. In their model the amount of strain softening or hardening is controlled with a control parameter. Tsiglifis and Pelekasis (2008) explain that the strain-softening of the shell coating may lead to the threshold behavior. A bubble driven below its resonance frequency responds with relatively low amplitude to the ultrasound field. Increasing the acoustic pressure may drive the bubble's resonance frequency due to the strain-softening nature of the shell towards the ultrasound frequency which results in a nonlinear increase of the bubble's response. The sudden increase in bubble response, or thresholding behavior, were calculated for acoustic pressures much higher (> 400 kPa) than the values observed by Overvelde *et al* (2010).

Doinikov and Bouakaz (2010) model threshold behavior in a different way. They propose a criterion in which the microbubble oscillation starts when the acoustic pressure amplitude exceeds a certain magnitude. They found radius-dependent threshold amplitude, which fits to the experimental data by Emmer *et al* (2007). The authors indicate that further research is required to understand the specific rheological laws that can be applied to describe this threshold amplitude.

Stride (2008) defined a model that although it was not specifically meant for large deformations, both the coating elasticity and viscosity are dependent on the instantaneous radius. The coating viscosity and elasticity do not follow a constitutive law, but a description of interfacial tension for insoluble films. For the surface tension a power law is applied with these parameters: σ_0 the surface tension of the resting bubble, K the proportionality constant and x the exponent of the power law. The viscosity is described by an exponential law including η_{s0} and Z which are constants for a specific surfactant and R_x which is the buckling radius comparable to the buckling radius defined by Marmottant *et al* (2005).

HARD SHELL BUBBLE MODELS

UCA with polymer shells were already introduced in 1990 by Wheatley *et al* The polymer shell is typically very stiff and does not vibrate significantly when insonified at low acoustic pressures (<200 kPa). The polymer UCA is activated once the acoustic pressure is high enough to crack the shell and thereby releases the gas content of the bubble (Bouakaz *et al* 2005). A gas bubble temporarily generates a high backscatter of the ultrasound wave. In 1990s different imaging strategies had been developed based on UCA destruction such as transient response imaging (Porter *et al* 1995) or using the decorrelation of echoes from successive pulses in Doppler modes such as harmonic power Doppler (Burns *et al* 1992) or pulse inversion imaging (Hope Simpson *et al* 1999). The signal-to-noise ratios (SNR) of polymer UCA used in these imaging methods are competitive with those of phospholipid coated UCA. Less favorable is that these SNR's are obtained at higher acoustic pressures which destroys the agent and makes real time imaging impossible.

None of the polymer UCA available was clinically approved. In 1996 Point Biomedical Corp. (San Carlos, CA) was established, which marketed several polymer UCA such as PB127. PB127 (CARDIOsphere) was tested in different clinical trials (Wei *et al* 2003, Main *et al* 2006). However no approval by the FDA followed and in 2008 Point Biomedical had to cease its activities. Currently there is a renewed interest in using polymer UCA (Bevan *et al* 2007) for high frequency (HF) imaging (Ketterling *et al* 2007) and its potential as a drug or gene carrier (Lentacker *et al* 2006, Kooiman *et al* 2009).

The nowadays still popular model by Hoff *et al* (2000) was originally developed to model an experimental UCA from Nycomed (Nycomed Amersham, Oslo, Norway), composed of air bubbles encapsulated in a polymer shell. This model, as described previously, considers a viscoelastic behavior for the polymer shell and is thereby only valid for small amplitude oscillations of the polymer bubbles. Taking into account that imaging polymer UCA occurs mainly at higher acoustic pressures, this model seems to have limited value to predict polymer encapsulated bubble responses. In 2004, Allen and Rashid (2004) defined a model to predict large amplitude oscillations of polymer bubbles. They did not consider UCA specifically, but treated polymer spheres in general. The polymer shell is relatively stiff and was therefore assumed to have a neo-Hookean elastic response. It was modeled having certain elasticity, but no shell viscosity was defined. This model does not incorporate the destruction of the polymer coating necessary for many imaging methods.

Marmottant *et al* (2011) formulated a model for solid shelled bubbles that does include shell rupture. This model is based on their model for soft lipid coated bubbles (Marmottant *et al* 2005). The model for solid shells incorporates an effective membrane tension, which allows the bubble to be in three states. Upon compression a negative tension builds up. As soon as the tension is negative enough, the coating starts to buckle and the membrane tension vanishes. The elastic state is recovered when the volume returns to its resting value. When the membrane tension exceeds a certain threshold value for coating rupture, the bubble ruptures and the membrane tension saturates to the surface tension of the gas-water interface. This state is irreversible, which is in contrast to the ruptured state for lipid coated bubbles. This model has been successfully tested in an experimental study on biodegradable polymeric microcapsules for selective ultrasound-triggered drug release by Lensen *et al* (2011).

DISCUSSION

The introduction of new UCA is the primary driving force for the development of new contrast agent bubble models, see also Fig. 2. The first contrast agent bubbles had relatively stiff shells and as a consequence a `simple' Kelvin-Voigt linear elastic relationship sufficed to predict their dynamic behavior when driven by an acoustic pressure. Currently contrast agents with lipid coatings are used in the clinic and it has become clear that models that include linear coating properties fail to predict experimentally observed radial bubble responses. The development of high-speed imaging of contrast bubbles has contributed to this insight. Optical recordings of lipid coated bubbles revealed `threshold' and `compression-only' behavior, which cannot be predicted without the use of a nonlinear material law for the contrast bubble coating.

The assumption of a viscoelastic behavior following the Kelvin-Voigt material law, results in a parameterization of the coating into three parameters; the coating thickness, its elasticity and viscosity. The advantage of using such a relatively simple law is that also in other areas this law is frequently applied and reasonable values for the coating parameters are known or can be measured in separate tensile tests. For other parameters such as the surface tension, the same advantage holds, its physical limits are known. For more complicated material laws with an increasing number of parameters the accuracy of its application and resulting parameter values are much more difficult to verify. Material laws are often developed for different research areas such as cell membranes or pulmonary surfactants with different requirements for the studied material. A major difference is that the contrast bubble vibrates in the MHz frequency range whereas material properties are in most cases tested at Hz frequencies. In addition we note that sophisticated material laws can incorporate multiple parameters to describe the influence of the coating. An increasing number of parameters often results in an improved fit between simulation and experiment, but has the drawback that the merit of the applied material law and the resulting parameterization cannot be judged easily.

In the past, bulk acoustic measurements on the whole population of contrast bubbles were employed to determine the values of the shell elasticity and viscosity constants. Using these kinds of measurements assumes that the coating parameters are independent of bubble size and equal for each contrast bubble in the population. There is increasing evidence based on high-speed recordings of individual contrast bubbles that this is not the case in reality. Coating properties may differ based on the bubble size. In addition it has been observed that individual responses of similar sized lipid coated bubbles can vary widely, indicating variations in the lipid distribution and concentration of the individual coatings. This should be accounted for when studying the responses of individual bubbles. Besides studying the responses of individual contrast agent bubbles, high-speed recordings are useful to study the influence of additional ligands and bubble adherence on the bubble dynamics, which is essential for future use of bubbles in therapeutic and molecular imaging applications. Initial results have shown changes in bubble resonance frequencies due to bubble attachment (Overvelde *et al* 2011), which may be a way to characterize bound versus unbound bubbles (i.e. to recognize bubbles targeted to the affected site) in the human body.

While discussions concerning the best approach of coated bubble modeling are ongoing, it is important to mention that the basis of all bubble models itself, the `Rayleigh-Plesset equation', can also be debated as the best choice to investigate bubble behavior. Applying the Rayleigh-Plesset equation assumes for example that the bubble remains spherical and is located in free space. However high-speed recordings have revealed that bubble oscillations in the presence of a wall are far from spherical (Vos *et al* 2008). Moreover it can be expected that a significant amount of bubbles in the blood circulation is situated near a (vascular) wall which additionally affects oscillation amplitudes (Caskey *et al* 2006, Garbin *et al* 2007, Thomas *et al* 2009, Overvelde *et al* 2011). Figure 4 illustrates a few cases for which additional contrast modeling work is needed.

To model the interaction between bubble and wall a finite element modeling (FEM) approach may be considered, see for example Pauzin *et al* (2007). An additional reason to consider this method for bubble modeling is the increasing use of coated bubbles for therapeutic and molecular imaging. These applications profit from the interaction between bubbles and the vascular wall, which may be modeled using a FEM approach.

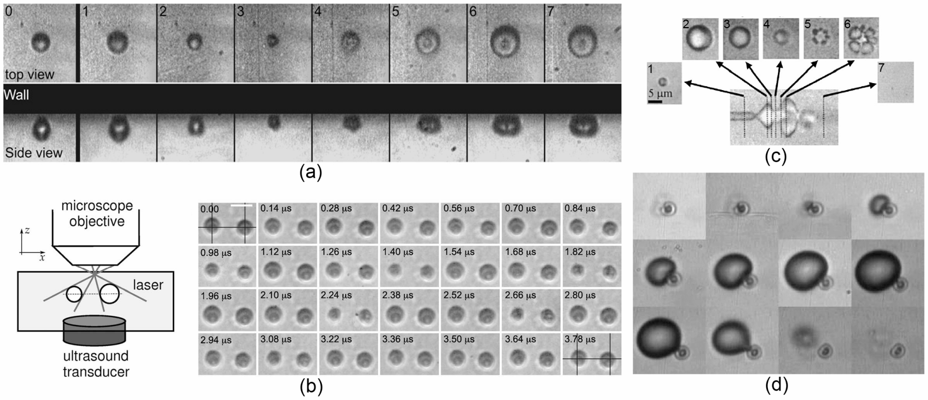

Fig 4. A few cases for which additional contrast modeling work is needed. a) Non-spherical oscillations and bubble/wall interactions, reproduced with permission from Vos *et al* (2011), b) bubble/bubble -interactions, reproduced with permission from Garbin *et al* (2009), c) rupture of soft shelled agent, reproduced with permission from Chomas *et al* (2000) and d) rupture of hard-shelled agent, reproduced with permission from Postema *et al* (2005).

Acknowledgement--Although the authors take full responsibility for the content of this paper, we acknowledge the advise and help we received from colleague researchers around the world. In particular we would like to thank Alexander Klibanov (University of Virginia), Joshua Rychak (Targeson Inc), Sibylle Pochon (Bracco Research, SA) and Jonathan Linder (Oregon Health & Science University) for their advice on the molecular imaging section. Peter Frinking (Bracco Research, SA) and Paula Miller (Lantheus Medical Imaging) provided information on the availability of UCA.

References

Allen, J., Rashid, M., 2004. Dynamics of a hyperelastic gas-filled spherical shell in a viscous fluid. J Appl Mech 71, 195-200.

Besant, W., 1859. A treatise on hydrodynamics. Cambridge University Press. Cambridge.

Bevan, P., Karshafian, R., Tickner, E., Burns, P., 2007. Quantitative measurement of ultrasound disruption of polymer-shelled microbubbles. Ultrasound Med Biol 33 (11), 1777-1786.

Bloch, S. H., Dayton, P. A., Ferrara, K. W., 2004. Targeted imaging using ultrasound contrast agents. IEEE Eng Med Biol Mag 4, 18-29.

Blomley, M., Claudon, M., Cosgrove, D., 2007. WFUMB safety symposium on ultrasound contrast agents: clinical application and safety concerns. Ultrasound Med Biol 33 (2), 180-186.

Bohmer, M., Klibanov, A., Tiemann, K., Hall, C., Gruell, H., Steinbach, O., 2009. Ultrasound triggered image-guided drug delivery. Eur J Radiol 70 (2), 242-53.

Borden, M., Kruse, D., Caskey, C., Zhao, S., Dayton, P., Ferrara, K., 2005. Influence of lipid shell physicochemical properties on ultrasound-induced microbubble destruction. IEEE Trans Ultrason Ferroelectr Freq Control 52 (11), 1992-2002.

Bouakaz, A., de Jong, N., 2007. WFUMB safety symposium on echocontrast agents: nature and types of ultrasound contrast agents. Ultrasound Med Biol 33 (2), 187-196.

Bouakaz, A., Versluis, M., de Jong, N., 2005. High-speed optical observations of contrast agent destruction. Ultrasound Med Biol 31 (3), 391-399.

Brenner, M., Hilgenfeldt, S., Lohse, D., 2002. Single-bubble sonoluminescence. Rev Mod Phys 74 (2), 425-484.

Brock-Fisher, G., Poland, M., Rafter, P., 1996. Means for increasing sensitivity in non-linear ultrasound imaging systems. US patent no 5577505.

Burns, P., Powers, J., Fritzsch, T., 1992. Harmonic imaging: New imaging and doppler method for contrast enhanced us. Radiology 185 (P), 142.

Caskey, C., Kruse, D., Dayton, P., Kitano, T., Ferrara, K., 2006. Microbubble oscillation in tubes with diameters of 12, 25, and 195 microns. Appl. Phys. Lett. 88, 33902-33905.

Chatterjee, D., Sarkar, K., 2003. A newtonian rheological model for the interface of microbubble contrast agents. Ultrasound Med Biol 29 (12), 1749-1757.

Chen, W., Matula, T., Crum, L., 2002. The disapearance of ultrasound contrast bubbles: observations of bubble dissolution and cavitation nucleation. Ultrasound Med Biol 28 (6), 793-803.

Chomas, J.E., Dayton, P.A., May, D., Allen, J., Klibanov, A., Ferrara, K. 2000. Optical observation of contrast agent destruction. Appl. Phys. Lett. 77, 1056-1059.

Chomas, J., Dayton, P., Allen, J., Morgan, K., Ferrara, K., 2001a. Mechanisms of contrast agent destruction. IEEE Trans Ultrason Ferroelectr Freq Control 48 (1), 232-248.

Chomas, J., Dayton, P., May, D., Ferrara, K., 2001b. Threshold of fragmentation for ultrasonic contrast agents. J Biomed Opt 6 (2), 141-150.

Chomas, J., Dayton, P., May, D., Ferrara, K., 2002. Nondestructive subharmonic imaging. IEEE Trans Ultrason Ferroelectr Freq Control 49 (7), 883-892.

Church, C., 1995. The effects of an elastic solid surface layer on the radial pulsations of gas bubbles. J Acoust Soc Am 97 (3), 1510-1521.

Cosgrove, D., 2006. Ultrasound contrast agents: An overview. Eur J Radiol 60 (3), 324-330.

Davidson, B., Chadderdon, S., Belcik, T., Gupta, T., Bettinger, T., Schneider, M., Lindner, J., 2010a. Ischemic memory imaging with a selectin-targeted microbubble contrast agent: eficacy and safety testing in a nonhuman primate model of myocardial ischemia. Circulation 122 (suppl. 21: A12763).

Davidson, B., Kaufmann, B., Belcik, T., Yue, Q., Lindner, J., 2010b. Molecular imaging using recombinant psgl-1 as a pan-selectin targeting moiety provides prolonged and selective tissue enhancement for detecting recent ischemia. Circulation 122 (suppl. 21: A12649).

de Jong, N., Cornet, R., Lancffee, C., 1994. Higher harmonics of vibrating gas-filled microspheres. part one: simulations. Ultrasonics 32 (6), 447-453.

de Jong, N., Emmer, M., Chin, C., Bouakaz, A., Mastik, F., Lohse, D., Versluis, M., 2007. \compression-only" behavior of phospholipid-coated contrast bubbles. Ultrasound Med Biol 33 (4), 653-656.

de Jong, N., Emmer, M., van Wamel, A., Versluis, M., 2009. Ultrasonic characterization of ultrasound contrast agents. Med Biol Eng Comput 47 (8), 861-873.

de Jong, N., Hoff, L., 1993. Ultrasound scattering properties of albunex microspheres. Ultrasonics 31 (3), 175-181.

de Jong, N., Ten Cate, F., Lancffee, C., Roelandt, J., Bom, N., 1991. Principles and recent developments in ultrasound contrast agents. Ultrasonics 29 (4), 324-330.

Doinikov, A., Dayton, P., 2007. Maxwell rheological model for lipid-shelled ultrasound microbubble contrast agents. J Acoust Soc Am 121 (6), 3331-3340.

Doinikov, A., Haac, J., Dayton, P., 2009. Modeling of nonlinear viscous stress in encapsulating shells of lipid-coated contrast agent microbubbles. Ultrasonics 49 (2), 269-275.

Doinikov, A., Bouakaz, A., 2010. Theoretical model for the threshold onset of contrast microbubble oscillations. J Acoust Soc Am 127 (2), 649-651.

Doinikov, A., Bouakaz, A., 2011. Review of shell models for contrast agent microbubbles. IEEE Trans Ultrason Ferroelect Freq Control 58 , 981-993.

Eatock, B., Nishi, R., Johnston, G., 1985. Numerical studies of the spectrum of low-intensity ultrasound scattered by bubbles. J Acoust Soc Am 77 (5), 1692-1701.

Emmer, M., van Wamel, A., Goertz, D., de Jong, N., 2007. The onset of microbubble vibration. Ultrasound Med Biol 33 (6), 941-949.

Emmer, M., Vos, H., Versluis, M., de Jong, N., 2009. Radial modulation of single microbubbles. IEEE Trans Ultrason Ferroelect Freq Control 56 (11), 2370-2379.

Epstein, P., Plesset, M., 1950. On the stability of gas bubbles in liquid-gas solutions. J Chem Phys 18 (11), 1505-1509.

Ferrara, K., Borden, M., Zhang, H., 2009. Lipid-shelled vehicles: engineering for ultrasound molecular imaging and drug delivery. Acc Chem Res 42 (7), 881-92.

Garbin, V., Cojoc, D., Ferrari, E., Di Fabrizio, E., Overvelde, M.L.J., van der Meer, S.M., de Jong, N., Lohse, D., Versluis, M. 2007. Changes in microbubble dynamics near a boundary revealed by combined optical micromanipulation and high-speed imaging. Appl. Phys. Lett. 90, 114103-114106.

Garbin, V., Dollet, B., Overvelde, M.L.J., Cojoc, D., Di Fabrizio, E., van Wijngaarden, L., Prosperetti, A., de Jong, N., Lohse D., Verluis, M. 2009. History force on coated microbubbles propelled by ultrasound. Phys. Fluids 21, 092003-092010.

Gessner, R., Dayton, P., 2010. Advances in molecular imaging with ultrasound. Mol Imaging 9 (3), 117-127.

Glazman, R., 1983. Effects of adsorbed films on gas bubble radial oscillations. J Acoust Soc Am 74 (3), 980-986.

Goldberg, B., Raichlen, J., Forsberg, F., 2001. Ultrasound Contrast Agents, Basic principles and clinical applications, 2nd edition. Martin Dunitz, London.

Gramiak, R., Shah, P., 1968. Echocardiography of the aortic root. Invest Radiol 3 (5), 356-366.

Guidi, F., Vos, H., Mori, R., de Jong, N., Tortoli, P., 2010. Microbubble characterization through acoustically induced deation. IEEE Trans Ultrason Ferroelect Freq Contr 57, 193-202.

Hernot, S., Klibanov, A., 2008. Microbubbles in ultrasound-triggered drug and gene delivery. Adv Drug Del Rev 60 (10), 1153-1166.

Hilgenfeldt, S., Lohse, D., Zomack, M., 1998. Response of bubbles to diagnostic ultrasound: a unifying theoretical approach. Eur Phys J B 4, 247-255.

Hoff, L., Sontum, P., Hovem, J., 2000. Oscillations of polymeric microbubbles: Effect of the encapsulating shell. J Acoust Soc Am 107 (4), 2272- 2280.

Hope Simpson, D., Chin, C., Burns, P., 1999. Pulse inversion doppler: A new method for detecting nonlinear echoes from microbubble contrast agents. IEEE Trans Ultrason Ferroelectr Freq Control 46 (2), 372-382.

Juffermans, L., van Dijk, A., Jongenelen, C., Drukarch, B., Reijerkerk, A., de Vries, H., Kamp, O., Musters, R., 2009. Ultrasound and microbubble induced intra- and intercellular bioeffects in primary endothelial cells. Ul8 trasound Med Biol 35 (11), 1917-1927.

Kaufmann, B., Wei, K., Lindner, J., 2007. Contrast echocardiography. Curr Probl Cardiol 32 (2), 51-96.

Kaul, S., 2008. Myocardial contrast echocardiography: a 25-year retrospective. Circulation 118 (3), 291-308.

Ketterling, J., Mamou, J., Allen III, J., Aristizabal, O., Williamson, R., Turnbull, D., 2007. Excitation of polymer-shelled contrast agents with high-frequency ultrasound. J Acoust Soc Am 121 (1), EL 48- EL 53.

Khismatullin, D., Nadim, A., 2002. Radial oscillations of encapsulated microbubbles in viscoelastic liquids. Physics of uids 14 (10), 3534-3557.

Klibanov, A., 2006. Microbubble contrast agents, targeted ultrasound imaging and ultrasound-assisted drug-delivery applications. Invest Radiol 41, 354-362.

Klibanov, A., 2009. Preparation of targeted microbubbles: ultrasound contrast agents for molecular imaging. Med Biol Eng Comput 47 (8), 875-82.

Kooiman, K., Bohmer, M., Emmer, M., Vos, H., Chlon, C., Shi, W., Hall, C., de Winter, S., Schroen, K., Versluis, M., de Jong, N., van Wamel, A., 2009. Oil-filled polymer microcapsules for ultrasound-mediated delivery of lipophilic drugs. J Control Release 133 (2), 109-118.

Kooiman, K., Emmer, M., Foppen-Harteveld, M., van Wamel, A., de Jong, N., 2010. Increasing the endothelial layer permeability through ultrasound activated microbubbles. IEEE Trans Biomed Eng 57 (1), 29-32.

Lauterborn, W., 1976. Numerical investigation of nonlinear oscillations of gas bubbles in liquids. J Acoust Soc Am 59 (2), 283-293.

Leighton, T., 1994. The acoustic bubble. Academic Press Limited, London.

Leighton, T., Dumbrell, H., 2004. New approaches to contrast agent modelling. Journal of Physics: Conference Series 1, 91-96.

Lensen, D., Gelderblom, E. C., Vriezema, D. M., Marmottant, P., Verdonschot, N., Versluis, M., de Jong, N., van Hest, J.C.M. 2011. Biodegradable polymeric microcapsules for selective ultrasound-triggered drug release. Soft Matter 7, 5417-5422.

Lentacker, I., De Geest, B., Vandenbroucke, R., Peeters, L., Demeester, J., De Smedt, S., Sanders, N., 2006. Ultrasound-responsive polymer-coated microbubbles that bind and protect dna. Langmuir 22 (7), 7273-7278.

Lindner, J., 2009. Molecular imaging of cardiovascular disease with contrast enhanced ultrasonography. Nat Rev Cardiol 6, 475481.

Main, M., Ehlgen, A., Coggins, T., Morris, B., Lanza, P., Tremblay, T., Schiller, N., Goldman, J., 2006. Pulmonary hemodynamic effects of dipyridamole infusion in patients with normal and elevated pulmonary artery systolic pressure receiving pb127. J Am Soc Echocardiogr 19 (8), 1038- 1044.

Marmottant, P., van der Meer, S., Emmer, M., Versluis, M., de Jong, N., Hilgenfeldt, S., Lohse, D., 2005. A model for large amplitude oscillations of coated bubbles accounting for buckling and rupture. J Acoust Soc Am 118 (6), 3499-3505.

Marmottant, P., Bouakaz, A., de Jong, N., Quillet, C., 2011. Buckling resistance of solid shell bubbles. J Acoust Soc Am 129 (3).

Medwin, H., 1977. Counting bubbles acoustically: a review. Ultrasonics 15, 7-13.

Meijering, B., Juffermans, L., van Wamel, A., Henning, R., Zuhorn, I., Emmer, M., Versteilen, A., Paulus, W., van Gilst, W., Kooiman, K., de Jong, N., Musters, R., Deelman, L., Kamp, O., 2009. Ultrasound and microbubble-targeted delivery of macromolecules is regulated by induction of endocytosis and pore formation. Circ Res 104 (5), 679-87.

Morgan, K., Allen, J., Dayton, P., Chomas, J., Klibanov, A., Ferrara, K., 2000. Experimental and theoretical evaluation of microbubble behavior: effect of transmitted phase and bubble size. IEEE Trans Ultrason Ferroelect Freq Contr 47 (6), 1494-1509.

Nakano, H., Ishida, Y., Hatakeyama, T., Sakuraba, K., Hayashi, M., Sakurai, O., Hataya, K., 2008. Contrast-enhanced intraoperative ultrasonography equipped with late kupffer-phase image obtained by sonazoid in patients with colorectal liver metastases.World J Gastroenterol 14 (20), 3207-3211.

Nanda, N., Wistran, D., Karlsberg, R., Hack, T., Smith, W., Foley, D., Picard, M., Cotter, B., 2002. Multicenter evaluation of sonovue for improved endocardial border delineation. Echocardiography 19 (1), 27-36.

Nigmatulin, R., Khabeev, N., Nagiev, F., 1981. Dynamics, heat and mass transfer of vapour-gas bubbles in liquid. Int J Heat Mass Trans 24, 1033-1044.

Noltingk, B., Neppiras, E., 1950. Caviation produced by ultrasonics. Proc Phys Soc London B 63, 674-685.

Overvelde, M., Garbin, V., Sijl, J., Dollet, B., de Jong, N., Lohse, D., Versluis, M., 2010. Nonlinear shell behavior of phospholipid-coated microbubbles. Ultrasound Med Biol 36 (12), 2080-2092.

Overvelde, M., Garbin, V., Dollet, B., De Jong, N., Lohse, D., Versluis M., 2011. Dynamics of coated microbubbles adherent to a wall. Ultrasound Med Biol 37, 1500-1508.

Pace, N., Cowley, A., A.M., C., 1997. Short pulse acoustic excitation of microbubbles. J Acoust Soc Am 102 (3), 1474-1479.

Paul, S., Katiyar, A., Sarkar, K., Chatterjee, D., Shi, W., Forsberg, F., 2010. Material characterization of the encapsulation of an ultrasound contrast microbubble and its subharmonic response: Strain-softening interfacial elasticity model. J Acoust Soc Am 127 (6), 3846-3857.

Pauzin, M.-C., Mensah, S., Lefebvre, J.-P., 2007. Development of a finite element model of ultrasound contrast agent. IEEE Ultrasonics Symposium, 1989-1992.

Plesset, M., 1949. The dynamics of cavitation bubbles. J Appl Mech 16, 277-282.

Pochon, S., Tardy, I., Bussat, P., Bettinger, T., Brochot, J., von Wronski, M., Passantino, L., Schneider, M., 2010. Br55: a lipopeptide-based vegfr2-targeted ultrasound contrast agent for molecular imaging of angiogenesis. Invest Radiol 45 (2), 89-95.

Porter, T., Xie, F., Kilzer, K., 1995. Intravenous peruorocarbon-exposed sonicated dextrose albumin produces myocardial ultrasound contrast that correlates with coronary blood ow. J Am Soc Echocardiogr 8, 710-718.

Postema, M., Bouakaz, A., Versluis M., de Jong, N. 2005. Ultrasound-Induced Gas Release from Contrast Agent Microbubbles. IEEE Trans. Ultrason. Ferroelectr. Freq. Control 52, 1035-1041.

Preston, A., Colonius, T., Brennen, C., 2002. A reduced-order model of heat transfer effects on the dynamics of bubbles. Proceedings of ASME FEDSM'02.

Prosperetti, A., 1991. The thermal behaviour of oscillating gas bubbles. J Fluid Mech 222, 587-616.

Qin, S., Caskey C. F., Ferrara, K. W., 2009. Ultrasound contrast microbubbles in imaging and therapy: physical principles and engineering. Phys Med Biol 54, 681-694.

Rayleigh, L., 1917. On the pressure developed in a liquid during collapse of a spherical cavity. Philosophical Magazine 34, 94-98.

Roy, R., Madanshetty, S., Apfel, R., 1990. An acoustic backscattering technique for the detection of transient cavitation produced by microsecond pulses of ultrasound. J Acoust Soc Am 87 (6), 2451-2458.

Sarkar, K., Shi, W., Chatterjee, D., Forsberg, F., 2005. Characterization of ultrasound contrast microbubbles using in vitro experiments and viscous and viscoelastic interface models for encapsulation. J Acoust Soc Am 118 (1), 539-50.

Schrope, B., Newhouse, V., 1993. Second harmonic ultrasonic blood perfusion measurement. Ultrasound Med Biol 19 (7), 567-79.

Schrope, B., Newhouse, V., Uhlendorf, V., 1992. Simulated capillary blood flow measurement using a nonlinear ultrasonic contrast agent. Ultrasonic Imaging 14 (2), 134-158.

Sheikov, N., McDannold, N., Sharma, S., Hynynen, K., 2008. Effect of focused ultrasound applied with an ultrasound contrast agent on the tight junctional integrity of the brain microvascular endothelium. Ultrasound Med Biol 34 (7), 1093-1104.

Shi, W., Forsberg, F., 2000. Ultrasonic characterization of the nonlinear properties of contrast microbubbles. Ultrasound Med Biol 26 (1), 93-104.

Sijl, J., Dollet, B., Overvelde, M., Garbin, V., Rozendal, T., de Jong, N., Lohse, D., Versluis, M., 2010a. Subharmonic behavior of phospholipid coated ultrasound contrast agent microbubbles. J Acoust Soc Am 128 (5), 3239-3252.

Sijl, J., Overvelde, M., Dollet, B., Garbin, V., de Jong, N., Lohse, D., Versluis, M., 2010b. “compression-only" behavior of single ultrasound contrast agent microbubbles. J Acoust Soc Am 129 (5), 1729-1739.

Skyba, D., Price, R., Linka, A., Skalak, T., Kaul, S., 1998. Direct in vivo visualization of intravascular destruction of microbubbles by ultrasound and its local effects on tissue. Circulation 98, 290-293.

Soliman, O., Geleijnse, M., Meijboom, F., Nemes, A., Kamp, O., Nihoy, annopoulos, P., Masanid, N., Feinstein, S., Ten Cate, F., 2007. The use of contrast echocardiography for the detection of cardiac shunts. Eur J of Echocardiography 8 (3), s2-s12.

Stride, E., 2008. The influence of surface adsorption on microbubble dynamics. Phil Trans R Soc 366, 2103-2115.

Tachibana, K., Tachibana, S., 1995. Albumin microbubble echo-contrast material as an enhancer for ultrasound accelerated thrombolysis. Circulation 92 (5), 1148-1150.

Thomas, D., Emmer, M., Vos, H., Sboros, V., de Jong, N., 2009. Optical observations of microbubble oscillation in small tubes. IEEE Ultrasonics Symposium, 2782-2784.

Tsiglifis, K., Pelekasis, N., 2008. Nonlinear radial oscillations of encapsulated microbubbles subject to ultrasound: The effect of membrane constitutive law. J Acoust Soc Am 123 (6), 4059-4070.

Tu J., Swalwell, J. E., Giraud, D., Cui, W., Chen, W., Matula, T. J. 2011. Microbubble sizing and shell characterization using flow cytometry. IEEE Trans. Ultrason. Ferroelectr. Freq. Control 58, 955-963.

Uhlendorf, V., Fritsch, T., Siegert, J., 1990. Ultraschallverfahren und schaltungen zu deren durchführung. German Patent, publication numer: WO/1990/002517, awarded to Schering AG, Berlin, Germany.

van Camp, G., Droogmans, S., Cosyns, B., 2007. Bio-effects of ultrasound contrast agents in daily clinical practice: fact or fiction? Eur Heart J 28, 1190-1192.

van der Meer, S., Dollet, B., Voormolen, M., Chin, C., Bouakaz, A., de Jong, N., Versluis, M., Lohse, D., 2007. Microbubble spectroscopy of ultrasound contrast agents. J Acoust Soc Am 121 (1), 648-656.

van Wamel, A., Kooiman, K., Harteveld, M., Emmer, M., ten Cate, F., Versluis, M., de Jong, N., 2006. Vibrating microbubbles poking individual cells: Drug transfer into cells via sonoporation. J Contr Release 112, 149-155.

Vokurka, K., 1986. Comparison of Rayleigh's, Herring's, and Gilmore's models of gas bubbles. Acustica 59 (3), 214-219.

Vos, H., Dollet, B., Bosch, J., Versluis, M., de Jong, N., 2008. Nonspherical vibrations of microbubbles in contact with a wall-a pilot study at low mechanical index. Ultrasound Med Biol 34 (4), 685-688.

Vos, H.J., Dollet, B., Versluis, M., de Jong, N. 2011. Nonspherical shape oscillations of coated microbubbles in contact with a wall. Ultrasound Med. Biol 37,935-948.

Wei, K., Crouse, L., Weiss, J., Villanueva, F., Schiller, N., Naqvi, T., Siegel, R., Monaghan, M., Goldman, J., Aggarwal, P., Feigenbaum, H., DeMaria, A., 2003. Comparison of usefulness of dipyridamole stress myocardial contrast echocardiography to technetium-99m sestamibi single-photon emission computed tomography for detection of coronary artery disease (pb127 multicenter phase 2 trial results). Am J Cardiol 91 (11), 1293-1298.

Wheatley, M., Schrope, B., Shen, P., 1990. Contrast agents for diagnostic ultrasound: developmenat and evaluation of polymer-coated microbubbles. Biomaterials 11, 713-717.

Wijkstra H., Smeenge M., De la Rosette J., Pochon S., Tardy-Cantalupi I., Tranquart, F. 2012. Targeted microbubble prostate cancer imaging with BR55. ICUS Conf. Proceeding Rotterdam, The Netherlands.

Chapter III

Characterization of Definity™ ultrasound contrast agent at a frequency range of 5-15 MHz

Telli Faez, David Goertz, Nico de Jong

Published in Ultrasound in Medicine and Biology January 21, 2011

Abstract

The status of vasa vasorum which can be imaged using UCAs is an indication for the progression of atherosclerosis (chapter I). The preferred ultrasound frequency for this purpose is between 5 and 15 MHz. Therefore it is essential to have knowledge about the acoustic properties of micro-bubbles such as elasticity and viscosity in order to be able to implement the current models for lipid encapsulated micro-bubbles, developed for frequencies used in precordial imaging. In this study the shell parameters, stiffness S_p and friction S_f, of Definity™ micro-bubbles have been calculated at a frequency range of 5-15 MHz by comparing the theoretical modeling of acoustic bubble response and experimental measurements. Derived parameters are in good agreement with previous estimations on SonoVue and Sonazoid contrast agent. However, the value of S_f is higher than previously estimated for Definity™ between 12-28 MHz.

INTRODUCTION

As explained in chapter I, atherosclerosis is an inflammatory process that causes lesions in both large and medium-sized arteries. The disease progresses slowly over many decades causing clinical manifestations only at advanced stages of the atherosclerotic process.

The use of noninvasive imaging tools for *in vivo* assessment of atherosclerotic plaque composition holds considerable promise for clinical decision-making and patient treatment monitoring. Current knowledge regarding plaque composition and associated clinical endpoints has been largely derived from single-time-point histopathological studies. However, serial monitoring of plaque progression using non-invasive imaging could provide insight into the process of plaque remodeling and disruption. Noninvasive ultrasound is the preferred methodology for the initial evaluation of carotid atherosclerosis. Carotid ultrasound is used to evaluate arterial stenosis or dissection in the cervical region. B-mode ultrasonography has been used in plaque progression/regression trials that involve either lipid-lowering drugs or calcium channel blockers (Crouse *et al* 2004; O'Leary and Polak 2002). The preferred ultrasound frequency for carotid imaging is 5 to 15 MHz.

A new assessment of the progression of atherosclerosis is provided by the existence and volume of the vasa vasorum which can be imaged using UCAs (chapter I). In healthy arteries the vasa vasorum usually has a single vessel that runs parallel to each side of the epicardial artery being nourished with occasional interconnecting conduits from one side of the artery to the other (Hayden and Tyagi 2004).

The unstable, vulnerable plaques are associated with a malignant like invasion of the intima-media by adventitial derived fragile vasa vasorum vessels, which are prone to rupture resulting in intraplaque hemorrhage. These intraplaque hemorrhages accelerate plaque vulnerability and are associated with plaque rupture and acute vascular events (Hayden and Tyagi 2004).

This vascular volume is therefore an indication of the condition of the plaque and can be monitored by diagnostic ultrasound and UCAs.There is increasing interest in the use of micro-bubble contrast agents at higher frequencies. For frequencies between 10 and 50 MHz several studies have investigated their use in “linear” imaging mode using ultrasound biomicroscopy (Deng *et al* 1998) and intravascular ultrasound (IVUS) systems (Cachard *et al* 1997; Demos *et al* 1999). More recent works have shown that it is also feasible to perform subharmonic and second harmonic imaging at high frequencies (Goertz *et al* 2005, 2006). In these studies, both conventional commercial agents (Definity™) and experimental liposomal preparations with micron to submicron mean diameters have been employed, since it is evident from linear theory that smaller bubbles are preferred for higher frequencies.

Current models for lipid encapsulated micro-bubbles, developed for frequencies used in precordial imaging (1-5 MHz) require input parameters like the viscosity and elasticity of the shell (chapter II). These shell properties for Definity™ microbubbles have been estimated previously by Goertz *et al* (2007) for the frequency range 12-29 MHz (i.e. high frequency). This study focuses on examining the linear response of Definity™ microbubbles and estimating the shell properties for 5-15 MHz, which is a frequency range used clinically for carotid scanning. We use the same methodology as described by Goertz *et al* (2007) except for the use of wide band transmission instead of pulse echo narrowband method in the attenuation experiments.

In the following, theoretical background for shell property estimation and the setup used for attenuation measurements are described. At the end, the results of attenuation measurements and estimated values for shell parameters are deduced and discussed.

MATERIAL AND METHOD

Acoustic response modeling of encapsulated bubbles

As mentioned in chapter II, theoretical studies about the dynamics of encapsulated micro-bubbles in response to an ultrasound field started with modifying the so called Rayleigh- Plesset free gas bubble equations (Plesset and Prospretti 1977 and the references therein). As was explained in the previous chapter, de Jong *et al* (1992) developed the first model by introducing ad hoc elasticity and friction shell parameters. Church (1995) enhanced the theory by considering the influence of the shell thickness and the surface tension in the nonlinear model. Hoff *et al* (2000) formulated the so called Church’s model for a thin shell, neglecting the surface tension term. The model proposed by Frinking and de Jong (1998) assumes that the shell behavior dominates the gas reaction inside the micro-bubbles.

The linearized approximations of all these models, which assume very small radial oscillation amplitude with respect to the resting radius, leads to very similar equations. Using the model of de Jong *et al* (1992) which considers the bubbles covered with a viscoelastic solid shell, the undamped natural resonant frequency of encapsulated bubbles (f_0) for small amplitude oscillations is defined as below:

$$f_0(r) = \frac{1}{2\pi}\sqrt{\frac{3\gamma p_0}{\rho r^2} + \frac{2S_p}{\rho r^3}} \qquad (1)$$

where γ is the polytropic exponent, p_0 the static pressure, ρ the liquid density, r the bubble radius and S_p the shell material stiffness (N / m).

Neglecting thermal losses, the total damping (δ_{tot}) is the sum of three damping coefficients, viscosity (δ_{vis}), radiation (δ_{rad}) and internal shell friction (δ_{sh})

$$\delta_{tot} = \delta_{rad} + \delta_{vis} + \delta_{sh}$$

$$\delta_{tot} = \frac{\omega r}{c} + \frac{4\mu_l}{\omega \rho r^2} + \frac{S_f}{4\pi\omega\rho r^3} \qquad (2)$$

where ω is the angular frequency ($2\pi f$), c is the acoustic velocity, μ_l is the liquid viscosity and S_f is the shell friction parameter (Kg / s).

A preferable method to estimate the shell parameters is to measure the attenuation coefficient, α (dB/ unit distance). An ultrasound wave experiences energy loss during propagation through a suspension of micro-bubbles. This attenuation is frequency dependent and is the product of number density (n) and scattering cross section (σ_s) which are both function of the bubbles' radius r.

$$\sigma_s(r,f) = \frac{4\pi r^2}{\left\{\left(\frac{f_0(r)}{f}\right)^2 - 1\right\}^2 + \delta_{tot}^2(r,f)} \qquad (3)$$

$$\alpha(f) = \frac{10}{\ln(10)} \cdot \sum_r n(r) \cdot \sigma_s(r,f) \cdot \frac{\delta_{tot}(r,f)}{\delta_{rad}(r,f)} \qquad (4)$$

Hence, measuring number density of bubbles one can calculate the attenuation in a certain frequency range using Eq. (4). Estimates for shell parameters are obtained by minimizing an error function, defined from the difference of the squares of the experimental and predicted coefficients, with the following form:

$$Err(S_p, S_f) = \sum_i (\alpha_{th}(f_i) - \alpha_{\exp}(f_i))^2 \qquad (5)$$

This method has been used previously by Gorce *et al* (2000), Hoff *et al* (2000) and Sarkar *et al* (2005) at lower frequency ranges (0.8–8 MHz) to estimate the shell properties of lipid encapsulated contrast agents (SonoVue™ and Sonazoid™). Also, Goertz *et al* (2007) reported the Definity™ shell parameters in the frequency range of 12-28 MHz for 15 minutes decanted and 2 µm filtered bubbles population.

Agent preparation

In this study two types of Definity™ vials were used. One vial contained fresh microbubbles while the other contained microbubbles that were 2 years older than the printed expiration date; however since their purchase they were kept in the fridge at 5^{o}C. For convenience we will address them as "fresh" and "expired" Definity respectively. The attenuation properties and size distribution of "expired" Definity™ were measured immediately after activation with the Vialmix™ agent activator (Bristol-Myers Squibb Medical Imaging, North Billerica, MA, USA). While for the "fresh" bottle of Definity™ the extraction was done after 5 minutes decantation.

Activation was performed at room temperature through a mechanical agitation process of 45 s duration according to company guidelines. After activation, two 19 gauge needles were inserted inside the inverted vial, one fully inserted for ventilation and the other up to the middle of the vial to gently extract the agent. Before extracting the agent the vial was mildly mixed by hand again to avoid any decantation. For the "fresh" Definity™ vial, the sample was extracted from the vial bottom.

0.5 mL of the agent was withdrawn from both "fresh" and "expired" vials and diluted in Isoton II (Coulter Electronics, Luton, UK) in the sample chamber at a dilution ratio of 1:15000. All experiments were conducted at room temperature. In order to minimize the flotation effects and to ensure all different populations of bubbles interact with ultrasound beam, the agent was mixed with a magnetic stirrer within the chamber.

Measurement setup

Figure 1 shows the scheme of the setup for the "expired" bubbles. Attenuation measurements were done using two commercially available transducers (Panametrics Inc., Waltham, MA, USA) as transmitter and receiver aligned coaxially on opposite sides of a water tank. Both transducers had the center frequency of 10 MHz and covered the frequency range of 5 to 15 MHz. Micro-bubbles were injected in a sample chamber within the center of the water tank. On both sides of the chamber a Mylar window was mounted for optimal transmission of the ultrasound beam. An arbitrary waveform generator (AWG 520 Tektronix, Beaverton, OR, USA) was used to create broadband pulses. On receive, signals were attenuated (30 dB HAT-30, Mini-Circuits Inc.), amplified (AU-1519, Miteq Inc., Hauppauqe, NY, USA) and low pass filtered (BLP-30, Mini-Circuits Inc.). A digital oscilloscope (Tektronix TDS 3014B) and a computer were used for monitoring and recording the signals.

A wideband pulse was employed (25 MHz). The pulse repetition rate was 200 ms which ensured independent sampling between the recordings. For each experiment 128 signals were recorded. Recordings started 1 min after agent was diluted in the chamber and the discrete Fourier transform of the recorded signals were averaged. The pressure level used was 107 kPa at focus, measured with a 0.075 mm needle hydrophone (Precision Acoustic Ltd., Dorchester, UK) in a water tank. The experiment was repeated three times for three samples of the same population and the results were averaged.

For the "fresh" sample, protocol for attenuation measurements and data analysis was the same as what has been explained in Goertz *et al* (2007). Two sets of measurements were done; each set was done for a different sample from the extraction, and consisted of 10 frequency sweeps, spaced at 5 second intervals. The frequency sweeps were comprised of 20 cycles per pulse, with center frequencies ranging from 7 to 27.5 MHz at 0.5 MHz intervals (25 kPa pressures). The results were averaged for the analysis. These measurements were conducted with a transducer (Panametrics Inc., Waltham, MA, USA) with focal length of 38.1 mm and aperture diameter of 63.5 mm. The path length within chamber to reflector was 21 mm.

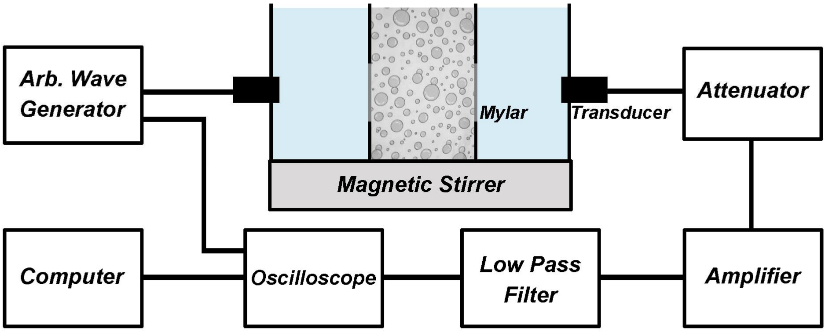

Fig 1. Scheme of the measurement setup

Size measurement

A Multisizer III (Beckman Coulter Inc., Fullerton, CA, USA) was used to measure the size distribution of the agent. A 20-μm aperture was used, which is able to measure in the size range of 0.46 to 12 μm with the resolution (bin size) of 0.039 μm. For the "fresh" vial, a 30-μm aperture was used with the resolution of 0.01 μm. Microbubbles were diluted at the same dilution ratio of 1:15000 as for the acoustic measurements. Each measurement was repeated three times and averaged and background noise was subtracted. Figure 2 shows the output of the Coulter counter, number and volume per unit volume versus the diameter of bubbles for both samples.

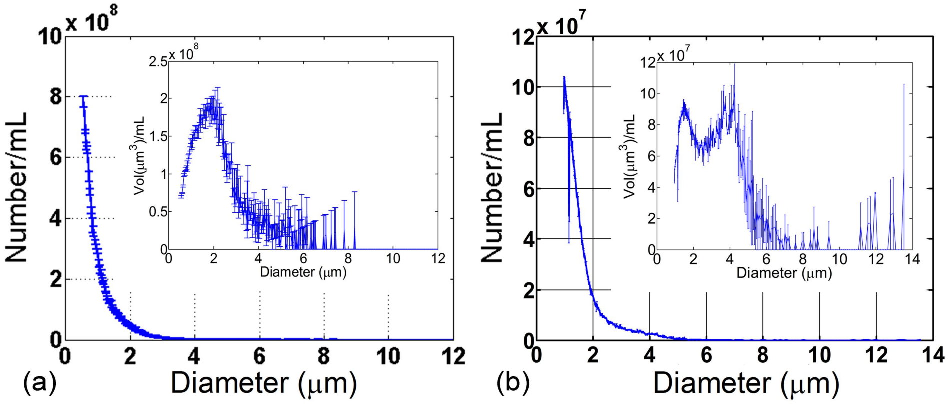

Fig 2. Coulter counter size distribution measurement for Definity™ in number/mL (inset: vol/mL) for a) "expired" and b) "fresh" bubbles.

RESULTS

Figure 3 presents the attenuation as a function of frequency for both studied cases. The maximum attenuation for "expired" and "fresh" microbubbles occurs around 8 MHz (1.55 dB/cm) and 18 MHz (1.80 dB/cm) respectively. The two shell parameters S_p and S_f were estimated in the frequency range of 5-15 MHz in figure 3a and 7-15 MHz in figure 3b by minimizing the value of the error function in equation 5. To find the limits for the confidence intervals of the shell stiffness and friction, the parameters S_p and S_f were varied separately until the error function indicator was doubled. The shell parameters are summarized in Table 1. For comparison all previously published values for S_p and S_f of different contrast agents are also added including the applied frequency range.

DISCUSSION AND CONCLUSION

Estimates on shell properties for both “expired” and “fresh” bubbles (table 1) indicate a similar value for shell stiffness (S_p) compared to previous studies at lower and higher frequencies (Goertz *et al* 2007; Gorce *et al* 2000; Hoff 2000; Sarkar *et al* 2005). The shell friction (S_f) estimates are very close to the reported values of other studied contrast agents at lower frequencies (e.g. SonoVue™ and Sonazoid™, 1-8 MHz). However there is a difference between derived values for S_f in the two studied samples. The source of this difference in the range of 5-15 MHz can be due to the differences in the size distributions presented in figure 2. The populations of larger bubbles which were shown before by Goertz *et al* (2007) and are still present after 5 minutes decantation were not detected in the “expired” Definity™ sample. The size measurements by Coulter counter showed no evidence on the presence of bubbles larger than 3 μm in our samples (figure 2a). The absence of larger bubbles which may be due to the aging of the vial is the source of different attenuation measurements (figure 3). The shell stiffness parameter seems to be independent of the variations in the size distribution but it slightly affects the shell viscosity.

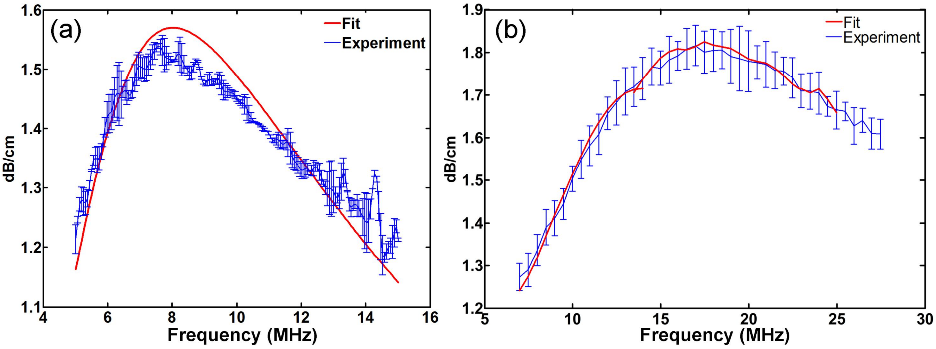

Fig 3. Attenuation measurements as a function of frequency for Definity™ and the fit made for shell properties estimation on a) “expired” and b) “fresh” bubbles.

Table 1- Estimated shell parameters for Definity™ and previously published measurements.

Agent		Study	Frequency range (MHz)	S_p (N/m)	S_f 10^{-6} (kg/s)
SonoVue		Gorce *et al* (2000)	0.8-3	1.1	0.27
SonoVue (10' dec.)		Gorce *et al* (2000)	3-7	1.1	0.56
Sonazoid		Hoff (2000)	1.5-8	1.2 ± 0.07	0.48 ± 0.06
Sonazoid		Sarkar *et al* (2005)	2-8	1.25 ± 0.24	0.60 ± 0.18
Definity (15' dec.)		Goertz *et al* (2007)	12-28	1.71 ± 0.24	0.015 ± 0.015
Definity (2 µm filt.)		Goertz *et al* (2007)	13-29	1.51 ± 0.36	0.016 ± 0.016
Definity	“Expired”	present	5-15	1.58 ± 0.16	0.44 ± 0.03
	“Fresh”		7-15	1.64 ± 0.33	0.15 ± 0.02
			15-25	2.04 ± 0.67	0.01 ± 0.01

Moreover the estimated values of S_f in the frequency range of 5-15 MHz are one order of magnitude higher than the estimations done by Goertz *et al* (2007) on Definity™ at higher frequencies (12-28 MHz). This difference can originate from the frequency dependence of shell properties. To test this hypothesis we estimated the values of S_p and S_f of the same “fresh” Definity™ sample in higher frequencies between 15-25 MHz. The values are presented in Table 1. The shell parameters in this frequency range are consistent with previously reported values in the similar frequency range (12-28 MHz, Goertz *et al* 2007). These results are in line with the findings of Van der Meer *et al* (2007) who observed the effect of shear thinning in phospholipid contrast agents. In Goertz *et al* (2007) it was hypothesized that the lower shell viscosities estimated for smaller bubbles at higher frequencies could be due to two factors. First, shear thinning at higher excitation frequencies may lead to a reduction in the estimated shell viscosity. A second factor may be size-dependant shell properties, possibly due to issues related to shell microstructure, inhomogeneities and thickness. Regardless of the origin, it was proposed that the reduction in viscosity may be a key factor in enabling the generation of nonlinear oscillations in small bubbles at high frequencies.

In conclusion, the shell viscosities estimated in this study for 5-15 MHz were greater than previous reported values in higher frequencies (12-28 MHz). We propose that this difference originates from the frequency and size dependence of rheological properties of the lipid shell.

Acknowledgments- Authors would like to thank Emma Huo for performing measurements and analysis on “fresh” Definity™, Miranda Harteveld for her assistance with Coulter counter measurements and Marcia Emmer and Rik Vos for inspiring discussions.

References

Cachard C, Finet G, Bouakaz A, Tabib A, Francon D and Gimenez G. Ultrasound contrast agent in intravascular echography: an in vitro study. Ultrasound Med Biol 1997;23: 705-717.

Church CC. The effects of an elastic solid surface layer on the radial pulsations of gas bubbles. J Acoust Soc Am 1995;97: 1510-1521.

Crouse JR, 3rd, Grobbee DE, O'Leary DH, Bots ML, Evans GW, Palmer MK, Riley WA and Raichlen JS. Measuring Effects on intima media Thickness: an Evaluation Of Rosuvastatin in subclinical atherosclerosis--the rationale and methodology of the METEOR study. Cardiovasc Drugs Ther 2004;18: 231-238.

De Jong N, Hoff L, Skotland T and Bom N. Absorption and scatter of encapsulated gas filled microspheres: theoretical considerations and some measurements. Ultrasonics 1992;30: 95-103.

Demos SM, Alkan-Onyuksel H, Kane BJ, Ramani K, Nagaraj A, Greene R, Klegerman M and McPherson DD. In vivo targeting of acoustically reflective liposomes for intravascular and transvascular ultrasonic enhancement. J Am Coll Cardiol 1999;33: 867-875.

Deng CX, Lizzi FL, Silverman RH, Ursea R and Coleman DJ. Imaging and spectrum analysis of contrast agents in the in vivo rabbit eye using very-high-frequency ultrasound. Ultrasound Med Biol 1998;24: 383-394.

Frinking PJ and de Jong N. Acoustic modeling of shell-encapsulated gas bubbles. Ultrasound Med Biol 1998;24: 523-533.

Goertz DE, Cherin E, Needles A, Karshafian R, Brown AS, Burns PN and Foster FS. High frequency nonlinear B-scan imaging of micro-bubble contrast agents. IEEE Trans Ultrason Ferroelectr Freq Control 2005;52: 65-79.

Goertz DE, Frijlink ME, de Jong N and van der Steen AF. Nonlinear intravascular ultrasound contrast imaging. Ultrasound Med Biol 2006;32: 491-502.

Goertz DE, de Jong N and van der Steen AFW. Attenuation and size distribution measurements of Definity™ and manipulated Definity™ populations. Ultrasound in Medicine and Biology 2007;33: 1376-1388.

Gorce JM, Arditi M and Schneider M. Influence of bubble size distribution on the echogenicity of ultrasound contrast agents: a study of SonoVue. Invest Radiol 2000;35: 661-671.

Hayden MR, Tyagi SC. Vasa vasorum in plaque angiogenesis, metabolic syndrome, type 2 diabetes mellitus, and atheroscleropathy: a malignant transformation. Cardiovascular Diabetology 2004;3: 1-16.

Hoff L. Acoustic characterization of contrast agents for medical ultrasound imaging. PhD. Thesis, Norwegian University of Science and Technology, 2000 Trondheim, Norway.

Hoff L, Sontum PC and Hovem JM. Oscillations of polymeric micro-bubbles: effect of the encapsulating shell. J Acoust Soc Am 2000;107: 2272-2280.

O'Leary DH and Polak JF. Intima-media thickness: a tool for atherosclerosis imaging and event prediction. Am J Cardiol 2002;90: 18L-21L.

Plesset MS. and Prosperetti A. Bubble dynamics and cavitation. Ann. rev. Fluid Mech. 1977;9: 145-185.

Sarkar K, Shi WT, Chatterjee D and Forsberg F. Characterization of ultrasound contrast micro-bubbles using in vitro experiments and viscous and viscoelastic interface models for encapsulation. J Acoust Soc Am 2005;118: 539-550.

Van der Meer SM, Dollet B, Voormolen MM, Chin CT, Bouakaz A, de Jong N, Versluis M and Lohse D. Microbubble spectroscopy of ultrasound contrast agents. J Acoust Soc Am 2007;121: 648-656.

Chapter IV

Characterizing the subharmonic response of phospholipid-coated microbubbles for carotid imaging

Telli Faez, Marcia Emmer, Margreet Docter, Jeroen Sijl, Michel Versluis,
Nico de Jong

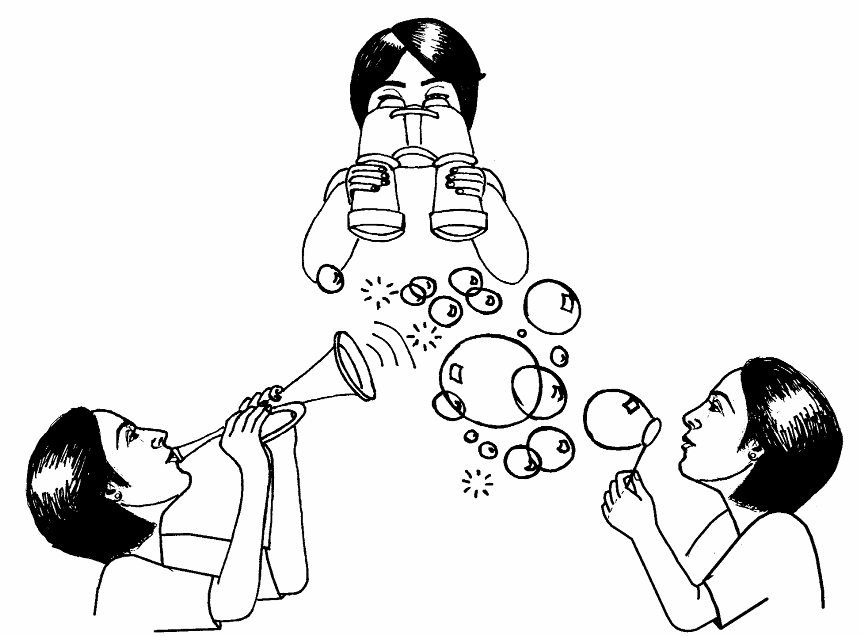

Published in Ultrasound in Medicine and Biology May 19, 2011

Abstract

The subharmonic vibration of BR14 (Bracco Research S.A., Geneva, Switzerland) contrast agent microbubbles is investigated within the preferable frequency range for carotid ultrasound imaging (8-12 MHz). The response of the bubbles was recorded optically with the ultrafast recording camera (Brandaris 128) at three acoustic pressures (50, 100 and 120 kPa). The vibration of the microbubbles was measured as a function of the excitation frequency and its frequency content was determined. Among 390 recordings, 40% showed subharmonic oscillations. It was observed that for smaller microbubbles (diameter < 3µm) the frequency of the maximum subharmonic response increases for increasing pressures (shell hardening) opposite to what has been reported for larger microbubbles (3µm < diameter < 15µm). These findings are well predicted by the model proposed by Marmottant *et al* (2005) after including the dilatational shell viscosity of the microbubbles measured by Van der Meer *et al* (2007) which indicates a marked shear-thinning behavior of the phospholipid shell.

INTRODUCTION

Several experimental (de Santis *et al* 1967; Neppiras, 1969) and theoretical (Eller 1969; Prosperetti 1975; Lauterborn 1976) studies have been performed to investigate and to describe the subharmonic resonance of bubbles. This non-linear effect originates from a parametric instability in the equations describing the bubble dynamics (Plesset, 1949). Prosperetti (1974) showed analytically that subharmonic oscillations occur for the amplitude of acoustic pressure above a certain threshold value. This threshold value was found to be minimal when the bubble oscillates at a frequency of twice its resonance frequency. It was also shown that damping increases the threshold pressure for the occurrence of subharmonic for free gas bubbles (Eller 1969; Prosperetti 1974 and 1977).

As mentioned in chapter II, ultrasound contrast bubbles are coated to prolong their *in vivo* lifetime. The coating not only prevents a quick dissolution of the bubble gas, but also has an increased shell viscous damping effect on the bubble oscillations in an ultrasound field. Since the visco-elastic shell of contrast agent microbubbles is known to increase the damping considerably (de Jong 1993; Van der Meer *et al* 2007), it is expected that the subharmonic threshold pressure increases. This hypothesis was supported by Shankar *et al* (1999). In that study**,** a purely visco-elastic shell model (de Jong *et al* 1993; Church 1995; Hoff *et al* 2000) was used to analyze the subharmonic behavior of coated bubbles. They confirmed the increase of the threshold pressure for the generation of the subharmonic by an increased damping. However, experimental studies on both albumin-coated (Optison™ and Albunex®) and phospholipid-coated (SonoVue®) contrast agents have shown that the threshold pressure to generate a subharmonic echo is lower than what was found for the uncoated bubbles (Chang *et al* 1995; Lotsberg *et al* 1996; Shankar *et al* 1998 and 1999; Krishna *et al* 1999; Biagi *et al* 2007; Frinking *et al* 2010).

Frinking *et al* (2009) and Sijl *et al* (2010) have shown that the coating of lipid bubbles decreases the subharmonic threshold pressure. During buckling of the lipid coated shell, the bubbles show a highly nonlinear behavior at low acoustic pressures, such as asymmetric oscillation amplitudes whereby the compression amplitude outweighs expansion. Marmottant *et al* (2005) explained that this so called 'compression-only' behavior (de Jong *et al* 2007) is caused by a variable surface tension of lipid coated bubbles. Sijl *et al* (2010) showed that the initiation of subharmonic in phospholipid-coated microbubbles at lower threshold pressure can be explained with the Marmottant *et al* (2005) model. They employed a weakly non-linear analysis of the Rayleigh-Plesset equation and instead of using a purely elastic model they described the shell elasticity of coated bubble as an effective surface tension which varies strongly with the amplitude of oscillation, as proposed by Marmottant *et al* (2005). Sijl *et al* showed that this mechanism is responsible for the generation of subharmonic oscillations at low acoustic pressures. They reported subharmonic threshold values down to 5 kPa for individual lipid-coated BR14 bubbles at driving frequencies between 1-4 MHz.

At present, studies on microbubbles subharmonic response have been performed at frequencies relevant for precordial imaging (1-4 MHz). However, as mentioned before, the preferred ultrasound frequency for carotid imaging is between 5-15 MHz, involving microbubbles which are substantially smaller and which may have different behavior. It is however unclear at what driving frequency the subharmonic response is maximal and how the response changes with varying driving pressure. The aim of this study is to investigate the dependence of the subharmonic response of a phospholipid-coated microbubble to the acoustic pressures applied at frequencies near 10 MHz.

For uncoated bubbles it is well known that the fundamental resonance curve becomes asymmetrical and that the frequency of maximum response decreases with increasing acoustic pressure (Prosperetti 1975; Lauterborn 1976). Van der Meer *et al* (2007) studied experimentally the fundamental resonance curve of phospholipid-coated microbubbles at constant acoustic pressure of 40 kPa and found an increase of the resonance frequency with respect to uncoated bubbles as a result of increased stiffness of the system. Later on Overvelde *et al* (2010) investigated the fundamental resonance curves of the same microbubbles as a function of the acoustic pressure. They observed a decrease in the resonance frequency of the microbubbles by increasing the amplitude of the acoustic pressure. Their results were in good agreement with the predictions of the Marmottant *et al* model (2005). Yet it is not known if the subharmonic response of a microbubble follows the same trend as its fundamental response. Furthermore, the radial dependence of shell viscosity characterized by Van der Meer *et al* (2007) from the linearized bubble dynamics equations has not been implemented yet in the full context of the Marmottant *et al* (2005) model (see for example Overvelde *et al* 2010; Sijl *et al* 2010).

In the present study we investigate the subharmonic response of a microbubble around 10 MHz as a function of the acoustic pressure both numerically and experimentally. The influence of shell properties, effective surface tension and shell viscosity reported by Van der Meer *et al* (2007), on the subharmonic response of phospholipid-coated microbubbles is determined in the simulations based on the Marmottant *et al* (2005) model. The subharmonic responses of single bubbles are recorded optically using an ultra-high speed camera system. We apply microbubble spectroscopy as described by Van der Meer *et al* (2007) by recording the subharmonic response of the bubbles at driving frequencies ranging from 4 to 7 MHz and from 8 to 12 MHz with a frequency step of 200 kHz leading to its subharmonic resonance curve. Bubble responses are measured at acoustic pressures of 50, 100, and 120 kPa. The experimental results are compared with bubble dynamics simulations based on the model of Marmottant *et al* (2005).

THEORY AND MODELLING

Numerical model

In order to investigate the influence of the acoustic pressure and the driving frequency on the fundamental and subharmonic response of coated bubbles, we simulate the bubble dynamics with the model of Marmottant *et al* (2005). The difference between this equation and that of a free gas bubble equation is the radius dependency of the effective surface tension and an additional dissipative term representing the viscosity of the shell. The Marmottant model has been shown to accurately simulate highly nonlinear behavior such as compression-only behavior and subharmonic oscillations which is observed for individual bubbles using high-speed imaging (De Jong *et al* 2007; Sijl *et al* 2010).

The Rayleigh-Plesset-type equation used here is the following (Keller and Miksis 1980; Marmottant *et al* 2005):

$$\rho\left(R\ddot{R}+\frac{3}{2}\dot{R}^2\right)=\left(P_0+\frac{2\sigma(R_0)}{R_0}\right)\left(\frac{R_0}{R}\right)^{3\kappa}\left(1-\frac{3\kappa}{c}\dot{R}\right)-P_0-\frac{2\sigma(R)}{R}-\frac{4\mu\dot{R}}{R}-\frac{4\kappa_s\dot{R}}{R^2}-P(t) \qquad (1)$$

where R_0 and R are the initial and time-dependent radius of the bubble, ρ is the liquid density, μ is the dynamic viscosity of the liquid, c the speed of sound and κ the polytropic exponent of the gas inside the bubble. P_0 and $P(t)$ are the ambient and driving pressures respectively. κ_s is the surface viscosity of the shell which in the original equation is assumed to be independent of the initial bubble radius and $\sigma(R)$ is the effective surface tension. Three regimes are considered for a bubble shell in this model: buckled, elastic and ruptured. $\sigma(R)$ is defined as follows:

$$\sigma(R)=\begin{cases}0 & \text{If } R<R_b \text{ (buckled)}\\ \chi\left(\dfrac{R^2}{R_b^2}-1\right) & \text{If } R_b<R<R_r \text{ (elastic)}\\ \sigma_w & \text{If } R\geq R_r \text{ (ruptured)}\end{cases} \qquad (2)$$

Where χ represents the shell elasticity. When the bubble is smaller than a defined buckling radius (R_b) the surface tension is zero and the elastic term vanishes. This state is called the buckled regime. The bubble is in the ruptured regime when its radius exceeds a certain radius *(R_r)* where the coating of the bubble breaks up and the gas inside the bubble is in direct contact with the surrounding liquid. In this case the surface tension equals the surface tension of water *(σ_w)* and the elastic term is again zero. Between these two regimes the shell coating is considered a purely elastic material.

From this model we derive the resonance frequency of a coated microbubble. We assume small oscillation amplitudes and approximate the effective surface tension in the visco-elastic regime to its first-order Taylor expansion:

$$\sigma(R) = \sigma(R_0) + 2\chi\left(\frac{R}{R_0} - 1\right) \qquad (3)$$

Combining Eq. (3) with the linearization of Eq. (1) yields the resonance frequency of a bubble with a linear visco-elastic shell:

$$f_{res} = \frac{1}{2\pi}\sqrt{\frac{1}{\rho R_0^2}\left[3\kappa P_0 + \frac{2(3\kappa - 1)\sigma(R_0)}{R_0} + \frac{4\chi}{R_0}\right]} \qquad (4)$$

For $\chi = 0$ and $\sigma(R_0) = \sigma_w$, f_{res} represents the resonance frequency of an uncoated bubble, also known as the Minnaert frequency f_M (Minnaert, 1933), including surface tension.

We used the Marmottant *et al* (2005) model to simulate the fundamental and subharmonic responses of bubbles of different size (2 and 4 μm diameter), for increasing acoustic pressures (1-120 kPa). The pressure signal used in these simulations was a burst of 25 cycles tapered with a Gaussian envelope at the first and last two cycles.

In order to get subharmonic oscillations a rapid change in the elasticity is required. In the elastic regime the elasticity doesn't change or at least not very rapidly. Among the other two possible regimes, it has been observed (Sijl *et al* 2010) that a bubble in the buckled state shows the highest amplitude of subharmonic response. Therefore in the simulations we choose the buckled state as the initial state of the bubble at its equilibrium position, $R=R_0$, i.e. the initial surface tension is negligible, and $\sigma(R_0)=0$. $\sigma(R_0)$ reveals immediately the bubble's initial state, therefore we derive R_b from $\sigma(R_0)$ via the following equation:

$$R_b = R_0 / \sqrt{\frac{\sigma(R_0)}{\chi} + 1} \qquad (5)$$

instead of taking R_b as a constant as was done by Marmottant *et al* (2005) (see also Overvelde *et al* 2010). The other shell parameters were set as $\chi = 2.50$ N/m (Overvelde *et al* 2010) and $\kappa_s(R_0)$ was considered dependent on the initial bubble radius using the measurements done by Van der Meer *et al* (2007). The fundamental and subharmonic oscillation amplitudes of the bubbles were determined using the squared Fourier transform *(FT)* of the normalized radial excursion of the bubble.

$$A(f) = \left(FT\left[\frac{R(t)}{R_0}\right]\right)^2 \qquad (6)$$

The results were plotted versus the normalized frequency, Ω, which is defined as the driving frequency divided by the Minnaert frequency, f_M, (Minnaert, 1933) of an uncoated bubble. This leads to the fundamental and subharmonic resonance curves of the bubble.

Simulation results

Figure 1 shows the fundamental and subharmonic resonance curves of a 2 µm (a, b) and a 4 µm (c,d) diameter coated bubble as a function of the acoustic pressure (1-120 kPa). It can be seen that the coated bubble with 2 µm diameter indicates an over damped system in which no local maximum exists in the radial oscillation amplitudes at the fundamental response of the bubble (Fig. 1a). Whereas for a 4 µm diameter bubble (Fig. 1c) the maximum fundamental response occurs when Ω is 1.3. For the subharmonic resonance curves, it is indicated that the maximum subharmonic amplitude for a coated bubble (Fig. 1b and 1d) occurs when Ω is around 3 whereas for an uncoated bubble it is expected to occur when Ω is equal to 2 (Eller *et al* 1969).

To better compare the fundamental and subharmonic “resonance frequencies” of the bubbles at various acoustic pressures, the frequency of maximum response was plotted as a function of the acoustic pressure in Fig. 2 for three bubble sizes (2, 4 and 6 µm diameter). As before the shell parameters were: $\sigma(R_0) = 0$, $\chi = 2.50$ N/m and $\kappa_s(R_0)$.

As explained before in Fig. 1a, the 2 µm diameter bubble indicates no local maximum in the fundamental response due to overdamping. However the peak of the subharmonic resonance curve slightly shifts towards higher frequencies from 4.1 MHz at 1 kPa to 4.50 MHz at 120 kPa. For the other two bubbles the fundamental and subharmonic responses follow a different trend with increasing acoustic pressure. The fundamental resonance frequency of the 4 µm bubble tends to decrease with increasing pressure while the subharmonic response behaves just the opposite. On the other hand, the fundamental and subharmonic resonance frequencies of the 6 µm diameter bubble seem to follow a different trend: a lower resonance frequency at higher acoustic pressure; the fundamental resonance frequency decreases almost 21% from 1.40 MHz to 1.10 MHz by increasing the pressure from 1 kPa to 120 kPa. The same happens for the subharmonic response, with the difference that the resonance frequency falls off less evidently (4%). This behavior is in agreement with the numerical and experimental results of Overvelde *et al* (2010) for the resonance curves of a 6 µm diameter bubble derived from the oscillation amplitudes at the fundamental frequency.

EXPERIMENTS

Experimental setup

Fig. 3 shows the schematic view of the setup. Highly diluted BR14 microbubbles (Bracco Research S.A., Geneva, Switzerland) were injected with a syringe inside a 200 µm diameter acoustically transparent cellulose capillary fiber with an 8 µm wall thickness (Product No. 132294, Spectrum Europe, Breda, The

Netherlands) kept in a small water tank filled with Isoton II (Beckman Coulter, The Netherlands). The capillary was located at the focal point of the transducer. A wide band transducer (Panametrics V311; 3-13 MHz or Precision Acoustics PA076; 1-9 MHz) was used for transmit. The transducer was connected to a power amplifier (Amplifier Research, 150A100B) which amplified the wave generated by an arbitrary wave generator (8026, Tabor Electronics Ltd., Tel Hanan, Israel). Bursts of a 25-cycle sinusoidal wave, tapered with a Gaussian envelope at the first and last two cycles were transmitted. For the majority of small bubbles (diameter < 3 μm) transmitted frequencies between 8-11 MHz with a frequency step of 200 kHz were chosen. And most of the larger bubbles were insonified in the frequency range of 4-7 MHz with frequency steps of 200 kHz. The pressure at focus for each experiment was changed from 50 kPa to 100 kPa and finally 120 kPa. These pressure values were calibrated using a 0.2 mm PVDF probe hydrophone (Precision Acoustics Ltd., Dorchester, UK). The relatively low pressures used ensured no changes in the bubble size after insonification.

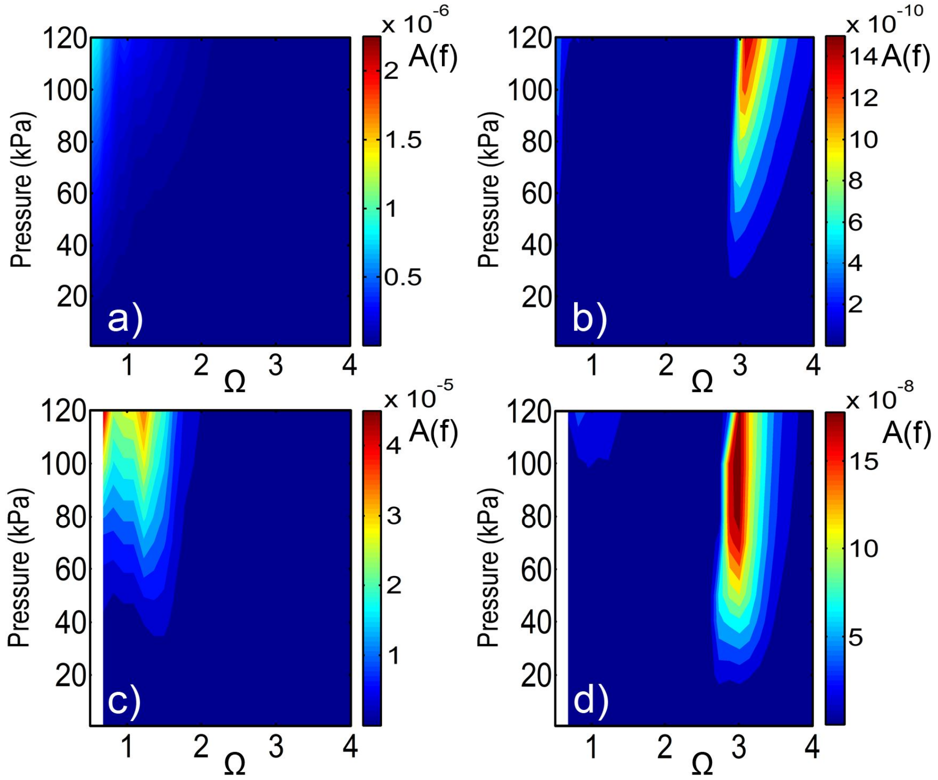

Fig 1. Fundamental (left panel) and subharmonic (right panel) resonance curves of a 2 μm diameter coated bubble (a,b) and a 4 μm diameter coated bubble (c,d) versus acoustic pressure amplitudes of 1-120 kPa. The normalized frequency (Ω) is defined as the driving frequency divided by the Minnaert frequency (Minnaert 1993) of an uncoated bubble. Shell parameters: $\sigma(R_0) = 0, \chi = 2.50$ N/m and $\kappa_s(R_0)$ taken from Van der Meer *et al* (2007).

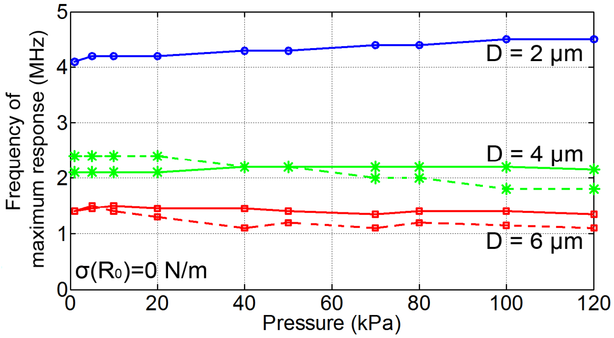

Fig 2. Frequency of maximum response at the fundamental (driving) frequency (dashed lines) and the frequency of maximum response at the subharmonic frequency (solid lines) of different bubble sizes versus applied acoustic pressures. Shell parameters: $\sigma(R_0) = 0$ N / m, $\chi = 2.50$ N / m, $\kappa_s(R_0)$.

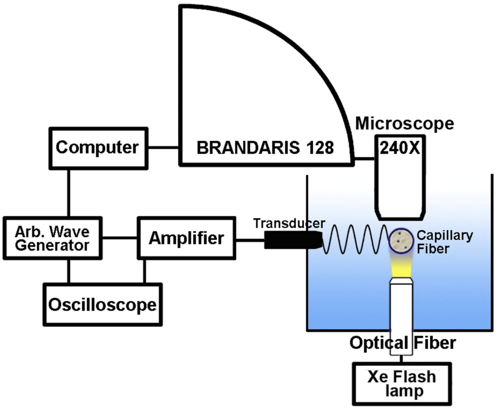

Fig 3. Schematic view of the setup.

The region of interest was illuminated with an optical light guide (SCHOTT AG, Germany) connected to a Xenon flash lamp (Vision Light Tech A-260). An Olympus microscope with a 60x water-immersed objective (NA = 0.9) was focused on the bubbles inside the capillary. The total magnification of the system was further increased to 240x by using an additional 2x2x magnification lens inside the microscope. The radial response of the insonified bubble was recorded with the ultrafast recording camera, the Brandaris 128, (Chin *et al* 2003) at a frame rate of 20 million frames per second. The camera was set to record 49 movies of 128 frames in a single run. The first recording was always done without ultrasound to have an estimate of the resting radius of the bubbles and of the noise level of the system. In the subsequent movies, the frequency was swept in 16 steps in ascending order to cover the required frequency range at acoustic pressure of 50 kPa, followed by 16 frequency steps at 100 kPa and finally 16 frequency steps at 120 kPa. As an example we display 28 frames from the recording of a 4.6 μm bubble insonified at transmitting frequency of 4.2 MHz and acoustic pressure of 100 kPa (Fig. 4). The frames show clearly the buckling of the shell during oscillations in this bubble.

Each recording was stored in the computer for further analysis. From each individual movie the diameter of the microbubble as a function of time (DT-curve) was measured using custom-designed image analysis software (Van der Meer *et al* 2007). An edge detection algorithm based on a minimum-cost analysis (MCA) was used to trace the circumference of the bubbles. At the first frame a circle is defined around the bubble. The center point of this contour is used to resample the bubbles and its direct surrounding using the gray scale slope along the radial direction as the cost function. The algorithm finds the optimal path along the contour indicating the boundary of the bubble area. We define the diameter of the bubble the diameter of a circle with an area equal to the detected boundary. This procedure is repeated for all the frames and at the end the diameter of the bubble is plotted versus time producing a DT-curve. The Discrete Fourier transform of DT-curves was then calculated which gives the maximum amplitude of radial excursion at resonance of the bubble.

The ideal case would be to measure both the fundamental and subharmonic resonance curves of a bubble in a single experiment. For that purpose one should sweep the driving frequency in a wide range going at least from half to three times the fundamental resonance frequency. At high frequencies applied here, there are however two unavoidable limiting factors: first the bandwidth of the transmitting and receiving transducers mentioned above and secondly the sampling frequency of the ultra-high speed camera (21 MHz) which has to be at least twice the maximum driving frequency to avoid aliasing. Therefore, for each single bubble, we are here practically bounded to measure only either the fundamental or the subharmonic resonance curve.

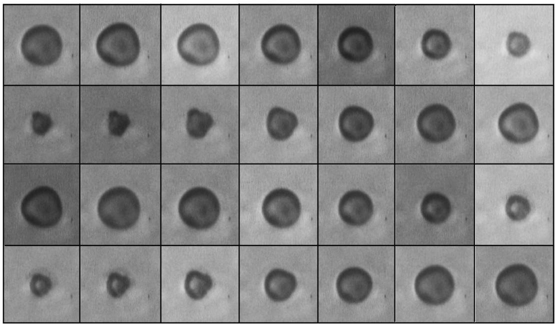

Fig 4. 28 frames from the recording of a 4.6 µm bubble insonified at transmitting frequency of 4.2 MHz and acoustic pressure of 100 kPa.

Experimental Results

The responses of 390 individual single bubbles were recorded and analyzed. Thirty bubbles in the frequency range of 4-7 MHz and 360 in the range of 8-12 MHz. As a typical example we display six DT-curves (out of the set of 16) of a 4.40 µm diameter bubble in Fig. 5. The transmit frequency in these selected graphs increases from 4.40 MHz to 6.40 MHz The amplitude of the acoustic pressure was 50 kPa. The discrete Fourier transform of the first recording from each bubble which was done without ultrasound was used as the estimate of the noise level (gray area in Fig. 5). The corresponding power spectra show a peak at the fundamental driving frequency and at the subharmonic frequency (half the driving frequency). In this example at a driving frequency of 5.20 MHz the amplitude of subharmonic reaches a maximum at 2.70 MHz.

In order to study the dependence of the subharmonic amplitude as a function of the transmitted frequency, the amplitude of excursion at the subharmonic frequency was extracted from the DT-curves for all the recordings and plotted versus frequency. The subharmonic resonance frequency was derived for each bubble by fitting the subharmonic resonance curves with a functional form displaying a single absolute maximum. We use for simplicity a Lorentzian function as follows:

$$\mathrm{Re}(f) = \frac{\mathrm{Re}_0}{(1 - f^2/f_0^2)^2 + (\delta f/f_0)^2} \qquad (7)$$

where f_0, δ and Re_0 are the fitting parameters.

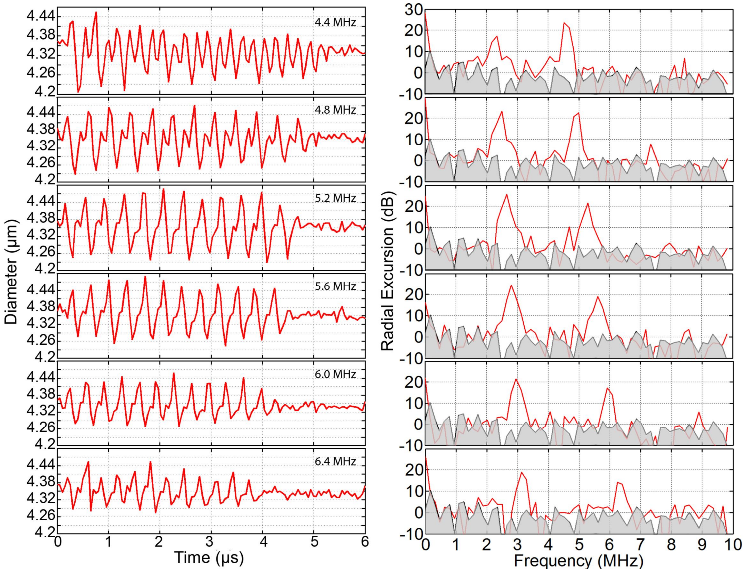

Fig 5. Selected DT-curves (left panel) and corresponding power spectra (right panel) of a bubble with a diameter of 4.40 µm. Driving frequencies range between 4 to 7 MHz. The applied acoustic pressure is 50 kPa. The sampling time is 0.05 µs. The selection has been done between 4.4 MHz and 6.4 MHz with frequency step of 400 kHz. The gray area in the power spectra indicates the noise floor.

The occurrence of the subharmonic

Fig. 6 shows the size distribution of the recorded bubbles together with the size distribution of the bubbles showing subharmonic response. The median bubble diameter was 2.40 µm and the diameter ranged from 1 to 7 µm. Among the 30 measurements performed at frequency range between 4 and 7 MHz, one third showed a subharmonic response. For the rest of the bubbles which were insonified at 8-12 MHz, forty percent indicated subharmonic oscillations. Although these bubbles had a diameter between 1.50 and 4.50 µm and the recorded bubble sizes are not equally distributed over the whole range, there are no indications that the amounts of bubbles that show a subharmonic response are related to the bubble resting diameter.

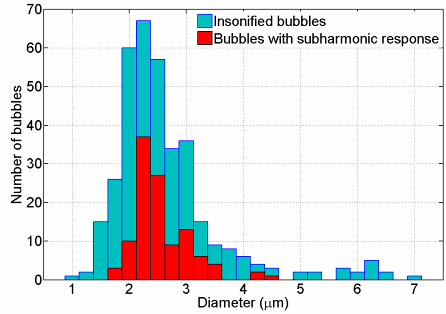

Fig 6. Size distribution of investigated bubbles (blue bars) and those showing subharmonic response (red bars).

The influence of the acoustic pressure on the subharmonic

Fig. 7 shows the subharmonic resonance curves of two bubbles with a diameter of 4.40 µm and 2.47 µm insonified at a frequency of 4-7 MHz and 8-11 MHz, respectively. The first bubble (Fig. 7a) has a subharmonic resonance frequency of 2.70 MHz at 50 kPa which decreases to 2.15 MHz at 120 kPa. The amplitude at the subharmonic resonance frequency increases for higher pressures. The smaller bubble (Fig. 7b) shows its maximum amplitude at the subharmonic resonance frequency of 4.70 MHz. The subharmonic frequency shifts to 5.10 MHz for higher pressures. In this case the amplitude at the subharmonic resonance frequency first increases and then decreases. In general for relatively large bubbles investigated in the experiments (diameter > 3 µm) the subharmonic resonance frequency decreases with increasing driving pressure amplitude while it increases for smaller bubbles (diameter < 3 µm).

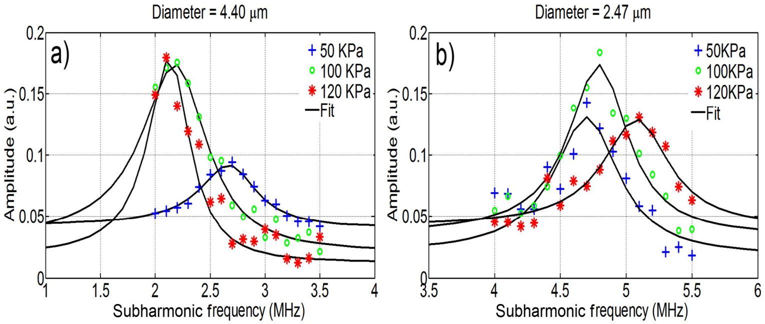

Fig 7. The subharmonic amplitude as a function of the subharmonic frequency for a) 4.40 µm and b) 2.47 µm bubble at driving amplitude pressures of 50, 100 and 120 kPa. The fit on the experimental data was done using the Lorentzian function defined in Eq. (7). Data on the abscissa have an uncertainty of ±0.1 MHz.

The influence of the bubble size on the subharmonic

Fig. 8 shows the subharmonic resonance frequency of the bubbles versus their diameter. Binning was performed over 100 nm. The bubble diameter varied between 1.40 µm and 4.40 µm. In the left panel the results are plotted for an acoustic pressure of 50 kPa and in the left panel for 100 kPa.

For comparison the fundamental resonance frequencies of an uncoated bubble (dash dotted line) and a linear visco-elastic bubble (dashed line) were also calculated using equations 4. The effective value for shell elasticity $\chi = 0.54$ N / m is the value determined by Van der Meer *et al* (2007) using Eq. (4).

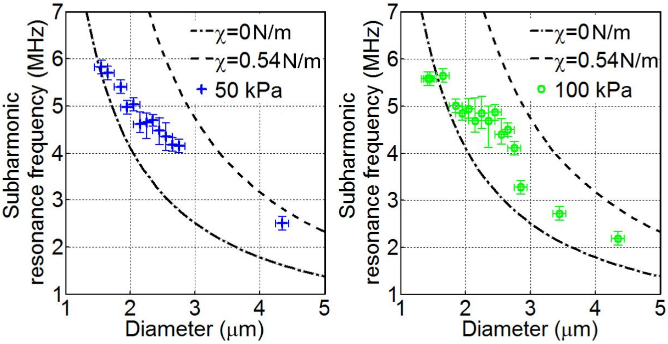

Fig 8. Measured subharmonic resonance frequencies versus diameter for two applied pressure of 50 kPa and 100 kPa after binning over 100 nm. Theoretical resonance frequencies obtained with Eq. (4) for $\sigma(R_0) = \sigma_w$, $\chi = 0.54$ (dash line) and $\chi = 0$ (dash-dot line).

Our data set contains predominantly smaller bubbles as shown in Fig. 6. To cover a larger range of microbubble size we added 93 measurements which were performed at larger bubble range at acoustic pressure level of 100 kPa and described by Sijl *et al* (2010). Figure 9 shows now the subharmonic resonance frequency for all the bubbles together with the predictions of the visco-elastic model. It can be concluded that the visco-elastic model matches very well with the experimental values of a bubble diameter larger than 5 µm, but the prediction clearly fails for smaller bubbles.

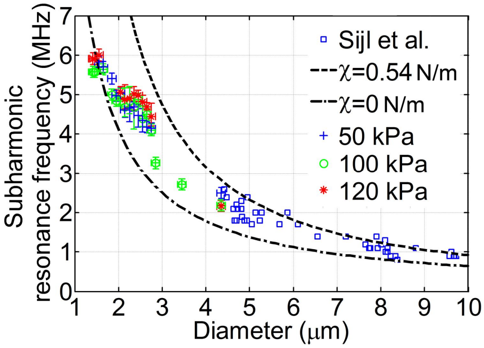

Fig 9. Subharmonic resonance frequency versus diameter of BR14 microbubbles. Dashed line is the fundamental resonance frequency predicted by the linearized visco-elastic model for $\chi = 0.54$ N / m and the dash-dotted line corresponds to $\chi = 0$ N / m.

DISCUSSION

The subharmonic behavior of a lipid coated contrast agent was investigated in the favored frequency range for carotid imaging (4-12 MHz). Forty percent of the investigated BR14 bubbles showed subharmonic oscillations (Fig. 6) and all of them vibrated with asymmetrical amplitude and by that showing the so called compression-only behavior. The fact that at low acoustic pressures the lipid coating induces highly nonlinear behavior e.g. compression-only has been observed before (de Jong *et al* 2007) and is also well described by Marmottant *et al* (2005) model. It is likely that the reason for the absence of the subharmonics in the remainder 60% of studied bubbles is due to the difference in the concentration of the shell lipids. This difference in the framework of the Marmottant model corresponds to having different values of the surface tension at rest for bubbles of the same size. The value of $\sigma(R_0)$ fixes also the value of the so called buckling radius R_b, i.e. the radius below which the phospholipid elastic coating does not exert any tensional effect. The case $\sigma(R_0) = 0$ in particular implies $R_b=R_0$, meaning compressive bubble oscillations (compression-only) are strongly favored in this case since the surface tension is totally absent for $R<R_0=R_b$; while it increases quadratically with R for $R>R_0$ (see Eq. 2). As it has been shown in the study by Sijl *et al* (2010), a compression-only behavior is associated with the presence of subharmonic resonances even at very low (5 kPa) driving pressures. When instead $\sigma(R_0)>0$, one has $R_b<R_0$. In this case buckling conditions are reached at higher driving pressures and therefore subharmonic resonance occurs less.

This hypothesis is also supported by our numerical simulations in which we have derived the amplitude of subharmonic as a function of $\sigma(R_0)$. Fig. 10 displays the dependence of the subharmonic amplitude on the surface tension of a 2.40 µm diameter bubble. The value of $\sigma(R_0)$ is varied from 0 to σ_w and normalized by the surface tension of water. The amplitude of resonance is normalized by the amplitude of subharmonic at $\sigma(R_0)=0$. The other shell parameters are kept the same as the previous simulations (Fig. 2). This result is also in very good agreement with the parametric study conducted by Sijl *et al* (2010) for a 7.6 µm diameter bubble at driving pressure amplitude and frequency of 40 kPa and 2.4 MHz. The highest subharmonic response is observed when the surface tension of a coated bubble at rest is zero. A slight increase in the value of $\sigma(R_0)$ results in a dramatic decrease in the subharmonic amplitude in which at $\sigma(R_0)=0.04$ N/m no subharmonic response is detected. The output of these simulations all together shows the sensitivity of bubble dynamics to shell parameters. A little change in the resting surface tension results in a completely different behavior for the bubbles even with the same size (see also Frinking *et al* 2010).

Secondly, we observed a size dependent behavior for the subharmonic resonance frequency of microbubbles with the increase of acoustic pressure. Extracting the resonance curves of bubbles with subharmonic spectroscopy versus applied acoustic pressure specifies two different regimes; bigger bubbles (>3 µm diameter) showed a decrease in the subharmonic resonance frequency for increasing the pressure; whereas for smaller bubbles (≤ 3 µm diameter) the subharmonic resonance frequency increases for increasing the pressure (Fig. 6). This phenomenon has not been observed for the fundamental resonance frequency. Overvelde *et al* (2010) showed that the fundamental resonance frequency decreases for increasing acoustic pressure for all bubble sizes. This is confirmed by the simulations using the Marmottant model as shown in Fig. 2.

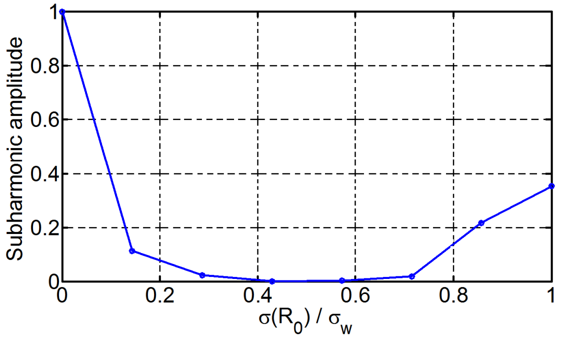

Fig 10. Amplitude of subharmonic versus the surface tension at rest of a 2.40 µm diameter bubble. The value of $\sigma(R_0)$ in the x-axis is normalized by σ_w. The amplitude of subharmonic in the y-axis is normalized by the amplitude of subharmonic at $\sigma(R_0)=0$.

The subharmonic resonance and its dependency on the acoustic pressure however, is also predicted correctly by the Marmottant model as shown in Fig. 11 using as shell parameters: $\sigma(R_0) = 0$, $\chi = 2.50$ N / m and $\kappa_s(R_0)$ adopted from Van der Meer *et al* (2007). In the same figure we also plot the ratio of the subharmonic resonance frequencies at 50 kPa and at 120 kPa versus bubble diameter as derived from the measurements. The graph shows up to 10% increase in the resonance frequency of bubbles smaller than 3 µm in diameter by increasing the pressure from 50 kPa to 120 kPa. For larger bubbles less experimental data are available. Nevertheless, opposite to what was explained before the subharmonic frequency ratio decreases. This is qualitatively supported also by numerical simulations.

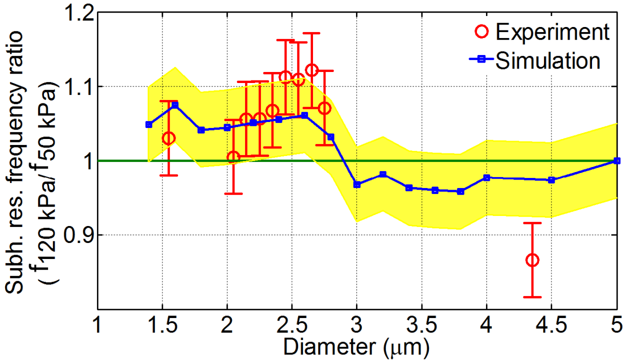

Fig 11. Subharmonic resonance frequency ratio of 120 kPa and 50 kPa acoustic pressures versus bubble diameter derived from experiment (circles) and simulation (squares). The filled area indicates the level of uncertainty in the simulations.

The explained behavior for small bubbles (≤ 3 µm diameter) is a phenomenon known as shell (strain) hardening in contrast to bigger bubbles (> 3 µm diameter) which show shell softening for the acoustic pressure increase. Shell (strain) softening is a rheological effect which indicates the decrease in the shell elasticity of a material as the deformation strength increases (Doinikov *et al* 2009). The comparison between these two regimes once again asserts the choice of zero surface tension at rest for the small bubbles.

We also compared the results of the experiments with the predictions of the linearized visco-elastic model using the value for shell elasticity ($\chi = 0.54$ N/m) reported by Van der Meer *et al* (2007). This value was found with the assumption of a linearized visco-elastic model on the fundamental resonance frequency of bubbles. Using this value delivered disappointing results for small bubbles although it has a good agreement for bigger bubbles (Fig. 9).

One important feature neglected in the derivation of the linearized visco-elastic model is the dynamic surface tension (Eq. 2) which is variable for different bubble sizes. Though, another size-dependent shell parameter is the shell viscosity. Van der Meer *et al* (2007) have shown that κ_s decreases for increasing dilatation rate, corresponding to a shear-thinning behavior. Pseudoplastic or shear-thinning fluids have a lower apparent viscosity at higher shear rates, and are usually solutions of large, polymeric molecules in a solvent with smaller molecules (Schowalter 1978; Macosko 1994). It is generally supposed that the large molecular chains tumble at random and affect large volumes of fluid under low shear, but they gradually align themselves in the direction of increasing shear and produce less resistance. By taking all these points into consideration, inserting the shell parameters: $\sigma(R_0) = 0$, $\chi = 2.50$ N/m and $\kappa_s(R_0)$ as derived by Van der Meer *et al* into the Marmottant *et al* model presents an excellent agreement with the experiment as shown in Fig. 12.

Finally, it was shown that the frequency of the subharmonic response of coated bubbles is not locked to the frequency of the fundamental resonance; instead their respective ratio depends on the applied acoustic pressure (Fig. 2). Therefore it is not exact to assume that the highest value of subharmonic amplitude occurs always at the double frequency of the fundamental resonance frequency of a microbubble. Depending on the size and shell parameters this factor can vary from one bubble to the other. For example the 4 µm diameter bubble reported in Fig. 2, has the subharmonic resonance frequency of 2.1 MHz at 1 kPa. This means that the transmitting frequency in which the subharmonic resonance frequency was derived was 4.2 MHz. The ratio between this value and the fundamental resonance frequency of the bubble at the same pressure (which is also reported in the same figure as 2.4 MHz) is 1.7. The same calculation at 120 kPa gives a ratio equal to 2.4. Therefore, for a 4 µm diameter bubble with a resting surface tension of zero, this factor varies between 1.7 and 2.4 at different acoustic pressures.

As already mentioned at the end of section *Experimental Setup*, at present the simultaneous comparison of the fundamental and subharmonic responses of a bubble is not experimentally feasible. Therefore we had to limit the analysis to the comparison of the experimental results with the outcomes of the simulations. This highlights the importance of a predictive model explaining the behavior typical for bubble sizes < 3 µm and careful choice of shell parameters.

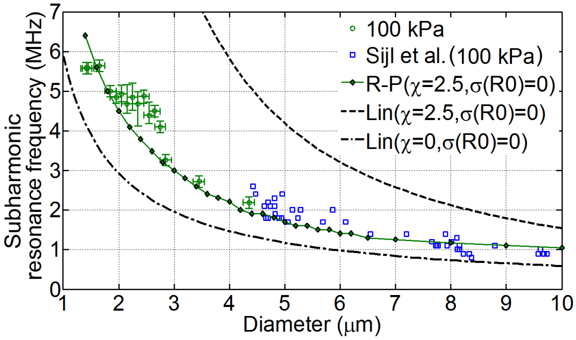

Fig 12. comparison between linearized Rayleigh- Plesset (Lin) (Eq. 4) at two values of shell elasticity (0 and 2.50 N/m) and $\sigma(R_0) = 0$, the modified Rayleigh- Plesset (R-P) (Eq. 1) and the experimental measurements at acoustic pressure amplitude of 100 kPa.

The results derived from this study provide the basic knowledge for using the subharmonic response of UCAs in carotid imaging. For clinical applications normally pulse lengths shorter than the 25 cycle burst applied in our experiments are used. Nevertheless, we show in the following (Fig. 13) that the same can be achieved by implementing a shorter pulse which is more relevant for clinical scanners. The results of numerical simulations, presented in Fig. 13, show the response of a 4 µm diameter bubble to the pressure pulse described previously (see section numerical model) with the amplitude of 120 kPa at the insonifying frequency of 4.4 MHz. The length of the burst has increased from 5 cycles to 10 and 25 respectively. As can be seen in the figures, the subharmonic energy is already present in the first cycles and its level compared to the fundamental response remains equal.

Furthermore, in order to adapt the existing clinical scanners for subharmonic carotid imaging it is crucial to characterize the subharmonic oscillation of contrast agent microbubbles also acoustically, which is what a scanner would actually measure. Acoustical studies on the subharmonic response of these microbubbles, complementary to the optical study presented here, are presented in the forthcoming chapters VII and VIII.

CONCLUSION

For the frequencies between 4 and 12 MHz 40% of the bubbles exhibited a subharmonic response. These bubbles had a diameter between 1 and 4 µm. The subharmonic resonance frequency for bubbles smaller than 3 µm is not the same as the fundamental resonance frequency. Furthermore the subharmonic resonance frequency of this bubble size increased up to 10% with increasing acoustic pressure from 50 to 120 kPa. This observation indicates a shell hardening effect, just the opposite of what was observed for the fundamental response.

The proper choice of shell parameters: $\sigma(R_0) = 0$, $\chi = 2.50$ N / m and $\kappa_s(R_0)$ presenting shear thinning resulted to an excellent agreement between the Marmottant model and the experimental data.

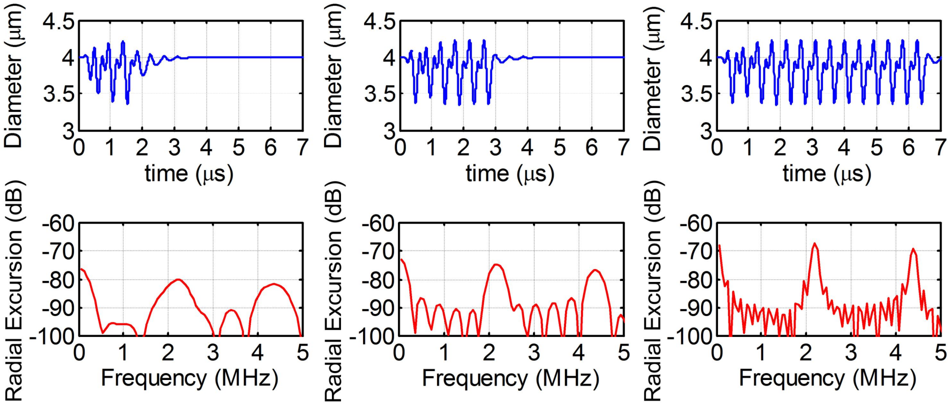

Fig 13. Response of a 4 μm diameter bubble to a pressure pulse with the amplitude of 120 kPa at the transmitting frequency of 4.4 MHz. The length of the burst (from left to the right) has increased from 5 cycles to 10 and 25 respectively. DT-curves are shown in the upper panels and the lower panels present the corresponding power spectra.

Acknowledgement- Authors would like to thank Frits Mastik for his support on Brandaris recordings and Benjamin Dollet, Guillaume Renaud and Enrico Calzavarini for their valuable comments.

References

Biagi E, Breschi L, Vannacci E, Masotti L. Stable and transient subharmonic emissions from isolated contrast agent microbubbles. IEEE Trans Ultrason Ferroelectr Freq Control 2007;54:480-497.

Chang PH, Shung KK, Wu S, Levene HB. Second harmonic imaging and harmonic doppler measurements with albunex. IEEE Trans Ultrason Ferroelectr Freq Control 1995;42:1020-1027.

Chin CT, Lancee C, Borsboom J, Mastik F, Frijlink M, de Jong N, Versluis M, Lohse D. Brandaris 128: a 25 million frames per second digital camera with 128 highly sensitive frames. Rev. Sci. Instru. 2003;74:5026-5034.

Church CC. The effects of an elastic solid surface layer on the radial pulsations of gas bubbles. J Acoust Soc Am 1995;97:1510-1521.

de Jong N, Cornet R, Lancée CT. Higher harmonics of vibrating gas-filled microspheres. Part one: simulations. Ultrasonics 1994;32:447-453.

de Jong N, Emmer M, Chin CT, Bouakaz A, Mastik F, Lohse D, Versluis M. Compression-only behavior of phospholipid-coated contrast bubbles. Ultrasound Med Biol 2007;33:653-656.

de Jong N, Hoff L. Ultrasound scattering properties of Albunex microspheres. Ultrasonics 1993;31:175-181.

de Santis P, Sette D, Wanderlingh F. Cavitation detection: The use of the subharmonics. J. Acoust. Soc. Am 1967;42:514-516.

Doinikov AA, Haac JF, Dayton PA. Modeling of nonlinear viscous stress in encapsulating shells of lipid-coated contrast agent microbubbles. Ultrasonics 2009;49:269-275.

Eller HGF. Generation of Subharmonics of Order One-Half by Bubbles in a Sound Field. J. Acous. Soc. Am 1969;46:722-727.

Frinking P, Gaud E, Arditi M. Compression-only Behavior and Subharmonic Scattering of Phospholipid-Shell Microbubbles. IEEE International Ultrasonics Symposium Proceedings 2009;978:4244-4390.

Frinking PJA, Gaud E, Brochot J, Arditi M. Subharmonic scattering of phospholipid-shell microbubbles at low acoustic pressure amplitudes. IEEE Trans. Ultrason. Ferroelec. Freq. Contr. 2010;57:1762-1771.

Hoff L, Sontum P, Hovem, J. Oscillations of polymeric microbubbles: Effect of the encapsulating shell. J Acoust Soc Am 2000;107:2272-2280.

Keller JB, Miksis MJ. Bubble oscillations of large amplitude. J Acoust Soc Am 1980;68:628-633.

Krishna PD, Shankar PM, Newhouse VL. Subharmonic generation from ultrasonic contrast agents. Phys Med Biol 1999;44:681-94.

Lauterborn W. Numerical investigation of nonlinear oscillations of gas bubbles in liquids. J. Acoust. Soc. Am. 1976;59:283-293.

Leighton TG. The acoustic bubble. 1994 Academic Press Limited, London.

Lotsberg O, Hovem JM, Aksum B. Experimental observation of subharmonic oscillations in infoson bubbles. J. Acoust. Soc. Am. 1996;99:1366-1369.

Macosko CW. Rheology Principles, Measurements and Applications. 1994 Wiley-VCH.

Marmottant P, Van der Meer S, Emmer M, Versluis M, de Jong N, Hilgenfeldt S, Lohse D. A model for large amplitude oscillations of coated bubbles accounting for buckling and rupture. J Acous Soc Am. 2005;118:3499-3505.

Minnaert M. On musical air bubbles and the sound of running water. Philos. Mag. 1933; 16:235-248.

Neppiras EA. Subharmonic and other low-frequency emission from bubbles in sound-irradiated liquids. J. Acoust. Soc. Am. 1969;46:587-601.

Overvelde M, Garbin V, Sijl J, Dollet B, De Jong N, Lohse D, Versluis M. Nonlinear shell behavior of phospholipid-coated microbubbles." Ultrasound Med. Biol. 2010;36:2080-2092.

Plesset MS. The dynamics of cavitation bubbles. J. Appl. Mech. 1949;16:277-282.

Prosperetti A. Nonlinear oscillations of gas bubbles in liquids: steady state solutions. J. Acoust. Soc. Am. 1974;56:878-885.

Prosperetti A. Nonlinear oscillations of gas bubbles in liquids. Transient solutions and the connection between subharmonic signal and cavitation. J. Acoust. Soc. Am. 1975;57: 810-821.

Prosperetti A. Application of the subharmonic threshold to the measurement of the damping of oscillating gas bubbles. J. Acoust. Soc. Am. 1977;61:11-16.

Schowalter WR. Mechanics of Non-Newtonian fluids. 1978 Pergamon Press, Oxford-Frankfurt.

Shankar PM, Krishna PD, Newhouse VL. Advantages of subharmonic over second harmonic backscatter for contrast-to-tissue echo enhancement. Ultrasound Med Biol 1998;24:395-399.

Shankar PM, Krishna PD, Newhouse VL. Subharmonic backscattering from ultrasound contrast agents. J. Acoust. Soc. Am. 1999;106:2104-2110.

Sijl J, Dollet B, Overvelde M, Garbin V, Rozendal T, De Jong N, Lohse D, Versluis M. Subharmonic behavior of phospholipid-coated ultrasound contrast agent microbubbles. J. Acoust. Soc. Am. 2010;128:3239-3252.

Van der Meer SM, Dollet B, Voormolen MM, Chin CT, Bouakaz A, de Jong N, Versluis M, Lohse D. Microbubble spectroscopy of ultrasound contrast agents. J Acoust Soc Am 2007;121:648-56.

Chapter V

Liposome-loaded microbubble spectroscopy

Ying Luan, Telli Faez, Erik Gelderblom, Ilya Skachkov, Bart Geers, Ine Lentacker, Antonius F W van der Steen, Michel Versluis, Nico de Jong

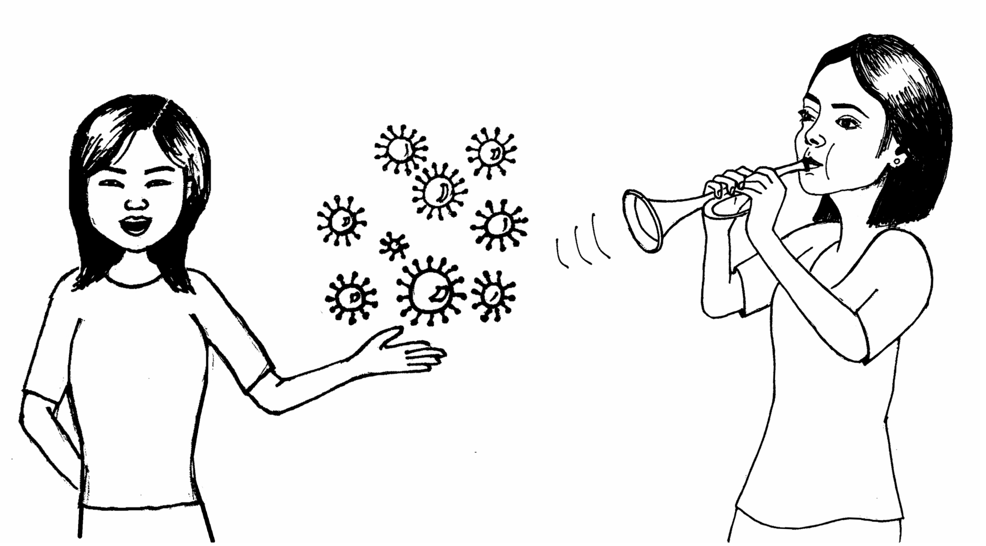

In Press, Ultrasound in Medicine and Biology July 13, 2012

Abstract

A comparison between phospholipid-coated microbubbles with and without liposomes attached to the microbubble surface was performed using the ultra-high speed imaging camera (Brandaris 128). We investigated 73 liposome-loaded microbubbles (loaded microbubbles) and 41 microbubbles without liposome loading (unloaded microbubbles) with a diameter ranging from 3 μm to 10 μm at frequencies ranging from 0.6 to 3.8 MHz, and acoustic pressures from 5 to 100 kPa. The experimental data showed nearly the same shell elasticity for the loaded and unloaded bubbles but the shell viscosity was higher for loaded bubbles compared to unloaded bubbles. For loaded bubbles a higher pressure threshold for the bubble vibrations was noticed. In addition, an “expansion-only” behavior was observed for up to 69% of the investigated loaded bubbles, which mostly occurred at low acoustic pressures (≤30 kPa). Finally, fluorescence imaging showed heterogeneity of liposome distributions of the loaded bubbles.

INTRODUCTION

The applications of ultrasound-mediated drug delivery systems and their underlying physical mechanisms are nowadays under extensive investigations due to their enormous clinical potential, especially in oncology and cardiovascular applications (Ferrara *et al* 2007; Newman *et al* 2007; Hernot *et al* 2008). The general goal of drug delivery is to improve the efficiency of drug uptake in the region of interest while reducing undesired side effects, such as toxicity in healthy tissue (Hernot *et al* 2008). It has been shown that the oscillations of co-administered contrast agent microbubbles are capable of greatly enhancing the drug transfer efficiency (Frinking *et al* 1998; van Wamel *et al* 2006; Kooiman *et al* 2010). Microbubbles are also designed to be preloaded with pharmaceutical agent, which is locally released by an ultrasound pulse (Unger *et al* 1998; Lentacker *et al* 2009; Tinkov *et al* 2010).

An even more advanced drug loading system consists of nanoparticles containing drugs, attached to the shell of the microbubble. This ensures a larger drug-carrying capacity and a higher drug transportation safety. Liposome nanoparticles, composed of an aqueous core entrapped by one or more lipid bilayers, are investigated as functional micro-particulate drug carriers for both hydrophobic and hydrophilic drugs (Sharma *et al* 1997; Kheirolomoom *et al* 2007). To combine the advantages of the acoustical properties of the microbubbles and the fusogenicity of the liposomes, Kheirolomoom *et al* (2007) introduced novel liposome-loaded microbubbles by mounting liposomes to the microbubble shell via avidin-biotin conjugation. Based on this formulation, Lentacker *et al* (2007) presented PEGylated lipoplexe-loaded microbubbles, which showed strongly improved gene transfer efficiency. Recently, Geers *et al* (2011) further improved the system by covalent thoil-maleimide linkages between liposomes and microbubbles through a single step self-assembly process. The size distribution of lipid-shelled microbubbles (unloaded microbubbles) and loaded microbubbles was measured by a MultisizerTM 4 Coulter Counter, with a measurement range of 0.4-12 μm.

Results indicated an average volume diameter of 4 µm for loaded bubbles, which is approximately 400 nm larger than the diameter of the unloaded microbubbles (Geers *et al* 2011). This is in agreement with the liposome layer thickness of 200 nm. The drug loading capacity of the loaded bubbles was also evaluated by flow cytometry. The number of liposomes attached to each microbubble surface is about 600 to 1300. *In vitro* and *in vivo* characterizations evaluated the biological efficiency of drug containing loaded microbubbles and the results indicated a great enhancement in the cellular uptake (Lentacker *et al* 2009; Geers *et al* 2011).

Optimal use of loaded bubbles for drug delivery in (pre-) clinical research requires a thorough characterization of the loaded bubble, to get the optimal ultrasonic parameters for bubble activation and feedback for bubble preparation. Extensive work has been performed in recent years on the characterization of the acoustical behavior of unloaded microbubbles both experimentally and theoretically. Examples of experimental work has been presented by Dayton *et al* (1999), van der Meer *et al* (2007), Emmer *et al* (2009), Overvelde *et al* (2010), Sijl *et al* (2010), chapter IV and VI. They showed the nonlinear bubble dynamics in response to ultrasound and their experimental results were compared with theoretical models introduced by for instance de Jong *et al* (1994), Church (1995) and Marmottant *et al* (2005). Shell properties of the unloaded bubbles were also investigated through acoustic attenuation and scattering measurements (Chang 1995; Shun 1995; Morgan *et al* 2000; chapter III), atomic force microscopy (Sboros *et al* 2006), and light scattering (Tu *et al* 2009).

Experimental and theoretical investigations on unloaded bubbles have provided rich knowledge concerning microbubbles, which can be applied as a reliable reference in studying LOADED bubbles. In this study, the acoustic behavior of unloaded and loaded bubbles as a function of transmitting frequency and applied acoustic pressure are investigated, using an ultra-high speed imaging technique. The shell properties of loaded bubbles are derived and compared with unloaded bubbles. Finally, with the aid of confocal fluorescence imaging, the morphological structure of liposome attachment of loaded bubbles is studied.

MATERIAL AND METHOD

Microbubble Preparation

Unloaded microbubbles were prepared by mixing 1,2-dipalmitoyl-sn-glycero-3-phosphocholine (DPPC) (Lipoid, Ludwigshafen, Germany) and 1,2-distearoyl-sn-glycero-3-phosphoethanolamine-N-[PDP(polyethylene glycol)-2000] (DSPE-PEG-SPDP) in a molar ratio of 65:35 in chloroform. After chloroform evaporation, the lipid film was dissolved in a 1:2:7 glycerine-propyleneglycol-H2O mixture to obtain a clear solution with a final lipid concentration of 4 × 10-4 mmol/mL. This lipid solution was aliquotted in 2.5mL chromatography vials of which the headspace was filled with perfluorobutane gas (F2 chemicals, Preston, UK). Finally, bubbles were obtained by high speed shaking of the chromatography vial in a Vialmix agent activator (Bristol-Myers Squibb Medical Imaging, North Billerica, MA, USA) for 15 seconds. For loaded microbubbles, maleimide-functionalized liposomes were prepared by mixing DPPC, 1,2-distearoyl-snglycero-3-phosphoethanolamine-N-[maleimide(polyethyleneglycol)-2000] (ammonium salt) (DSPE-PEG maleimide) (Laysan Bio Inc, Arab, AL), cholesterol, all dissolved in chloroform in a round-bottom flask at a 49:15:35 molar ratio with a final lipid concentration of 16 mg/mL lipids. The chloroform was evaporated and the remaining lipid film was hydrated with distilled water. The liposomes were sized by extruding through a 200nm polycarbonate filter using a mini-extruder at 60 °C (Avanti Polar Lipids, Alabaster, AL). Then liposomes were added with a concentration of 100 mmol/mL to the lipid solution used for the preparation of unloaded microbubbles. The mechanical activation forms loaded bubbles with a liposomes layer coupled to the microbubble surface through a covalent thiol-maleimide link.

For fluorescence labeling of loaded microbubbles, the bubble samples were prepared with nearly the same procedure as described previously, only the lipid mixture used for the preparation of unloaded microbubbles was added with bodipy (Invitrogen, Merelbeke, Belgium) labeled liposomes and the lipophilic dye DiI (Sigma-aldrich, Bornem, Belgium). High speed shaking of the vial generates loaded bubbles with DiI-labeled lipid shell and bodipy-labeled liposomes attached on the bubble shell. (Geers *et al* 2011). Figure 1 schematically depicts the structure of an unloaded bubble and a loaded bubble.

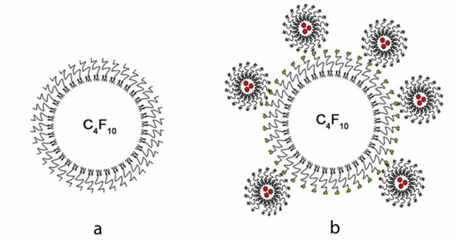

Fig 1. The schematic view of a) an unloaded bubble and b) a loaded bubble.

Experimental Setup

Frequency scanning experiment

Figure 2a shows a schematic view of the experimental setup showing the ultrasound, optical microscope and the ultra-high speed camera. An acoustically transparent cellulose capillary tube with an inner diameter of 200 μm and a wall thickness of 20 μm (Product No. 132294 Spectrum Europe, Breda, NL) was submerged and fixed in a water tank at room temperature. A broadband transducer (PA086, 0.5-4 MHz, Precision Acoustics, Dorchester, UK) was mounted on the side of the water tank and was focused on the capillary tube. Before the experiments, the transducer was calibrated in a separate set-up with a calibrated 0.075 mm needle hydrophone (Precision Acoustic Ltd., Dorchester, UK). The transmit signal was generated by an arbitrary wave generator (8026, Tabor Electronics Ltd., Tel Hanan, Israel) and amplified with a power amplifier (150A100B Amplifier Research, Limerick, Ireland). An optical light guide

(SCHOTT AG, Mainz, Germany) connected to a Xenon flash lamp (A-260 Vision Light Tech, Uden, NL) was mounted at the bottom of the water tank to illuminate the region-of-interest in the capillary tube. An Olympus microscope with a 60×water-immersed objective (NA=0.9) and a 2× magnifier was focused on the bubbles inside the capillary. Microbubbles were withdrawn from the vial and diluted in Isoton II (Coulter Electronics, Luton, UK). Then the dilution was injected with a syringe into the capillary. Bubbles with a diameter ranging from 3 to 10 μm were insonified at driving frequencies between 0.5 MHz and 3.9 MHz with a frequency step of 200 kHz and at acoustic pressures of 50 kPa and 100 kPa. Bursts of a 10 cycle sinusoidal wave, tapered with a Gaussian envelope at the first and last 2 cycles were transmitted. The dynamics of the bubbles was captured by the Brandaris 128 (Chin *et al* 2003) at a frame rate of 15 million frames per second (Mfps). For each single bubble the camera was set to record 35 movies of 128 frames so that all frequencies could be acquired in a single run. For each movie the diameter of the microbubble as a function of time (DT-curve) was measured using custom-designed image analysis software (van der Meer *et al* 2007). The discrete Fourier transforms of the DT-curves were calculated. The maximum amplitude of excursion at each transmitted frequency was determined and, by plotting the amplitude as a function of the transmitting frequency, the resonance curve of each individual bubble was constructed.

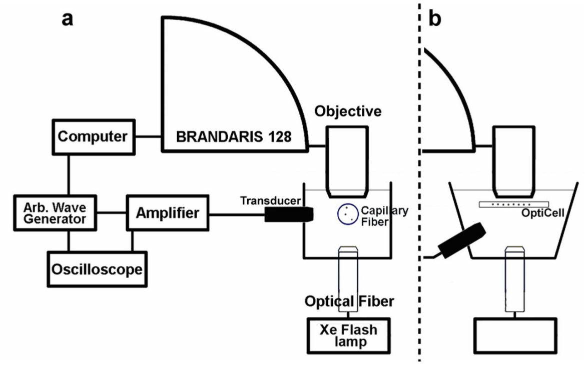

Fig 2. Schematic view of the experimental setups with a) a capillary tube, and b) an OptiCell chamber.

Pressure scanning experiment

For the pressure scanning measurements the capillary tube was replaced by an OptiCell chamber (NUNC™, Thermo Fisher Scientific, city, country) as depicted in figure 2b.The optical focal point of the objective and the acoustical focus of the transducer were aligned by a needle hydrophone (HPM02/1, Precision Acoustics, Dorchester, UK) which was positioned at the focus of the objective. The bubble solution was injected into the OptiCell chamber which was filled with Milli-Q water (Millipore, Billerica, MA). The transmitted frequency range was from 0.6 to 3.8 MHz, with frequency steps of 200 kHz. The applied acoustic pressures were 5 kPa to 50 kPa with pressure steps of 5 kPa, followed by 75 kPa and 100 kPa, leading in total to a set of 204 experiments on each single bubble.

Fluorescence Imaging

Confocal fluorescence microscopy (Zeiss LSM510META JNI, Jena, Germany) was performed on individual loaded bubbles with bodipy-labeled liposomes and a DiI-labeled microbubble lipid shell to observe the morphological features of liposomes attachment. A 100× oil-immersed objective (Plan Apochromat, Carl Zeiss, Oberkochen, Germany) (NA=1.4) was used. The excitation wavelengths applied for bodipy and DiI were 488 nm and 633 nm, while the emission filters for detecting these two fluorophores were BP 505-530 nm and LP 560 nm, respectively.

RESULTS

Resonance and damping

The responses of 38 loaded bubbles and 27 unloaded bubbles were recorded in the frequency scanning measurement. As an example, 6 DT-curves of a 7.5 μm loaded bubble and their corresponding power spectra are displayed in figure 3. The driving frequency in these selected graphs increases from 0.7 MHz to 1.7 MHz and the acoustic pressure is 50 kPa. The figure shows that the amplitude of bubble response varies for different driving frequencies and reaches a maximum at a driving frequency of 0.9 MHz.

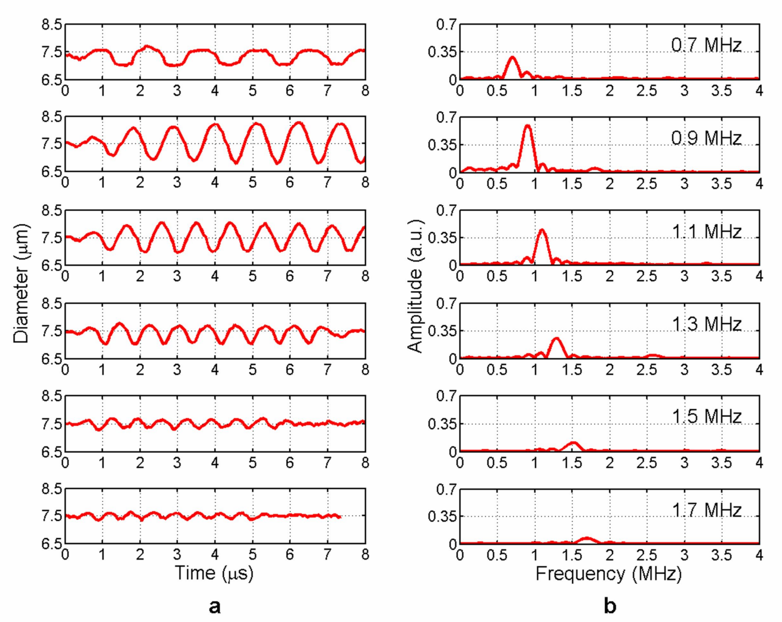

Fig 3. a) Selected DT-curves and b) corresponding power spectra of a loaded bubble with a diameter of 7.5 μm. The selection has been done between 0.7 MHz to 1.7 MHz with the step frequency of 200 kHz. The applied acoustic pressure is 50 kPa.

The resonance curves of two unloaded bubbles and two loaded bubbles are displayed in figure 4. Unloaded bubbles and loaded bubbles of similar size are compared. By fitting the data to the Lorentzian function (Eq. 7) introduced in chapter IV, two parameters are obtained: the eigenfrequency and the total damping coefficient (van der Meer *et al* 2007). Figure 5 depicts the total damping coefficient of the studied bubbles as a function of the bubbles' diameter.

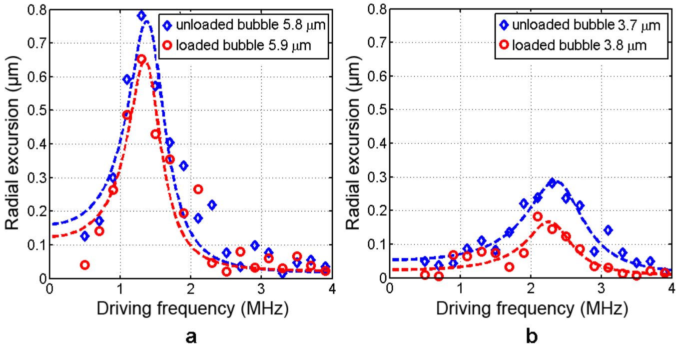

Fig 4. Resonance curve and the fit on the data of two pairs of unloaded bubbles and loaded bubbles with similar size of about a) 5.9 μm and b) 3.8 μm respectively. The applied acoustic pressure is 50 kPa.

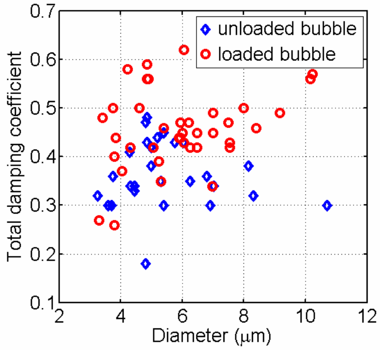

Fig 5. The total damping coefficient of unloaded bubbles and loaded bubbles as a function of bubble size.

Shell viscosity

The shell viscosity (κ_s) is estimated from the total damping coefficient (δ_{tot}) as follows (Eq. 2, chapter III):

$$\delta_{tot} = \frac{\omega_0 R_0}{c} + \frac{4\mu}{R_0^2 \rho \omega_0} + \frac{4\kappa_s}{R_0^3 \rho \omega_0} \qquad (1)$$

δ_{tot} is the sum of the contributions of acoustic re-radiation, viscous damping of the liquid and the shell viscous damping coefficient respectively. $\omega_0=2\pi f_0$ is the angular frequency of the microbubble; R_0 is the equilibrium radius; $c=1.5\times10^3$ m/s is the speed of sound in water; $\rho=10^3$ kg/m^3 is the density of water; $\mu=2\times10^{-3}$ Pa s is an effective viscosity parameter, which indicates the real viscosity of the surrounding liquid and the effect of the thermal damping, as proposed by Devin (1959) and Medwin (1977).

The estimated shell viscosity of the unloaded bubbles and loaded bubbles as a function of the bubble diameter and the dilatation rate as described by van der

Meer *et al* 2007 are depicted in figure 6a and b respectively. An apparent difference of the shell viscosity between the loaded and the unloaded bubble is found for bubbles larger than 6 μm in diameter. The averaged shell viscosity among the loaded bubbles larger than 6 μm in diameter is 4×10^{-8} kg/s which is almost twice the shell viscosity of unloaded bubbles within the same size range (2.3×10^{-8} kg/s). In figure 6b the shell viscosity is plotted against the dilatation rate showing shear thinning especially for the loaded bubble.

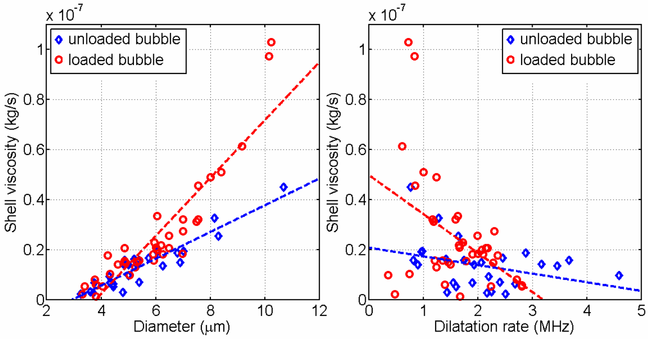

a b

Fig 6. The shell viscosity of unloaded bubbles and loaded bubbles as a function of a) bubble size and b) the dilatation rate. Dashed lines are the linear fit on the data with coefficients of a) 5.3×10^{-9} for unloaded bubbles and 1.2×10^{-8} for loaded bubbles, and b) -3.4×10^{-9} for unloaded bubbles and -1.6×10^{-8} for loaded bubbles.

Shell elasticity

Shell elasticity is estimated by fitting the experimentally measured resonance frequencies versus the bubble's diameter (Fig. 7) using a linear viscoelastic model (Marmottant *et al* 2005), as described below:

$$f_0 = \frac{1}{2\pi}\sqrt{\frac{1}{\rho R_0^2}[3\gamma P_0 + \frac{2(3\gamma-1)\sigma_\omega}{R_0} + \frac{4\chi}{R_0}]} \quad (2)$$

The resonance frequency is where the maximum amplitude of oscillations occurs and is lower than the eigenfrequency f_0 by a factor of   in the presence of damping. In our case, this factor is between 1 and 1.11. $P_0 = 10^5$ Pa is the ambient pressure; γ is the polytropic exponent of an isothermal vibration, and equals to the ratio of specific heats for a bubble behaving adiabatically (1.07 for C_4F_{10}); σ_ω is the surface tension of water-gas interface and χ is the shell elasticity. At 50 kPa, a shell elasticity of χ =0.17±0.09 N/m was found for loaded bubbles, which is very similar to the value found for unloaded bubbles (χ=0.19±0.07 N/m).

Pressure dependent resonance

Figure 8 shows the experimentally obtained amplitude of oscillations of an unloaded bubble and a loaded bubble, with the diameter of 4.5 μm and 4.3 μm respectively, for the full driving frequency and pressure scan. The color indicates the amplitude of the vibration. A total of 204 DT-curves have been measured at 12 different acoustic pressures in the range of 10 to 100 kPa. For each pressure, 17 different frequencies were applied. It can be seen that by increasing the acoustic pressure, the resonance frequencies of the unloaded and loaded bubbles slightly decrease. However, at the same acoustic pressure, unloaded bubbles have higher amplitude of oscillation compared to the loaded bubbles. Also the threshold pressure, that is the pressure below which no vibration amplitude can be noticed, differs between loaded and unloaded bubbles.

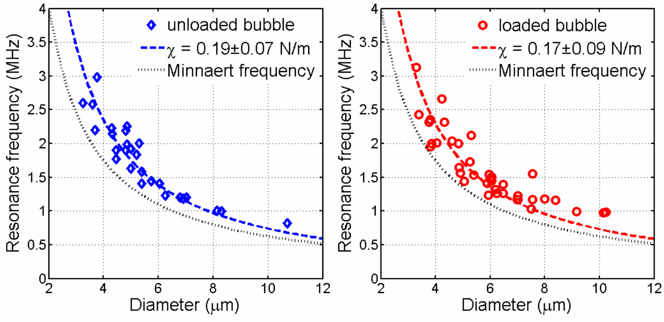

a

b

Fig 7. The resonance frequency of a) unloaded bubbles and b) loaded bubbles as a function of the bubble diameter at an acoustic pressure of 50 kPa. A fit on the data was performed using Eq. 2.

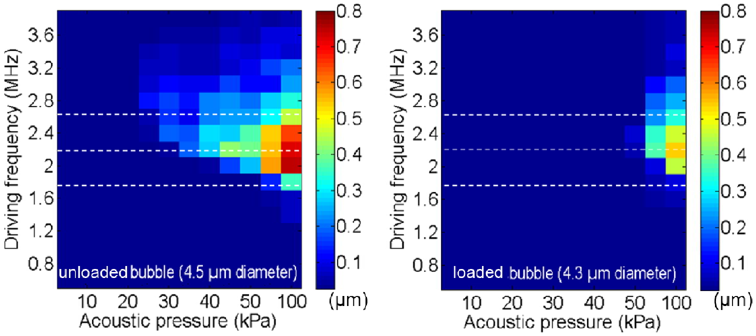

a

b

Fig 8. Amplitude of oscillation as functions of acoustic pressure and driving frequency for a) an unloaded bubble with 4.5 μm diameter and b) a loaded bubble with 4.3 μm diameter. Dashed lines indicate the experimental data obtained at 2.6 MHz, 2.2 MHz and 1.8 MHz, which are plotted in Fig. 9.

To better demonstrate this effect we plot the amplitude of oscillation of the same bubbles presented in figure 8 as a function of the acoustic pressure at three driving frequencies: 2.2 MHz, which is the frequency of maximum response (FMR) of the two microbubbles at 100 kPa, and 2.6 MHz and 1.8 MHz, which are 400 kHz above and below the indicated FMR, respectively. The results are shown in figure 9. Figures 9a, b and c show the thresholding behavior for both microbubbles below the resonance, at the resonance and above the resonance, respectively. The threshold pressure for the initiation of bubble oscillations is significantly higher for the loaded bubble compared with the unloaded bubble with a similar size. Moreover, the threshold pressure for the unloaded bubble is higher with decreasing driving frequency (Fig. 8a). In other words, the thresholding behavior of unloaded bubbles is driving frequency dependent. The noise level of the amplitude of oscillation was estimated by the discrete Fourier transform of the DT-curves if no ultrasound was applied.

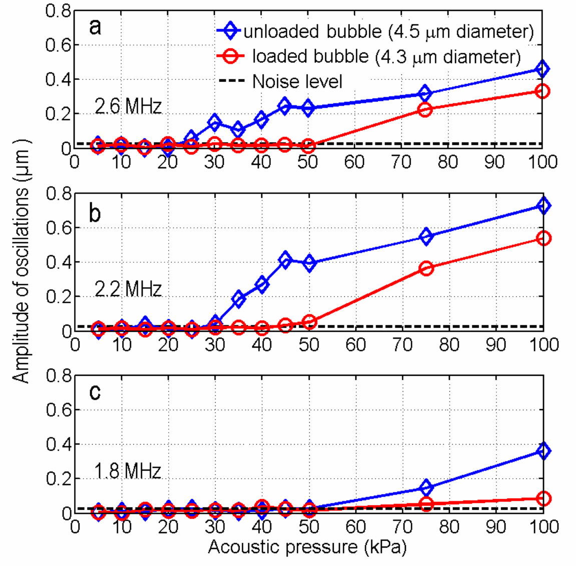

Fig 9. Amplitude of oscillation as a function of the acoustic pressure a) at 400 kHz above the resonance (2.6 MHz) b) at the resonance (2.2 MHz) and c) at 400 kHz below the resonance (1.8 MHz). Dashed lines indicate the noise level in the experiments.

Figure 10 shows the threshold pressure for all the unloaded and loaded bubbles investigated in the pressure scanning experiment as a function of the bubble size. Similar to figure 9, the threshold pressure of the bubbles was derived at the resonance frequency of the bubbles (Fig. 10b) and at 400 kHz above and below their resonance frequencies (Fig. 10a and c respectively). The threshold pressures decrease with increasing bubble size, and decrease by increasing the driving frequency, as indicated before (Fig. 9). The increase of the pressure threshold are estimated by comparing loaded bubbles to unloaded bubbles of similar size range ($\Delta d<0.5$ μm, Δd is the size difference). For frequencies above resonance, the pressure thresholds of the loaded bubbles are estimated to be 0.1 to 4 times higher than for unloaded bubbles of similar size. For frequencies near resonance, the value is in the range of 0.08 to 2.75. In case of frequencies below resonance, the range is 0.06 to 1.5. In average, loaded bubbles show a higher pressure threshold values than unloaded bubbles of a similar size.

Expansion-only behavior

An "expansion-only" behavior was frequently observed for loaded microbubbles. A typical example is given in figure 11 showing a loaded microbubble driven at 1.5 MHz at an acoustic pressure of 50 kPa. The occurrence and dependence of the expansion-only behavior to the driving frequency and applied acoustic pressure was investigated for 73 loaded bubbles and 41 unloaded bubbles, among which 38 unloaded bubbles and 27 loaded bubbles were insonified at acoustic pressures of 50 kPa and 100 kPa in the frequency scanning experiment. The rest of the microbubbles were insonified with increasing pressures, ranging from 5 to 100 kPa as explained in the pressure scanning experiment.

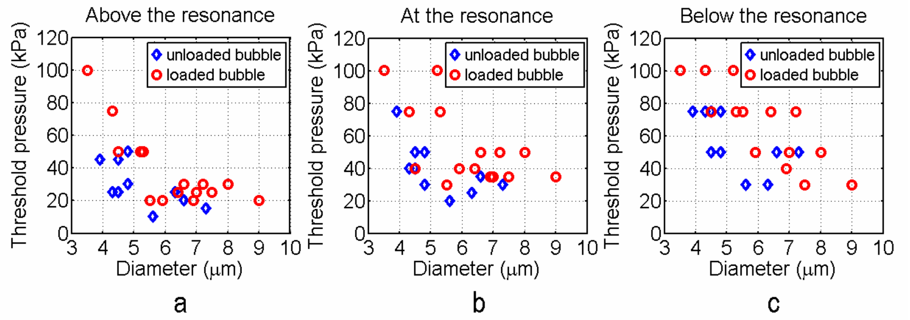

Fig 10. Threshold pressure for the initiation of bubble oscillations for unloaded and loaded bubbles at a) 400 kHz above the resonance, b) the resonance and c) 400 kHz below the resonance.

In the frequency scanning experiment, 87% of the studied unloaded bubbles showed no expansion-only behavior. The remaining 13% of the unloaded bubbles exhibited expansion-only behavior at an elevated acoustic pressure of 100 kPa. As for the loaded bubbles, 31% showed no expansion-only behavior, 53% showed expansion-only behavior at the acoustic pressure of 50 kPa and 16% exhibited expansion-only behavior at a pressure of 100 kPa. No apparent frequency dependency was noticed for the expansion-only behavior.

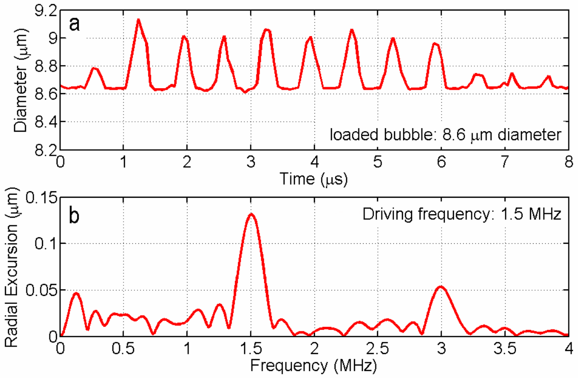

Fig 11. a) DT-curve and b) the power spectra of the oscillations of a loaded bubble (8.6 μm diameter) exhibiting an expansion-only behavior. The applied acoustic pressure is 50 kPa and the driving frequency is 1.5 MHz.

For the pressure scanning experiment, the occurrence of the expansion-only behavior for both unloaded and loaded bubbles as a function of the applied acoustic pressure is depicted in figure 12. The results showed that loaded bubbles exhibit expansion-only behavior at lower acoustic pressures compared to the unloaded bubbles and the occurrence of expansion-only behavior decreases with increasing acoustic pressure. Around half of the loaded bubbles show expansion only, below or at 30 kPa, while this number reduces to 14% for the unloaded bubbles.

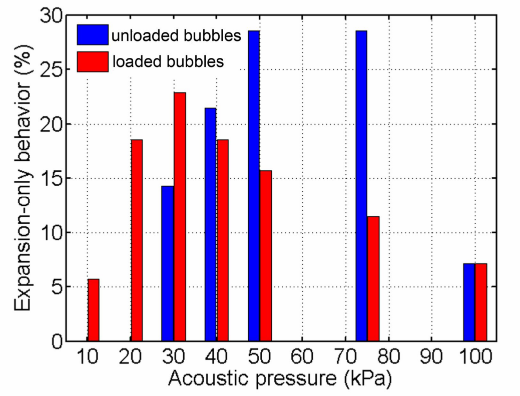

Fig 12. The occurrence of expansion-only behavior as a function of acoustic pressure for unloaded bubbles and loaded bubbles.

Liposome attachment

Figure 13 shows the bright-field and fluorescence images of a loaded bubble taken with a confocal microscope. The liposome (Fig. 13b) and the lipid shell of the microbubbles (Fig. 13c) were both fluorescently labeled and showed to have a heterogeneous distribution of the shell coating (Fig. 13d). This is in agreement with observations of Kooiman *et al* (2010) by 4Pi microscopy, in which they reported inhomogeneous distributions of phospholipids on the microbubble shell.

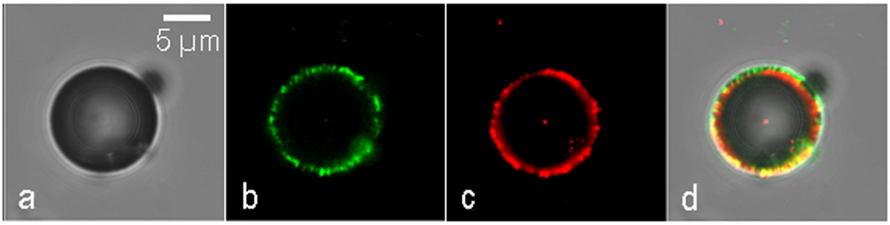

Fig 13. a) bright-field image of a loaded bubble and the fluorescent images with b) bodipy-labeled liposomes and c) DiI labeled lipid shell. d) The combined image of both layers on the bright field image.

DISSCUSSION

Shell properties

The effective shell properties (elasticity and viscosity) of the 27 unloaded bubbles and the 38 loaded microbubbles were derived experimentally. For unloaded bubbles, an elasticity of 0.19±0.07 N/m was estimated (Fig. 7). Also it was observed that the shell dilatational viscosity increases with the bubble size, and a typical viscosity of 4×10^{-8} kg/s was derived for loaded bubbles larger than 6 μm (Fig. 6a). The shell elasticity of unloaded bubbles derived from this study is lower than the value (0.54±0.1 N/m) reported in previous experimental observations for phospholipid-coated microbubbles (BR14), while the shell viscosity values are compatible with previously reported values of 0.72×10^{-8} kg/s and 1.5×10^{-8} kg/s (Gorce *et al* 2000; Marmottant *et al* 2005; van der Meer *et al* 2007). As shown previously in figure 8a, with the increase of the applied acoustic pressures, the frequency of maximum response decreases, leading to lower effective shell elasticity. Therefore, one possible reason for the lower shell elasticity may be due to the higher applied acoustical pressure (50 kPa), compared to pressures used in previous studies with the same setup (van der Meer *et al* 2007; Overvelde *et al* 2010). Another possible reason is the different bubble preparation techniques of BR14 and unloaded bubbles used in this study. By comparing unloaded bubbles with loaded bubbles, we observed a slight change in the shell properties of loaded microbubbles. The averaged shell elasticity of loaded microbubbles (0.17 ± 0.09 N/m) was comparable to that of unloaded bubbles but the values of shell viscosities (2.5×10^{-8} kg/s), especially for larger bubbles ($\geq 6\mu m$) were found to be almost twice the reported value for unloaded bubbles. We hypothesize that the increase in the shell viscosity of large loaded microbubbles can be due to the change of the surface morphology of the bubble coating after the attachment of liposomes by thiol-maleimide cross-links. The hypothetical dynamics of loaded microbubbles during different oscillating phases are shown in figure 14.

Previous studies on the rheology of particle based coatings indicate that small and anisotropic-shaped particles tend to raise suspension bulk viscosity, due to the particle-to-particle interactions favored by the acicular particle shape and higher Brownian motions which randomize the particle configurations (Hoffman 1992; Chang *et al* 1994; Weitz 2004). Fluorescent images of the loaded microbubbles revealed the inhomogeneous distribution of liposomes on the loaded microbubbles (Fig. 13) and a high mobility of the microbubble lipid shell (Kooiman *et al* 2010). The interactions between liposomes during bubble oscillations can cause energy loss and results in a higher "internal friction" which altogether may lead to a higher shell viscosity.

Also a shear-thinning behavior was found for both unloaded and loaded microbubbles (Fig. 6b), as was reported for unloaded bubbles before (van der Meer *et al* 2007; Tu *et al* 2011). However, a large variation for the viscosity was found for the loaded bubbles, especially at low dilatation rate. The cause can be the liposome distribution around the lipid monolayer, which varies greatly for each individual microbubble. Similar variations in the lipids concentration for unloaded bubbles were reported by Stride *et al* (2008) and by Borden *et al* (2009).

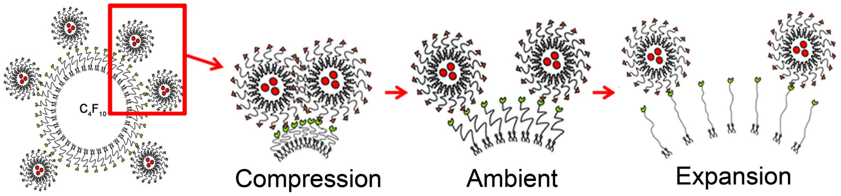

Fig 14. Cartoon of loaded microbubbles dynamics during compression and expansion.

Thresholding behavior

Thresholding behavior was found for both unloaded bubbles and loaded bubbles, where loaded bubbles show higher pressure thresholds (figure 8-10). Overvelde *et al* (2010) showed that this behavior is closely related to the nonlinear bubble dynamics. A bubble in the elastic regime shows a rapid decrease of the frequency of maximal response with increasing amplitude of oscillations, where the shell buckling and rupture are likely to occur, leading to a pronounced skewing of the resonance curves. On the other hand, bubble oscillation amplitude is greatly influenced by the shell viscosity. The experimental data showed decreased bubble oscillation amplitudes for loaded bubbles compared to unloaded bubbles (figure 4). It was also observed that loaded bubbles have higher shell viscosity than unloaded bubbles (figure 6). We hypothesize that the higher shell viscosity which leads to the higher “internal friction” during loaded bubbles oscillations is the cause of higher pressures needed for stimulating bubble oscillations. However, due to the complications of nonlinear bubble dynamics for loaded bubbles, further investigations on the exact cause for higher pressure thresholds are necessary and a new theoretical model is required to describe the loaded bubble dynamics.

Expansion-only behavior

“Expansion-only” behavior was found for loaded bubbles as a different type of nonlinear bubble oscillations. Previously reported expansion-only behavior for phospholipid-shelled microbubbles occurred at high acoustic pressures around 220 kPa (Emmer *et al* 2007). However, expansion-only behavior observed in this study for loaded bubbles occurred at low acoustic pressures (≤ 30 kPa) and showed strongly inhibited or even completely suppressed bubble compression. To explain the expansion-only behavior, the same mechanism can be applied as was proposed by Stride *et al* (2008) for microbubbles with coated gold nanoparticles. Stride *et al* (2008) developed microbubbles with an outer layer of a few hundred nanometers covered with gold particles. These microbubbles showed significantly increased expansion with inhibited bubble compression at low acoustic pressures. Stride and colleagues propose that the reason behind this phenomenon is the compacting of nanoparticles during compression. In case of loaded bubbles, the experimentally estimated number of liposomes loaded on a single loaded microbubble equals 600-1300 (Geers *et al* 2011). To calculate the maximum number of liposomes attached on the microbubble shell, we propose a simplified geometric model of loaded microbubbles by assuming liposomes are densely packed in a hexagonal pattern. Based on Thue’s Theorem on circle packing, the density of the circle configuration is $\frac{\pi}{\sqrt{12}}$ =0.91 (Hai-Chau *et al* 2010). Therefore, the maximum number of liposomes with radius r, which are densely packed on the surface of a microbubble of radius R, is given by:

$$n = \frac{4\pi(R+r)^2}{\pi r^2} \times \frac{\pi}{\sqrt{12}} \qquad (3)$$

Based on equation 3, a microbubble of 4 μm in diameter can be loaded with up to 1600 liposomes at maximum. Experimentally, a liposome loading of 1200 was measured (Geers *et al* 2011). Therefore it is very likely that the reason for dominant expansion-only oscillations in loaded microbubbles at low acoustic pressures is the compacting of the liposomes covering the surface of the microbubbles and inhibiting the compression of the bubbles.

In this study physical parameters for optimal bubble oscillation such as frequency and acoustic pressure were obtained for loaded microbubbles with different sizes. This information is essential for the preparation and application of loaded microbubbles in ultrasound triggered drug delivery systems. Larger loaded microbubbles are preferable for drug delivery due to their higher drug loading capacity and safer drug transportation. However, one drawback would be that, as it was shown in this study, compared to smaller microbubbles, larger loaded microbubbles have a higher damping, which may lead to lower efficiency of ultrasound application. In addition, higher nonlinearity at low acoustic pressures can be achieved by increasing the amount of liposome loading on the surface of microbubbles. In this way loaded or drug loaded microbubbles can be applied in clinical procedures such as contrast imaging and drug delivery at lower Mechanical Index (MI) with higher efficiency and minimized risk of cell damage or microbubble destruction.

The next step would be to study the acoustic response of loaded microbubbles as a function of the number of liposomes loaded on a single bubble and to develop a mathematical model describing loaded microbubble dynamics. In addition, complementary experiments to measure the acoustic attenuation and scattering response of a loaded bubble population are underway.

CONCLUSION

The shell elasticity of loaded bubbles is nearly the same as unloaded bubbles. A clear difference was found in the shell viscosity of loaded bubbles. Pressure dependent bubble resonance indicated a thresholding behavior for the initiation of bubble oscillations, and the loaded bubble showed a higher threshold pressure. Moreover, loaded bubbles showed an “expansion-only behavior” at low acoustic pressures (<30 kPa).

Acknowledgement-- This work was funded by the EU FP7 collaborative projects SONODRUGS (NMP-4-LA-2008-213706). The authors would like to thank Frits Mastik, Robert Beurskens and Michiel Manten for technical support, and also Guillaume Renaud, Marlies Overvelde and Klazina Kooiman for valuable discussions.

References

Borden M Nanostructural features on stable microbubbles. Soft Matter 2009; 5:716-720.

Chang C and Powell R L Effect of particle size distributions on the rheology of concentrated bimodal suspensions. Journal of Rheology 1994;38:85-98

Church C C The effect of an elastic solid-surface layer on the radial pulsations of gas-bubbles. Journal of the Acoustical Society of America 1995;97:1510-1521

Dayton P A, Morgan K E, Klibanov A L, Brandenburger G H and Ferrara K W Optical and acoustical observations of the effects of ultrasound on contrast agents. IEEE Trans Ultrason Ferroelectr Freq Control 1999;46:220-232

Devin J C Survey of Thermal, Radiation, and Viscous Damping of Pulsating Air Bubbles in Water. The Journal of the Acoustical Society of America.1959. 31: 1654-1667

de Jong N, Emmer M, Chin C T, Bouakaz A, Mastik F, Lohse D and Versluis M "Compression-only" Behavior of phospholipid-coated contrast bubbles. Ultrasound Med Biol 2007;33:653-656

Doinikov A A and Bouakaz A Theoretical model for the threshold onset of contrast microbubble oscillations. J Acoust Soc Am 2010;127:649-651

Emmer M, Vos H J, Goertz D E, van Wamel A, Versluis M and de Jong N Pressure-dependent attenuation and scattering of phospholipid-coated microbubbles at low acoustic pressures. Ultrasound in Medicine and Biology 2009;35:102-111

Ferrara K, Pollard R and Borden M Ultrasound microbubble contrast agents: Fundamentals and application to gene and drug delivery. Annual Review of Biomedical Engineering 2007;9:415-447

Frinking P J A, Bouakaz A, de Jong N, Ten Cate F J and Keating S Effect of ultrasound on the release of micro-encapsulated drugs. Ultrasonics 1998;36:709-712

Geers B, Lentacker I, Sanders N N, Demeester J, Meairs S and De Smedt S C Self-assembled liposome-loaded microbubbles: The missing link for safe and efficient ultrasound triggered drug-delivery. J Control Release 2011;152:249-256

Gorce, J M, M Arditi and M Schneider Influence of bubble size distribution on the echogenicity of ultrasound contrast agents: a study of SonoVue. Invest Radiol.2000. 35: 661-671.

Chang H C and Wang L C A Simple Proof of Thue's Theorem on Circle Packing. CORD Conference Proceedings 2010; arXiv:1009.4322v1

Hernot S and Klibanov A L Microbubbles in ultrasound-triggered drug and gene delivery. Advanced Drug Delivery Reviews 2008;60:1153-1166

Hoffman R L Factors affecting the viscosity of unimodal and multimodal colloidal dispersions. Journal of Rheology 1992;36:947-965

Kheirolomoom A, Dayton P A, Lum A F, Little E, Paoli E E, Zheng H and Ferrara K W Acoustically-active microbubbles conjugated to liposomes: Characterization of a proposed drug delivery vehicle. J Control Release 2007;118:275-284

Kooiman K, Emmer M, Foppen-Harteveld M, van Wamel A and de Jong N Increasing the endothelial layer permeability through ultrasound-activated microbubbles. Ieee Transactions on Biomedical Engineering 2010;57:29-32

Lentacker I, De Smedt S C and Sanders N N Drug loaded microbubble design for ultrasound triggered delivery. Soft Matter 2009;5:2161-2170

Marmottant P, van der Meer S, Emmer M, Versluis M, de Jong N, Hilgenfeldt S and Lohse D A model for large amplitude oscillations of coated bubbles accounting for buckling and rupture. Journal of the Acoustical Society of America 2005;118:3499-3505

Medwin H Counting bubbles acoustically: a review. Ultrasonics.1977. 15: 7-13.

Morgan K E, Allen J S, Dayton P A, Chomas J E, Klibaov A L and Ferrara K W Experimental and theoretical evaluation of microbubble behavior: Effect of transmitted phase and bubble size. IEEE Trans Ultrason Ferroelectr Freq Control 2000;47:1494-1509

Newman C M H and Bettinger T Gene therapy progress and prospects: Ultrasound for gene transfer. Gene Therapy 2007;14:465-475

Overvelde M, Garbin V, Sijl J, Dollet B, de Jong N, Lohse D and Versluis M Nonlinear shell behavior of phospholipid-coated microbubbles. Ultrasound Med Biol 2010;36:2080-2092

Sboros V, Glynos E, Pye S D, Moran C M, Butler M, Ross J, Short R, McDicken W N and Koutsos V Nanointerrogation of ultrasonic contrast agent microbubbles using atomic force microscopy. Ultrasound Med Biol 2006;32:579-585

Sharma A and Sharma U S Liposomes in drug delivery: Progress and limitations. International Journal of Pharmaceutics 1997;154:123-140

Stride E and Edirisinghe M Novel microbubble preparation technologies. Soft Matter 2008;4:2350-2359.

Tinkov S, Winter G, Coester C and Bekeredjian R New doxorubicin-loaded phospholipid microbubbles for targeted tumor therapy: Part i - formulation development and in-vitro characterization. J Control Release 2010;143:143-150

Tu J, Swalwell J E, Giraud D, Cui W, Chen W and Matula T J Microbubble sizing and shell characterization using flow cytometry. IEEE Trans Ultrason Ferroelectr Freq Control 2011;58:955-963

Unger E C, McCreery T P, Sweitzer R H, Caldwell V E and Wu Y Acoustically active lipospheres containing paclitaxel: A new therapeutic ultrasound contrast agent. Invest Radiol 1998;33:886-892

van Wamel A, Kooiman K, Harteveld M, Emmer M, ten Cate F J, Versluis M and de Jong N Vibrating microbubbles poking individual cells: Drug transfer into cells via sonoporation. Journal of Controlled Release 2006;112:149-155

Weitz D A Packing in the spheres. Science 2004;303:968-969

Chapter VI

In vivo microbubble spectroscopy

Telli Faez, Ilya Skachkov, Michel Versluis, Nico de Jong

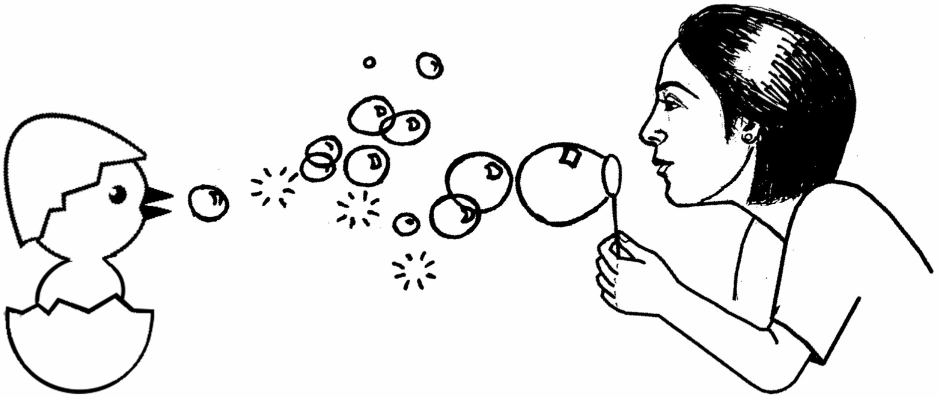

Published in Ultrasound in Medicine and Biology July 3, 2012

Abstract

The dynamics of coated microbubbles was studied in an *in-vivo* model. Biotinylated lipid-coated microbubbles were prepared in-house and were injected into a chick embryo chorioallantoic membrane (CAM) model on the fifth day of incubation. The microbubbles, ranging between 1.0 and 3.5 μm in diameter, were insonified in the frequency range of 4-7 MHz. Two amplitudes of acoustic pressure were applied: 300 kPa and 400 kPa. The fundamental and subharmonic responses were recorded optically with an ultra-fast camera (Brandaris 128) at 20 million frames per second. A subharmonic response was observed for 44% of the studied bubbles. From the data the frequency of the maximum fundamental and subharmonic response was derived for each individual bubble and resulted in the resonance curves of the microbubbles. All the bubbles showed shell (strain) hardening behavior for a higher acoustic pressure. We conclude that the subharmonic oscillations observed in this study belonged to the transmit at resonance (TR) regime.

INTRODUCTION

It was mentioned that UCAs are used extensively in medical ultrasound imaging (chapters I and II). The fundamental understanding of the interaction of these bubbles with the ultrasound, and its resulting nonlinear vibration dynamics, is an ongoing field of research, since the quantitative knowledge of the bubbles' characterization is essential for a better engineered and optimal agent for its use in the clinic.

In-depth studies have been performed to quantify the acoustic response of the microbubbles acoustically, both in a bubble population (chapter III) and for single bubbles (Sijl *et al* 2008, Sijl *et al* 2011), as well as optically for single bubbles (Morgan *et al* 2000, chapters IV and V). Optical methods for acoustical characterization of contrast agent microbubbles have been a huge step forward in understanding the behavior of these bubbles in an ultrasound field. The physical properties of single bubbles reported for various contrast agents have shown that the acoustical response of a bubble is strongly size dependent (chapter IV). However, until now the physical influence of biological parameters, e.g. blood flow, blood cells, vicinity or attachment to the vessel wall, floatation in the blood pool, etc, on the dynamics of contrast agent microbubbles has been neglected or simplified. A genuine understanding of the acoustical behavior and resulting physical properties of the microbubbles can be achieved by investigating their acoustical response *in vivo*. For this purpose we propose the chick embryo chorioallantoic membrane (CAM) model.

Chicken embryo is a well known animal model, which has been extensively used in various areas of research such as angiogenesis and anti-angiogenesis (Ribatti *et al* 2000, 2001, Richardson and Singh 2003), wound healing (Ribatti *et al* 1996), tissue engineering (Borges *et al* 2003), biomaterials and implants (Zwadlo-Klarwasser *et al* 2001, Valdes *et al* 2002, Klueh *et al* 2003), biosensors (Valdes *et al* 2003) and drug delivery systems (Tartis *et al* 2006, Vargas *et al* 2007). The increasing interest in the chick embryo model and specifically its CAM is due to its simplicity, ease of visualization and low cost compared with mammalian models. The CAM of a developing chicken embryo is an extra-embryonic membrane and has a very dense capillary network, which makes it suitable for the intravenous injection of contrast agent microbubbles (Lange *et al* 2001) and is easily accessible with standard optical microscopy. Moreover, the vascular network of a CAM is located in the chick mesoderm, a transparent matrix, which does not significantly absorb or scatter the incident visible light. This allows for high-contrast and high-resolution imaging.

It is reported that the vitelline network of a chicken embryo (extraembryonic vessels, connecting the embryo to the yolk sac vasculature) is a good model for the human blood vessel network (Poelma *et al* 2008). The CAM model is very often used in studying cardiac development and human birth defects because of similar structure and functionality between human and chicken embryonic hearts at early developmental stages (Antin 2004, Liu *et al* 2011). The chick during its morphogenesis undergoes true growth similar to the situation in the human embryo, whereas their developing organs increase dramatically in size. Therefore, the CAM model is considered to be one of the best model embryos for numerous *in vivo* manipulations such as, overexpressing secreted proteins and viral gene constructions (Antin 2004, Vargas *et al* 2007).

Another important aspect of using CAM models concerns studies on brain cancer tumors. Indeed, Hagedorn *et al* (2005) have proven that tumor growth with key features of human gliblastoma can occur in a highly reproducible manner on a CAM model. This opens a new option for preclinical *in vivo* testing of anticancer drugs which to date is mainly performed in adult rodents, raising major ethical concerns. There are however, several significant anatomic differences between chick embryo cardiovascular anatomy and the human fetal cardiovascular anatomy, such as the orientation of the heart within the chest cavity which are explained in details by Schellpfeffer and Kolesari (2012).

In vivo characterization of the microbubble dynamics is important for contrast-enhanced ultrasound imaging methods. The outcome of this type of studies defines the essential parameters for a suitable diagnostic imaging method such as the insonifying frequency and the acoustic pressure, in which microbubbles are more responsive to. So far, the results of *in vitro* experiments have been used as the reference. However, *in vitro* set ups lack the complexity of a clinical environment and the physical effect of the major biological parameters such as blood plasma, red blood cells and proteins are simply neglected. Moreover, an i*n vivo* study of the microbubble behavior has the advantage of testing the bioeffects which contrast-enhanced diagnostic ultrasound can induce e.g. capillary damage, cell sonoporation and hemolysis (Skyba *et al* 1998, Miller *et al* 2001, Li *et al* 2004, Samuel *et al* 2009).

To date, observations of bubble dynamics in actual vessels have been focused on the transient interaction of ultrasound-activated microbubbles and the blood vessel, by means of cavitation and microjetting phenomena (Caskey *et al* 2007, Samuel *et al* 2009, Chen *et al* 2011a, 2011b). However, all these studies have been performed *ex vivo* and the blood in the vessels was replaced with another fluid e.g. saline mixed with ink, which does not represent a real clinical environment.

In the present study, the dynamics of ultrasound-activated microbubbles are studied in real time. Home-made microbubbles are injected into a chick embryo CAM whilst, for the first time, investigating their *in vivo* fundamental and subharmonic responses at two different acoustic pressures. The dynamic response of a single bubble to pressure pulses driven at frequencies of 4-7 MHz is recorded optically using an ultra high-speed camera system. Microbubble spectroscopy techniques (chapter IV and V) were applied at acoustic pressures of 300 and 400 kPa to characterize the physical properties of the bubbles. The results are compared with *in vitro* experiments reported in the literature using the very same experimental technique.

MATERIAL AND METHOD

Microbubble preparation

Biotinylated lipid coated microbubbles with a C_4F_{10} gas core were made by sonication as described by Klibanov *et al* (2004). Biotinylation has no influence on the dynamics of microbubbles (Overvelde *et al* 2011), and it is generally applied as a preparation step to functionalize the bubbles for targeting which was not in the scope of this study.

The coating was composed of DSPC (59.4 mol%; P 6517; Sigma-Aldrich, Zwijndrecht, the Netherlands); PEG-40 stearate (35.7 mol%; P 3440; Sigma-Aldrich); DSPE-PEG (2000) (4.1 mol%; 880125 P; Avanti Polar Lipids, Alabaster, AL, USA) and DSPE-PEG (2000)-biotin (0.8 mol%; 880129 C; Avanti Polar Lipids). 600 µg of DiI (Molecular Probes, Leiden the Netherlands) fluorescent lipid dye dissolved in 20 µl of absolute ethanol was added to the lipid solution before sonication.

Chicken embryo preparation

As an animal model the chicken embryo chorioallantoic membrane (CAM) was used and specifically prepared for ultra high-speed imaging under a microscope. Fertilized White Leghorn chicken eggs (*Gallus gallus domesticus*) were purchased from a supplier (Drost BV Loosdrecht, the Netherlands). After 5 days of incubation in a humidified incubator (Heraeus, Thermo Scientific, Erembodegem-Aalst, Belgium) at 37°C (stage HH27-27$^+$) according to Hamburger-Hamilton (1992) criteria, the embryo was taken out of the eggshell. Then 5 µl of the microbubble solution was injected in one of the vitelline veins using a home-made capillary glass needle and a commercial injection system (VisualSonics Inc., Toronto, Canada). Next, the yolk was removed to enhance the transparency of the embryo (Williams and Ordahl 1996). The upper part of an OptiCell chamber (NUNC, Wiesbaden, Germany) was cut out and the space was filled with 1% agarose (Sigma Aldrich, Zwijndrecht, the Netherlands). The yolkless embryo was placed on the agarose and incubated in the humidified incubator for 5 minutes to allow the contrast agent to redistribute in the blood. Then the embryo was transferred to the experimental setup and covered with acoustically transparent polystyrene cover slip made out of OptiCell membrane. Figure 1 shows a chicken embryo before the yolk was removed.

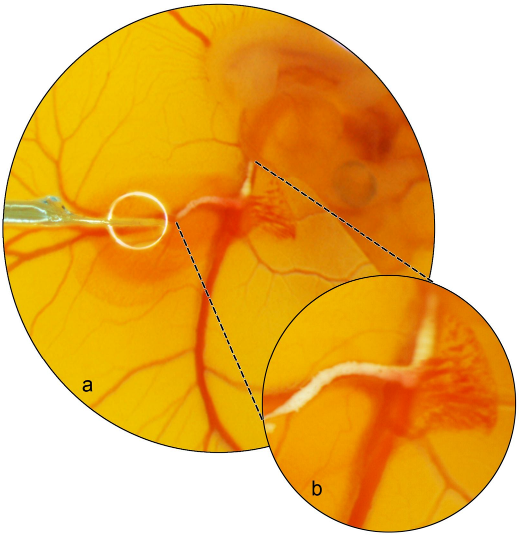

Fig 1. a) Injection of microbubbles into a vitelline vein of a chicken embryo with a capillary glass needle. b) the zoomed in area of part of the vein where the microbubbles were injected.

Experimental Setup

Figure 2 shows the schematic view of the setup. The yolkless embryo placed on an OptiCell was fixed on a triangular water tank at the focal area of the transducer. The temperature of the water was kept at 37°C using a heating element. A wide band transducer (V311; 3-13 MHz, Panametrics, Aarselaar, Belgium, or PA076; 1-9 MHz, Precision Acoustics, Dorchester, UK) was used for transmission. The transducer was connected to a power amplifier (150A100B; Amplifier Research, Limerick, Ireland), which amplified the pulse generated by an arbitrary waveform generator (8026; Tabor Electronics Ltd., Tel Hanan, Israel). Bursts of a 25-cycle sinusoidal wave, tapered with a Gaussian envelope at the first and last two cycles were transmitted. Microbubbles were insonified at 4–7 MHz with a frequency step of 200 kHz. Two acoustic pressures of 300 kPa and 400 kPa were applied at the focus for each experiment. These pressure values were calibrated using a 0.2 mm PVDF probe hydrophone (Precision Acoustics Ltd., Dorchester, UK). The region-of-interest was illuminated with three optical light guides (SCHOTT AG, Mainz, Germany) from below and two sides. The light guides were connected to a Xenon flash lamp (A-260, Vision Light Tech, Uden, The Netherlands). An Olympus microscope (Olympus, Zoeterwoude, the Netherlands) with a 40× water-immersed objective (NA = 0.7) was focused on the microbubbles in the chicken embryo. The total magnification of the system was further increased to 80× by using an additional 2× magnification lens inside the microscope.

Before insonification the microbubbles were tracked in the vitelline vessels using a mercury lamp light source and fluorescent light (510-550 nm) excitation and a 590 nm long-pass emission filter cube (U-MWG2, Olympus Zoeterwoude, The Netherlands). With the fluorescent light we were able to differentiate the real microbubbles from other flowing particles in the blood. Figure 3 shows the bright field and the fluorescent snapshot of a microbubble (2.3 µm diameter) floating inside the vessel. The images were taken with a high sensitivity CCD camera (LCL-902K, Watec, Orangeburg, NY, USA) connected to the microscope. The red blood cells and vessel walls are also evident in the bright field image (Fig. 3a).

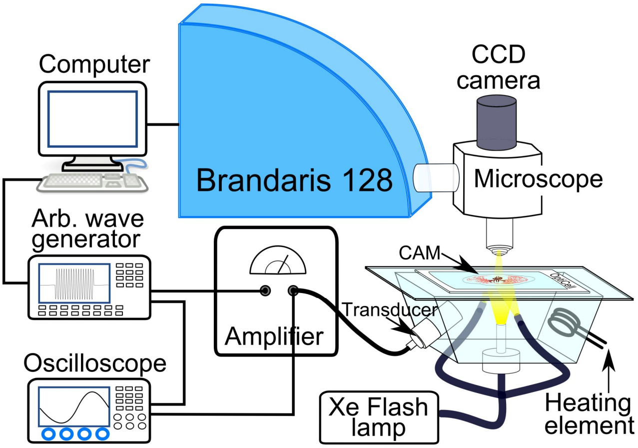

Fig 2. Schematic view of the setup.

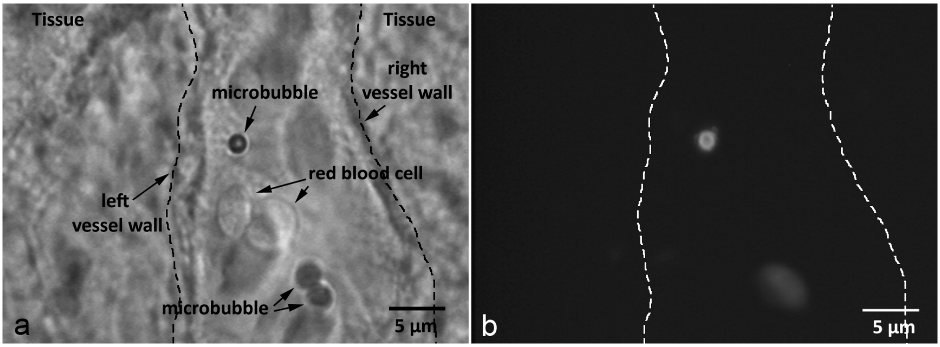

Fig 3. a) Bright field and b) fluorescent snapshots of 3 microbubbles, floating in a chicken embryo vein. The microbubble in focus is 2.3 µm in diameter. The other two microbubbles are out of focus.

Different from an *in vitro* setting, the pulsation of the blood flow and the circulation of red blood cells add more complexity to the tracking of the bubbles. Keeping a bubble fixed and in focus for a single microbubble spectroscopy is very challenging. To overcome these difficulties we had to look for bubbles mostly floating inside smaller capillaries with slower blood flow, relatively far from the heart or in the vicinity of a vessel wall, to avoid the vibrations and have a more stable focus. Very often the focus had to be adjusted simultaneously during the recordings. Many experiments failed because a microbubble was hit by red blood cells in the blood flow and was removed from its initial position before the recording was complete. Therefore several trial runs had to be done before capturing an acceptable recording.

The radial responses of the insonified bubbles were recorded with an ultra-fast recording camera, the Brandaris 128 (Chin *et al* 2003), at a frame rate of 20 million frames per second. The camera was set to record 33 movies of 128 frames in a single run. The first recording was always done without ultrasound to estimate the resting radius of the bubbles and the noise level of the system. In the subsequent movies, the frequency was swept in 16 200-kHz steps in ascending order from 4 to 7 MHz at an acoustic pressure of 300 kPa, followed by 16 200-kHz frequency steps at 400 kPa. As an example, we display 12 time frames from the recording of a 2.3 µm bubble depicting the vibration at a driving frequency of 4.0 MHz and acoustic pressure of 300 kPa (Fig. 4). The bubble is located next to the right vessel wall and the red blood cells in the blood flow in the vicinity of the microbubble are also evident in the recorded frames.

From each individual movie, the diameter of the microbubble as a function of time (DT-curve) was measured using custom-designed image analysis software (chapter IV). The Discrete Fourier transform of the DT-curves was then calculated, which gives the maximum amplitude of radial excursion of the bubble at that given frequency and pressure. Plotting the maximum amplitude as a function of the frequency gives the resonance curve of the bubble. Both the fundamental and the subharmonic (at half the driving frequency) resonance curves of a bubble were measured in a single experiment. The resonance frequency and the maximum subharmonic response were extracted using the same procedure explained in chapter IV and V.

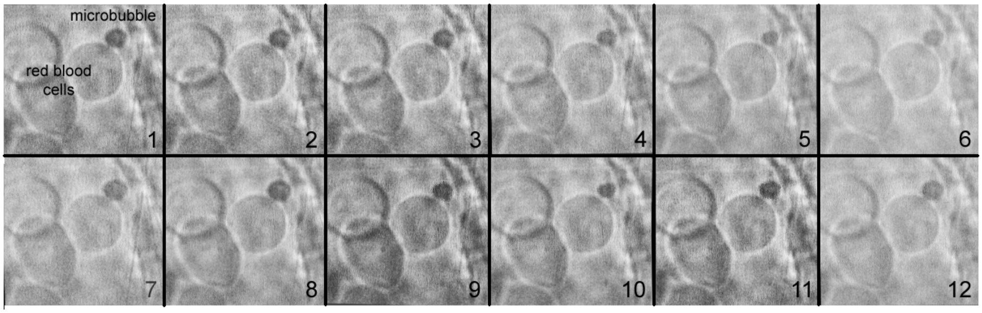

Fig 4. Twelve time frames out of 128 frames with 50 ns inter-frame time of a 2.3 µm bubble, indicating its radial oscillations, and red blood cells in a vessel. The driving frequency and acoustic pressure are 4 MHz and 300 kPa respectively.

RESULTS

A total of 80 individual bubbles were recorded and their response was analyzed. As a typical example we display five DT-curves (out of the set of 16) of a 2.8 µm diameter bubble in figure 5. The transmit frequency in these selected graphs increases from 4 MHz to 5.6 MHz with a frequency interval of 400 kHz. The amplitude of the acoustic pressure is 300 kPa. The maximum amplitude in the

Fourier transform of the first recording from each bubble, which was done without ultrasound, was set as the noise level (gray area in Fig. 5). The corresponding power spectra show a peak at the driving frequency and at the subharmonic frequency. In this example the fundamental amplitude decreases with increasing driving frequency, which indicates that all driving frequencies are above the resonance frequency of the bubble. At a driving frequency of 4.8 MHz the subharmonic amplitude reaches a maximum.

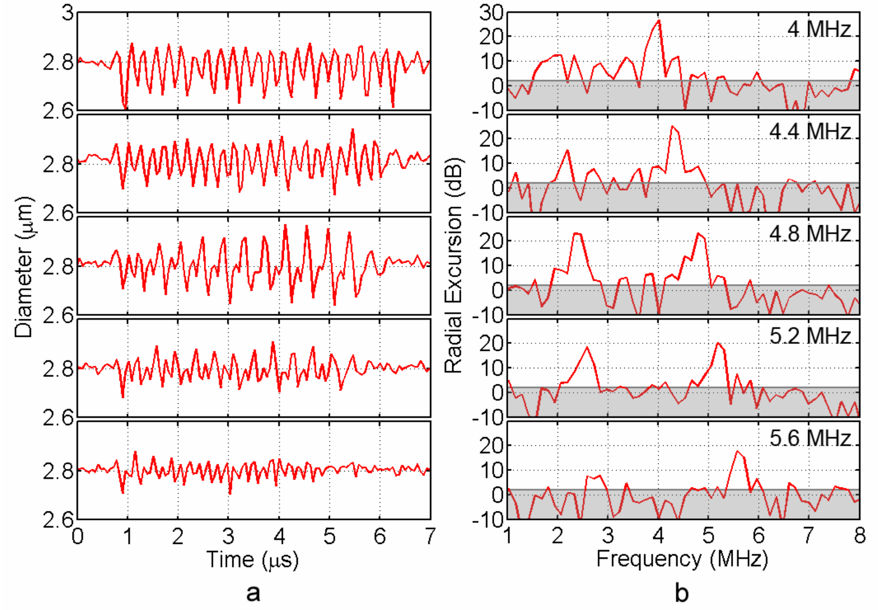

Fig 5. a) Selected DT-curves and b) corresponding power spectra of a microbubble with 2.8 μm diameter. The selected driving frequencies range between 4 to 5.6 MHz with a frequency step of 400 kHz. The applied acoustic pressure is 300 kPa. The sampling time is 50 ns. The gray area in the power spectra indicates the noise floor.

For all the recordings, the amplitude of excursion at the driving frequency and subharmonic frequency were extracted from the DT-curves and plotted versus frequency. As an example, the resonance curve and subharmonic response curve of a 2.3 μm bubble are presented in figure 6 for two amplitudes of acoustic pressures of 300 kPa and 400 kPa. Figure 6a shows that a 2.3 μm bubble in diameter has a resonance frequency around 4.5 MHz at a driving acoustic pressure of 300 kPa. The resonance frequency shifts slightly to 4.6 MHz by increasing the amplitude of the acoustic pressure to 400 kPa. The same bubble shows a subharmonic peak amplitude at a driving frequency of 6 MHz, which also tends to increase when driven at a frequency of 6.2 MHz when increasing the amplitude of the acoustic pressure from 300 kPa to 400 kPa (Fig. 6b).

In the studied bubble population (1.0 to 3.5 μm in diameter), 44% of the microbubbles showed subharmonic responses in the applied driving frequency range, similar to the in vitro results reported previously (chapter IV). The bubbles with a subharmonic response had a size between 1.7 µm and 3.5 µm in diameter. In this size range, for microbubbles with a diameter smaller than 1.9 µm only the fundamental resonance was detectable. For bubbles larger than 2.65 µm only the subharmonic response peaks could be extracted as their resonance frequencies were below 4 MHz, which was the lower limit of our transmitted frequencies. However, only for bubbles between 2 µm and 2.65 µm in diameter both a fundamental and a subharmonic peak in the applied driving frequency range could be clearly identified. The resonance frequency and the frequency of maximum subharmonic response of microbubbles versus their diameters are presented in figure 7.

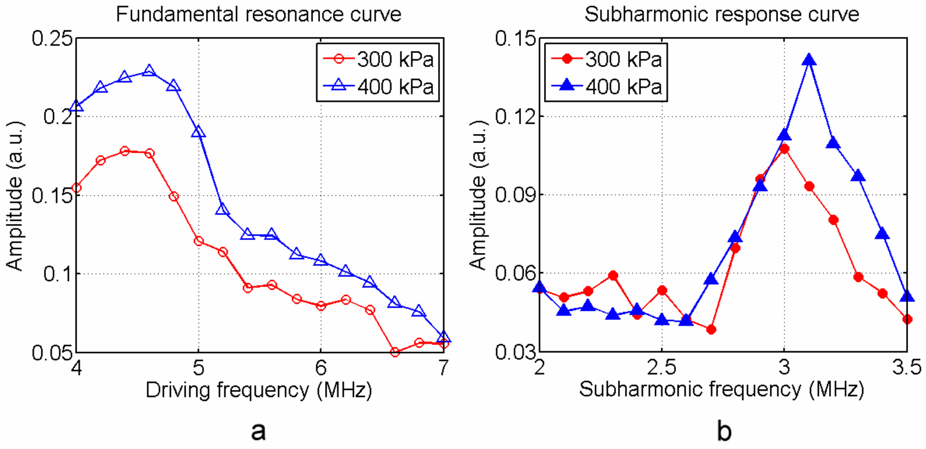

Fig 6. a) The fundamental amplitude as a function of the driving frequency and b) the subharmonic amplitude as a function of the subharmonic frequency (half the driving frequency) for a 2.3 µm bubble at acoustic pressures of 300 kPa and 400 kPa. Data on the abscissa have an uncertainty of ±0.1 MHz.

In order to estimate a relation between the resonance frequency and the maximum subharmonic response frequency of the microbubbles, the ratio of these two frequencies is depicted for the bubble diameters between 2 µm and 2.65 µm in figure 8. It can be seen that in the mentioned diameter range the maximum subharmonic response never occurs at a frequency which is twice the resonance frequency, but slightly lower. Overall the fundamental to subharmonic frequency ratios vary between 1.21±0.07 and 1.66±0.07 for acoustic pressure of 300 kPa. At 400 kPa, these ratios change from 1.24±0.07 to 1.83±0.07.

DISCUSSION

The fundamental and subharmonic behaviors of home made biotinylated lipid coated microbubbles were studied *in vivo* in the frequency range of 4-7 MHz. 44% of the total studied bubble population showed a subharmonic response in the applied driving frequency range. Similar to previous *in vitro* experiments (chapter IV) all the microbubbles showed asymmetrical oscillations known as compression-only behavior (Fig. 5a).

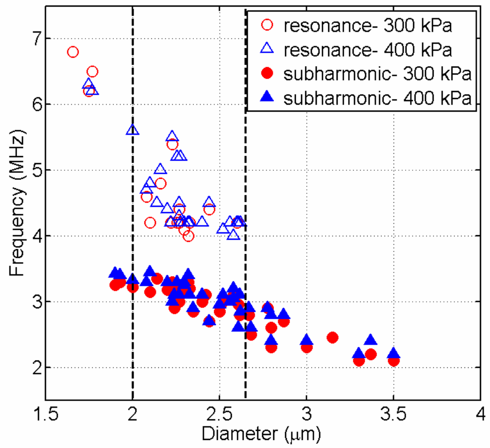

Fig 7. Resonance frequency and maximum subharmonic response frequency as functions of bubble size for acoustic pressure amplitudes of 300 kPa and 400 kPa. Vertical dashed lines indicate the diameter range which was used to calculate the data plotted in figure 8.

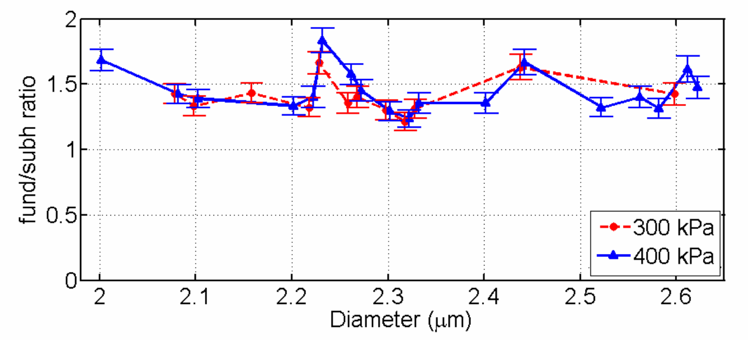

Fig 8. Fundamental to subharmonic response frequency ratio of microbubbles with the size range between 2 μm and 2.65 μm for acoustic pressure amplitudes of 300 kPa and 400 kPa.

The main difference between this *in vivo* study and the former *in vitro* experiments was the required higher amplitude of the acoustic pressure. At lower acoustic pressures (<100 kPa) no clear bubble oscillation could be detected for the bubbles inside the chicken embryo. We hypothesize that the main reason for this difference is due to the higher viscosity of the blood compared to water and the presence of the red blood cells (Al-Roubaie *et al* 2011). The supporting argument for this assumption is the quantitative estimation of the total damping from the measured resonance curves of the microbubbles, which gives an indication of the viscous contributions of the liquid surrounding the bubble (van der Meer *et al* 2007). Comparing the resonance curves of a 2.3 μm bubble *in vivo* (presented in Fig. 6a) and *in vitro* (Fig. 5, Van der Meer *et al* 2007), indicates that the width of the resonance curve *in vivo* is approximately twice that of the one *in vitro*. This results to a higher damping coefficient, which can be attributed to a higher viscosity of the liquid for bubble oscillations *in vivo*. Since the measured resonance curves in our study were not covered completely in the applied frequency range (Fig. 6a), a quantitative estimation of the values of the contributions arising from the blood viscosity was not possible. For this purpose further experiment in a wider frequency range is required.

Moreover, to study the effect of the acoustic pressure on the bubble oscillations, two amplitudes of acoustic pressure were applied (300 kPa and 400 kPa). The increase of the acoustic pressure by 100 kPa, or 33%, resulted in a slight increase of the resonance frequency and that of the subharmonic response, by 100 kHz on average, which is known as shell (strain) hardening (Fig. 6). This phenomenon was observed before for the subharmonic resonance frequency of BR14 microbubbles below 3 µm in diameter (chapter IV).

The estimated resonance frequencies of the bubbles as a function of bubble size in this experiment (Fig. 7), are in a very good agreement with the reported values for the BR14 microbubbles (chapter IV). The composition of the home made bubbles used in this study is very similar to the BR14 and SonoVue microbubbles. Therefore a similar range of resonance frequencies as compared to the mentioned commercial microbubbles was expected. However, the values of the resonance frequencies derived in this study are slightly higher than the reported values, which can be attributed to the higher acoustic pressures applied in our case and the shell hardening phenomenon observed for increasing acoustic pressures. The differences between an *in vivo* and an *in vitro* medium in which the microbubbles are exposed can also play an important role. And finally, even though the composition of these two groups of microbubbles is very similar, the shell properties of them can be significantly different due to variations in the shell composition of the individual microbubbles, see Sijl *et al* 2010. The combination of these factors can affect the physical properties of our microbubbles including resonance frequency and shell properties.

Disregarding the slight increase in the estimated resonance frequencies of biotinylated lipid coated and BR14 microbubbles, it is noted that the current values of the resonance frequencies presented in figure 7 are in the same range as the subharmonic resonance frequencies reported in chapter IV. In that study the driving frequency was set to approximately twice the resonance frequency of BR14 microbubbles. It is known that subharmonic oscillations are categorized in two regimes (Chomas *et al* 2002); transmit at resonance (TR) subharmonic and transmit at twice resonance (T2R) subharmonic. The TR subharmonic oscillations are predicted to occur when a bubble is insonified at its resonance frequency. T2R subharmonic emission is predicted to occur when the transmit frequency is at twice the resonance frequency of a bubble. Therefore, the subharmonic oscillations observed in that experiment belonged to T2R subharmonic category. Consequently, the subharmonic response frequencies indicated in our study (Fig. 7) belong to the TR subharmonic regime.

The occurrence of TR and T2R subharmonic responses has been reported by Chomas *et al* (2002) and theoretically predicted by Katiyar and Sarkar (2011). In the following chapter (chapter VII), we show that simulations based on Marmottant *et al* (2005) model are able to predict both categories of subharmonic oscillations: T2R at MI ≈< 0.05 and TR at MI ≈> 0.05. We will also present experimental evidence on the occurrence of TR subharmonics for BR14 bubble population. However, for single bubbles *in vivo* this phenomenon is reported for the first time in this study.

Calculating the ratio between fundamental resonance and subharmonic response of microbubbles in the size range of 2-2.65 µm indicates that TR subharmonic response never occurs exactly at half the resonance frequency of a microbubble. Instead, this ratio varies from 1.2 to 1.8 for different bubbles. This observation is also in accordance with the theory (Katiyar and Sarkar 2011). The comparison between the present *in vivo* study and the similar *in vitro* experiment (chapter IV) is summarized in Table 1.

Table 1. The comparison between the *in vitro* and *in vivo* microbubble spectroscopy.

Microbubble spectroscopy			***In vitro***	***In vivo***
Input parameters	Microbubble coating		Phospholipid (BR14)	Phospholipid (Home-made)
	Driving Frequency (MHz)		8-11	4-7
	Acoustic Pressure (kPa)		50-120	300-400
Output	Radial oscillation		Compression-only	Compression-only
	Subharmonic response (%)		40	44
	Subharmonic regime		T2R	TR
	Resonance frequency (MHz) (bubble diameter: 2-2.5 µm)	Fundamental	-----	5.6-4.1
		Subharmonic	5-4.5	3.2-2.8
	Shell elasticity		Strain hardening	Strain hardening
	Shell viscosity (kg/s)		~ 10^{-9}	~ 10^{-9}
	Total damping (bubble diameter: 2.3 µm)		~ 0.25	~ 0.5

Microbubble spectroscopy *in vivo* provides more accurate information concerning the bubble behavior and physical properties of contrast agent microbubbles. Shell properties such as elasticity and viscosity can also be extracted from this kind of experiments, similar to what has been done previously in several *in vitro* experiments (chapter V). Very often, the influence of biological aspects on the dynamics of microbubbles such as the blood flow, pulsation of the arteries, circulation of red blood cells and the vicinity of vessel walls, etc. are neglected or simplified in similar *in vitro* models. As compared to *in vitro* set ups, the chicken embryo model is one step closer to the clinical case, which therefore makes the outcome of this kind of preclinical studies much more reliable and realistic.

More interestingly, several cases of surface modes (Dollet *et al* 2008) were recorded for the microbubbles confined in a vessel. As an example five snapshots of a microbubble exhibiting surface modes of orders of 4, 5 and 6 are presented in figure 9. Comparison between our *in vitro* and *in vivo* experiments has shown that surface modes occur more frequently in the latter case. This may be due to the additional perturbation present in the *in vivo* situation, possibly caused by the unsteady blood flow, the presence of the red blood cells or the rheological properties of blood such as visco-elasticity. However this phenomenon certainly deserves further investigations.

Also biological and physical phenomena involving the interaction of cells and microbubbles such as sonoporation (van wamel *et al* 2008, Chen *et al* 2011a) can easily be investigated in similar set ups. The following step is to characterize targeted bubbles for drug delivery purposes and experiments in this direction are currently underway.

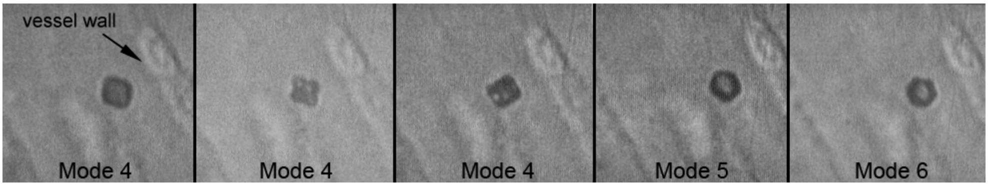

Fig 9. Surface modes of a 3 µm bubble in orders of 4, 5 and 6.

CONCLUSION

The fundamental and subharmonic response of home made microbubbles were measured in a chicken embryo CAM by means of microbubble spectroscopy at 4-7 MHz. 44% of the microbubbles exhibited subharmonic response which belonged to the TR subharmonic regime. All the microbubbles showed shell hardening by increasing the amplitude of acoustic pressure. Chick embryo CAM proved to be an excellent model to study microbubble dynamics *in vivo*.

Acknowledgement-- The authors appreciate the efforts of Marcia Emmer and Miranda Foppen-Harteveld in the development of the CAM model.

References

Al-Roubaie S, Jahnsen ED, Mohammed M, Henderson-Toth C, Jones EA. Rheology of embryonic avian blood. Am J Physiol Heart Circ Physiol 2011;301:H2473–H2481.

Antin PB. The Chick Embryo Rules (Still)! Developmental Dynamics 2004; 229:413.

Borges J, Tegtmeier FT, Padron NT, Mueller MC, Lang EM, Stark GB. Chorioallantoic membrane angiogenesis model for tissue engineering: a new twist on a classic model. Tissue Eng 2003;9:441–450.

Caskey CF, Stieger SM, Qin SH, Dayton PA, Ferrara KW. Direct observations of ultrasound microbubble contrast agent interaction with the microvessel wall. J. Acoust. Soc. Am. 2007;122:1191-1200.

Chen H, Kreider W, Brayman AA, Bailey MR, Matula TJ. Blood Vessel Deformations on Microsecond Time Scales by Ultrasonic Cavitation. PRL 2011a;106:034301.

Chen H, Brayman AA, Kreider W, Bailey MR, Matula TJ. Observations of translation and jetting of ultrasound-activated microbubbles in mesenteric microvessels. Ultrasound in Med. & Biol., 2011b;37:2139–2148.

Chin CT, Lancee C, Borsboom J, Mastik F, Frijlink M, de Jong N, Versluis M, Lohse D. Brandaris 128: a 25 million frames per second digital camera with 128 highly sensitive frames. Rev. Sci. Instru. 2003;74:5026-5034.

Chomas J, Dayton P, May D, Ferrara K. Nondestructive subharmonic imaging. IEEE Trans Ultrason Ferroelectr Freq Control 2002;49:883-892.

Dollet B, van der Meer SM, Garbin V, de Jong N, Lohse D, Versluis M. Nonspherical oscillations of ultrasound contrast agent microbubbles. Ultrasound Med Biol 2008;34:1465-1473.

Eisenbrey JR, Dave JK, Halldorsdottir VG, Merton DA, Machado P, Liu JB, Miller C, Gonzalez JM, Park S, Dianis S, Chalek CL, Thomenius KE, Brown DB, Navarro V, Forsberg F Simultaneous grayscale and subharmonic ultrasound imaging on a modified commercial scanner Ultrasonics 2011;51:890-897.

Hagedorn M, Javerzat S, Gilges D, Meyre A, de Lafarge B, Eichmann A, Bikfalvi A. Accessing key steps of human tumor progression in vivo by using an avian embryo model PNAS 2005;102:1643-1648.

Hamburger V, Hamilton HL. A series of normal stages in the development of the chick embryo. Dev Dyn 1992;195:231-272.

Katiyar A, Sarkar K. Excitation threshold for subharmonic generation from contrast microbubbles. J Acoust Soc Am 2011;130:3137-3147.

Klibanov AL, Rasche PT, Hughes MS, Wojdyla JK, Galen KP, Wible JH, Brandenburger GH. Detection of individual microbubbles of ultrasound contrast agents: imaging of free-floating and targeted bubbles. Invest Radiol 2004;39:187–195.

Klueh U, Dorsky DI, Moussy F, Kreutzer DL. Ex ova chick chorioallantoicmembrane as a novelmodel for evaluation of tissue responses to biomaterials and implants. J Biomed Mater Res 2003;67:838–843.

Lange N, Ballini JP, Wagnieres G, van den Bergh H. A New Drug-Screening Procedure for Photosensitizing Agents Used in Photodynamic Therapy for CNV. Investig Ophthalmol Vis Sci 2001;42:38-46.

Li P, Armstrong WF, Miller DL. Impact of myocardial contrast echocardiography on vascular permeability: comparison of three different contrast agents. Ultrasound Med Biol 2004;30:83–91.

Liu A, Nickerson A, Troyer A, Yin X, Cary R, Thornburg K, Wang R, Rugonyi S. Quantifying blood flow and wall shear stresses in the outflow tract of chick embryonic hearts. Computers and Structures 2011; 89:855–867.

Marmottant P, Van der Meer S, Emmer M, Versluis M, De Jong N, Hilgenfeldt S, Lohse D. A model for large amplitude oscillations of coated bubbles accounting for buckling and rupture. J Acous Soc Am 2005;118:3499-3505.

Miller MW, Everbach EC, Cox C, Knapp RR, Brayman AA, Sherman TA. A comparison of the hemolytic potential of Optison and Albunex in whole human blood in vitro: Acoustic pressure, ultrasound frequency, donor and passive cavitation detection considerations. Ultrasound Med Biol 2001;27:709–721.

Morgan K, Allen J, Dayton P, Chomas J, Klibanov A, Ferrara K. Experimental and theoretical evaluation of microbubble behavior: effect of transmitted phase and bubble size. IEEE Trans Ultrason Ferroelect Freq Contr 2000;47:1494-1509.

Overvelde M, Garbin V, Dollet B, De Jong N, Lohse D, Versluis M. Dynamic of Coated Microbubbles Adherent to a wall. Ultrasound Med Biol 2011;37:1500-1508.

Poelma C, Vennemann P, Lindken R, Westerweel J. In vivo blood flow and wall shear stress measurements in the vitelline network. Exp Fluids 2008; 45:703–713.

Ribatti D, Vacca A, Ranieri G, Sorino S, Roncali L. The chick embryo chorioallantoic membrane as an in vivo wound healing model. Pathol Res Pract 1996;192:1068–1076.

Ribatti D, Vacca A, Roncali L, Dammacco F. The chick embryo chorioallantoic membrane as a model for in vivo research on antiangiogenesis. Curr Pharm Biotechnol 2000;1:73–82.

Ribatti D, Nico B, Vacca A, Roncali L, Burri PH, Djonov V. Chorioallantoic membrane capillary bed: a useful target for studying angiogenesis and anti-angiogenesis in vivo. Anat Rec 2001;264:317–324.

Richardson M, Singh G. Observations on the use of the avian chorioallantoic membrane (CAM) model in investigations into angiogenesis. Curr Drug Targets Cardiovasc Haematol Disord 2003;3:155–185.

Samuel S, Cooper MA, Bull JL, Fowlkes JB, Miller DL. An ex vivo study of the correlation between acoustic emission and microvascular damage. Ultrasound in Med. & Biol. 2009;35:1574–1586.

Schellpfeffer MA and Kolesari GL. Microbubble contrast imaging of the cardiovascular system of the chick embryo. Ultrasound in Med. & Biol. 2012:38:504–510.

Sijl, J., Gaud, E., Frinking, P.J.A., Arditi, M., Jong, N. de, Lohse, D., & Versluis, M. Acoustic characterization of single ultrasound contrast agent microbubbles. J. Acoust. Soc. Am. 2008;124:4091-4097.

Sijl J, Dollet B, Overvelde M, Garbin V, Rozendal T, De Jong N, Lohse D, Versluis M. Subharmonic behavior of phospholipid-coated ultrasound contrast agent microbubbles. J Acoust Soc Am 2010;128:3239-3252.

Sijl, J., Vos, H.J., Rozendal, T., Jong, N. de, Lohse, M. & Versluis, M. Combined optical and acoustical detection of single microbubble dynamics. J. Acoust. Soc. Am. 2011;130:3271.

Skyba DM, Price RJ, Linka AZ, Skalak TC, Kaul S. Direct in vivo visualization of intravascular destruction of microbubbles by ultrasound and its local effects on tissue. Circulation 1998;98:290–293.

Tartis MS, McCallan J, Lum AFH, LaBell R, Stieger SM, Matsunaga TO, Ferrara KW. Therapeutic effects of paclitaxel-containing ultrasound contrast agents. Ultrasound in Med. & Biol. 2006;32:1771–1780.

Valdes TI, Kreutzer D, Moussy F. The chick chorioallantoic membrane as a novel in vivo model for the testing of biomaterials. J Biomed Mater Res 2002;62:273–282.

Valdes TI, Klueh U, Kreutzer D, Moussy F. Ex ova chick chorioallantoic membrane as a novel in vivo model for testing biosensors. J Biomed Mater Res 2003;67A:215–223.

Van der Meer SM, Dollet B, Voormolen MM, Chin CT, Bouakaz A, De Jong N, Versluis M, Lohse D. Microbubble spectroscopy of ultrasound contrast agents. J Acoust Soc Am 2007;121:648-656.

Van wamel A, Kooiman K, De Jong N. Ultrasound contrast agents pushing drug delivery: high speed optical observations. J Acoust Soc Am 2008;123:3215.

Vargas A, Zeisser-Labouèbe M, Lange N, Gurny R, Delie F. The chick embryo and its chorioallantoic membrane (CAM) for the in vivo evaluation of drug delivery systems. Advanced Drug Delivery Reviews 2007;59:1162–1176.

Williams BA, Ordahl CP. Manipulation of the Avian Segmental Plate in Vivo. Methods in Cell Biology 1996;51:81-92.

Zwadlo-Klarwasser G, Gorlitz K, Hafemann B, Klee D, Klosterhalfen B. The chorioallantoic membrane of the chick embryo as a simple model for the study of the angiogenic and inflammatory response to biomaterials. J Mater Sci Mater Med 2001;12:195–199.

Chapter VII

Dynamic manipulation of the subharmonic scattering of phospholipid-coated microbubbles

Telli Faez, Guillaume Renaud, Marielle Defontaine, Samuel Calle, Nico de Jong

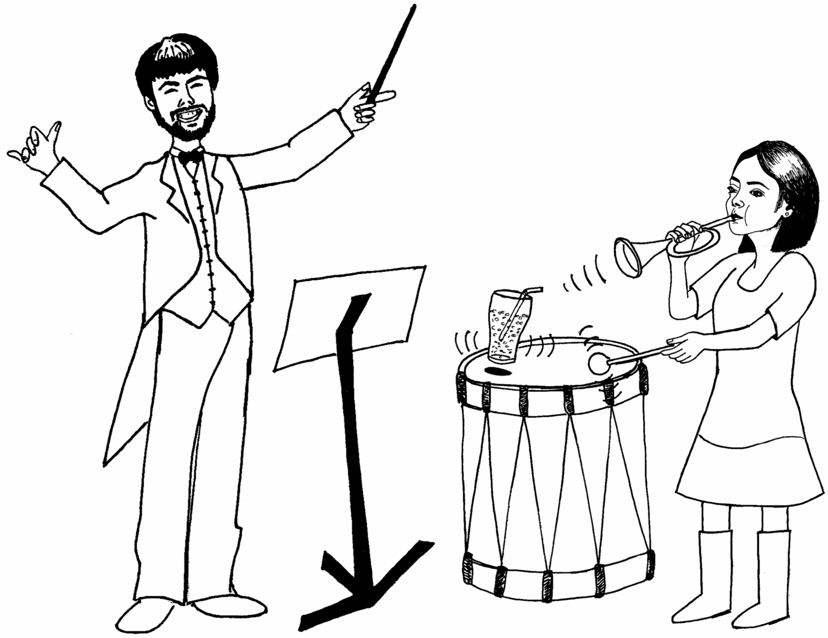

Published in Physics in Medicine and Biology September 20, 2011

Abstract

The influence of a dynamic variation in the ambient pressure on the subharmonic response of phospholipid-coated microbubbles was investigated. The ambient pressure in water was modulated by a 2.5 kHz acoustic wave with peak amplitude of 15 kPa. We investigated the fundamental and subharmonic emission at two driving frequencies: 5 and 10 MHz. The modulation of the bubble radius induced by the dynamic variation in the liquid ambient pressure subsequently causes modulations of the scattered acoustic pressure at the fundamental and subharmonic frequencies (half the fundamental frequency). As a first result we measured that the variation in the ambient pressure of 15 kPa can modulate the subharmonic amplitude up to 10 dB as compared to the static atmospheric pressure condition. As a second result we noticed that the relative subharmonic amplitude modulation as a function of the LF acoustic pressure was symmetrical for the 5 MHz driving frequency but asymmetric for 10 MHz. In the latter case the subharmonic amplitude was more enhanced for an ambient overpressure than reduced for an ambient depression of the same amplitude likely due to the buckling of the lipid shell. However the fundamental amplitude was symmetrically modulated during bubble compression and expansion. Moreover, subharmonic and fundamental amplitude modulations were found to be either in phase or out of phase with the low-frequency acoustic pressure. Numerical simulations showed that these behaviors can be obtained depending on the bubbles' diameter. The highest subharmonic amplitude was measured when microbubbles were insonified at 10 MHz. This fact together with the asymmetry observed in the subharmonic modulation suggests that smaller bubbles with buckling shell are excited at 10 MHz compared to 5 MHz. These results present new potentials for in vitro characterization of contrast agent microbubbles and possibly a new imaging modality.

INTRODUCTION

Optical characterization of contrast agent microbubbles presented in chapter IV, using a high-speed camera, within the interested frequency range for carotid imaging (8-12 MHz) showed the potential of applying this method for vascular imaging. It was shown that subharmonic oscillation of BR14 microbubbles can be generated by low acoustic pressures of order 50 kPa peak amplitude at frequencies around 10 MHz. The experimental results indicated that 40% of the microbubbles exhibit subharmonic vibrations. These microbubbles may have a very low initial surface tension such that an acoustic overpressure induces the buckling of the phospholipid shell. This was supported by numerical calculations based on Marmottant *et al* (2005) model. Zero surface tension in this model corresponds to bubbles with a buckled shell. These simulations showed that bubbles in the buckling regime generate the highest subharmonic emission. So subharmonic imaging requires engineering bubbles with buckled shell (zero initial surface tension). To overcome this, we developed a method to manipulate microbubbles such that they exhibit a higher subharmonic response. Frinking *et al* (2010) have shown experimentally and numerically (based on Marmottant *et al* (2005) model) that the subharmonic amplitude increases when an ambient overpressure is applied to the system for transmit acoustic pressures below 120 kPa. They demonstrate that this can be caused by a change in the value of initial surface tension at equilibrium. The closer the initial surface tension is to the buckling state (zero surface tension) the more subharmonic energy is generated. Their experiments show an increase in the subharmonic amplitude up to 20 dB in power by applying an ambient overpressure of around 10 kPa (75 mmHg).

In this study we propose an alternative way to dynamically manipulate the response of the microbubbles by using a very low frequency (LF) wave to change the ambient pressure. We measure and analyze the acoustic scattering of contrast agent microbubbles at the fundamental and subharmonic frequencies for two different driving frequencies of 5 MHz and 10 MHz at a low mechanical index (MI) of 0.07 (156 kPa at 5 MHz and 240 kPa at 10 MHz). The low frequency acoustic pressure acts as a quasi-static increase and reduction in the ambient pressure. This method is inspired by a similar technique developed to detect micro-cracks in bone tissue (Renaud *et al* 2008, Renaud *et al* 2009).

MATERIAL AND METHOD

Experimental Setup

Figure 1 shows a schematic view of the setup. A sealed container with acoustically transparent walls was filled with a highly diluted (1:15000) suspension of BR14 microbubbles. The bubble container was mounted on a magnetic stirrer to obtain a homogeneous distribution of microbubbles. The center of the container was positioned at the focal distance of the transmitting and receiving US transducers (76 mm). A wide band transducer (V311; 3-13 MHz, Panametrics Inc., Waltham, MA, USA) was used to transmit either 15-cycle 5 MHz or 25-cycle 10 MHz sinusoidal bursts with a repetition rate of 16 kHz and MI of 0.07. The US echoes scattered by the microbubbles were received by two other focused transducers (V308; 1-7 MHz and V315; 3-13 MHz, Panametrics Inc., Waltham, MA, USA). The transducers were positioned with a 120 degree angle from each other. The LF acoustic wave was produced by a 15 cm diameter glass disk connected to a shaker, which was excited by a 100-cycle 2.5 kHz sinusoidal burst. Given the LF wavelength and the LF diffraction pattern, the LF wave induced a dynamic modulation of the ambient pressure in the bubble container. A hydrophone (8103, Brüel and Kjær, Nærum, Denmark) was also mounted near the bubble container to measure the pressure wave experienced by microbubbles in the container. The peak amplitude of the LF acoustic wave in the bubble container was 15 kPa. The whole setup was immersed in water inside a large water tank. The water tank was designed deep enough to prevent significant reflections of the low frequency wave from the walls of the water tank (Renaud *et al* 2010). 50 measurements with a 5 MHz transmit frequency and 50 measurements with a 10 MHz transmit frequency were acquired.

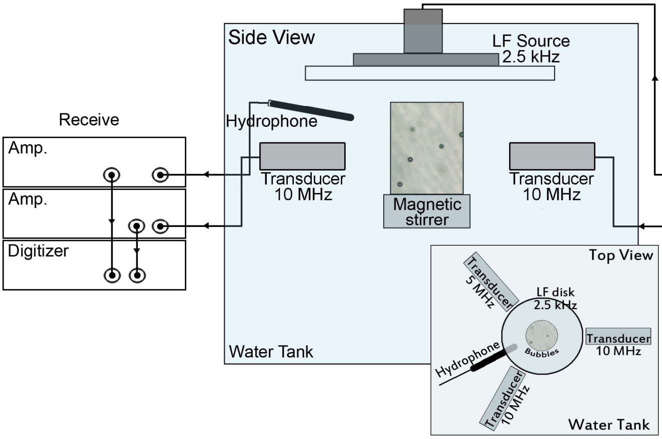

Fig 1. Schematic view of the experimental setup

Signal processing

A 50 ms delay was applied in the firing of the LF wave in order to have a reference when comparing the perturbed to the non-perturbed US signals. A 2 ms section of the full signal (with the total duration of 100 ms) is shown in figure 2. The whole US signal contained 1600 US pulses. For the analysis each received US burst was truncated and its discrete Fourier transform was calculated to retrieve the fundamental (at the transmit frequency) and subharmonic (at half the transmit frequency) amplitudes. Finally each US burst is associated with the LF pressure value recorded half an US time of flight before the actual time when the US burst is received.

In order to indicate the importance of the variation in the subharmonic and fundamental amplitudes induced by the LF pressure, we estimated the subharmonic and fundamental amplitudes expected without the effect of the LF perturbation by applying a low-pass (LP) filtering (cutoff frequency: 1.1 kHz) on the data. This base line is depicted as a yellow line in figures 3 and 4 where the fundamental and subharmonic amplitudes are presented as functions of time for transmit frequencies of 5 MHz and 10 MHz. The relative fundamental and subharmonic modulations (RFM and RSM) are defined as the difference between the fundamental/subharmonic amplitude and the LP filtered fundamental/subharmonic amplitude, normalized by the LP filtered fundamental/subharmonic amplitude:

$$RFM = \frac{F - F_0}{F_0} \qquad \begin{cases} F: & \text{Fundamental amplitude} \\ F_0: & \text{LP filtered fundamental amplitude} \end{cases} \tag{1}$$

$$RSM = \frac{S - S_0}{S_0} \qquad \begin{cases} S: & \text{Subharmonic amplitude} \\ S_0: & \text{LP filtered subharmonic amplitude} \end{cases}$$

Thus the changes in the fundamental and subharmonic amplitudes are expressed relatively to their values in the absence of a LF pressure.

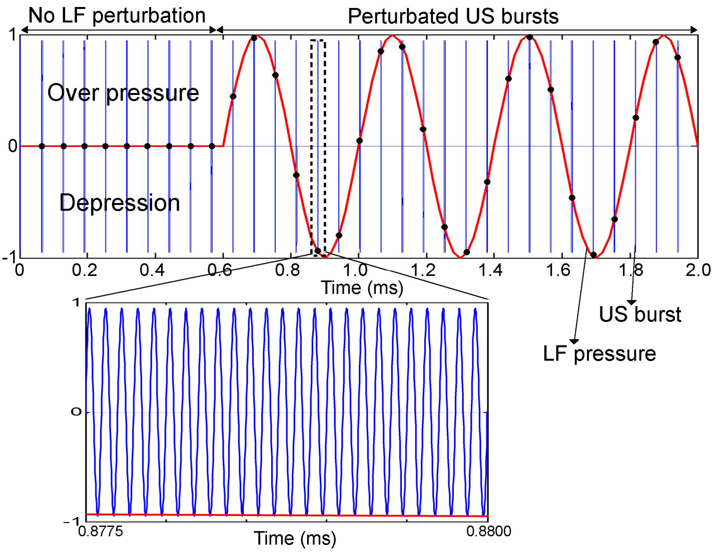

Fig 2. Schematic view of LF and US signals.

RESULTS

Time-signals

The recorded LF pressure pulse and measured fundamental and subharmonic amplitudes are presented in figure 3 and figure 4 for driving frequencies of 5 MHz and 10 MHz respectively. During the first 50 ms before the firing of the LF wave, no perturbation at 2.5 kHz is observed in the fundamental and subharmonic amplitudes. The slow variation in the fundamental amplitude is due to the passage of single or a cluster of microbubbles in the focal area of the transducers. During the next 50 ms, the scattering properties of contrast agent microbubbles are perturbed by the LF pressure and modulations of the subharmonic and fundamental amplitudes are clearly evident. The zoomed-in region in the right panel of figures 3 and 4, presents an enlarged view of the fundamental and subharmonic modulations around a peak of the fundamental amplitude and during 2 ms, such that the microbubbles are considered quasi-static and located at the focal area of the transducers. This duration equals to 5 LF periods and contains 32 high frequency US bursts. Such time-windows are employed for the instantaneous analysis in the following section.

For 5 MHz and 10 MHz transmitting frequencies we observe an increase in the subharmonic amplitude for a positive LF pressure (compression) while for a negative LF pressure (tension) the subharmonic amplitude decreases. However, the subharmonic variation is smaller when microbubbles undergo an expansion (negative LF pressure) than when they are compressed (positive LF pressure) for a transmit frequency of 10 MHz (figure 4). On the contrary the subharmonic modulation is symmetrical for a transmit frequency of 5 MHz (figure 3). As far as the fundamental amplitude is concerned, we observed that for both transmitting frequencies the fundamental variation follows the dynamic changes in the ambient pressure symmetrically, increasing for a negative LF pressure and decreasing for a positive LF pressure.

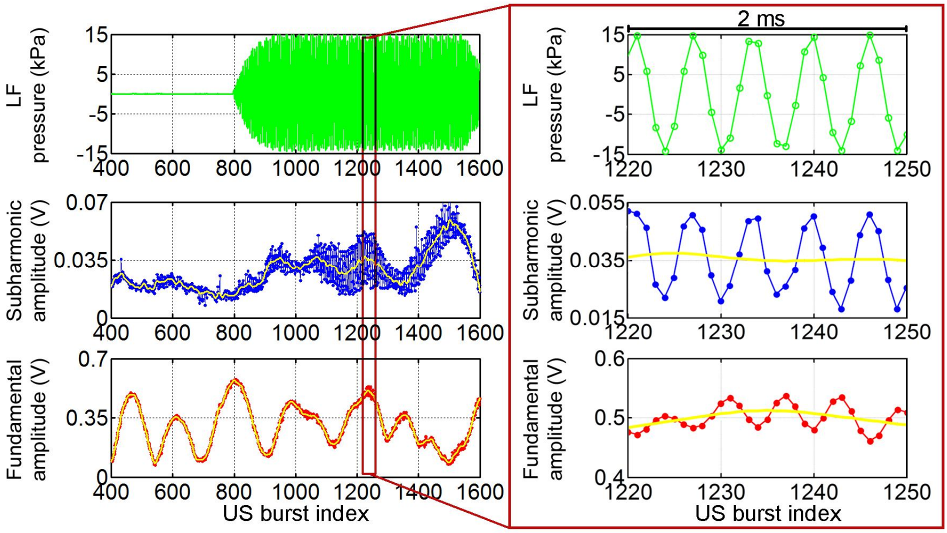

Fig 3. The LF pressure, the fundamental and the subharmonic amplitudes as functions of time (US burst index) for transmitting frequency of 5 MHz. The yellow line is obtained by low-pass filtering and corresponds to the fundamental and the subharmonic amplitudes expected without the effect of the LF perturbation. Each data point is associated to one US burst. The 3 right panels show a typical time-window of 2 ms used for the instantaneous analysis.

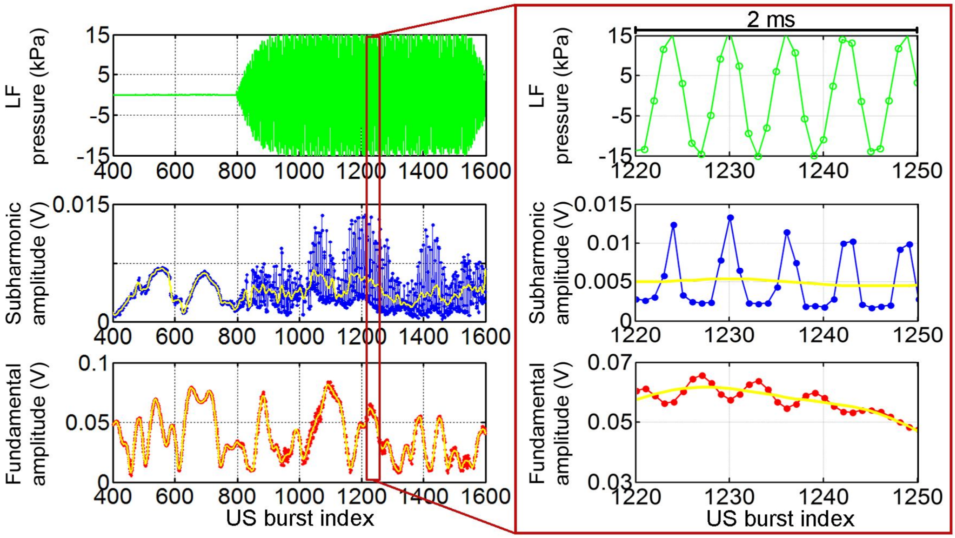

Fig 4. Same caption as figure 3 for a transmitting frequency of 10 MHz.

Instantaneous Analysis

From the whole 100 ms recorded signal a time window of 2 ms was positioned, around each maximum of the fundamental amplitude and during the steady state of the LF pressure signal (US burst index of 1000:1500), to plot the subharmonic and fundamental amplitudes as functions of the LF pressure. In figure 5 and 6, RFM and RSM as functions of the LF pressure for a 5 MHz and 10 MHz driving frequency are shown respectively. As shown in figures 5 and 6, four typical cases were observed. Case 1 is when RFM and RSM are both in phase with the LF pressure. In case 2 and 3 either RFM or RSM is out of phase with the LF pressure and in case 4 both RFM and RSM are out of phase with the LF pressure.

From 50 measurements, roughly 400 peaks were identified in the slow variation in the fundamental amplitude such that around 400 microbubbles were investigated at transmit frequencies of 5 MHz and 10 MHz. Figure 7 indicates the total number of the microbubbles analyzed at each driving frequency and a histogram specifying the percentage of microbubbles behaving according to cases 1 to 4 defined above and presented in figures 5 and 6. For a 5 MHz driving frequency, the four cases exhibit a rather equal prevalence between 20% and 35%. On the contrary, at 10 MHz transmit frequency 60% of microbubbles follow case 3 and 26% behave like case 1. Cases 2 and 4 are rarely observed with respectively 6% and 8%.

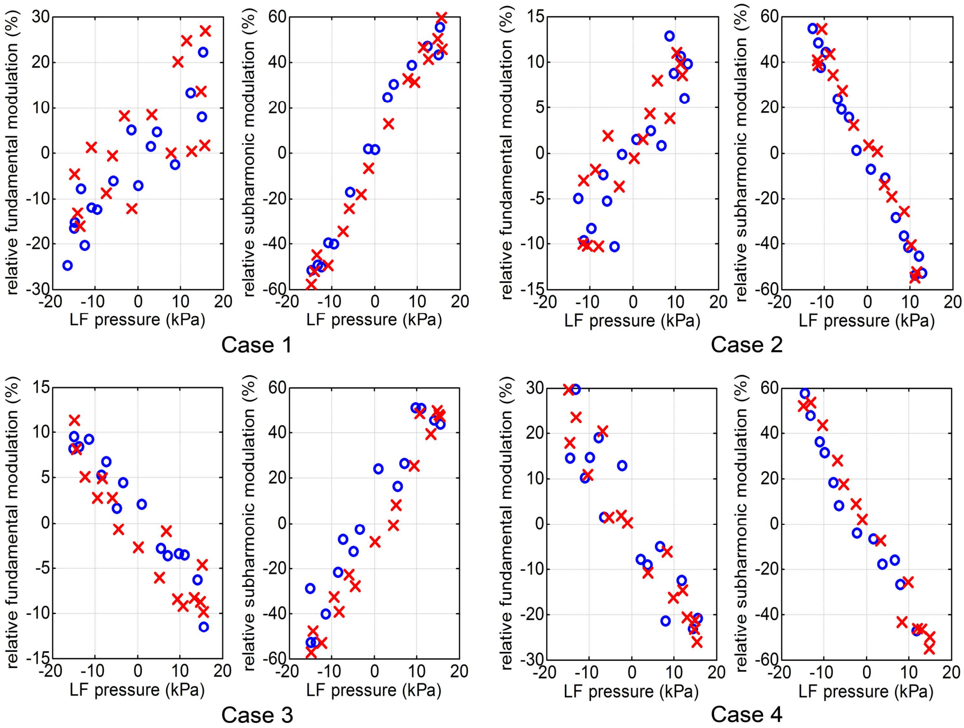

Fig 5. RFM and RSM as functions of the LF pressure for a transmitting frequency of 5 MHz. Circles: increasing LF pressure, Crosses: decreasing LF pressure.

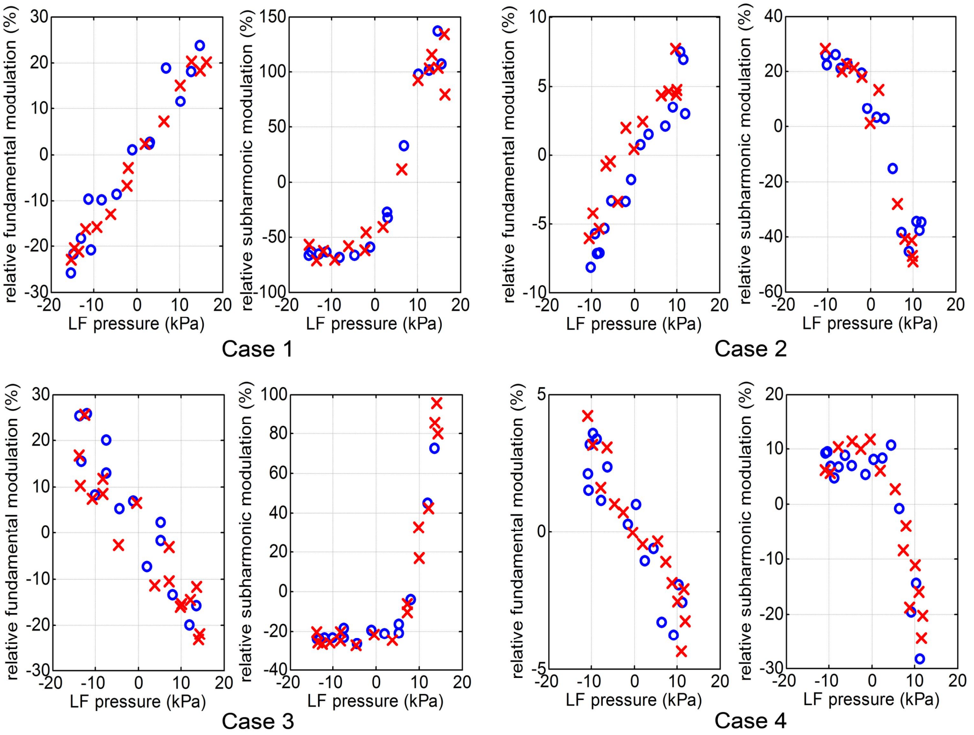

Fig 6. RFM and RSM as functions of the LF pressure for a transmitting frequency of 10 MHz. Circles: increasing LF pressure, Crosses: decreasing LF pressure.

DISCUSSION

Effect of ambient pressure change on the fundamental and subharmonic scattering

It was observed that the modulation of the subharmonic and fundamental amplitudes in the signal scattered by microbubbles versus the dynamic change in the ambient pressure can be categorized in four cases; these cases are summarized in Table 1. The four mentioned cases were observed for both 5 MHz and 10 MHz transmitting frequencies. However, at 10 MHz, a majority of microbubbles belong to cases 3 and 1.

Table 1. Four categories of modulation of the subharmonic and fundamental amplitudes versus the ambient pressure change

Case 1	RFM in phase	&	RSM in phase
Case 2	RFM in phase	&	RSM out of phase
Case 3	RFM out of phase	&	RSM in phase
Case 4	RFM out of phase	&	RSM out of phase

In order to understand the effect of the LF pressure on the scattering properties of US contrast agents, the scattered pressure signal as a function of the bubble diameter for transmitting frequencies of 5 MHz and 10 MHz was calculated based on Marmottant *et al* (2005) model and de Jong *et al* (1994) model.

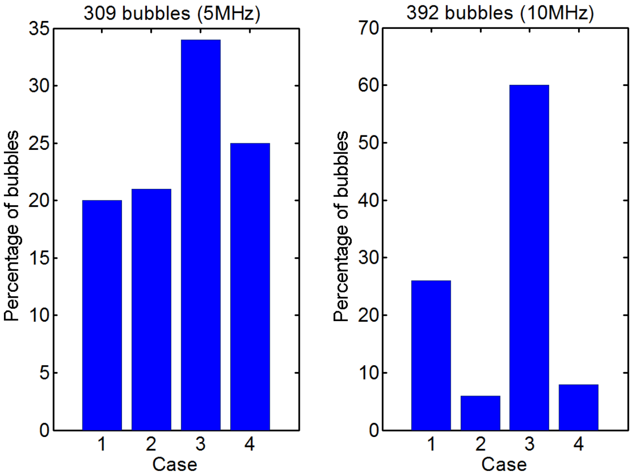

Fig 7. Prevalence of the four cases presented in figures 5 and 6 for transmitting frequencies of 5 MHz (left panel) and 10 MHz (right panel).

Numerical simulations based on Marmottant model (buckling - rupturing shell)

As explained in chapter II, Marmottant *et al* (2005) model was designed to describe the large amplitude response of lipid-coated microbubbles in terms of a varying surface tension. Based on this definition the bubble dynamics divide into three regimes; buckled, visco-elastic and ruptured. The same US signal transmitted in the experiments was applied in the simulations as the input for the bubble excitation. To mimic the effect of LF pressure signal, which results in the change of the bubbles' initial diameter, the scattered US signal was also calculated for the same bubbles after considering ±5% radial strain from their equilibrium diameter. Such a radial strain is expected when applying an overpressure/depression of 15 kPa (Frinking *et al* 2010, Katiyar *et al* 2011). Then fundamental and subharmonic scattered pressure amplitudes were extracted from the Fourier transform of the signals and RFM and RSM for each bubble size were calculated. At last, by comparing the phase between RFM, RSM and the LF pressure, the four possible cases observed in the experiments were constructed. As an example the fundamental and subharmonic scattered pressure amplitudes as a function of bubble diameter are presented in figure 8. These results are calculated using Marmottant *et al* (2005) model at a transmit frequency of 10 MHz. The shell parameters needed for this model were chosen as follows: initial surface tension ($\sigma(R_0)$) at equilibrium equals to 0.06 N/m, elasticity (χ) and shell viscosity (κ_s) are set to 0.4 N/m and 10^{-10} kg/s, respectively. Solid curves in figures 8a and 8b indicate the fundamental and subharmonic amplitudes without LF perturbation. Dashed curves represent the scattered amplitudes after ambient pressure decrease (+5% radial strain, i.e. bubble expansion). Dash-dotted curves show the fundamental and subharmonic amplitudes after ambient pressure increase (-5%

radial strain, i.e. bubble compression). Whenever the difference between the scattered fundamental amplitudes in compression and expansion is positive, by definition, the relative modulation is in phase with the LF pressure. If this difference is negative, the modulation is out of phase with the LF pressure. The combination of different phase behaviors for RFM and RSM presents the four cases defined in experimental results. Note that the same simulations were conducted for a 5 MHz transmit frequency. They lead to the same conclusions and very similar patterns were obtained except that subharmonic emission occurs for bubble diameters ranging between 2.7 µm and 4.5 µm.

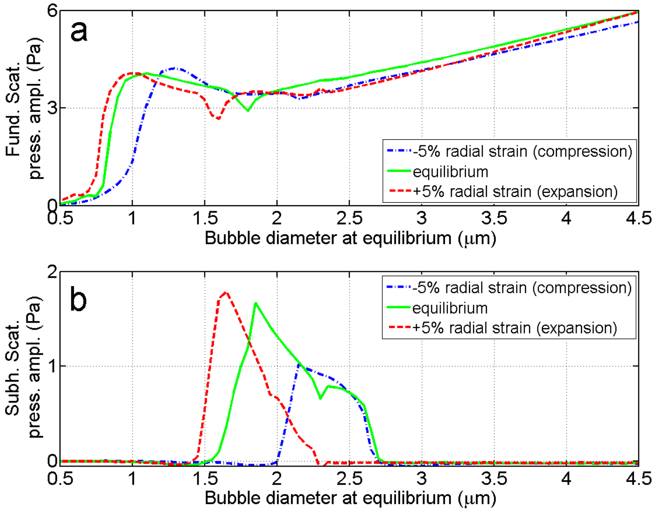

Fig 8. (a and b): Numerical computations of fundamental and subharmonic scattered pressure amplitudes (at 76 mm from the bubble) as functions of the bubble diameter based on Marmottant *et al* (2005) model for a transmit frequency of 10 MHz. Shell parameters were set as $\sigma(R_0) = 0.06$ N/m, $\chi = 0.4$ N/m and $\kappa_S = 10^{-10}$ kg/s.

Numerical simulations based on de Jong model (visco-elastic shell)

The simulations were repeated using de Jong *et al* (1994) model. This model approximates the coating of the microbubbles as a visco-elastic material. The equilibrium surface tension is equal to the surface tension between the core gas and the surrounding medium (in this case water). The other shell parameters (elasticity and viscosity) were kept the same as the previous simulations. The outcome of the simulations predicted only cases 2 and 3 independently of the choice of shell elasticity and viscosity. This indicates that the behaviors of contrast agent microbubbles observed experimentally can not be fully explained with de Jong *et al* model. However the Marmottant *et al* model, taking into account buckling and rupture of the phospholipid shell is able to predict all four cases. Note that the same simulations were conducted for a 5 MHz transmit frequency. They lead to the same conclusions and very similar patterns were obtained except that subharmonic emission occurs for bubble diameters ranging between 2.7 µm and 4.5 µm.

The influence of shell parameters on the modulation of subharmonic scattering

The determining factors in the reaction of the coated micrbubbles to a change in ambient pressure are their shell properties. It is known that among the three elastic, buckled and ruptured regimes defined for phospholipid coated microbubbles by Marmotant *et al* (2005) depending on the initial surface tension, buckled and ruptured bubbles produce the highest subharmonic response (Sijl *et al* 2010, chapter IV). Moreover stiffness (or elasticity) and shell viscosity (van der Meer *et al* 2007, chapter IV) are crucial parameters that influence the occurrence of subharmonic oscillations exhibited by phospholipid coated bubbles. Therefore, we extended our simulations to a parametric study for a transmit frequency of 10 MHz by investigating the responses of microbubbles with diameters between 0.5 µm and 9 µm for initial surface tensions from 0.06 N/m to 0 N/m and shell elasticities from 2.5 N/m to 0.25 N/m. We repeated the simulations for two different values of shell viscosity (10^{-9} kg/s and 10^{-10} kg/s) reported in the literature (van der Meer *et al* 2007, Overvelde *et al* 2010, chapter IV). The results are shown in figures 9a and b for $\kappa_s = 10^{-9}$ kg/s and 10^{-10} kg/s, respectively.

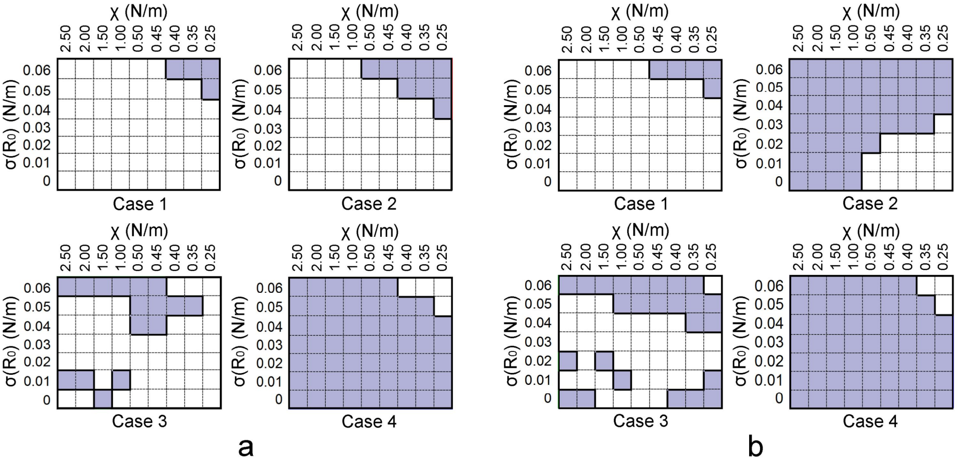

Fig 9. Occurrence of the four experimentally observed cases as functions of initial surface tension and shell elasticity of microbubbles with diameter range of 0.5-9 µm in the simulations based on Marmottant *et al* model for a) $\kappa_s = 10^{-9}$ kg/s and b) $\kappa_s = 10^{-10}$ kg/s. A square is filled if the case is observed.

Based on the results of simulations in figure 9, microbubbles showing cases 1 and 2 are bubbles with high initial surface tension (close to rupture) and low elasticity. Microbubbles presenting cases 3 and 4 can be either close to rupture or buckling regimes and have higher elasticity of those presenting cases 1 and 2. Moreover, the main effect of shell viscosity is on the occurrence of case 2.

Decreasing the value of shell viscosity reduces the damping of the system and subsequently enhances the conditions under which case 2, and to some extent case 3, occur.

The experimental results showed that a majority of the bubbles investigated at 10 MHz belong to cases 3 and 1 (figure 7). Simulations indicated that these bubbles should be either in (or very close to) the buckled or ruptured state. These bubbles are expected to respond asymmetrically to the change of ambient pressure because the subharmonic emission as mentioned before is much higher at these two regimes compared to the elastic state (Sijl *et al* 2010, chapter IV). This hypothesis is confirmed by the experiment (figure 6, cases 1 and 3).

Asymmetry and efficiency of subharmonic scattering modulation

A significant difference between 5 MHz and 10 MHz transmitting frequencies is the expansion/compression asymmetry in the modulation of the subharmonic amplitude as a function of the LF pressure that occurs frequently when bubbles are insonified at 10 MHz (figure 6) but very rarely when insonified at 5 MHz (figure 5). Therefore we performed a second-order polynomial fit on RFM and RSM vs. LF pressure which provides the average curvature and the slope to obtain quantitative information about the asymmetry and the efficiency in the modulation, respectively. The slope and the curvature exhibited by the subharmonic modulation averaged for each case are displayed in figure 10. Based on figure 10 the most efficient subharmonic modulation occurs at 10 MHz for cases 1 and 3. As for the asymmetry in the modulation, for all four cases at 5 MHz there is no significant asymmetry while at 10 MHz, cases 1 and 3 indicate a substantial asymmetry.

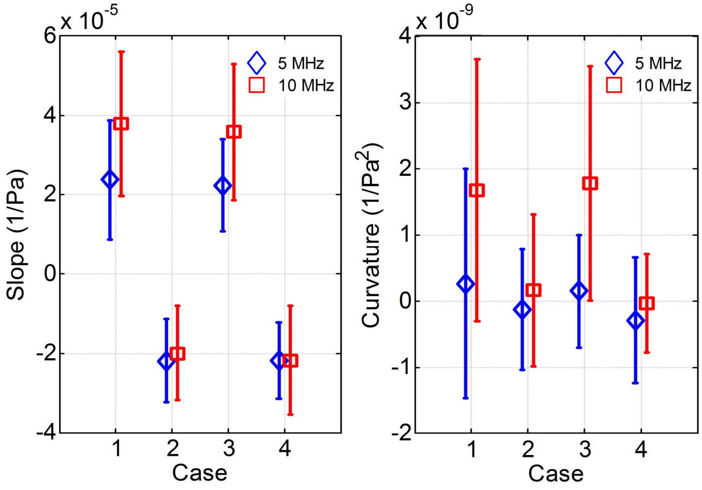

Fig 10. Subharmonic modulation efficiency (slope) and extent of the asymmetry in the subharmonic modulation (curvature) for the four cases, when bubbles are insonified at 5 MHz (diamonds) and 10 MHz (squares).

Estimation of bulk elastic modulus

When bubbles are insonified at a transmitting frequency far above their resonance frequency, the scattered acoustic pressure is proportional to the diameter of the bubble (Maresca *et al* 2010). Therefore by looking at the fundamental amplitude modulation of the bubbles at 10 MHz, one can estimate the relative modulation of the bubble radius. Subsequently the bulk elastic modulus (K_v) of these bubbles can be deduced as follows (Marmottant *et al* 2005):

$$\mathrm{K}_v = \frac{P_{LF}}{\Delta V / V_0} = \frac{P_{LF}}{3\Delta R / R_0} = \frac{1}{3RFM_{slope}} \qquad (2)$$

RFM_{slope} is the slope of the fit on the relative fundamental modulation with the LF pressure (see figure 6). For a buckled bubble K_v is equal to κP_0, (Marmottant *et al* 2005) where κ is the polytropic exponent which is 1 for an isothermal vibration, and equals the ratio of specific heats for a bubble behaving adiabatically (1.07 for C_4F_{10}). P_0 is the ambient pressure. Figure 11 shows the bulk elastic modulus calculated from Eq. 2. The estimated bulk elastic modulus in four cases is around 100 kPa, i.e. the atmospheric pressure, hence in the same order of magnitude as theoretical predictions for a buckling bubble.

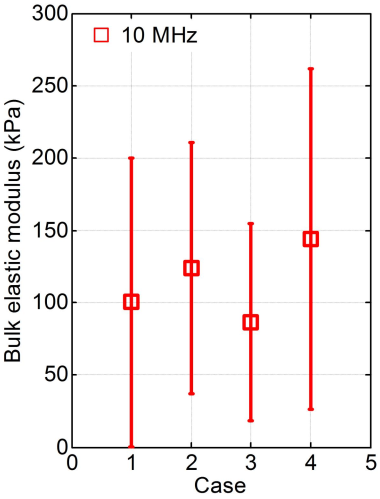

Fig 11. Bulk elastic modulus of the microbubbles deduced from RFM at 10 MHz driving frequency.

TR and T2R subharmonic oscillations

As mentioned in chapter VI, two categories of subharmonic oscillations are described in the literature (Chomas *et al* 2002); transmit at resonance (TR) subharmonic and transmit at twice resonance (T2R) subharmonic. The results of our simulations based on Marmottant *et al* (2005) model are able to predict both categories of subharmonic oscillations; T2R at MI ≈<0.05 (chapter VII) and TR at MI ≈>0.05. However, in our experimental conditions the TR subharmonic radiation (diameter range of 1.5- 2.7 µm) is always dominant, in agreement with Katiyar and

Sarkar (2011). On the contrary, by applying de Jong *et al* (1994) model only T2R subharmonic contents (diameter range of 2.7- 4.5 µm) are constructed (also indicated by Katiyar and Sarkar 2011). All four cases observed in the experiments are predictable by Marmottant *et al* (2005) model producing TR subharmonic emission only (figure 8b). Based on de Jong *et al* (1994) model only cases 2 and 3 are predicted. Therefore it can be concluded that investigated bubbles in these experiments have mainly exhibited TR subharmonic oscillations.

Prevalence of four cases

The prevalence of the four cases derived experimentally (figure 7) indicates that for a 10 MHz transmit frequency cases 1 and 3 are dominant. Simulations predict that these cases occur within the bubble range of 2.1 µm and 2.7 µm. The size distribution of BR14 microbubbles is peaked around the diameter of 2-2.5 µm and typically looks like a chi-square function (Schneider *et al* 1997, Conversano *et al* 2010). Therefore, cases 1 and 3 result to be the most probable for a 10 MHz transmit frequency and TR subharmonic scattering.

By reducing the transmit frequency, the size range of the bubbles producing TR subharmonic scattering shifts to larger diameters. At 5 MHz, the bubble range in which the four cases occurs shifts to bubble diameters between 2.7 µm and 4.5 µm. Looking back to the size distribution of BR14, in this case the possibility for all four cases to occur increases, in agreement with experimental observations (figure 7).

Comparison with literature

We report enhancement from 2 to 10 dB (in amplitude) in the subharmonic scattering of phospholipid coated microbubbles by applying an ambient overpressure of 15 kPa. This observation is lower than the previously mentioned results of Frinking *et al* (2010). This discrepancy may arise from two reasons, presumably due to either a novel property of the experimental agent used by Frinking and colleagues or a lower acoustic pressure amplitude which was employed in their experiments, 50 kPa peak negative pressure at 4 MHz (MI=0.025). Consequently they may have observed T2R subharmonic emission while mostly TR subharmonic was generated in our study. Besides, the possibility to manipulate the subharmonic oscillations of microbubbles in a dynamic manner makes this method suitable for imaging.

Katiyar *et al* (2011) have presented a numerical study investigating the effect of ambient pressure on the subharmonic response of contrast microbubbles. According to their simulations, the ratio of the excitation frequency *(f)* to the resonance frequency of the microbubbles (f_0) is the determining parameter for the subharmonic response of a bubble to either increase or decrease with ambient pressure increase. However, their criterion can not be applied in our study because the effect of buckling and rupture has not been taken into account in their simulations. In fact their study applies for free gas bubbles and coated bubbles with a visco-elastic shell only. We discussed before that models with assumption of a visco-elastic coating (de Jong *et al* 1994, Hoff *et al* 2000) can only predict two typical cases out of four experimentally observed behaviors.

Another important factor in the occurrence of different observed behaviors is the amplitude of the US burst. When this amplitude is high enough, the radial excursion can induce both buckling and rupture of the shell which amplifies the subharmonic oscillations compared to a bubble which oscillates either towards the bucking or the ruptured regimes. This was the case in our simulations based on Marmottant *et al* (2005) model. For a bubble around the resonant diameter at 10 MHz (1.2 µm) the large bubble oscillations induce both buckling and rupture of the shell.

The results derived from this study provide the basic knowledge to apply a novel method for enhancing the subharmonic response of US contrast agents. However, using a 2.5 kHz LF wave is not realistic for *in vivo* imaging, since this frequency range is audible and may cause destruction of ear drum for an acoustic pressure of 15 kPa peak amplitude. Instead applying a relatively higher frequency around 35 kHz can be an excellent substitution for *in vivo* applications of this method. Complimentary experiments in this direction are underway.

CONCLUSION

We measured the fundamental and subharmonic scattering amplitude of phospholipid microbubbles insonified at 5 MHz and 10 MHz while changing the ambient pressure of the surrounding liquid in a quasi-static manner by applying a LF acoustic wave of 2.5 kHz frequency (15 kPa peak amplitude). The subharmonic amplitude was enhanced up to 10 dB by this method. Four cases were observed in the experiments and reproduced by simulations as a function of microbubbles' diameter. The prevalence of these four behaviors is determined by the size distribution of contrast agent microbubbles. We believe this experimental method may be a useful tool for *in vitro* characterization and design of contrast agent microbubbles. Furthermore this technique could be employed as a new subharmonic imaging modality.

References

Chomas J E, Dayton P, May D and Ferrara K 2002 Nondestructive subharmonic imaging *IEEE Trans. Ultrason. Ferroelectr. Freq. Control* 49 883-892

Conversano F, Franchini R, Casciaro S 2010 Characterization of microbubble contrast agents for echographic imaging through time-scheduled size distribution measurements *Sensors and Transducers J.* 9 21-27

de Jong N, Cornet R and Lancee C T 1994 Higher harmonics of vibrating gas-filled microspheres. Part one: simulations *Ultrasonics* 32 447-453

Frinking P J A, Gaud E, Brochot J and Arditi M 2010 Subharmonic scattering of phospholipid-shell microbubbles at low acoustic pressure amplitudes *IEEE Trans. Ultrason. Ferroelectr. Freq. Control* 57 1762-1771

Hoff L, Sontum P C and Hovem J M 2000 Oscillations of polymeric microbubbles: effect of the encapsulating shell *J. Acoust. Soc. Am.* 107 2272-2280

Katiyar A and Sarkar K 2011 Excitation thresholds for subharmonic response of ultrasound contrast microbubbles *POMA* 11 1-15

Katiyar A, Sarkar K and Forsberg F 2011 Modeling subharmonic response from contrast microbubbles as a function of ambient static pressure *J. Acoust. Soc. Am.* 129 2325-2335

Maresca D, Emmer M, Van Neer P, Vos H J, Versluis M, Muller M, de Jong N and Van der Steen A F 2010 Acoustic Sizing of an Ultrasound Contrast Agent *ultrasound Med. Biol.* 36 1713-1721

Marmottant P, van der Meer S, Emmer M, Versluis M, de Jong N, Hilgenfeldt S and Lohse D 2005 A model for large amplitude oscillations of coated bubbles accounting for buckling and rupture *J. Acoust. Soc. Am.* 118 3499-3505

Overvelde M, Garbin V, Sijl J, Dollet B, de Jong N, Lohse D and Versluis M 2010 Nonlinear shell behavior of phospholipid-coated microbubbles *Ultrasound Med. Biol.* 36 2080-2092

Renaud G, Calle S and Defontaine M 2009 Remote dynamic acoustoelastic testing: Elastic and dissipative acoustic nonlinearities measured under hydrostatic tension and compression *Appl. Phys. Lett.* 94 011905-011905-3

Renaud G, Calle S and Defontaine M 2010 Dynamic acoustoelastic testing of weakly pre-loaded unconsolidated water-saturated glass beads *J. Acoust. Soc. Am.* 128 3344-3354

Renaud G, Calle S, Remenieras J P and Defontaine M 2008 Exploration of trabecular bone nonlinear elasticity using time-of-flight modulation *IEEE Trans. Ultrason. Ferroelectr. Freq. Control* 55 1497-1507

Schneider M, Broillet A, Bussat P, Giessinger N, Puginier J, Ventrone R and Yan F 1997 Gray-scale liver enhancement in VX2 tumor-bearing rabbits using BR14, a new ultrasonographic contrast agent *Investigative Radiology* 32 410-417

Sijl J, Dollet B, Overvelde M, Garbin V, Rozendal T, de Jong N, Lohse D and Versluis M 2010 Subharmonic behavior of phospholipid-coated ultrasound contrast agent microbubbles *J. Acoust. Soc. Am.* 128 3239-3252

van der Meer S M, Dollet B, Voormolen M M, Chin C T, Bouakaz A, de Jong N, Versluis M and Lohse D 2007 Microbubble spectroscopy of ultrasound contrast agents *J. Acoust. Soc. Am.* 121 648-656

Chapter VIII

Effect of self-demodulation on the subharmonic response of contrast agent microbubbles

Verya Daeichin, Telli Faez, Guillaume Renaud, Johanus G Bosch, Antonius F W van der Steen, Nico de Jong

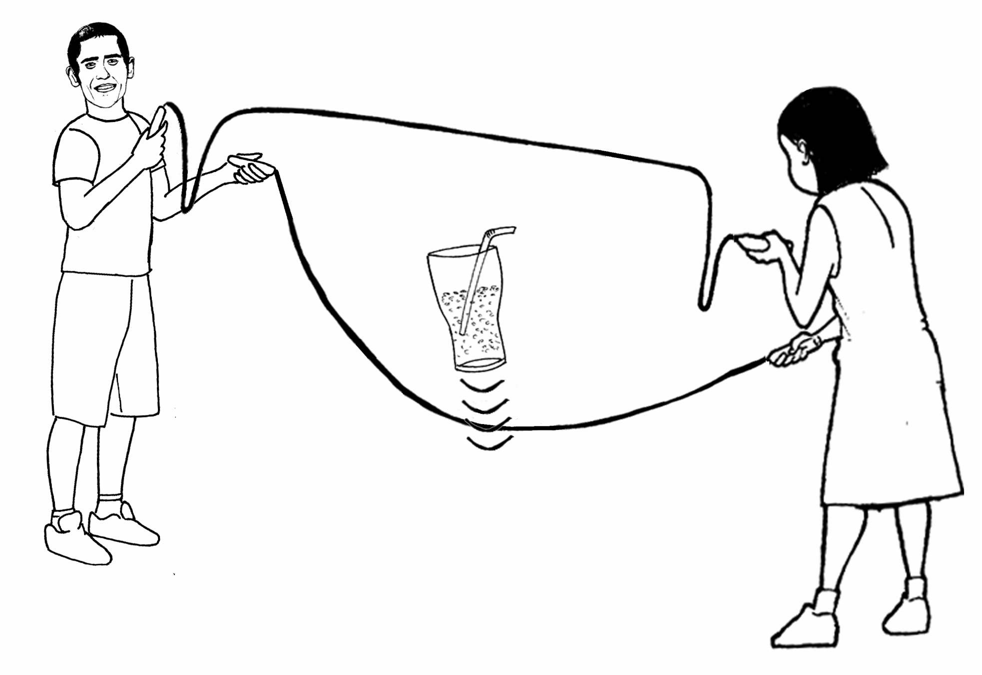

Published in Physics in Medicine and Biology May 23, 2012

Abstract

In this work the use of the self-demodulation (S-D) signal as a mean of microbubble excitation at the subharmonic frequency to enhance the subharmonic emission of UCA is studied. The S-D wave is a low-frequency signal produced by weakly nonlinear propagation of an ultrasound wave. The S-D signal is proportional to the second time derivative of the squared envelope of the transmitted signal. A diluted population of BR14 UCA was insonified by a 10 MHz transducer focused at 76 mm firing bursts with different envelopes, durations and peak pressure amplitudes. The center frequency of the S-D signal changes from low frequencies (around 0.5 MHz) towards the transmitted frequency (10 MHz) by modifying the envelope function from Gaussian to rectangular. For 6 and 20 transmitted cycles, the subharmonic response is enhanced up to 25 dB and 22 dB, respectively, when using a rectangular envelope instead of a Gaussian one. The experimental results are confirmed by numerical simulation. The effects of the excitation duration and pressure amplitude are also studied. This study shows that a suitable design of the envelope of the transmit excitation to generate a S-D signal at the subharmonic frequency can enhance the subharmonic emission of UCA and the subharmonic imaging is feasible at high frequencies with shorter transmit burst (6-cycle) and low acoustic pressure (~100 KPa).

INTRODUCTION

In general, nonlinear imaging approaches are thought to perform best when the bubbles are insonified at or near their resonance frequencies (Vos *et al* 2011). The resonance frequencies of conventional UCA bubbles range generally between 1 MHz and 8 MHz (Gorce *et al* 2000, Shi *et al* 2002, Feinstein 2004, Sarkar *et al* 2005), which are therefore well-suited for the majority of diagnostic ultrasound applications. However, for applications requiring a higher spatial resolution, transmit frequencies of 10 MHz and beyond are required such as carotid (10 MHz), intravascular coronary vasa vasorum imaging and small animal imaging (15 to 50 MHz) (Feinstein 2004, Goertz *et al* 2006, Goertz *et al* 2007, Needles *et al* 2010). Under these circumstances the performance of nonlinear imaging techniques is degraded because the driving frequency is higher than the resonance frequency (Needles *et al* 2010). In addition second harmonic imaging techniques are hampered because of the increase in the amplitude of harmonics produced by tissue as a result of nonlinear propagation of ultrasound.

Gas filled microbubbles can also act as nonlinear mixers producing frequency cross-products in dual frequency insonations (Newhouse *et al* 1984, Shankar *et al* 1998, Wu *et al* 2003, Chen *et al* 2006). Recently, several techniques utilizing radial modulation of the microbubbles have been reported (Bouakaz *et al* 2007, Chérin *et al* 2008, Masoy *et al* 2008). In these techniques as was described in chapter VII, microbubbles are excited simultaneously with two ultrasound waves, a low-frequency manipulation wave to modulate the microbubble size, and a high-frequency imaging pulse for high-resolution detection of the changes in the acoustic cross section of UCA induced by the manipulated wave. Such periodic changes in the acoustic cross section of microbubbles modulate the amplitude and the phase of the backscattered imaging signal. Also a dual-frequency difference excitation technique was developed to induce an efficient low-frequency nonlinear scattering from microbubbles using high-frequency ultrasound (Chen *et al* 2006, Yeh *et al* 2008, Yeh *et al* 2009, Vos *et al* 2011). The dual-frequency excitation involves the simultaneous transmission of two high-frequency sinusoids to produce a component at the difference frequency. When the difference frequency is equal to the mean resonance frequency of the UCA, the difference frequency component scattered by the UCA is maximal (Shen *et al* 2007).

Zheng *et al* (2005) presented an application of multi-frequency excitation, where rectangular and triangular waveforms with four harmonics were used to excite the UCA through numerical modeling via a modified Rayleigh-Plesset equation. They showed that the rectangular envelope is effective in improving the nonlinear signal scattered by microbubbles, with effective scattering cross-section area significantly higher (up to 35 times) than the widely-used Gaussian envelope. The subharmonic signal is also strongly dependent on the envelope of the excitation signal (Zheng *et al* 2005, Biagi *et al* 2006, Masotti *et al* 2007, Zhang *et al* 2009). Biagi *et al* (2006) examined ultrasound bursts with three different envelopes in order to evaluate the subharmonic response of the contrast agent. They found a decrease up to 30 dB and 21 dB in the subharmonic response for a pulse with a Gaussian envelope and a composite pulse (two-tone burst), respectively, compared with a sinusoidal burst having a rectangular envelope. Their experimental results confirmed that the envelope of the transmitted signal strongly affects the subharmonic emission. They hypothesized that the smoothness of the beginning of an excitation with Gaussian envelope can inhibit the generation of subharmonic from the contrast agents. In another study, Masotti *et al* (2007) reported that the subharmonic behavior of UCA is not only pressure and concentration dependent but also a phase dependent phenomenon. Changing the phase between the transmitted signals of different frequencies modifies the envelope of the excitation burst. It has been shown that the phase between the two high frequency transmit pulses in the dual-frequency excitation method, therefore the shape of the excitation burst, plays an important role in maximizing the amplitude response of the microbubbles at the subharmonic frequency (Masotti *et al* 2007, Shen *et al* 2011). Zhang *et al* (2009) also compared an excitation technique, made of dual-frequency, with the conventional single frequency sinusoidal technique to enhance the subharmonic emission from UCA. They showed numerically and experimentally that a dual-frequency signal (2 and 4 MHz) is able to improve the amplitude of the subharmonic component up to 13 dB over the single frequency sinusoidal excitation technique. In another study Zhang *et al* (2007) showed theoretically and experimentally that using chirp excitation techniques with a center frequency of 5 MHz, a frequency range of 1 MHz and a pulse length of 40 μs can enhance the amplitude of the subharmonic emission of the UCA by 15-22 dB compared with a sine burst having a Gaussian envelope.

Needles *et al* (2010) studied different conventional nonlinear contrast imaging methods such as pulse inversion, amplitude modulation and combination of these two together with subharmonic imaging technique both *in vitro* and *in vivo.* They wanted to optimize a strategy for real time nonlinear contrast imaging with good performance in canceling the signal from the tissue, using a commercial high frequency ultrasound system (18-24 MHz) with an array based transducer. Using pulse inversion with subharmonic imaging and excitation bursts with rectangular envelopes showed 15 dB enhancement in contrast to tissue ratio compared with the fundamental imaging.

In this paper, we investigate the effect of the self-demodulation (S-D) signal on the subharmonic response of phospholipid-coated microbubbles excited at 10 MHz. Our hypothesis is that the enhancement of the subharmonic signal using an excitation wave with a rectangular envelope can be explained by the S-D stimulation effect on the subharmonic response of the UCA. This may be the origin of experimental findings reported in literatures (Biagi *et al* 2006, Needles *et al* 2010). We show that understanding the effect of the S-D signal on the UCA behavior can help to optimize the envelope of the excitation signal for subharmonic imaging especially at high frequencies.

THEORY AND NUMERICAL SIMULATIONS

In order to investigate the influence of the S-D signal and the driving frequency on the subharmonic response of the UCA, we analytically extracted the frequency components of the S-D signal for waves with different envelopes. Then we linked the KZK model as implemented by Vos *et al* (2011) to a model describing the dynamics of lipid-coated microbubbles (Marmottant *et al* 2005). The calculated pressure wave from the KZK model is used as an excitation wave in the Marmottant model in order to compute the radial response of a microbubble with a diameter of 2 µm. Fig. 1 indicates the flow chart of the simulation steps and the input and output acoustic signals in the time and frequency domains for each simulation model.

Theoretical derivation of the frequency content of the self-demodulation signal

In a weakly nonlinear regime the propagation of an ultrasound pulse gives rise to a low-frequency signal due to the S-D phenomenon. The S-D pressure wave, $p_{sd}(t)$, is related to the envelope of the transmitted signal, E(t), as follows (Berktay 1965, Averkiou *et al* 1993, Vos *et al* 2010):

$$p_{sd}(t) \propto \frac{\partial^2 E^2(t)}{\partial t^2} \tag{1}$$

The frequency content of the S-D signal of different envelopes is calculated analytically. Let us assume that the envelope function of the transmit burst is:

$$E(t) = e^{-(\frac{2t}{T})^{2M}} \tag{2}$$

where T is the duration of the signal and the integer M determines the rise and decay time of the envelope. For M equal to 1 this function represents a Gaussian envelope which can be approximated by a cosine term and a constant (Raab *et al* 1961). Assuming these simplifications one can rewrite the envelope function (Eq. 2) as the following:

$$\begin{aligned} E(t) = e^{-(\frac{2t}{T})^{2M}} &\cong (A + B.\cos(\omega_e t))^M \\ &= \sum_{k=0}^{M} \binom{M}{k} A^{M-k}.B^k.\cos^k(\omega_e t) \\ &= \sum_{n=1}^{M} A_n + B_n \cos(n\omega_e t) \quad , \quad -\frac{T}{2} \le t \le \frac{T}{2} \end{aligned} \tag{3}$$

Where $\omega_e = 2\pi/2T$ is the center frequency of the envelope for M=1, A_n and B_n are the coefficients in the Fourier series.

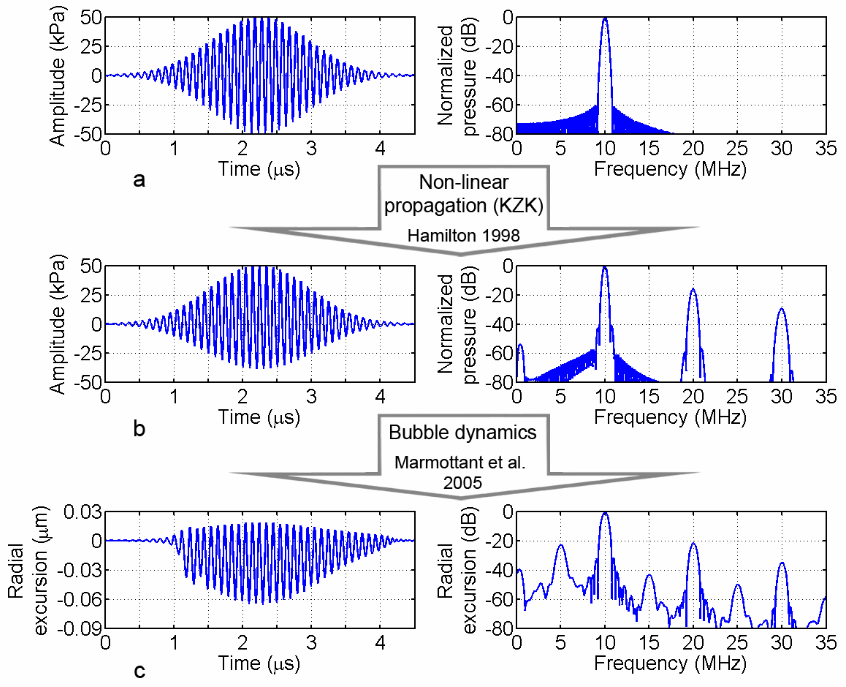

Fig 1. Flow chart of the simulation steps showing the pressure wave (for M=1) and its spectra at a) the surface of the transducer (input of the KZK model) and b) the focus of the transducer (76 mm) (KZK output). c) Radial excursion of a 2 μm bubble with initial surface tension of 0.014 N/m (output of Marmottant model).

Eq. 3 demonstrates the leakage of energy into higher harmonics of ω_e for higher integer values of M. For example for M=3, the envelope contains the second and the third harmonics of ω_e. This means that for a rectangular envelope, more harmonics of ω_e are present.

Combining Eq. 3 and Eq. 1 we obtain the frequency component of the S-D signal for an arbitrary value of M:

$$p_{sd}(t) \propto \frac{\partial^2 E^2(t)}{\partial t^2} \cong \frac{\partial^2}{\partial t^2}[\sum_{n=1}^{M} A_n + B_n \cos(n\omega_e t)]^2 \tag{4}$$

$$\Rightarrow |p_{sd}(t)| \cong \sum_{n=1}^{M} B_n' \cos((2n-1)\omega_e t) + C_n' \cos(2n\omega_e t)$$

Where A_n' and C_n' are constants. Eq. 4 presents a series of the envelope center frequency and its harmonics. It can be seen that for higher M values, more harmonics of the envelope center frequency are involved in the frequency content of the S-D pressure signal.

Effect of the transmit signal envelope on the self-demodulation signal

We used the equation derived by Khokhlov, Zabolotskaya, and Kuznetsov (KZK) (Hamilton *et al* 1998) to calculate the nonlinear propagation of a collimated ultrasound beam. The KZK model considers diffraction, absorption, and nonlinear propagation in the medium. It has been shown that such a model can accurately simulate the S-D of a sine burst (Averkiou *et al* 1993, Lee *et al* 1995, Averkiou *et al* 1997, Callé *et al* 2002, Vos *et al* 2010). We adopted this model as implemented by Vos *et al* (2011) for our simulations. As an excitation source, a transducer focused at 76 mm with a diameter of 10 mm was used.

Fig. 2 depicts the results of the KZK simulations to estimate the nonlinear propagation of a 10 MHz ultrasound pulse, for three different envelopes (M=1; 3; 15 and T=2 μs). The transmitted acoustic pressure at focus was set to 50 kPa. For M=1 (Gaussian envelope), the S-D signal is concentrated at low frequencies around ω_e and $2\omega_e$ (Eq. 4) which appears as a peak around 0.75 MHz in the frequency domain (Fig. 2c, M=1). For M=3 (Fig. 2c, M=3) a more distributed S-D signal with center frequency around 1 MHz is obtained. Increasing M to higher values (e.g. M=15) results in the leakage of energy to higher harmonics of ω_e until when no distinct peak can be seen for the S-D signal in the frequency domain due to the distribution of the energy from ω_e up to the 30th harmonic of ω_e (Fig. 2c, M=15).

Comparing the frequency content of the propagated waves with the three different envelopes (Fig. 2c) indicates that the transmitted pulse with a rectangular envelope has the highest S-D energy around the subharmonic frequency (5 MHz). It can be seen in Fig. 2c that the amplitude of the S-D signal is around 50 dB below the fundamental frequency for M=1 and M=3. For M=15 the S-D signal is a broad band low frequency signal which overlaps with the side lobes of the fundamental frequency peak (10 MHz).

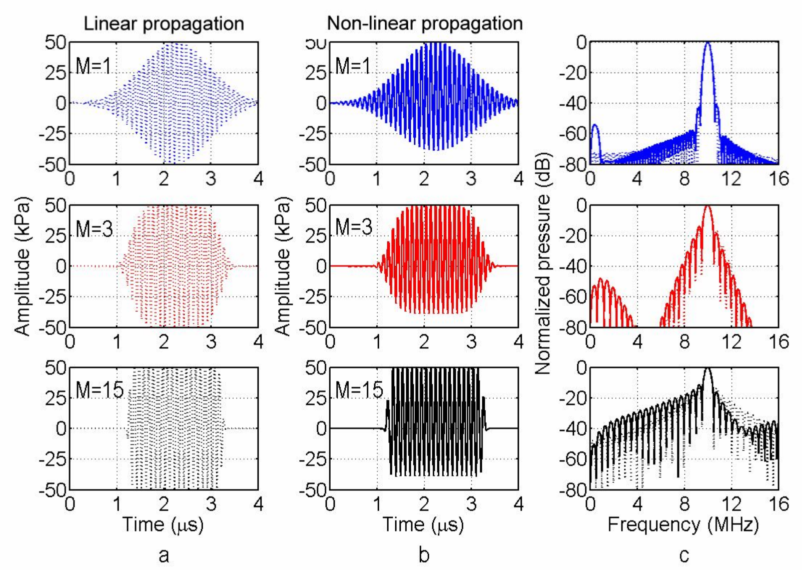

Fig 2. Numerical computations based on KZK model (Vos *et al* 2011) showing the propagation of a 10 MHz burst with three different envelopes (M=1, 3 and 15) in a nonlinear medium; a) after linear propagation, b) after non-linear propagation, and c) their corresponding frequency spectra.

Effect of the self-demodulation signal on the subharmonic emission of a microbubble

According to the model of Marmottant *et al* (2005), a sharp change in the shell stiffness, occurring when the coating buckles, can enhance the subharmonic response. The initial surface tension was shown to be a key parameter in the generation of low amplitude subharmonic emission by lipid coated microbubbles (Sijl *et al* 2010, chapter IV). We conducted a parametric study by varying the initial surface tension from 0 to 0.07 N/m (the surface tension of water) and investigated the amplitude of the subharmonic oscillation of a single microbubble in response to three different excitation bursts as shown in Fig. 3. The shell elasticity (χ) and the shell viscosity (κ_s) were set to *2.5* N/m and 10^{-9} kg/s, values for BR14 UCA used for *in vitro* experiments (Sijl *et al* 2010, chapter IV). The diameter of the microbubble was set to 2 µm which is also the mean diameter of BR14 UCA (Conversano *et al* 2010).

The amplitude of the subharmonic signal is strongly dependent on the initial surface tension $\sigma(R_0)$ of the microbubble. Fig. 3 shows the subharmonic amplitude of a 2 µm bubble as a function of its initial surface tension in the Marmottant model. The subharmonic oscillations are observed only when the bubble is around either the buckling or the rupturing regimes. However the margins for these regimes are wider for the excitation bursts with higher M values. By increasing the value of M, the amplitude of the subharmonic vibration is enhanced for an initial surface tension between 0.01 and 0.02 N / m and between 0.05 and 0.065 N / m. As an example, the radial excursions of such a 2 µm diameter microbubble in response to the three excitation bursts in time and frequency domains are shown in Fig. 4 for the initial surface tension of 0.014 N / m indicated by a vertical line in Fig. 3. Figure 3 shows that the stimulation effect of the S-D signal on the subharmonic response of the microbubble is significant when the initial state of the microbubble is just outside the buckling regime ($0.01<\sigma(R_0)<0.02$ N / m) or close to the rupturing regime ($0.05<\sigma(R_0)<0.07$ N / m).

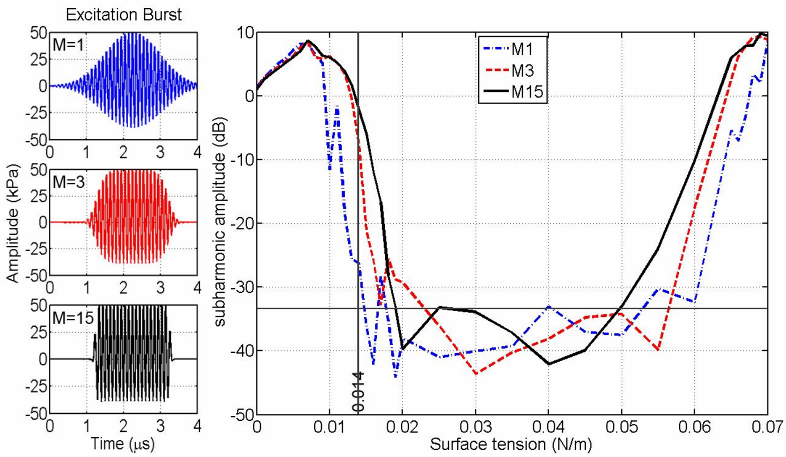

Fig 3. Simulation results showing the amplitude of the subharmonic radial response of a single microbubble (2 µm diameter) as a function of the initial surface tension to a burst with three different envelops after nonlinear propagation (at the focus): M=1 dashed-dotted curve, M=3 dashed curve and M=15 solid curve. The horizontal line indicates the noise level in the simulations.

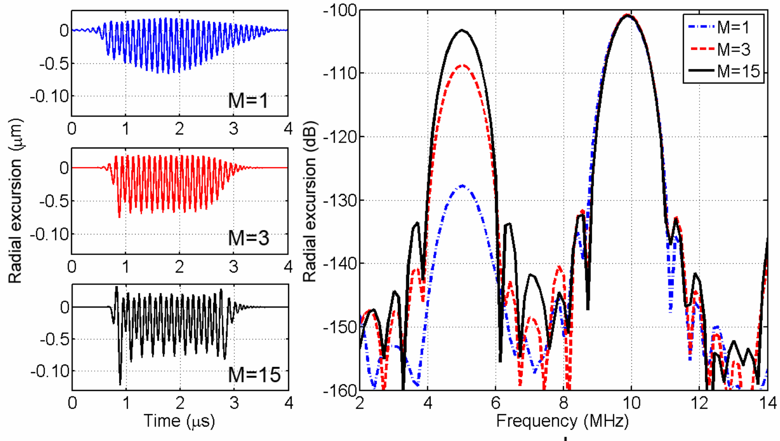

a b

Fig 4. Radial excursion of a 2 µm microbubble excited by a 20-cycle burst with three different envelopes after nonlinear propagation (at the focus): M=1 (dashed-dotted curve), M=3 (dashed curve) and M=15 (solid curve) and their corresponding amplitude spectra for an initial surface tension of 0.014 N / m.

The energy of the S-D signal is located at the beginning and the end of the transmitted burst (Averkiou *et al* 1993). Therefore in order to remove that part of the signal which corresponds to the linear response to the S-D signal, three periods at 10 MHz from the beginning and the end of the radial excursion signal were discarded. Then a Hanning time window was applied to the rest of the signal to smoothen the spectra. Since the energy of the excitation bursts is the same, fundamental peaks appear to be at the same level. However the subharmonic response of such a bubble is enhanced up to 23 dB by increasing the M in the envelope function of the excitation burst.

MATERIAL AND METHOD

The schematic view of the setup is depicted in Fig. 5. A 10 mm diameter thin shell cylindrical tube made of Polypropylene film backing coated with a water based acrylic adhesive (tesa® 4024 PV 2) having a total thickness of 52 μm was mounted in the center of a triangular water tank at the focus of two transducers used for transmitting and receiving the ultrasound signals. The tube was filled with distilled, saturated water (Isoton II, Beckman Coulter, The Netherlands). BR14 microbubbles were reconstituted to manufacturer's specifications and diluted 10,000 times then poured in the tube and mixed gently using a magnetic stirrer in order to have a homogeneous suspension. The microbubbles consist of a phospholipid monolayer shell with a perfluoropropane gas core. A broad-band transducer with centre frequency of 10 MHz and 76 mm focal length, (Panametrics V311; 3-13 MHz) was used for transmit. The transducers were calibrated using a 0.2 mm PVDF probe hydrophone in a separate experiment (Precision Acoustics Ltd., Dorchester, UK). The echoes from the microbubbles were received at half the transmitting frequency (5 MHz) by another focused transducer with the same focal length (Precision Acoustics PA076; 1-9 MHz). Acoustic pressure amplitudes of 50, 100 and 150 kPa were applied. The transmitted signals were calculated in MATLAB using Eq. 2 and generated by an arbitrary wave generator (8026, Tabor Electronics Ltd., Tel Hanan, Israel) and amplified with a 60 dB pulse amplifier (150A100B; Amplifier Research, Limerick, Ireland). The scattered pressure waves were received, amplified by 60 dB and digitized by a 12-bit digitizer with a sampling frequency of 500 MHz.

10 MHz bursts of 2, 6, 10 and 20 cycles were transmitted. The envelope of the transmit burst was varied from the Gaussian to the rectangular shape by changing the value of M to 1, 3 and 15 (Eq. 2). Averaging over 50 pulses in the frequency domain with a pulse repetition frequency of 1 kHz was applied, and this sequence was repeated for each of the transmitted signals with different envelopes. The amplitude spectrum of the received pressure signals (Fig. 6a) have been calculated after discarding three cycles at 10 MHz from the beginning and the end of the received scattered signals for the 20-cycle burst and applying a hanning window. The beginning and the end of the received scattered signal was taken away to remove the direct effect of the 5 MHz component of the S-D signal linearly

scattered by UCA which could be mistaken as enhancement of the subharmonic response.

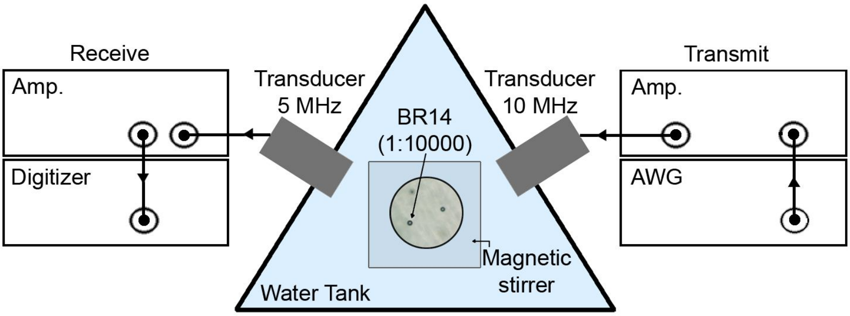

Fig 5. Schematic view of the experimental setup

RESULTS

Effect of the self-demodulation signal on the subharmonic emission of microbubbles

Fig. 6 shows the signals scattered by the microbubbles in response to a 20-cycle 10 MHz burst with three envelopes changing from a Gaussian shape (M=1) to a more rectangular shape (M=15). The energy of the subharmonic response produced by the UCA increases from -55 dB to -33 dB for M=1 to M=15, thus a 22 dB enhancement is observed. The acoustic pressure amplitude at the focus of the transducer was set to 50 kPa. This is the pressure that the microbubbles experience. Clear subharmonic peaks for all the three different excitation bursts in Fig. 6 show that 50 kPa pressure amplitude is already above the subharmonic threshold level of the BR14 UCAs.

Effect of the excitation duration on the subharmonic emission of microbubbles

Short signals are more favored for imaging purposes since they provide a higher spatial resolution. However, with such signals, it is difficult to separate the subharmonic component from the fundamental component in the frequency domain. To investigate the effect of the excitation burst duration on the subharmonic emission of the UCAs, four bursts with the same rectangular envelope (M=15) and acoustic pressure peak amplitude of 50 kPa but different number of cycles (2, 6, 10 and 20) were applied. Fig. 7 shows examples of time signals scattered by the UCA for each transmitted burst and their amplitude spectra averaged over 30 sequences in frequency domain.

The excitation with only 2 cycles results in a very broad-band scattered signal with no distinguishable peak around the subharmonic frequency. Increasing the transmit burst durations to 6, 10 and 20 cycles results in the equal 22 dB ratio of the subharmonic amplitude to fundamental amplitude. The advantage of using a longer pulse as can be seen in Fig. 7 is that a better separation of the subharmonic and fundamental peaks is obtained. Independently from the duration of the transmitted burst, the enhancement of the subharmonic response due to the envelope of the burst is still valid for a short burst of 6 cycles (Fig. 8). Similar to a 20-cycle burst (Fig. 6) the energy of the subharmonic response produced by the microbubbles increases up to 25 dB when changing the value of M from M=1 to M=15, for a 6-cycle burst.

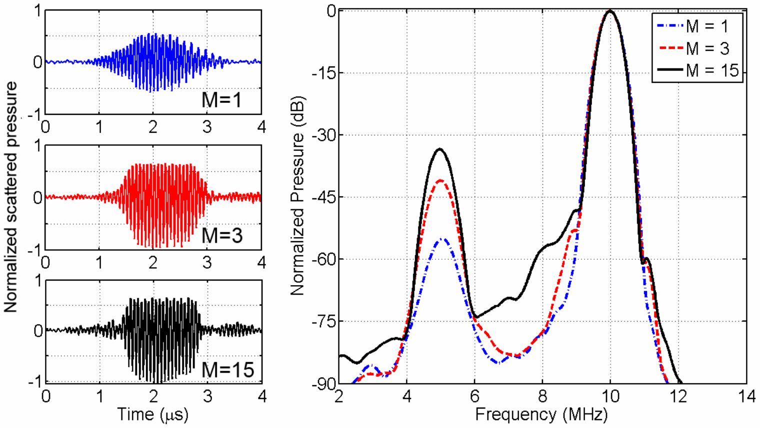

a b

Fig 6. a) Pressure signal scattered by the microbubbles excited by a 10 MHz, 50 kPa peak pressure burst with three different envelopes in time domain. b) The amplitude spectrum of the scattered signal from the microbubbles (average of 30 acquisitions in the frequency domain).

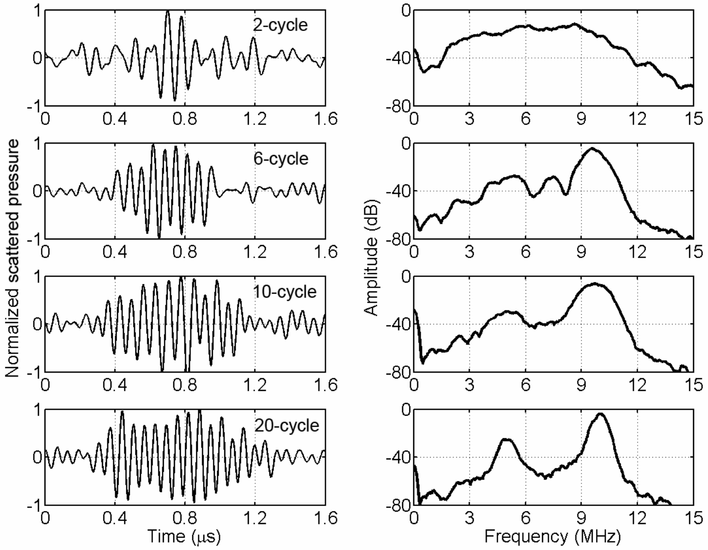

a b

Fig 7. a) Pressure signals scattered by the microbubbles excited by a 10 MHz burst with 2, 6, 10 and 20 cycles in time domain. b) Corresponding amplitude spectra (average of 30 acquisitions in frequency domain). All the pulses were modulated with a rectangular envelope (M=15) and the applied acoustic pressure peak amplitude is 50 kPa.

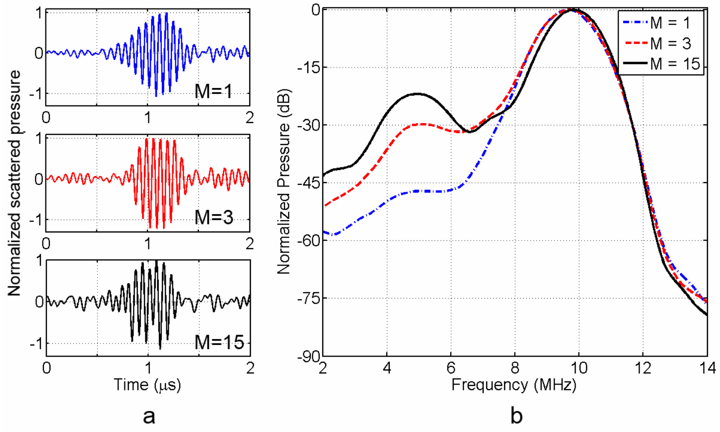

Fig 8. a) Pressure signal scattered by the microbubbles excited by a 6-cycle, 10 MHz, 50 kPa peak pressure burst with three different envelopes in time domain. b) The amplitude spectrum of the signal scattered from the microbubbles (average of 50 acquisitions in frequency domain).

Effect of acoustic pressure on the subharmonic emission of microbubbles

To see how the subharmonic response of the microbubbles is influenced by the incident pressure amplitude, a 6-cycle burst was transmitted with three different acoustic pressures of 50 kPa, 100 kPa and 150 kPa (peak negative). Fig. 9 shows the amplitude spectra of the scattered signals from the microbubbles averaged 30 times in the frequency domain. For a 50 kPa transmitted pressure, the increase in the subharmonic amplitude for M=15 compared with M equal to 1 and 3 is about 31 dB and 10 dB, respectively (Fig. 9a). Increasing the transmit pressure to 100 kPa decreases the enhancement of the subharmonic response with M=15 to 0 dB and 9 dB compared with M=3 and M=1, respectively (Fig. 9b). Rising the transmit pressure even higher to 150 kPa results in even less enhancement of the subharmonic response due to a rectangular envelope (M=15), -4 dB and 7 dB compared with M=3 and M=1, respectively (Fig. 9c). The other interesting point in this figure is the appearance of different low frequency components which are enhanced for a burst with a rectangular envelope. These peaks become more dominant when the transmit pressure is increased.

DISCUSSION

Effect of the self-demodulation signal on the subharmonic emission of microbubbles

The frequency content of S-D signal for different burst envelopes was derived according to the KZK equation (Eq. 4 & Fig. 2). For a 2 μs burst with a Gaussian envelope (M=1), the frequency content of the S-D signal is limited to the very low frequency and it appears as a clear peak around 0.75 MHz (Fig. 2c, M=1). This peak becomes broader by increasing M to 3 (Fig. 2c). Finally such a clear peak in the frequency domain disappears for an ultrasound burst with a rectangular envelope (Fig. 2c, M=15). The S-D signal for a rectangular envelope contains a large number of harmonics of the center frequency of the envelope (up to 30th harmonic for M=15). Although the S-D signal is not concentrated at a specific low frequency for a burst with a rectangular envelope, it has higher energy at half the transmit frequency ($\omega_0/2$) than for a Gaussian envelope. Our results including numerical simulations and *in vitro* experiments suggest that such a broad-band frequency content of the S-D signal acts as a stimulator which triggers enhanced subharmonic responses of microbubbles.

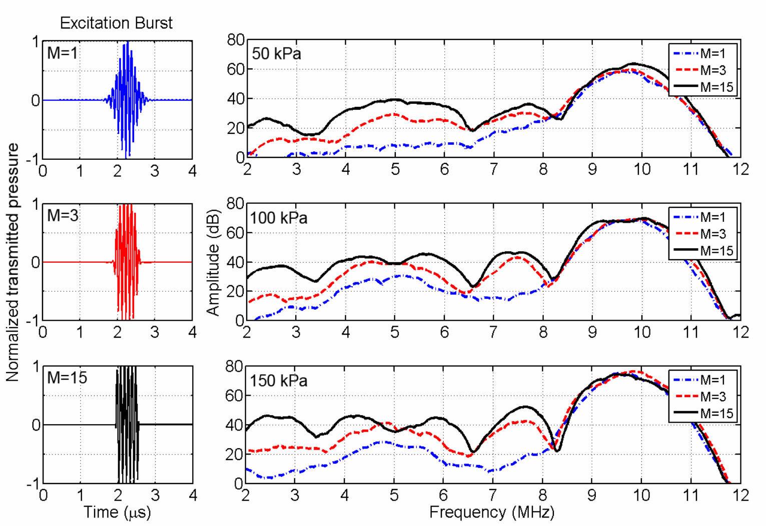

Fig 9. Amplitude spectra of the signals scattered from the microbubbles excited by a 6-cycle pulse with different envelopes at three acoustic pressure amplitudes of a) 50 kPa, b) 100 kPa and c) 150 kPa.

Simulation results (Fig. 3) show that the stimulation effect of the S-D signal on the subharmonic response of the microbubble is significant when the initial state of the microbubble is close to the buckling regime but not in the buckled state ($0.01<\sigma(R_0)<0.02$ N/m) and close to the rupturing regime ($0.05<\sigma(R_0)<0.07$ N/m) (Fig. 3). Far from the buckling regime ($0.02<\sigma(R_0)<0.05$ N/m), the microbubble exhibits no subharmonic oscillation and the S-D signal is not strong enough to "push" the bubble into that regime in the range of acoustic pressure investigated in this study (50-150 kPa). Also, when the bubble is already placed in the buckled state ($\sigma(R_0)=0$) the S-D signal does not enhance the subharmonic emission since it is already in its maximum level. However for intermediate state, the S-D signal in the burst with rectangular envelope has enough energy to "push" the bubble towards the buckling regime and increase the subharmonic response of the microbubble. The same reasoning applies for the bubbles close to their rupturing state. The enhancement of the subharmonic energy at $\sigma(R_0)=0.014$ N/m is depicted in Fig. 4. As can be seen the subharmonic response of a microbubble, thanks to the S-D signal, increases up to 23 dB by changing the burst envelope from Gaussian (M=1) to rectangular (M=15).

A microbubble with a diameter of 2 µm was chosen for the numerical simulation since it is reported as the mean diameter of BR14 UCA (Conversano *et al* 2010). The subharmonic resonance frequency of such a microbubble is around 5 MHz (chapter IV). Therefore the 10 MHz excitation bursts have a center frequency of twice the resonance frequency of the microbubble which is known to give the minimum threshold of subharmonic emission from the UCA (Katiyar *et al* 2011). Exciting the microbubbles at around twice their resonance frequencies results in the maximum amplitude of subharmonic signal. In such a condition the enhancement of the subharmonic response of UCA due to the S-D signal is more visible. Deviating from this excitation frequency decreases the amplitude of the subharmonic response and consequently the effect of the S-D will be less detectable. Such a limitation in using the subharmonic signal is less of a concern for *in vivo* applications because in the UCA solution usually there are enough microbubbles with desired radius for the applied frequency. However, choosing the appropriate frequency for the excitation burst or manipulating the size distribution of the UCAs can be beneficial when performing subharmonic imaging.

To validate experimentally the stimulating effect of the S-D signal on the subharmonic emission predicted by numerical simulations, scattering measurements were performed on a population of microbubbles. Experimental results (Fig. 6) showed that the subharmonic amplitude scattered by the UCA increases monotonically up to 22 dB by changing the burst envelope from Gaussian (M=1) to rectangular (M=15). These results are in excellent agreement with the simulations (Fig. 4). At this stage a quantitative comparison between the absolute subharmonic amplitude in the simulation and experiment is not possible since the initial surface tension $\sigma(R_0)$ as well as the size distribution of the microbubbles in the experiment is a priori not known.

The enhancement of the subharmonic emission because of the envelope of the pulse was also reported before (Zheng *et al* 2005, Biagi *et al* 2006, Masotti *et al* 2007, Zhang *et al* 2009). However, none provided a physical explanation for this observation. We believe that the stimulation effect of a burst having a rectangular envelope is due to its S-D signal as shown in Fig. 2. The enhancement in the subharmonic response of the UCA caused by the low frequency S-D signal is supported by numerical simulation and experiments performed in this study.

To see the effect of the S-D signal on the subharmonic emission for excitation bursts with similar rectangular envelopes, new sets of simulations were conducted at a peak negative pressure of 30 kPa and shown in Fig. 10. The S-D signal was filtered out using an 8th order Butterworth high pass filter with cutoff frequency of 9 MHz (Fig. 10a and b). The radial response of a 2 µm microbubble with initial surface tension of 0.014 (N/m) was calculated using the Marmottant model (Fig. 10c and d). It can be seen from the radial excursion of the microbubble in Fig. 10c that with the S-D signal the frequency becomes half (blue curve) of the one without S-D signal (red curve). The broadband low frequency S-D signal at the beginning of the excitation burst effectively stimulates the resonance of the microbubble and pushes it to the buckling regime. We believe such an effect results in much higher amplitude oscillation at subharmonic frequency even in response to the rest of the excitation signals which are identical in both bursts. The spectra of the radial response of the microbubble to these two excitation bursts shows 38 dB enhancement of the subharmonic response for the burst having the S-D signal compared with the one without the S-D signal (Fig. 10d).

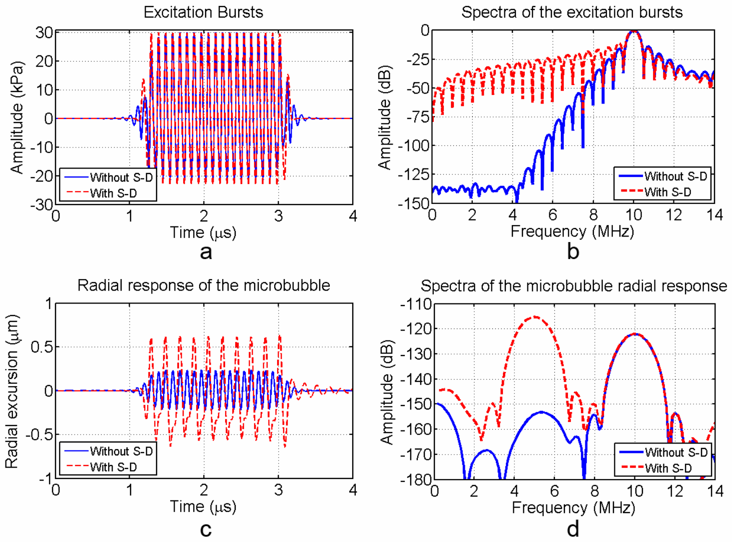

Fig 10. a) Excitation bursts with and without the S-D signal in time domain, b) Corresponding amplitude spectra of the excitation bursts, c) Radial response of the microbubbles in time domain, d) Corresponding amplitude spectra of the microbubble radial response. All the pulses were modulated with a rectangular envelope (M=15) and the applied acoustic pressure peak amplitude is 30 kPa. The microbubble has a diameter of 2 μm and the initial surface tension ($\sigma(R_0)$) of 0.014 N/m.

Effect of the excitation duration on the subharmonic emission of microbubbles

Short signals are more favored for imaging purposes since they provide a higher spatial resolution. However, with such signals, it is difficult to separate the subharmonic component from the fundamental component in the frequency domain (Fig. 7). The effect of the burst duration on the subharmonic response of the UCA for a rectangular envelope (M=15) is demonstrated. Rectangular envelope was chosen because it gives the maximum enhancement in the subharmonic emission (Fig. 6). It was reported before in chapter IV that the ratio between the subharmonic amplitude and the fundamental amplitude is independent from the excitation duration above three cycles. The same result was obtained in this study (Fig. 7). The excitation with only 2 cycles results in a very broad-band scattered signal with no distinguishable peak around the subharmonic frequency. Increasing the transmit burst durations to 6, 10 and 20 cycles results in the equal 22 dB ratio of the subharmonic amplitude to fundamental amplitude. However the enhancement of subharmonic emission due to the S-D signal is still evident for a shorter transmitting pulse consisting of 6 cycles (Fig. 8).

Effect of acoustic pressure on the subharmonic emission of microbubbles

The effect of acoustic pressure on the subharmonic enhancement stimulated by the S-D signal was also investigated in a separate experiment (Fig. 9). Three acoustic pressures of 50, 100 and 150 kPa were applied with a 6-cycle burst and three different envelopes. A 6-cycle burst was chosen since it provides a good compromise between the axial resolution and subharmonic peak separation in the frequency domain. Three different states have been observed for amplitude of the subharmonic response of UCAs by increasing the incident pressure (Eisenbrey *et al* 2011): First stage is the initial occurrence stage where the incident pressure surpasses the threshold level needed for subharmonic oscillation. Growth stage is the next one where the subharmonic amplitude increases with increasing the incident pressure. The third state is the saturation state where increasing the pressure of the excitation burst does not change the subharmonic amplitude. It can be seen in Fig. 9 that when the excitation burst has a Gaussian envelope (M=1) and a peak pressure of 50 kPa, no subharmonic signal is observed from the UCAs. However, increasing the incident pressure to 100 kPa results in 22 dB increase in the subharmonic signal above the noise level. Further increase in incident pressure to 150 kPa does not change the amplitude of the subharmonic response. This suggests that the saturation state has been already reached by 100 kPa incident pressure. For M=3, 50 kPa peak pressure has already passed the threshold level for subharmonic emission from the UCAs. Increasing the incident pressure to 100 kPa results in 10 dB increase in the subharmonic amplitude showing the growth state as well as reaching the saturation level since further increase in the incident pressure to 150 kPa does not change the amplitude of the subharmonic response of the microbubbles. However, for a burst with rectangular envelope (M=15) there is no growth state and the maximum subharmonic amplitude is reached by 50 kPa incident pressure. Instead, appearance of peaks in different frequencies is observed. We believe this is due to the broad-band low frequency S-D signal in the excitation burst with rectangular envelope triggering different bubbles with different sizes and therefore different resonance frequencies.

Practical implications for subharmonic imaging

The stimulation effect of the S-D signal on the subharmonic response of the UCA can be even more effective if combined with the conventional contrast imaging techniques such as pulse inversion. Excitation bursts with rectangular envelopes were used by Needles *et al* (2010) for subharmonic imaging together with pulse inversion resulting in 15 dB enhancement in contrast to tissue ratio compared with fundamental imaging. Such an increase in the subharmonic response of the microbubbles using waves with rectangular envelopes together with pulse inversion techniques can be explained by the stimulation effect of the S-D signal on the subharmonic emission.

Since the subharmonic response of the UCAs is strongly dependent on their initial surface tension, $\sigma(R_0)$, subharmonic imaging can be difficult for detecting a single bubble with an initial surface tension far from buckling or rupturing regime. However using an excitation burst with a rectangular envelope increases the range of the $\sigma(R_0)$ in which the subharmonic emission takes place.

Although the enhancement of the subharmonic response because of the S-D signal is significant, and high enough for subharmonic imaging the amplitude of the enhanced subharmonic signal is still 33 dB below the fundamental amplitude in our experiment (Fig. 7). This amplitude can be increased to improve the signal to noise ratio by adjusting the size distribution of the UCAs. Our simulation result in Fig. 4 shows that if the excitation fundamental frequency is twice the resonance frequency of the microbubbles, the amplitude of the subharmonic signal can be as high as the fundamental amplitude.

The S-D signal is developed during the nonlinear propagation of the acoustic wave in the medium, therefore it is scattered by UCA and also by tissue. However, for a low acoustic pressure (50 kPa) since the amplitude of the S-D signal is very low (around 0.2 kPa) the direct scattering of this signal by the tissue does not affect the contrast to tissue ratio. On the other hand, the enhancement of the subharmonic response of UCAs due to the S-D signal is considerably high (around 20 dB). Therefore optimizing the shape of the transmit signal in a way to have the maximum energy of the S-D signal at the subharmonic frequency, will always be beneficial in increasing signal scattered at the subharmonic frequency and subsequently the contrast to tissue ratio.

CONCLUSION

The low frequency self-demodulation acoustic signal resulting from nonlinear propagation of the ultrasound wave stimulates the subharmonic response of UCAs. The microbubbles are pushed towards the buckling or rupturing regimes by the self-demodulation signal resulting in enhanced subharmonic emission.

Acknowledgment-- This research was supported by the Center for Translational Molecular Medicine and the Netherlands Heart Foundation (PARISK).

References

Averkiou M, Lee Y S and hamilton M F 1993 Self-demodulation of amplitude- and frequency-modulated pulses in a thermoviscous fluid *J Acoust Soc Am* 94 2876-83

Averkiou M A and Hamilton M F 1997 Nonlinear distortion of short pulses radiated by plane and focused circular pistons *J Acoust Soc Am* 102 2539-48

Berktay H O 1965 Possible exploitation of non-linear acoustics in underwater transmitting applications *J sound vibration* 2 435-61

Biagi E, Breschi L, Vannacci E and Masotti L 2006 Subharmonic emissions from microbubbles: effect of the driving pulse shape *IEEE transactions on ultrasonics, ferroelectrics, and frequency control* 53 2174-82

Bouakaz A, Versluis M, Borsboom J and de Jong N 2007 Radial Modulation of Microbubbles for Ultrasound Contrast Imaging *IEEE transactions on ultrasonics, ferroelectrics, and frequency control* 54 2283-90

Callé S, Remenieras J P, Bou Matar O and Patat F 2002 Presence of nonlinear interference effects as a source of low frequency excitation force in vibro-acoustography *Ultrasonics* 40 873-8

Chen S, Kinnick R, Greenleaf J F and Fatemi M 2006 Difference frequency and its harmonic emitted by microbubbles under dual frequency excitation *Ultrasonics* 44 123-6

Chérin E, Brown J, Måsøy S E, Shariff H, Karshafian R, Williams R, Burns P N and Foster F S 2008 Radial modulation imaging of microbubble contrast agents at high frequency *Ultrasound Med Biol* 34 949-62

Conversano F, Franchini R, Casciaro S 2010 Characterization of microbubble contrast agents for echographic imaging through time-scheduled size distribution measurements *Sensors and Transducers J.* 9 21-27

Eisenbrey J R, Dave J K, Halldorsdottir V G, Merton D A, Machado P, Liu J B, Miller C, Gonzalez J M, Park S, Dianis S, Chalek C L, Thomenius K E, Brown D B, Navarro V and Forsberg F 2011 Simultaneous grayscale and subharmonic ultrasound imaging on a modified commercial scanner *Ultrasonics* 51 890-897

Feinstein S B 2004 The powerful microbubble: from bench to bedside, from intravascular indicator to therapeutic delivery system, and beyond *American journal of physiology* 287 450-7

Goertz D E, Frijlink M E, Tempel D, Bhagwandas V, Gisolf A, Krams R, de Jong N and van der Steen A F W 2007 Subharmonic Contrast Intravascular Ultrasound for Vasa Vasorum Imaging *Ultrasound Med. Biol.* 33 1859-72

Goertz D E, Frijlink M E, Tempel D, van Damme L C, Krams R, Schaar J A, Ten Cate F J, Serruys P W, de Jong N and van der Steen A F 2006 Contrast harmonic intravascular ultrasound: a feasibility study for vasa vasorum imaging *Investigative radiology* 41 631-8

Gorce J M, Arditi M and Schneider M 2000 Influence of bubble size distribution on the echogenicity of ultrasound contrast agents: a study of SonoVue *Investigative radiology* 35 661-71

Hamilton M F and Morfey C L eds 1998 *Model equations* vol 3 (San Diego: Nonlinear Acoustics Academic)

Katiyar A and Sarkar K 2011 Excitation thresholds for subharmonic response of ultrasound contrast microbubbles *POMA* 11 020003

Lee Y S and Hamilton M F 1995 Time-domain modeling of pulsed finite amplitude sound beams *J Acoust Soc Am* 97 906-17

Marmottant P, van der Meer S, Emmer M, Versluis M, de Jong N, Hilgenfeldt S and Lohse D 2005 A model for large amplitude oscillations of coated bubbles accounting for buckling and rupture *J. Acoust. Soc. Am.* 118 3499-505

Masotti L, Biagi E, Breschi L and Vannacci E 2007 Study and Characterization of Subharmonic Emissions by Using Shaped Ultrasonic Driving Pulse *Acoustical Imaging* 28 307-15

Masoy S E, Standal O, Nasholm P, Johansen T F, Angelsen B and Hansen R 2008 SURF imaging: in vivo demonstration of an ultrasound contrast agent detection technique *IEEE transactions on ultrasonics, ferroelectrics, and frequency control* 55 1112-21

Needles A, Arditi M, Rognin N G, Mehi J, Coulthard T, Bilan-Tracey C, Gaud E, Frinking P, Hirson D and Foster F S 2010 Nonlinear contrast imaging with an array based micro-ultrasound system *Ultrasound Med. Biol.* 36 2097-2106

Newhouse V L and Shankar P M 1984 bubble size measurements using the nonlinear mixing of two frequencies *J. Acoust. Soc. Am.* 75 1473-7

Raab D H and Green E H 1961 A cosine approximation to the normal distribution *Psychometrika* 26 447-50

Sarkar K, Shi W T, Chatterjee D and Forsberg F 2005 Characterization of ultrasound contrast microbubbles using in vitro experiments and viscous and viscoelastic interface models for encapsulation *J Acoust Soc Am* 118 539-50

Shankar P M, Krishna P D and Newhouse V L 1998 Advantages of subharmonic over second harmonic backscatter for contrast-to-tissue echo enhancement *Ultrasound in Medicine and Biology* 24 395-9

Shen C C, Cheng C H and Yeh C K 2011 Phase-dependent dual-frequency contrast imaging at sub-harmonic frequency *IEEE Trans. Ultrason. Ferroelectr. Freq. Control* 58 379 - 88

Shen C C, Wang Y C and Hsieh Y C 2007 Third harmonic transmit phasing for tissue harmonic generation *IEEE transactions on ultrasonics, ferroelectrics, and frequency control* 54 1370-81

Shi W T, Hoff L and Forsberg F 2002 Subharmonic performance of contrast microbubbles: an experimental and numerical investigation *Ultrasonics Symposium Proceedings* 2 1957-60

Sijl J, Dollet B, Overvelde M, Garbin V, Rozendal T, De Jong N, Lohse D and Versluis M 2010 Subharmonic behavior of phospholipid-coated ultrasound contrast agent microbubbles *J. Acoust. Soc. Am.* 128 3239-52

Vos H J, Goertz D E and de Jong N 2010 Self-demodulation of high-frequency ultrasound *J Acoust Soc Am* 127 1208-17

Vos H J, Goertz D E, van der Steen A F W and de Jong N 2011 Parametric array technique for microbubble excitation *IEEE transactions on ultrasonics, ferroelectrics, and frequency control* 58 924-34

Wu C Y and Tsao J 2003 The ultrasonic weak short-pulse responses of microbubbles based on a two-frequency approximation *J Acoust Soc Am* 114 2662-71

Yeh C K, Su S Y and Shen C C 2009 Dual high-frequency difference excitation on ultrasound contrast agents destruction *IEEE transactions on ultrasonics, ferroelectrics, and frequency control* 56 1113-8

Yeh C K, Su S Y, Shen C C and Li M L 2008 Dual high-frequency difference excitation for contrast detection *IEEE transactions on ultrasonics, ferroelectrics, and frequency control* 55 2164-76

Zhang D, Gong Y, Gong X, Liu Z, Tan K and Zheng H 2007 Enhancement of subharmonic emission from encapsulated microbubbles by using a chirp excitation technique *Physics in medicine and biology* 52 5531-44

Zhang D, Xi X, Zhang Z, Gong X, Chen G and Wu J 2009 A dual-frequency excitation technique for enhancing the sub-harmonic emission from encapsulated microbubbles *Physics in medicine and biology* 54 4257-72

Zheng H, Mukdadi O, Kim H, Hertzberg J R and Shandas R 2005 Advantages in using multifrequency excitation of contrast microbubbles for enhancing echo particle image velocimetry techniques: initial numerical studies using rectangular and triangular waves *Ultrasound Med Biol* 31 99-108

Chapter IX

Second harmonic inversion for ultrasound contrast harmonic imaging

Mirza Pasovic, Mike Danilouchkine, Telli Faez, Paul L M J van Neer, Christian Cachard, Antonius F W van der Steen, Olivier Basset, Nico de Jong

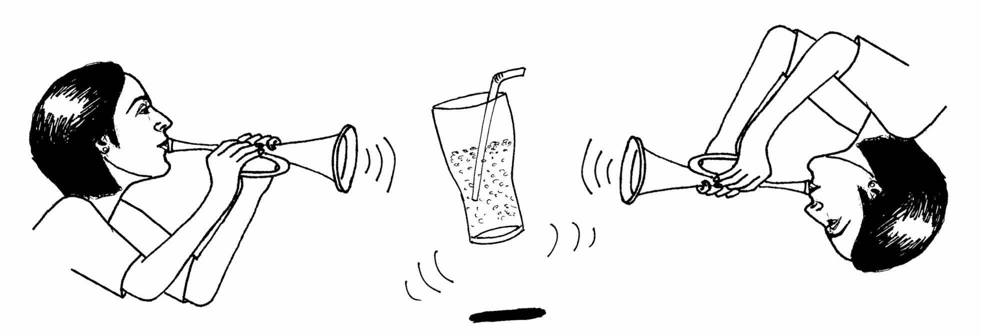

Published in Physics in Medicine and Biology May 4, 2011

Abstract

In past years several techniques have been proposed to detect or image harmonics produced by UCAs. In these proposed works, the harmonics generated in the medium during the propagation of the ultrasound wave played an important role, since these harmonics compete with the harmonics generated by the micro-bubbles. We present a method for the reduction of the second harmonic generated during nonlinear-propagation-dubbed second harmonic inversion (SHI). A general expression for the suppression signals is also derived. The SHI technique uses two pulses, *p*' and *p*", of the same frequency f_0 and the same amplitude P_0 to cancel out the second harmonic generated by nonlinearities of the medium. Simulations show that the second harmonic is reduced by 40 dB on a large axial range. Experimental SHI B-mode images, from a tissue-mimicking phantom and UCAs, show an improvement in the agent-to-tissue ratio (ATR) of 20 dB compared to standard second harmonic imaging and 13 dB of improvement in harmonic power Doppler.

INTRODUCTION

It was shown in previous chapters (IV, V and VI) that UCAs vibrate asymmetrically. As a consequence, the generated back-scattered echo is enriched with higher harmonics, which could be used for detection and to create an ultrasound image. On the other hand, ultrasound propagation itself is inherently a nonlinear process (Aanonsen *et al* 1984). For second harmonic imaging this is an undesirable effect, since then the harmonics generated by the bubbles have to compete with the harmonics generated by the tissue. A quantitative measure of discrimination between harmonic components produced by the UCA and tissue is expressed through the ATR (de Jong *et al* 2000, Bouakaz *et al* 2002)

$$ATR_n = 20.\log\left(\frac{P_n^{UCA}}{P_n^{tis}}\right) \qquad (1)$$

where P_n^{UCA} and P_n^{tis} are the back-scattered echo generated by the UCA and tissue at the *n*th harmonic, respectively. From Eq. 1 it is clear that ATR_2 (agent-to-tissue ratio at the second harmonic) increases by reducing the amount of the second harmonic generated by the tissue $\left(P_2^{tis}\right)$, while at the same time preserving the second harmonic pressure produced by UCAs in the back-scattered echo $\left(P_2^{UCA}\right)$. Most methods for reducing P_2^{tis} reported in the literature use some sort of source pre-biasing. The main difference between these techniques is how a source pre-biasing signal is computed. One of the first source pre-biasing methods was reported by Krishnan and O'Donnell (1996) and was intended to improve the ATR_2 by suppressing signals transmitted by the transducer at the second harmonic frequency. The method worked by applying an extra delay on alternate transmit elements equivalent to a π phase shift at the second harmonic frequency. Only simulation results were presented—the method improved the ATR_2 by 1.5 dB.

Same authors also presented the harmonic cancellation scheme (Krishnan *et al* 1998) which worked by first using a nonlinear wave propagation model to predict the waveform at the focus. Then, the second harmonic was filtered out and linearly back-propagated to the surface of the transducer. Finally, the source pre-biasing signal was obtained by inverting the obtained second harmonic signal and mixing it with the original imaging pulse. Christopher (1999) improved the aforementioned method by using a nonlinear wave propagation scheme for both forward- and backward-propagation. In a recent work, Krishnan and Thomenius (2008) used linear forward-propagation and nonlinear backpropagation to obtain a source pre-biased signal. The results reported in these contributions show a great promise for harmonic tissue suppression, as they maximize the suppression by fully controlling the parameters of the imaging protocol. However, disadvantages of these methods are that the tissue second harmonic is reduced over a narrow frequency band and on a limited section of the axial field. Recent work by Pasovic *et al* (2010) alleviates these drawbacks through the definition of a multiple-frequency component second harmonic pre-biasing signal. A slightly different approach was proposed by Shen *et al* (2007) and consisted of simultaneously transmitting a fundamental and a phase-shifted third harmonic component. In this case, the propagating wave will contain two extra spectral components equal to the sum and difference of the emitted signal frequencies. The difference component is used for the cancellation of the tissue harmonic response. The aforementioned method is promising but does require a transducer with a larger broadband (at −6 dB bandwidth> 100%) for its implementation. Currently, only the experimental transducers with interleaved high- and low-frequency elements are available (Bouakaz *et al* 2004, van Neer *et al* 2010).

An alternative method to improve the ATR_2 by reducing P_2^{tis} was introduced by Shen and Hsieh (2008), who proposed to use the harmonic leakage signal to generate the second harmonic reduction signal. The imaging protocol was based on a constant phase shift between the emitted fundamental pulse and the leakage signal. The amplitude and phase of the imaging pulse were adjusted for the maximum suppression of P_2^{tis} and resulted in an ATR_2 improvement of 5 dB.

Another approach for increasing the ATR_2 combines the well-known pulse-inversion technique (Chapman and Lazenby 1997, Jiang *et al* 1998) with a time-reversal method (Couture *et al* 2008). Pulse inversion works by successively transmitting two pulses: after the echo of *p*' (first pulse) is received and stored in the memory of the ultrasound scanner, a second pulse is transmitted as the phase-inverted replica of the first one, $p'' = -p'$. The two echoes are *a posteriori* summed to form a virtual echo *p*. The resulting sum exhibits no odd harmonics, while amplitudes of even harmonics are doubled. To reduce P_2^{tis}, Couture *et al* (2008) investigated a time-reversal approach for transmitting *p*' and *p*" based on the temporal invariance of the nonlinear wave equation (Tanter *et al* 2000). The method works as follows: the back-scattered echoes of *p*' and *p*" are stored in the scanner memory, time inverted and then used as excitation signals. Finally, the received echoes of the emitted time-inverted signals are summed to create an ultrasound image. The presented *in vitro* phantom images were obtained using the method which showed a reduction of P_2^{tis} by 10 dB compared to regular pulse-inversion imaging. However, the reduction of P_2^{tis} is optimized for a small region of tissue only, as the stored echoes of the back-scattered signals are obtained using pulse-echo wire reflections.

In contrast to previously discussed methods, harmonic power Doppler (HPD) (Burns *et al* 1994, Becher *et al* 1997) enhances the echoes of micro-bubbles $\left(P_2^{UCA}\right)$. The method uses power Doppler processing on the second harmonic of the received echo rather on the fundamental component. As a consequence, clutter and flash artifacts are reduced. Eckersley *et al* (2005) describe a combination of pulse inversion and amplitude modulation where the second pulse has been inverted and 50% lower amplitude than the first pulse $p'' = -0.5p'$. Using this method, the ATR increases by 6 dB compared to the conventional pulse-inversion technique.

Our technique is called the second harmonic inversion (SHI) and is based on the successive transmission of two pulses p' and p''. We show in simulations and experiments that by using the known properties of ultrasound propagation, using two pulses of equal frequency and amplitude but with different initial phases, one can substantially reduce the second harmonic.

THEORY

It is assumed that the shape of the transmitted ultrasound wave (i.e. the time dependence of the wave at a given distance from the source) changes slowly with the increasing distance. The assumption of slow change implies that the wave needs to travel many wavelengths to undergo substantial distortion caused by nonlinearities of the medium (Enflo and Hedberg 2002). To describe plane wave propagation under the aforementioned conditions, a lossless Burgers equation (Burgers 1948) for a non-viscous homogeneous medium can be used:

$$\frac{\partial p}{\partial z} = \frac{\beta p}{\rho_0 c_0^3}\frac{\partial p}{\partial \tau} \qquad (2)$$

In Eq. 2, p is the propagating pressure wave, c_0 is the speed of sound, β is the nonlinearity coefficient of the medium, ρ_0 is the density of the medium, z is the propagating direction and $\tau = t - z/c_0$ is the delayed time. Then, let the transmitted ultrasound wave, at the surface of transducer ($z = 0$), be expressed as

$$p(z = 0, t) = P_0 \cdot \sin(2\pi f_0 \cdot t + \phi) \qquad (3)$$

where t is the time, P_0 is the amplitude of the transmitted pressure at $z = 0$, f_0 is the fundamental frequency and ϕ is the initial phase. Fubini (1935) provided a solution of the Burger equation using Bessel functions to calculate the pressure disturbance at an arbitrary given distance z_1:

$$p(z_1,t) = P_0 \sum_{n=1}^{\infty} \frac{2}{n l_D} J_n(n l_D)\sin(n(2\pi f_0 .t + \varphi)) \qquad (4)$$

where J_n is the Bessel function of first kind and l_D is the normalized dimensionless propagation distance:

$$l_D = \frac{2\pi f_0 . P_0}{\rho_0 c_0^3} . z_1 \qquad (5)$$

Note that l_D depends on the amplitude and frequency (P_0 and f_0) of the transmitted wave, on the physical properties of the investigated medium (speed of sound c_0 and density ρ_0) and the propagating distance z_1.

METHOD

We propose using two successive transmissions to achieve the cancellation of the second harmonic. The following conditions are considered. First, the two emitted waves must have the same fundamental frequency f_0, so that the generated second harmonic frequencies are the same. Second, in order for the two pulses to generate the pressure with same amplitudes at second harmonic, *p'* and *p"* must be transmitted by the source with identical amplitudes P_0. Hence, only the initial phases of transmitted pulses are considered as the parameter with the potential for reducing the second harmonic *a posteriori*. Thus, at source ($z = 0$) the two pulses *p'* and *p"* are defined as

$$P'(z = 0, t) = P_0 \cdot \sin(2\pi f_0 \cdot t + \phi') \qquad (6)$$

$$P''(z = 0, t) = P_0 \cdot \sin(2\pi f_0 \cdot t + (\phi' + \phi'')) \qquad (7)$$

Note that *p'* and *p"* differ only by a phase difference ϕ''.

After propagating in the medium to some distance z_1 the two pulses will undergo harmonic distortion as described by (4)

$$p'(z_1, t) = P_0 \sum_{n=1}^{\infty} \frac{2}{nl_D} J_n(nl_D) \sin(n(2\pi f_0 . t + \varphi')) \quad (8)$$

$$p''(z_1, t) = P_0 \sum_{n=1}^{\infty} \frac{2}{nl_D} J_n(nl_D) \sin(n(2\pi f_0 . t + (\varphi' + \varphi''))) \quad (9)$$

Now a virtual pressure $p(z_1, t)$ that consists in the sum of (8) and (9) can be formed as

$$p(z_1, t) = P_0 \sum_{n=1}^{\infty} \frac{2}{nl_D} J_n(nl_D) . [\sin(n(2\pi f_0 . t + \varphi')) + \sin(n(2\pi f_0 . t + (\varphi' + \varphi'')))]$$

(10)

Using trigonometric properties, (10) can be rewritten as:

$$p(z_1, t) = 4P_0 \sum_{n=1}^{\infty} \frac{J_n(nl_D)}{nl_D} \sin\left(n . \left(2\pi f_0 . t + \varphi' + \frac{\varphi''}{2}\right)\right) \cos\left(\frac{n\varphi''}{2}\right) \quad (11)$$

Expression (11) contains three parts. First is the fraction $\frac{J_n(nl_D)}{nl_D}$, which is always non-zero for every *n*th harmonic as the propagation distance increases. The second part is the sin$(\cdots)$ and it describes the temporal evolution of the particular nth harmonic at distance z_1. For our aim, most interesting is the third part $\cos\left(\frac{n\varphi''}{2}\right)$ from which it follows that the amplitude of every nth harmonic doubles if

$$\varphi'' = \frac{2\pi}{n} \quad (12)$$

and every nth harmonic is zero when

$$\varphi'' = \frac{\pi}{n} \quad (13)$$

From (12) and (13), it can be noted that the cancellation or increase of one particular nth harmonic does not depend on the medium or the propagation distance, but on the phase difference between p' and p'', provided they have the same fundamental frequency f_0 and the same amplitude P_0 at the source z = 0. When the second harmonic cancellation is desired, Eq. 13 gives ϕ'' = $\pi/2$. Fundamental frequencies of p' and p'' are then in the quadrature phase and do not cancel each other. On the other hand, the generated second harmonics are phase shifted by π and summing those results in cancellation.

SIMULATION RESULTS

To simulate nonlinear propagation of the ultrasound wave, the KZK equation is used. The KZK equation for a rectangular transducer is given by

$$\frac{\partial p}{\partial z} = \frac{c_0}{2}\int_{-\infty}^{\tau}\left(\frac{\partial^2 p}{\partial x^2} + \frac{\partial^2 p}{\partial y^2}\right)dt + \frac{D}{2c_0^3}\frac{\partial^2 p}{\partial \tau} + \frac{\beta}{2\rho_0 c_0^3}\frac{\partial p^2}{\partial \tau} \quad (14)$$

In this study Eq. 14 was solved using the finite difference method (Voormolen 2007). The diffraction due to the finite size of the transducer in the xy-plane (perpendicular to the propagation direction) is described by the first term on the right-hand side of (14). The second and the third terms on the right-hand side of (14) account for the absorption and nonlinearity of the medium, whose properties were set to match those of water at 20° (density ρ_0 = 998.3 kg/m^3, nonlinear parameter β = 3.5, small amplitude pressure ultrasound speed c_0 = 1487 m/s). The ultrasound transducer geometry was set equal to an actual ultrasound cardiac transducer: number of elements 64, height 12.5 mm, pitch 310 μm and elevation focus 70 mm. The focal distance in the transmission was d = 70 mm.

The two pulses p' and p'' at z = 0 were defined as sine bursts with a center frequency f_0 = 1.5 MHz, an amplitude P_0 = 400 kPa, 3 cycles long with a Gaussian envelope and initial phases set to ϕ' = 0 and ϕ'' = $\pi/2$. Figure 1 shows the resulting pulses after they have reached the focal spot d = 70 mm. The phase shift of $\pi/2$ between two pulses is clearly visible. Furthermore, the shape distortion as a consequence of the nonlinear propagation is noticeable.

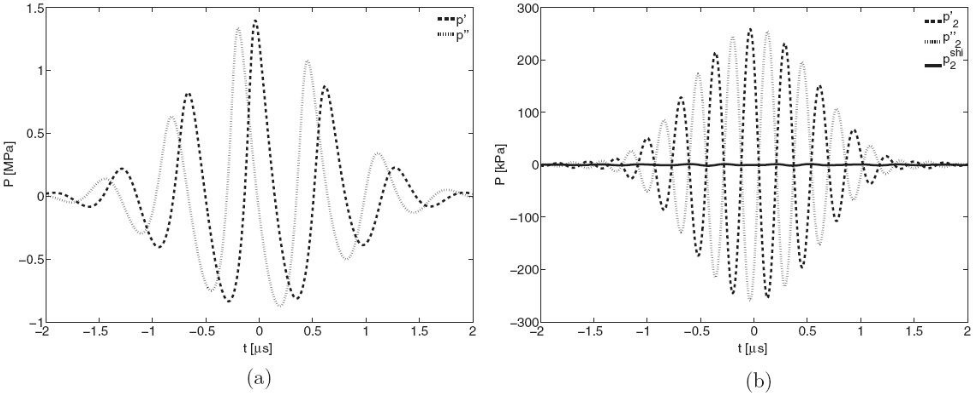

Fig 1. The simulated pulses *p'* and *p"* and their sum p^{shi} at the focal spot. a) Pulses *p'* and *p"* at the focal spot. b) The filtered second harmonics of p_2' and p_2'' and their sum p_2^{shi}.

From both pulses the second harmonic was filtered using the fifth-order Butterworth bandpass filter with cut-off frequencies f_{c1} = 2.4MHz and f_{c2} = 3.6 MHz. (This filter has been used throughout this study unless specified otherwise.) Figure 1b shows the two second harmonics p_2' and p_2'' (dashed and dotted lines, respectively). Note that the second harmonics are inverted (opposite) to each other; hence, the method is named *second harmonic inversion*. In the case of standard pulse inversion (phase difference between *p'* and *p"* is π), the odd harmonics (fundamental) are opposite. So for SHI, summing p_2' and p_2'' results in the second harmonic amplitude of p_2^{shi} (full line) 2 kPa, while separately each harmonic had a pressure amplitude of 260 kPa.

The influence of different pressure amplitudes emitted from the source

The amplitude of the second harmonic generated during propagation increases when the initial pressure P_0 is higher. We have investigated the reduction of the second harmonic for the initial pressures of *p'* and *p"* between P_0 = 50 kPa and 500 kPa, respectively, in step of 50 kPa.

For each setting of P_0, the pulses *p'* and *p"* were propagated until the focal spot *d* = 70 mm and then filtered to get the second harmonic component. The results are depicted in figure 2a. The left panel shows the absolute amplitude of the second harmonic for increasing source pressure. The second harmonic amplitude is close to 400 kPa for a source pressure of 500 kPa. Of course, the amplitudes of the generated second harmonics are equal for the two initial phases of the emitted signal—the dotted line (p_2') and dashed line (p_2'') overlap. The full line presents the filtered second harmonic p_2^{shi} after summation of two pulses. The maximum amplitude of p_2^{shi} is 4 kPa, and it can be concluded as independent of the source pressure. Figure 2b shows the normalized second harmonic relative to the fundamental in dB. The second harmonic of the propagating signal is approximately −30 dB for lower excitation pressures. With increasing P_0 the second harmonic raises to −13 dB. However, by applying the SHI scheme to the propagating signals the resulting second harmonic is reduced by about 40 dB.

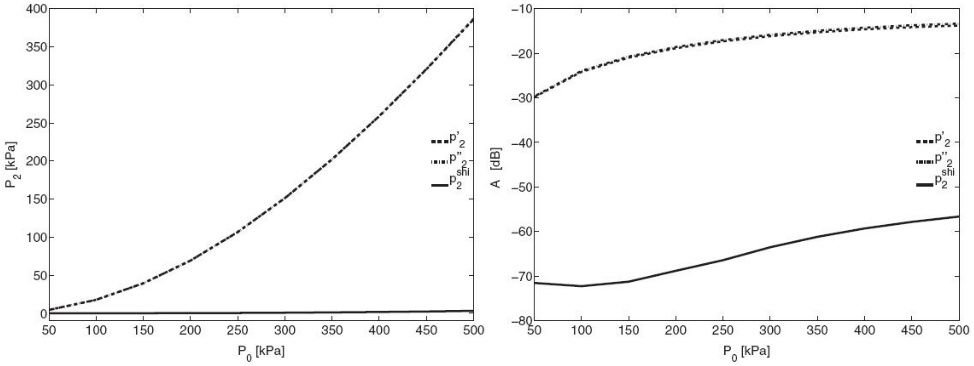

(a) (b)

Fig 2. The simulated maximum of the second harmonic of p' and p'' and their sum p^{shi} versus P_0 at the focal spot ($d = 70$ mm). a) Absolute second harmonic. b) Second harmonic normalized to the fundamental.

The ability of the SHI technique to reduce broadbanded and narrowbanded signals

The SHI method for reducing the second harmonic was further investigated for the narrowbanded and broadbanded signals. The amplitude and frequency of the emitted pulses p' and p'' were set to $P_0 = 500$ kPa and $f_0 = 1.5$ MHz. The bandwidth of the pulses was manipulated by emitting the different number of cycles. Note that in the present study the bandwidth is defined as the level of −20 dB below the maximum at second harmonic, which is in accordance with previous works (Shen and Li 2001, Pasovic *et al* 2010).

Figure 3 presents the normalized amplitude spectrum of p' and p'' (dotted and dashed lines) at the focal spot. A narrowbanded signal (figure 3a) consisted of ten cycles; while broadbanded signals had three cycles (figure 3b). The two horizontal lines present the maximum second harmonic value and −20 dB limit. The two vertical lines are the lower and upper limits of the second harmonic band (f_{c1} and f_{c2}). Note that for the two cases the limiting frequencies are not the same. The full line from figure 3 is the amplitude spectrum of the sum of the two signals. In both cases, the SHI method was able to reduce the amplitude of the second harmonic throughout the whole defined band.

Simulated axial profile

Ultrasound images provide information on a large axial range and not in one single spot. For that reason we investigated SHI as a function of the axial distance from $z = 0$ until $z = 130$ mm. The used pressure pulses had amplitude at transducer surface P_0 = 350 kPa, frequency f_0 = 1.5 MHz, were 3 cycles long, Gaussian apodizated with initial phases set to $\phi' = 0$ and $\phi'' = \pi/2$. In the near field, the steps of pressure calculation were shorter, so that near-field variations can be well approximated. At each point, the second harmonic was filtered.

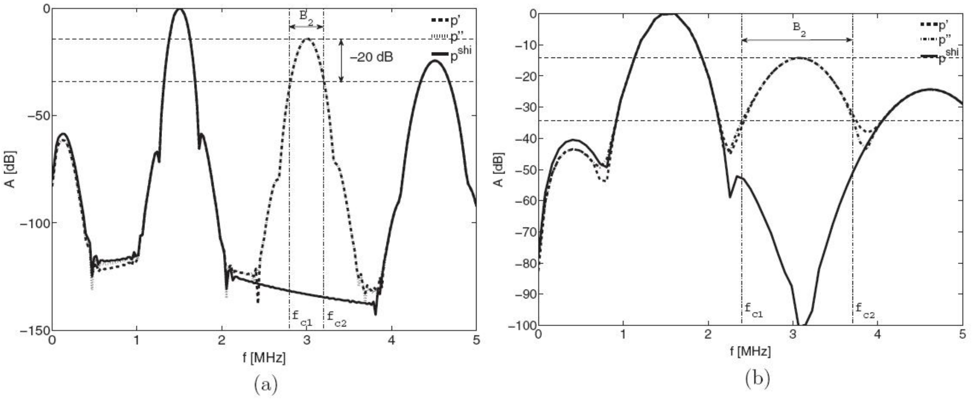

Fig 3. Simulated amplitude spectra of *p'* and *p"* and their sum p^{shi}, after propagation through water, with a different number of cycles versus frequency. a) Amplitude spectrum of a 10 cycle burst. b) Amplitude spectrum of a 3 cycle burst.

Figure 4 shows the maximum amplitude of the second harmonics p_2', p_2'' and p_2^{shi} as a function of the axial distance. Close to the source, the second harmonic is not present. The generated second harmonic increases with the propagation distance and reaches the peak value of 260 kPa (−13 dB) just before the focal spot. After the focal spot, the harmonic amplitude gradually decreases. This behavior can be observed for the second harmonics of both the pulses (dashed and dotted lines overlap). The full line represents the second harmonic component after applying the SHI method, which is below 2 kPa (−60 dB) over the entire axial range.

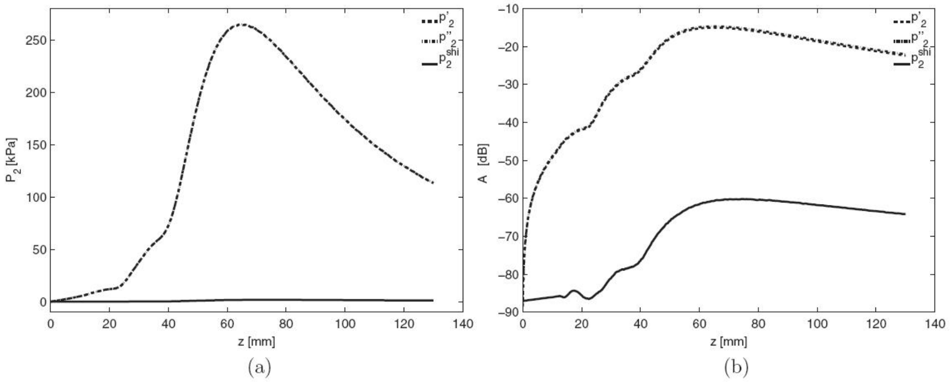

Fig 4. Simulated axial profiles of the second harmonics generated by *p'* and *p"* and their sum p^{shi}. a) Absolute axial second harmonic profiles. b) Axial second harmonic profiles normalized to their fundamental.

EXPERIMENTAL MEASUREMENTS

The simulation results were corroborated by water-tank experiments. Figure 5 shows an experimental setup used to perform hydrophone measurements. An ultrasound scanner (OPEN System, LeCoeur Electronique, Chuelles, France (Vignon *et al* 2005)), which offers the possibility of programming an arbitrary excitation signal (frequency, phase amplitude, envelope) of each element separately, was used to drive a cardiac ultrasound transducer (Vingmed 2.5 FPA, KG100001, General Electric Co., OH, USA, 64 elements, height 12.5 mm, width of element 230 μm and k_{erf} = 80μm). The ultrasound probe was mounted on the side of a water tank. A hydrophone was placed in a holder of *xyz*-system, which was used to precisely maneuver the hydrophone into the focal spot (d = 70 mm). The hydrophone was then connected to the LeCroy oscilloscope (9400A, LeCroy, Geneva, Switzerland), where the acquired signals were sampled with the sampling frequency f_s = 100 MHz and digitalized with an 8 bit digitizer. The GPIB bus was used to upload the signals to a computer for storage and post-processing.

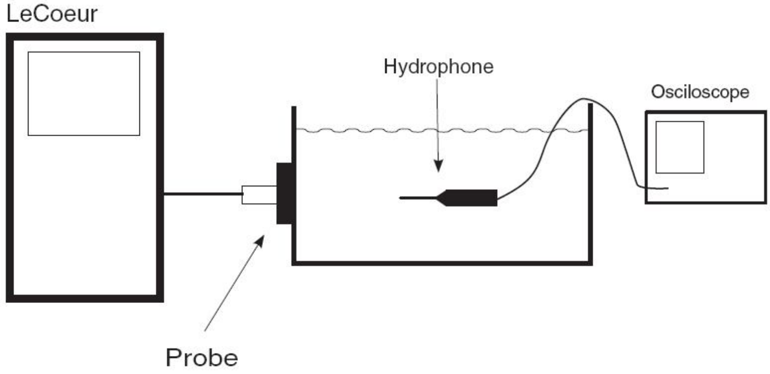

Fig 5. Schematic view of the experimental setup.

Figure 6a shows pulses *p'* (dotted line) and *p"* (dashed line) acquired with a hydrophone. The transmitted signals were Gaussian-apodized sine bursts 3 cycles in length and f_0 = 1.5 MHz. Using a fifth-order bandpass Butterworth filter, the second harmonics p_2' and p_2'' were filtered and are depicted in figure 6b. The π phase shift between p_2' and p_2'' is clearly notable. Separately each pulse generates the second harmonic with amplitude over 230 kPa. After summing p_2' and p_2'', the resulting second harmonic p_2^{shi} (full line) drops to about 12 kPa (-26 dB).

Dependence on the acoustic pressure

Figure 7a shows the second harmonics (p_2' and p_2'') of the emitted pulses *p'* and *p"* and the resulting p_2^{shi} as a function of P_0, the acoustic pressure on the surface of the transducer. The frequency of the transmitted signals *p'* and *p"* was f_0 = 1.5 MHz with each signal 3 cycles long and Gaussian envelope apodized. As expected, with increasing P_0 also the amount of generated second harmonic increases. For both pulses, the increase of the second harmonic is the same. However, after applying the SHI method the amplitude of the resulting second harmonic is below 20 kPa in all cases (full line). Figure 7b presents the second harmonic in dB, normalized to the fundamental. For *low* pressures the reduction is ≈3 dB, For increasing P_0, the amount of the generated second harmonic increases and as a consequence the overall reduction is higher (≈20 dB for $P_0 > 200$ kPa).

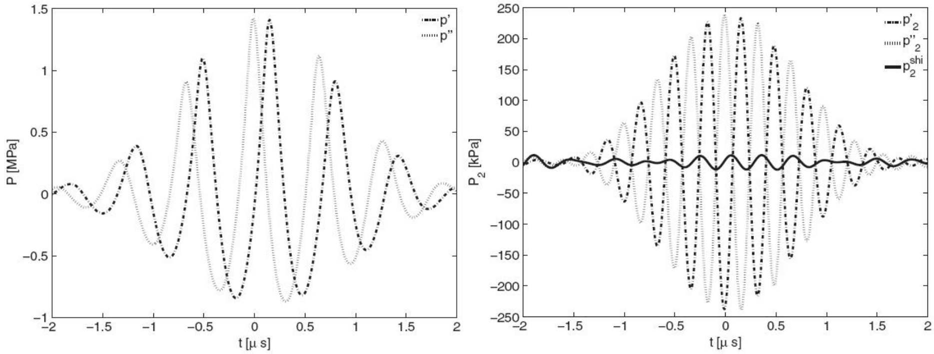

(a) (b)

Fig 6. The pulses *p'* and *p"* and their sum p^{shi}, as measured at the focal spot using a hydrophone setup in a water tank. a) Pulses *p'* and *p"* at the focal spot. b) The filtered second harmonics of p_2' and p_2'' and their sum p_2^{shi}.

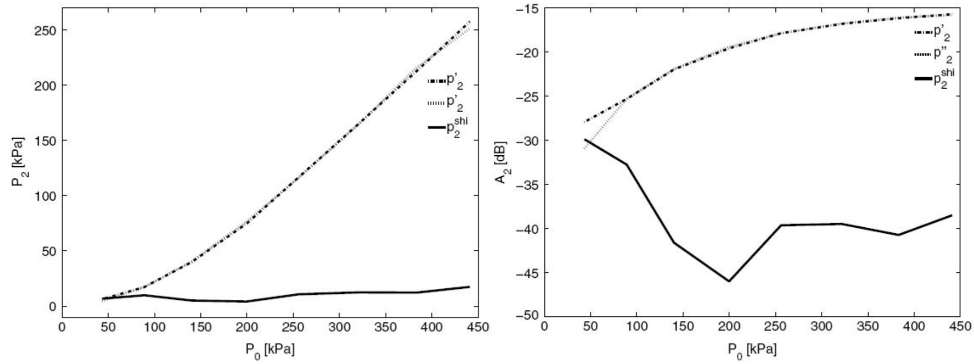

(a) (b)

Fig 7. The maxima of the second harmonic of *p'* and *p"* and their sum p^{shi} versus P_0, as measured at the focal spot using a hydrophone setup in a water tank. a) Absolute second harmonic. b) Second harmonic normalized to the fundamental.

Dependence on the bandwidth

The focal spot, where a hydrophone was placed, was set to $d = 70$ mm. The signals *p'* and *p"* were: $f_0 = 1.5$ MHz, $P_0 = 350$ kPa, $\phi' = 0$, $\phi'' = \pi/2$ with a Gaussian envelope. Figure 8 shows the amplitude spectrum when the excitation signals *p'* and *p"* were ten (figure 8a) and three (figure 8b) cycles long. Both pulses *p'* and *p"*, whether narrowbanded or broadbanded, generated the same amount of second harmonic, −15 dB normalized to the fundamental. After applying SHI, the reduced p_2^{shi} barely exceeds the −40 dB level around the second harmonic.

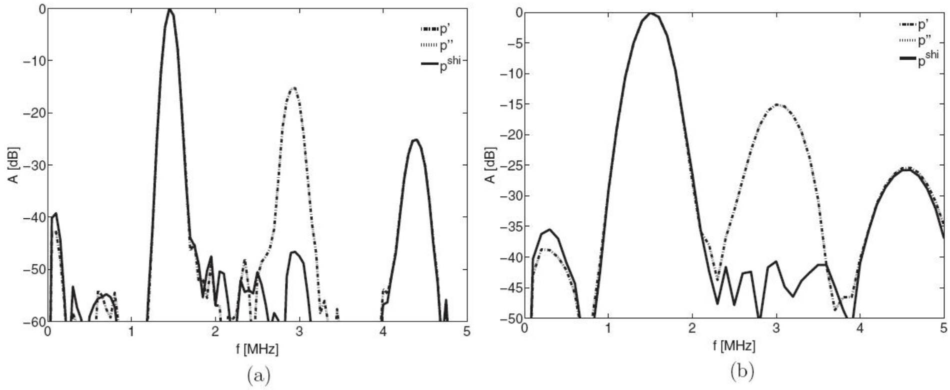

Fig 8. Amplitude spectra of *p'* and *p"* and their sum p^{shi} with a different number of cycles versus frequency, as measured at the focal spot using a hydrophone setup in a water tank. a) Amplitude spectrum of a 10 cycle burst. b) Amplitude spectrum of a 3 cycle burst.

Measured axial profile

The axial profile was measured with a hydrophone in a 3D *xyz*-system from $z = 10$ to 130 mm. The hydrophone was moved in step $z = 1$ mm. The signal was averaged from 30 acquisitions. From the resulting acquisitions, the second harmonic was filtered using the bandpass Butterworth filter of fifth-order with the cutoff frequencies $f_{c1} = 2.4$ and 3.6 MHz. Results of figure 9a show the maximum amplitude of the second harmonic at each step in absolute values, whereas figure 9b shows the second harmonic normalized to the fundamental in the focal spot.

Near the transducer surface ($z < 30$ mm, near field), *p'* and *p"* hardly generate a significant second harmonic; thus, it is hard to see any reduction in this region. As the wave further propagates, p_2' and p_2'' sharply increase and reach the maximum value of 250 kPa. The full line presents the resulting second harmonic after applying the SHI scheme. In this case, p_2^{shi} is only about 20 kPa throughout the whole axial extent. It can be noted that the second harmonic is reduced by 10 dB already at the axial distance $z = 30$ mm and by 20 dB for $z > 40$ mm. Actually on the entire axial range, the amplitude of the second harmonic as a result of the SHI scheme is always better than 35 dB compared to the fundamental.

Phantom imaging

The imaging setup is shown in figure 10. The tissue-mimicking phantom was designed as presented by Teirlinck *et al* (1998). After preparation the phantom was cut in two pieces. Since during the preparation the homogeneity of the phantom was not compromised, it can be assumed that the two parts have the same characteristics. In the next step, the two parts were placed at the bottom of a water tank, separated by 2 cm. This was done so that the UCAs (Definity©, Lantheus Medical Imaging, MA01862, USA), diluted to the concentration of 10^5 micro-bubbles/ml, could easily be administrated. During the acquisition of the ultrasound images, the solution with UCAs was constantly stirred to maintain a uniform distribution of the micro-bubbles.

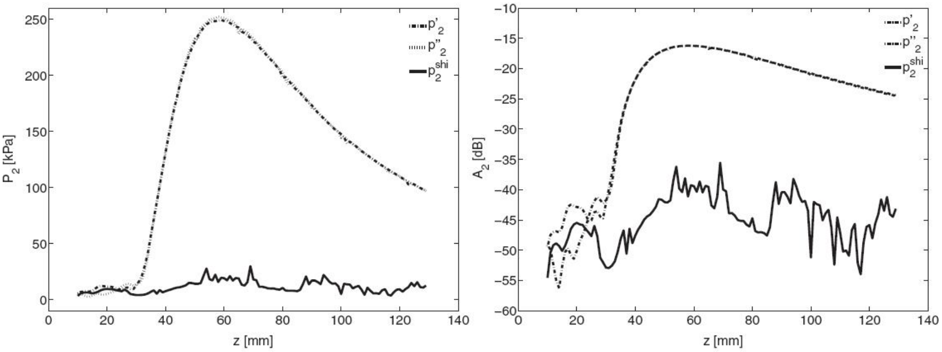

(a) (b)

Fig 9. Axial profiles of the second harmonics generated by *p'* and *p"* and their sum p^{shi}, as measured using a hydrophone setup in a water tank. a) Absolute axial second harmonic profiles. b) Axial second harmonic profiles normalized to their fundamental.

The ultrasound probe was connected to a LeCoeur open scanning system and excited with the sine burst of three cycles with the fundamental frequency f_0 = 1.5MHz and Gaussian envelope. Altogether, 50 frames were acquired. Each frame was made up of 60 scanning lines, with the scanning angle $a = 60^\circ$. The red region in figure 10 shows where SHI was implemented. After the back-scattered echo of the first shot *p'* was received; immediately through the same path a second pulse *p"* was emitted. On receiving both back-scattered echoes a simple summation was preformed. The resulting sum was filtered with the bandpass Butterworth filter of third order and cutoff frequencies f_{c1} = 2.5 MHz and f_{c2} = 3.5 MHz. After that, the next line was investigated in the same manner. This procedure was repeated on first 30 lines (half of the imaging setup). On last 30 lines (blue region in figure 10), only the echo of *p'* was bandpass filtered with the previously mentioned filter and used to present the investigated path (*standard second harmonic imaging*), while the echo from *p"* was disregarded. From the resulting lines, the envelope was extracted and log compressed.

Figure 11 is showing the acquired second harmonic image at the 35 dB dynamic range. The red (denoted A) and blue boxes (denoted C) mark the regions with the tissue-mimicking phantom. The yellow line indicates the boundary between SHI and the standard second harmonic imaging method. It can be observed that in the region C the boundary between tissue and UCAs is hardly notable. However, in the A region the resulting signal is much lower and the boundary between tissue and UCAs is much stronger. To emphasize this more clearly, the maximum, minimum and mean of the amplitude of the back-scattered echo on all the frames were calculated for the regions A and C and are presented in table 1.

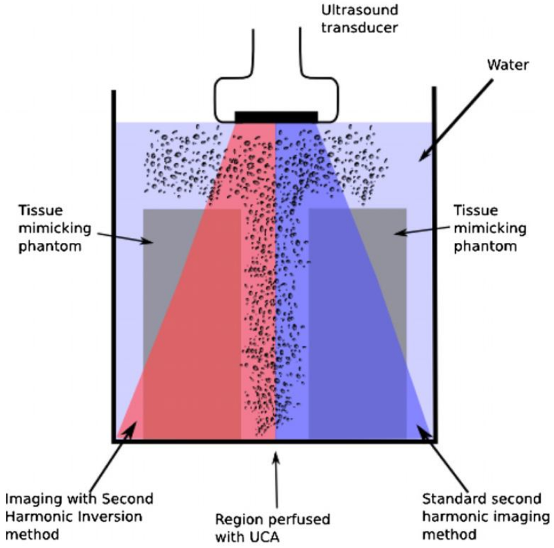

Fig 10. Imaging set up. The two gray squares are the tissue-mimicking phantoms. The red region is scanned using the SHI method and the blue region is scanned using regular second harmonic contrast imaging. The blue circles schematically represent the UCA.

The table shows that SHI reduces the second harmonic from tissue in average by over 20 dB (first line of table 1). Note also that the maximum and minimum values are reduced constantly with the SHI approach. Table 1 also shows the effect of SHI on the amplitude of the back-scattered echo from the UCA compared to that of standard second harmonic imaging. This is important to investigate since, for a meaningful increase of ATR_2, the preservation of the second harmonic generated by the UCA $\left(P_2^{UCA}\right)$ is equally essential to the reduction of the second harmonic generated by the tissue $\left(P_2^{tis}\right)$, see Eq. 1). The green box (marked B, region perfused with UCAs) was divided in two regions: B_1 where SHI was used and B_2 where second harmonic imaging was performed (the two regions are separated by the yellow line in figure 11). The same statistical analysis was conducted as for the tissue areas. Note that the maximum value is lowered by 0.4 dB with the SHI technique, indicating that some loss of pressure generated by the UCA is achieved. However, it should be noted that the minimum value is larger for SHI which tells that some constructive addition of the back-scattered echo also appears. Furthermore, the average value of the back-scattered pressure from the UCA when imaged with SHI and standard second harmonic are similar. Thus, it can be concluded that SHI well preserves the nonlinear behavior of the UCA.

Furthermore, we compared SHI with HPD, which is known for its good suppression of the second harmonic generated by tissue. The technique uses a successive transmission of two equal pulses which are subtracted on reception. Since the response of the tissue is equal for two signals, the subtraction will yield zero in the tissue area. On the other hand, UCAs in our setup are constantly moving; thus, the full subtraction of the UCA echo is not to be expected. To compare the SHI method to HPD, a second set of experiments were conducted. In this case, the SHI technique was used on one half of the frame and HPD on the second part of the acquired frame. From the resulting ultrasound image (figure 12), it is clear that both methods are extremely good in suppressing the harmonics generated by the tissue (left and right to the green box).

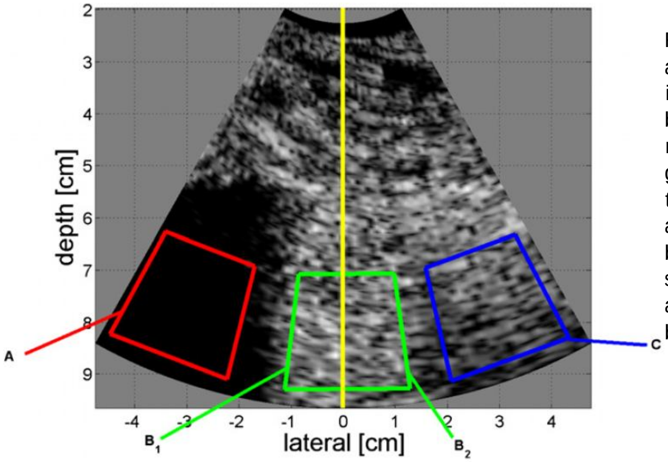

Fig 11. Second harmonic image acquired using the setup shown in figure 10. The red and blue boxes denote the tissue-mimicking phantoms, while the green box is water perfused with the UCA. The SHI scheme is applied to the area surrounded by the red box, and regular second harmonic imaging is applied to the area surrounded by the blue box.

Table 1. Statistical analysis of regions A and C (tissue), and region B from figure 11.

	Tissue regions		UCA perfused region	
	Second harmonic Inversion (A)	Second harmonic Imaging (C)	Second harmonic Inversion (B_1)	Second harmonic Imaging (B_2)
Mean	−40.3	−19.9	−18.2	−17.5
Max	−25.8	−6.0	−2.7	−3.1
Min	−60.7	−42.7	−40.1	−39.7

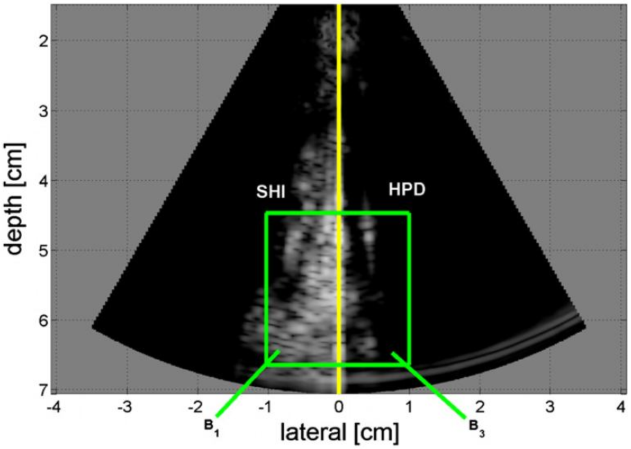

Fig 12. Comparison between second harmonic inversion and harmonic power Doppler.

A closer look at figure 12 reveals that SHI is better than HPD for imaging the contrast agents (green box). The yellow line in the figure separates the regions imaged with the SHI and HPD techniques. The left part of the green box (B_1), where SHI is implemented is clearly brighter than the right part (B_3), where HPD was used. The resulting SHI signal is a combined contribution of the nonlinear response of the UCA and the movement of the UCA between the subsequent pulses, while HPD comes from the movement of the UCA alone. From the statistical analysis performed on the green box (table 2), we note that with the SHI method the average amplitude of the echo back-scattered by the UCA stands at 21.55 dB, whereas in the case of HPD the average amplitude is 34.6 dB. Thus, the overall improvement of SHI over HPD is 13 dB.

DISCUSSION

Ultrasound contrast harmonic imaging is a competition between the harmonic scattering of the bubbles and the harmonics generated during ultrasound propagation, the so-called tissue harmonics. Reduction of the tissue harmonics should be effective over a large axial range and over a large bandwidth. In this study, we proposed the second harmonic inversion (SHI) technique, based on the transmission of two signals shifted by 90° at the fundamental frequency, which has a highly efficient axial as well as a broad second harmonic frequency reduction performance.

Table 2. Comparison of UCA response to the SHI or HPD method.

	Second harmonic Inversion (B_1)	Harmonic power Doppler (B_3)
Mean	−21.5	−34.6
Max	−0.1	−0.3
Min	−55.7	−64.9

The axial depth performance of the previous work (Krishnan *et al* 1998, Christopher 1999) was limited to a reduction of 30 dB in a shallow region of 10mm around the focal spot. Outside this region the reduction was only 15 dB. The results reported by Krishnan and Thomenius (2008) were more uniform over the axial range; however, the reduction was only between 6 and 10 dB. Couture *et al* (2008) tested their method on a wire, effectively evaluating a small spot. In a former study (Pasovic *et al* 2010), we showed a reduction of 10 dB over 5 cm around the focus. Using the SHI technique we demonstrated a reduction of the second harmonic by about 40 dB in simulations and 20 dB in measurements, over the entire axial range from 30 to 130 mm.

The SHI method also performs well over the frequency band. In the present study, the simulation and experimental results show a reduction of the second harmonic amplitude of more than 25 dB over the whole bandwidth (100%) as shown in figures 3 and 8. Previous simulation studies by Krishnan *et al* (1998) showed a reduction of 12 dB of the second harmonic amplitude over the whole bandwidth, but this was not confirmed by the experimental results. Similar findings were reported by Christopher (1999). Experimental results were reported by Couture *et al* (2008), but the excitation signals used were relatively long, between 12 and 50 cycles. With a multiple-component second harmonic reduction signal (Pasovic *et al* 2010), it was shown that the amplitude of the second harmonic can be successfully reduced over 75% of the bandwidth. The only limitation is the bandwidth of the ultrasound transducer. One cycle excitation has a 100% band coverage which makes SHI impossible. Our experiments showed that the minimal number of cycles in the emitted burst should be around 3 or higher for SHI to be effective. The implementation of the SHI protocol for shorter pulse durations would require a larger bandwidth in the pulse-echo mode than the one of the modern piezoelectric phased array transducers.

The reduction of the second harmonic as reported by Christopher (1999) is from approximately 80 kPa to about 12 kPa. Pasovic *et al* (2010) present a reduction from 80 kPa to approximately 5 kPa. Both Christopher (1999) and Pasovic *et al* (2010) report a strong dependency on the excitation level of their methods. In our study, we investigate the influence of the peak of the emitted pressure on the level of suppression in order to demonstrate the applicability of the proposed technique for contrast imaging. The main conclusion from the simulation suggests that the method provides an adequate level of second harmonic suppression in tissue. The experimental results generally agree with the simulations for higher acoustic pressures. However, the level of suppression in the experiments for the lower acoustic pressure differs from the one in the simulation. For this range of emitted pressures the SNR of the induced second harmonic is relative low, and almost negligible after suppression to accurately quantify with our laboratory equipment. The absolute inaccuracies are related to the transmit amplifier (amplitude and phase) and the hydrophone (mainly phase). Hence, the measurements for the lower acoustic pressures suffer from the sensitivity of the setup, rather than reflect the reduced efficacy of the proposed technique for lower emitted pressures. Using the SHI method the second harmonic amplitude is reduced from 260 kPa to ≈ 2 kPa in simulations and from 230 kPa to ≈ 12 kPa in experiments as shown in figures 1b and 6b. These results are almost independent of the used acoustic pressure as shown in figures 2 and 7, which is an additional advantage of the SHI method.

The ATR_2 as achieved with the new SHI shows an improvement of 20 dB in an experimental setting using the tissue-mimicking phantom. The improvement as reported by Couture *et al* (2008) was only 10 dB, while Pasovic *et al* (2010) show the improvement of 7.4 dB. The second harmonic inversion approach was also compared to harmonic power Doppler. Both techniques used two pulses in excitation, with two crucial differences; firstly, SHI demands the summation of received echoes, while HPD uses subtraction and secondly SHI uses pulses phase shifted by $\pi/2$ for excitation, whereas HPD uses two equal pulses. Figure 12 and table 2 show that SHI is better in preserving nonlinear response from UCA. The reason might be that the UCAs do not respond in the same manner to a signal with a different starting phase. This can be substantiated by previous studies (Morgan *et* *al* 1998, 2000) which evidently show that the response of the UCA depends on the staring phase of the excitation signal.

The SHI method can be implemented quite straightforward since it transmits two signals which are shifted by 90° in phase. In previously reported studies, there is a need to acquire correct parameters of the reduction signal. In the work of Krishnan *et al* (1998), the phase and amplitude have to be adjusted manually and no information is given on how to compute these parameters. Christopher (1999) encountered the same problem and as a solution suggested using some arbitrary scaling of the amplitude of the predistorted signal. In a previous study, Pasovic *et al* (2010) showed that reduction signals can be predetermined, however, only in homogeneous tissue.

The SHI method belongs to a multiple-pulse technique, in which the reflected echoes from the emitted acoustic waves are used in the post-processing to construct an image. In this study, the amplitude of the emitted pulses was equal, which is similar to the conventional pulse-inversion technique. The difference between the two methods lies in the fact that the phase shift amounted to $\pi/2$ instead of π. One of the extensions for the pulse-inversion scheme includes simultaneous inversion and amplitude modulation. In the work of Eckersley *et al* (2005), the effect of amplitude modulation showed an improved harmonic image. Pairing SHI with amplitude modulation would not achieve the same effect for two reasons; one: the fundamental components are not in perfect opposite phase and would not cancel each other and two: since the second pulse is emitted with a lower amplitude the generated second harmonic would not be sufficiently high to accomplish substantial reduction after the summation of two pulses. However, it would be interesting to incorporate the aforementioned extensions to the Doppler or PI sequences in the future.

As a multiple pulse technique, SHI not only reduces the frame rate, but is also susceptible to the motion artifacts. The latter stems either from the blood or tissue displacement. Indeed, since UCAs are injected into blood that is constantly moving, there is some possibility that when using a multi-pulse technique destructive adding of echoes from micro-bubble might appear. We estimated the maximum displacement of the bubbles under investigation on 10μm (1 cm/s fluid velocity and 1 ms between the interrogation pulses) which would ensure the absence of destructive adding. This is confirmed by the results displayed in figure 11 where the region perfused with the UCA has a homogeneous gray level indicating that although half of the window is created with SHI and half with standard second harmonic imaging (1 pulse technique), second harmonic pressure produced by the UCA is well preserved. However, just as other multiple-pulse techniques, also SHI is sensitive to tissue motion. The tissue motion is not considered as a limitation for larger vessels containing moving bubbles, since multi-pulse methods focus exactly on the difference in sequential pulses. For smaller vessels like in the myocardium, motion artifacts should be taken into account.

CONCLUSION

The SHI method presented in this chapter reduces the second harmonic generated by nonlinear wave propagation. The method is simple to implement. *In vitro* measurements show an improvement in ATR_2 by +20 dB.

References

Aanonsen S I, Jacqueline T B, Tjotta N and Tjotta S 1984 Distortion and harmonic generation in the nearfield of a finite amplitude sound beam *J. Acoust. Soc. Amer.* 75 749–69

Becher H, Tiemann K, Schlief R, Luderitz B and Nanda N 1997 Harmonic power doppler contrast echocardiography: preliminary clinical results *Echocardiography* 14 637–42

Bouakaz A, Frigstad S, Ten Cate F and de Jong N 2002 Improved contrast to tissue ratio at higher harmonics *Ultrasonics* 40 575–8

Bouakaz A, ten Cate F and de Jong N 2004 A new ultrasonic transducer for improved contrast nonlinear imaging *Phys. Med. Biol.* 49 3515–25

Burgers J 1948 *Advances in Applied Mechanics (Advances in Applied Mechanics* vol 1*)* ed R V Mises and T V K´arm´an (Amsterdam: Elsevier) pp 171–99

Burns P, Powers J, Simpson D, Brezina A and Kolin A 1994 Harmonic power mode Doppler using microbubble contrast agents: an improved method for small vessel flow imaging *Proc. IEEE Ultrasonics Symp.* vol 3 p 1547

Chapman C S and Lazenby J C 1997 Ultrasound imaging system employing phase inversion subtraction to enhance the image *US Patent Specification* 5,632,277

Christopher T 1999 Source prebiasing for improved second harmonic bubble responce imaging *IEEE Trans. Ultrason. Ferroelectr. Freq. Control* 46 556–63

Couture O, Aubry J, Montaldo G, Tanter M and Fink M 2008 Suppression of tissue harmonics for pulse-inversion contrast imaging using time reversal *Phys. Med. Biol.* 53 5469–80

de Jong N, Frinking P, Bouakaz A and ten Cate F J 2000 Detection procedures of ultrasound contrast agents *Ultrasonics* 38 87–92

Eckersley R J, Chin C T and Burns P N 2005 Optimising phase and amplitude modulation schemes for imaging microbubble contrast agents at low acoustic power *Ultrasound Med. Biol.* 31 213–9

Enflo B and Hedberg C 2002 *Theory of Nonlinear Acoustics in Fluids* 1st edn (Berlin: Springer) Frinking P J and de Jong N 1997 Modeling of ultrasound contrast agents *Proc. IEEE Ultrasonics Symp.* vol 2 pp 1601–4

Fubini G 1935 Anomalie nella propagazione di onde acustiche di grande ampiezza *Alta Freq.* 4 530

Jiang P, Mao Z and Lazenby J C 1998 A new tissue harmonic imaging scheme with better fundamental frequency cancellation and higher signal-to-noise ratio *Proc. IEEE Ultrasonics Symp.* vol 2 pp 1589–94

Krishnan K and Thomenius K 2008 Improved contrast ultrasound with tissue harmonic minimizing pulse *IEEE Trans. Ultrason. Ferroelectr. Freq. Control* 55 249–53

Krishnan S, Hamilton J D and O'DonnellM1998 Suppression of propagating second harmonic in ultrasound contrast imaging *IEEE Trans. Ultrason. Ferroelectr. Freq. Control* 45 704–11

Krishnan S and O'Donnell M 1996 Transmit aperture processing for nonlinear contrast agent imaging *Ultrason. Imaging* 18 77–105

Kuznetsov V 1970 Equation of nonlinear acoustics *Sov. Phys. Acoustics* 16 749–68

Morgan K, Allen J, Dayton P, Chomas J, Klibaov A and Ferrara K 2000 Experimental and theoretical evaluation of microbubble behavior: effect of transmitted phase and bubble size *IEEE Trans. Ultrason. Ferroelectr. Freq. Control* 47 1494–509

Morgan K, Averkiou M and Ferrara K 1998 The effect of the phase of transmission on contrast agent echoes *IEEE Trans. Ultrason. Ferroelectr. Freq. Control* 45 872–5

Pasovic M, Danilouchkine M, Matte G, van der Steen A F, Basset O, de Jong N and Cachard C 2010 Broadband reduction of the second harmonic distortion during nonlinear ultrasound wave propagation *Ultrasound Med. Biol.* 36 1568–80

Shen C C and Hsieh Y C 2008 Optimal transmit phasing on tissue background suppression in contrast harmonic imaging *Ultrasound Med. Biol.* 34 1820–31

Shen C C and Li P C 2001 Tissue harmonic image analysis based on spatial covariance *IEEE Trans. Ultrason. Ferroelectr. Freq. Control* 48 1648–56

Shen C C, Wang Y C and Hsieh Y C 2007 Third harmonic transmit phasing for tissue harmonic generation *IEEE Trans. Ultrason. Ferroelectr. Freq. Control* 54 1370–81

Tanter M, Thomas J L and Fink M 2000 Time reversal and the inverse filter *J. Acoust. Soc. Amer.* 108 223–34

Teirlinck C, Bezemer R, Kollmann C, Lubbers J, Hoskins P, Ramnarine K, Fish P, Fredfeldt K E and Schaarschmidt U 1998 Development of an example flow test object and comparison of five of these test objects, constructed in various laboratories *Ultrasonics* 36 653–60

van Neer P L M J, Matte G, Danilouchkine M G, Prins C, van den Adel F and de Jong N 2010 Super harmonic imaging: development of an interleaved phased array transducer *IEEE Trans. Ultrason. Ferroelectr. Freq. Control* 57 455–68

Vignon F, Aubry J F, Tanter M, Margoum A, Fink M and Lecoeur J 2005 Dual-arrays brain imaging prototype: experimental in vitro results *Proc. IEEE Ultrasonics Symp.* vol 1 pp 504–7

Voormolen M 2007 3D Harmonic Echocardiography. *Phd Thesis* Erasmus University Rotterdam

Zabolotskaya E and Khokhlov R 1969 Quasi-plane waves in the nonlinear acoustics of confined beams *Sov. Phys. Acoust.* 15 35–40

Chapter X

Conclusion and future perspectives

Subharmonic carotid imaging is one step away

Contrast agent microbubbles are versatile tools for ultrasound imaging. In this thesis we focused on their non-linear properties and in particular their subharmonic behavior with the aim of exploring their possible applications in carotid imaging. Experimental studies showed that the subharmonic response of contrast agent microbubbles has a great potential for imaging purposes. It is easily detectable and tunable for different applied frequencies and acoustic pressures. It was also shown that even if as a population microbubbles exhibit a certain dominant behavior, when studied individually, there is a clear variability in their properties. Besides the physical conditions in which microbubbles are exposed to, e.g. exciting frequency and acoustic pressure, the subharmonic response of the mirobubbles is also influenced by their physical properties such as size distribution and the shell coatings. Therefore it was indicated that it is of extreme importance to have an accurate estimate of the shell properties of the microbubbles in order to be able to drive them optimally for any desired application.

The main outcomes of our acoustical and optical microbubble characterization experiments are as follows:

Bubble population study presented in chapter III showed that the stiffness of the shell seems to be independent of the size distribution but shell viscosity is slightly affected by it. Moreover, shell viscosity showed to be frequency dependent as well. The value of the shell viscosity decreases by increasing the excitation frequency which is an indication of shear thinning. It was hypothesized that the reason behind size-dependent shell properties may be due to the microstructure, inhomogeneities and different thicknesses of the shell for each individual bubble. This hypothesis grew stronger when the single bubble measurements by means of ultra-high speed imaging were performed and the fluorescent images of the lipid shell (figure 13C, chapter V) clearly indicated the heterogeneity of lipid distribution on the microbubbles.

The results of these sets of experiments, presented in chapter IV, revealed that not all the bubbles, even if mono dispersed, exhibit a subharmonic response. Only 40 percent of the phospholipid microbubbles of our study were subharmonically responsive. Optical recordings indicated asymmetrical amplitude of oscillation for these bubbles, which is known as compression-only phenomenon. Numerical simulations and their fit on the experimental data proved that in fact the reason behind the absence of the subharmonic oscillations in the remainder sixty percent of our studied bubble population is due to the difference in the lipid concentration of their coatings. This translates to the difference in the surface tension of the microbubbles at rest even with the same size. Consequently, bubbles with zero surface tension at rest exhibit the highest subharmonic response. These bubbles have either a buckled or a ruptured coating at rest or reach one of these two states during oscillation.

Another shell property observed for the first time in our single bubble experiments was the size-dependent effect of acoustic pressure on the subharmonic resonance frequency of the phospholipid coated bubbles. Before, it was believed and demonstrated experimentally that the fundamental resonance frequency of the microbubbles, independently from their size, always decreases for increasing acoustic pressure indicating shell (strain) softening. This is not the case for the subharmonic. Instead in the subharmonic domain, both rheological effects, shell softening and hardening, can take place. Small bubbles (≤ 3 µm diameter) which are more responsive in the frequency range favorable for carotid imaging, show strain hardening, an increase in the shell elasticity as the deformation strength increases. These results were confirmed when the same experiments were performed *in vivo* and presented in chapter VI.

Last but not least important outcome of the single bubble experiments *in vitro* (chapter IV) and *in vivo* (chapter VI) was to demonstrate that the ratio between fundamental and subharmonic resonance frequencies of the microbubbles is not always a factor of two. In other words, it is not accurate to assume that the highest subharmonic amplitude occurs always at twice the fundamental resonance frequency of the microbubbles. Instead this ratio varies from one microbubble to another depending on the acoustic pressure, size and shell properties of each bubble.

Even more exciting than shear thinning, strain hardening and subharmonic threshold was the practical manifestation of the existence of two subharmonic regimes. The theoretical prediction of the presence of two minimum thresholds for the occurrence of subharmonics (one at the resonance and another at half the resonance frequency) was never experimentally confirmed before. The most common subharmonic response was always generated when microbubbles were excited by a transmitting frequency which is twice their approximate resonance frequency. TR (transmit at resonance) subharmonic regime was successfully observed in a bubble population study presented in chapter VII and also in single bubble experiments performed *in vivo* (chapter VI).

Another progressive step in the characterization of contrast agent microbubbles was the performance of the experiments *in vivo* presented in chapter VI. To be able to see, track and analyze the behavior of a microbubble exposed to an ultrasound field in a live network of blood vessels was a dream come true. We learnt that to excite microbubbles inside a living blood vessel, higher acoustic pressures are required; damping is higher in such an environment and consequently microbubbles exhibit higher subharmonic oscillations when excited around their resonance frequencies (TR subharmonic regime) compared to excitation at twice resonance (T2R subharmonic regime). It was also shown that other physical properties such as compression-only, resonance frequency, strain hardening and shear thinning, extracted from *in vitro* experimental data, despite the simplifications of *in vitro* setups, accurately reproduce the same properties observed in an *in vivo* model.

Nevertheless, the implications deduced from the chicken embryo experiments in this study are a minor fraction of what this *in vivo* model can actually offer. Future experiments focusing on the interaction of the oscillating microbubbles with the living cells can shed more light on the mechanism and conditions of inducing sonoporation and drug release. Performing the same experiments on targeted bubbles, similar to the liposome-loaded bubbles presented in chapter V will provide an important insight on the differences in the behavior of loaded and unloaded bubbles. Moreover, the capillary network of the chicken embryo model has a dimension similar to the human vasa vasorum which makes it a perfect platform to test the feasibility of different imaging modalities. Also the bioeffects of each imaging modality, such as capillary damage and hemolysis can be investigated with this model.

Knowing that not all the microbubbles exhibit a subharmonic response and those which are subharmonically active do have specific shell properties (chapters IV and VI) inspired us to develop a method to manipulate microbubbles such that they exhibit a higher subharmonic response. For that reason two approaches were applied. One was the use of a very low frequency (2.5 kHz) wave for mimicking the changes in the ambient pressure, and the other was the use of the self-demodulation signal which is a low-frequency signal produced by weakly nonlinear propagation of an ultrasound wave, presented in chapters VII and VIII respectively.

With the help of a low frequency acoustic wave the ambient pressure in water was modulated at a low mechanical index of 0.07 (=15 kPa) which dynamically influences the subharmonic response of phospholipid-coated microbubbles. The modulation of the bubble radius induced by the dynamic variation in the liquid ambient pressure subsequently causes modulations of the scattered acoustic pressure at the fundamental and subharmonic frequencies. The variation in the ambient pressure of 15 kPa can modulate the subharmonic amplitude up to 10 dB as compared to the static atmospheric pressure condition. The highest subharmonic amplitude was measured when small microbubbles, showing buckling, were insonified at 10 MHz (chapter VII).

The low frequency self-demodulation acoustic signal on the other hand, acts as a stimulator for the generation of the subharmonic response of contrast agent microbubbles when their initial state is close to the buckling or rupturing regimes. This signal pushes the microbubbles towards these two regimes in which they exhibit the highest subharmonic oscillation. The effect of self-demodulation signal can be tuned by modifying the envelope of the transmitting acoustic wave. Experiments and simulations performed in chapter VIII demonstrated that excitation bursts with rectangular envelopes contain the strongest self-demodulation signal. Experimental results showed that the scattering subharmonic amplitude of phospholipid microbubbles can be increased up to 22 dB by just changing the burst envelope from Gaussian to rectangular.

While changing the ambient pressure of the liquid surrounding the microbubbles using a low frequency acoustic wave can be considered a new imaging modality for subharmonic imaging, which may be technically more complicated to implement, the stimulation effect of the self-demodulation signal can be easily combined with any conventional contrast imaging technique in the subharmonic mode. All has to be done is to transmit excitation bursts with rectangular envelopes in any conventional imaging technique (e.g. pulse inversion) in the subharmonic mode and a considerable enhancement in the contrast to tissue ratio of the image will be observed. Nevertheless, the sensitivity of the subharmonic response of the contrast agent microbubbles to the small changes in the hydrostatic pressure can be beneficial for noninvasive estimation of the cardiac pressure.

Based on this property of contrast agents' subharmonic emission, a successful technique has been developed (Shi et al 1999); Subharmonic aided pressure estimation (SHAPE) is based on the principle that the subharmonic amplitude in the received signal spectrum is linearly and inversely related to an increase in ambient pressures. SHAPE has been used to monitor pressure changes in the aorta of open-chest canines using single-element transducers (Forsberg et al 2005) followed by noninvasive assessments of left ventricular pressures *in vivo* with a commercially available ultrasound scanner (Dave et al 2012). Recently, SHAPE has been proposed also to be used for noninvasive monitoring of neoadjuvant chemotherapy in the breast (Halldorsdottir et al 2011). Interstitial fluid pressure in breast cancer tumors has been shown to be higher than that of surrounding breast tissue (Less et al 1992). This increase is believed to be due to vascularity, fibrosis and difference in the interstitial matrix in tumors and it can result in poor transport of therapeutic drugs to tumors (Heldin et al 2004). The level of interstitial fluid pressure in breast cancer tumors could potentially be used to monitor the response to neoadjuvant chemotherapy and SHAPE can be employed to monitor treatment response by noninvasively measuring the interstitial fluid pressure in breast tumors.

Another important aspect in the characterization of the contrast agent microbubbles concerns the modeling of their dynamic behavior. As explained in details in chapter II, in twenty years which passes from the introduction of the ultrasound contrast agents for clinical use many attempts have been done to predict and explain the dynamics of the bubble vibration. As a consequence many theoretical models have been developed. However, the experimental observations of the dynamic behavior of phospholipid coated microbubbles have demonstrated that the current models fail to predict accurately their acoustic response. In my opinion two major points can be derived from the characterization experiments, in particular those presented in chapters IV, VII and VIII; linear regime does not exist for these microbubbles, and there will never be a universal model that can predict the phospholipid coated microbubbles dynamic behavior. For example, shell parameters in all current models are assumed to be independent of the bubble size and equal for all the bubbles. We know very well now that this is not the case in reality. Coating properties differ based on the size of the bubbles. Even more interestingly, the lipid distribution and concentration of two microbubbles with the same size can still vary immensely. Consequently, unless the manufacturing techniques of the contrast agent microbubbles advances to the point of producing monodispersed, identically coated microbubbles, the ultimate model describing the dynamics of ultrasound contrast agent microbubbles will remain a myth.

When this project started four years ago, very few had faith on the imaging potential of the subharmonic response of the ultrasound contrast agents. There was also little motivation to explore the capabilities of the microbubbles' subharmonic emission as possibly a new imaging technique, since the existing nonlinear modalities, specifically pulse inversion and power modulation, which were employed in all the commercially available scanners were considered a break through in enhancing the imaging quality of ultrasound scanners (Averkiou 2011). Since then subharmonic imaging has gone a long way and has gained more trust. Medical tests have shown that the conventional nonlinear contrast imaging techniques despite their strong superiorities over traditional B-mode images are not yet without defects (Kate et al 2012) and we are not yet "at the end of our technological development!"

While the quest for developing the ultimate imaging modality is still on, and various techniques based on the harmonic response of contrast agent microbubbles such as second harmonic inversion, introduced in chapter IX, have been proposed, subharmonic imaging has been successfully tested in several pre-clinical and clinical studies. As an example, the most recent publication of Eisenbrey et al (2012) reports the implementation of 3D subharmonic ultrasound imaging on a modified Logiq 9 ultrasound scanner (GE Healthcare, Milwaukee, WI) at a transmit frequency of 5.8 MHz. Authors have reported that subharmonic imaging has improved contrast to tissue ratio relative to harmonic imaging and 3D imaging has the ability to depict vascularity over an entire volume within a flow phantom and the lower pole of two canine kidneys. This system will be explored further for its effectiveness in breast imaging. The feasibility of subharmonic imaging for the detection of breast lesion was already reported by the same authors in 2007 (Forsberg et al 2007). In that study, Forsberg and colleagues had compared the accuracy of gray-scale subharmonic imaging with standard gray-scale ultrasonography, power Doppler US (with and without contrast agent), and mammography for the diagnosis of breast cancer, with histopathologic or clinical follow-up results. They were the first to present the subharmonic images acquired in humans and it was shown that subharmonic imaging appears to improve the diagnosis of breast cancer relative to conventional ultrasound imaging and mammography.

Subharmonic modality can be implemented in almost any conventional ultrasound imaging scanner equipped with suitable low pass filters and broad band probes which makes it possible to transmit at any desired frequency and to receive the echo at half that frequency. As an example the subharmonic images acquired by Lecoeur open system scanner (Lecoeur Electronique, Chuelles, France) from a cylindrical tissue mimicking phantom are presented below. These preliminary results were recorded at a transmit frequency of 6 MHz with a burst of

15 cycles long. The images in figure 1 show the clear enhancement in the contrast to tissue ratio from the fundamental to the subharmonic mode.

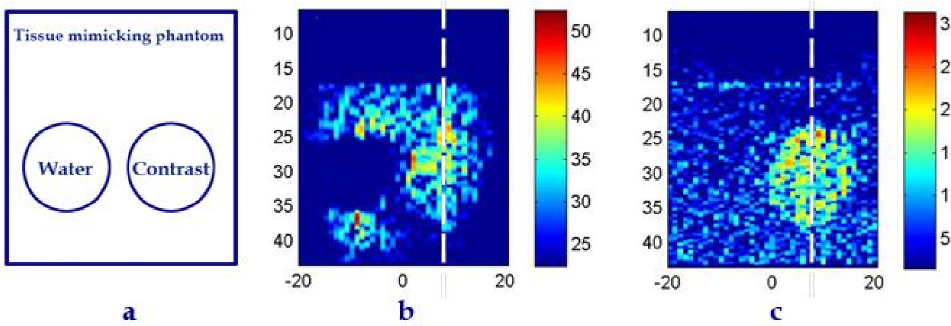

Fig 1. a) Scheme, b) fundamental and c) subharmonic images of a tissue mimicking phantom. Transmit frequency is 6 MHz. CTR measured along the dashed line for the fundamental and the subharmonic images are 7.6 and 16.7 respectively.

Very recently, subharmonic mode has also been implemented on a modified Vevo 2100 system, a high frequency scanner for animal models (VisualSonics Inc., Toronto, Canada). The scanner acquires real-time subharmonic images *in vivo.* Subharmonic mode in this system can be combined with other imaging modalities such as pulse inversion or power modulation as well. Figure 2 shows a series of images presenting the B-mode, amplitude modulation and pulse inversion combined with subharmonic mode images of the aortic arch of a mouse, indicating the side branches arteries. The transmit frequency in this experiment was 30 MHz, applied acoustic pressure was set to 200 kPa and bursts of 6 cycles were used. The differences between Images indicate the higher resolution and contrast to tissue ratio of the subharmonic image of the aortic arch (Fig 2f) compared to the equivalent of it taken in the fundamental (Fig 2b) and the nonlinear fundamental mode (Fig 2d).

As a last example, a subharmonic image of a 6-day old chicken embryo is presented in figure 3. This image was acquired with Vevo 2100 as well. The transmitting frequency was 18 MHz, using a 6-cycle excitation burst and acoustic pressure of 200 kPa. The image depicts the heart and all the arteries and branching vessels connecting to the heart.

The presented examples here can be defined as the state-of-the-art subharmonic images. However they have all been produced by employing the existing ultrasound scanners available in the market. So far subharmonic mode has not been optimized specifically on any commercial scanner. All the experiments performed, have been restricted to the limitations of the current settings of the system. Experiments are still forced to be done with probes in a certain frequency range which are not optimal for subharmonic imaging. Despite all these confining lines, subharmonic emission of contrast agent microbubbles has proven to be an effective tool and a prospective imaging technique. And therefore I am confident that subharmonic carotid imaging is just one step away.

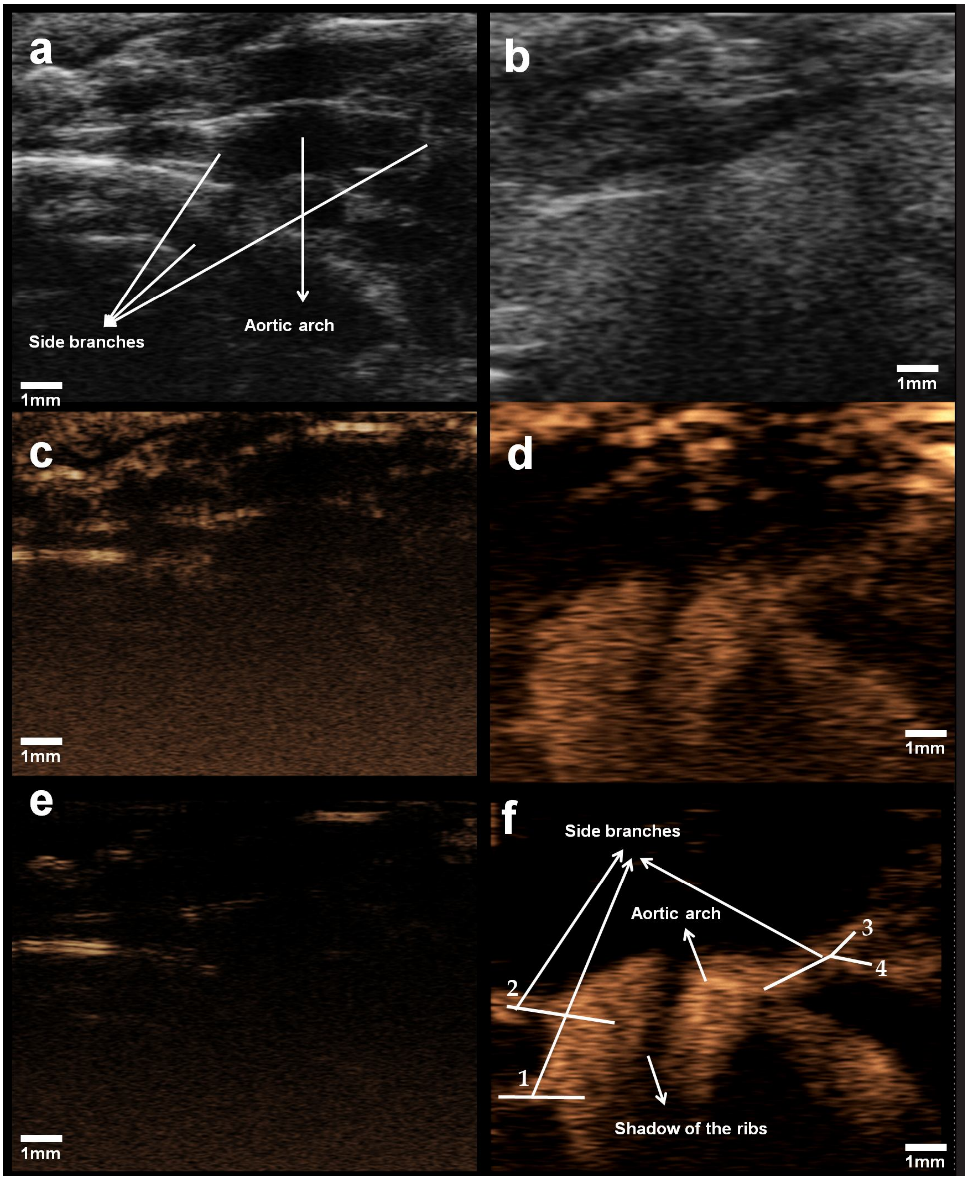

Fig 2. High frequency (30 MHz) ultrasound images of aortic arch of a mouse before and after MicroMarker ultrasound contrast agent administration taken by Vevo 2100 and MS 250 probe using a 6-cycle excitation bursts (~200 KPa) in three different modalities: a and b) B-mode, c and d) AM-mode, e and f) PI-mode + subharmonic. Side branches in figure (f): 1) Right subclavian artery, 2) right common carotid artery, 3) left common carotid artery and 4) left subclavian artery. Credits: Verya Daeichin (Erasmus MC).

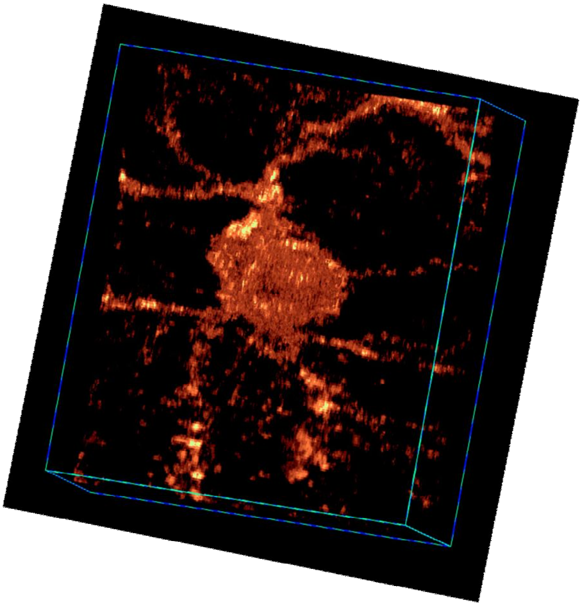

Fig 3. Subharmonic image of a 6-day old chicken embryo acquired with Vevo 2100. The transmitting frequency was 18 MHz, using a 6-cycle excitation burst and acoustic pressure of 200 kPa. Credits: Verya Daeichin (Erasmus MC).

References

Averkiou M. Bubble detection for perfusion: Are we at the end of our technological development? 16th European Symposium on Ultrasound Contrast Imaging 20-21 January 2011, Rotterdam, The Netherlands.

Dave JK, Halldorsdottir VG, Eisenbrey JR, Raichlen JS, Liu JB, McDonald ME, Dickie K, Wang Sh, Leung C, Forsberg F. Noninvasive LV Pressure Estimation Using Subharmonic Emissions From Microbubbles JACC: Cardiovascular Imaging 2012;5:87–92.

Eisenbrey JR, Sridharan A, Machado P, Zhao H, Halldorsdottir VG, Dave JK, Liu JB, Park S, Dianis S, Wallace K, Thomenius KE, Forsberg F. Three-Dimensional Subharmonic Ultrasound Imaging In Vitro and In Vivo. Academic Radiology 2012;19:732-739.

Forsberg F, Liu J, Shi W, Furuse J, Shimizu M, Goldberg B. In vivo pressure estimation using subharmonic contrast microbubble signals: proof of concept. IEEE Trans Ultrason, Ferroelec Freq Contr 2005;52:581–3.

Forsberg F, Piccoli C, Merton DA, et al. Breast lesions: imaging with contrast-enhanced subharmonic US—initial experience. Radiology 2007; 244:718–726.

Halldorsdottir VG, Dave JK, Eisenbrey J, Machado P, Liu JB, Merton DA, Cavanaugh BC, Forsberg F. Subharmonic aided pressure estimation for monitoring interstitial fluid pressure in tumors: in vitro and in vivo proof of concept. J Ultrasound Med, 2011;30:S28.

Heldin CH, Rubin K, Pietras K, Ostman A. High interstitial fluid pressure - an obstacle in cancer therapy. Nat Rev Cancer, 2004;4:806-813.

Kate GL, Renaud GG, Akkus Z, Oord SC, Cate FJ, Shamdasani V, Entrekin RR, Sijbrands EJ, Jong Nd, Bosch JG, Schinkel AF, Steen AF. Far-wall pseudoenhancement during contrast-enhanced ultrasound of the carotid arteries: clinical description and in vitro reproduction. Ultrasound Med Biol 2012;38:593-600.

Less JR, Posner MC, Boucher Y, Borochovitz D, Wolmark N, Jain RK. Interstitial hypertension in human breast and colorectal tumors. Cancer Res 1992;52:6371-6374.

Shi W, Forsberg F, Raichlen J, Needleman L, Goldberg B. Pressure dependence of subharmonic signals from contrast microbubbles. Ultrasound Med Biol 1999;25:275– 83.

Summary

Subharmonic venture is an attempt to explore the possibility of a new imaging modality. Contrast agent microbubbles are coated gas bubbles that are used as intravascular tracers for visualization by ultrasound. Their nonlinear response to an ultrasound wave separates them from the linear tissue response and therefore translates them to an optimal imaging implement. The aim of this study is to investigate and characterize one of the nonlinear responses of contrast agent microbubbles in particular, subharmonic emission, for carotid imaging.

Subharmonic energy is generated at half a transmitting frequency and is not produced by the tissue. The goal is to utilize the higher contrast to tissue ratio achieved by subharmonic response of mirobubbles to visualize the carotid artery, particularly vasa vasorum. This technique will be used for the early detection and diagnosis of atherosclerosis plaques. For this purpose the subharmonic response of the microbubbles has to be characterized accurately. The dependence of the subharmonic emission to the transmitting frequency, acoustic pressure and also physical properties of the microbubbles such as size distribution and shell properties are influential parameters in the optimal generation of the subharmonic energy. This study is dedicated to the characterization and optimization of these parameters.

In chapter I the imaging techniques for diagnosis of atherosclerosis and among them contrast-enhanced ultrasound, are introduced. Vasa vasorum which is the key sign in the early detection of a carotid plaque is explained and the advantages of subharmonic carotid imaging are discussed.

Chapter II is focused on the theoretical models describing the dynamics of contrast agent microbubbles. The developments in the production and properties of contrast agents in the past twenty years and their corresponding theoretical models are presented.

In chapter III the shell properties, elasticity and viscosity, of phospholipid coated microbubbles are calculated in an attenuation experiment. The frequency range of 5-15 MHz which is optimal for carotid imaging is used. A shear thinning behavior is observed for the studied bubbles in the applied frequency range.

Characterization of the phospholipid coated microbubbles is continued by means of single bubble experiments in chapter IV, V and VI. In chapter IV, the subharmonic resonance frequencies of the microbubbles are derived and their dependence to the amplitude of the acoustic pressure is investigated. It is shown that not all the bubbles exhibit a subharmonic response. Bubbles with a subharmonic response have zero surface tension and size dependent rheological properties; smaller bubbles show shell hardening in contrast to the bigger bubbles which show shell softening.

The same characterization experiments are performed in chapter V on liposome-loaded microbubbles as perspective vehicles of drug delivery. These bubbles have shell properties similar to unloaded bubbles with the exception of exhibiting a different asymmetrical bubble oscillation know as “expansion-only”.

Next step in the characterization process of microbubbles is to study their behavior *in vivo.* This is done in chapter VI. Bubbles are injected into the capillary network of a chicken embryo and their acoustic response is recorded optically. It is shown that the subharmonic response of the microbubbles *in vivo* belongs to a different regime while the shell properties remain the same.

With the knowledge achieved from the characterization experiments, the next two chapters, VII and VIII, are dedicated to the optimization of the subharmonic response of microbubbles. The subharmonic emission of contrast agent microbubbles can be enhanced by manipulating the ambient pressure of the medium. This is done by transmitting a low frequency signal which modulates the hydrostatic pressure and consequently effects the scattered subharmonic emission from the microbubbles. This method is explained in chapter VII.

Another way to enhance the subharmonic response of the microbubbles is to change the shape of the envelope of the transmitting signal. Acoustic bursts with a rectangular envelope have a higher stimulating effect in the generation of the subharmonic energy. An acoustic signal with a rectangular envelope contains more self-demodulation energy which is a low-frequency signal produced by weakly nonlinear propagation of an ultrasound wave. It is shown in chapter VIII that a suitable design of the envelope of the transmitting burst to generate a self-demodulation signal at the subharmonic frequency can enhance the subharmonic response of contrast agent microbubbles considerably.

As an alternative imaging modality, a method for the reduction of second harmonic is proposed in chapter IX. In this method which is called “second harmonic inversion” two pulses of the same frequency and amplitude are transmitted to cancel out the second harmonic generated by nonlinearities of the medium. The experiments indicate the enhancement of the contrast to tissue ratio in this method compared to the standard second harmonic imaging.

Finally, the implications of subharmonic response of contrast agent microbubbles in carotid imaging as a powerful imaging technique and its future perspectives are discussed in chapter X.

Samenvatting

Het *subharmonische avontuur* is een zoektocht naar nieuwe wegen om microbellen met ultrageluid te detecteren. Microbellen zijn heel kleine ingekapselde gasbelletjes die intra-venous worden ingespoten. De microbellen verhogen de reflectie van het ultrageluidsignaal en hierdoor kan de doorbloeding van organen (hart, lever, nieren) en tumoren met echografie in beeld worden gebracht. Belangrijk hierbij is om het niet-lineaire gedrag van deze microbellen in een ultrageluidsveld te gebruiken omdat juist dit gedrag er voor zorgt dat de microbellen zich van het omliggende weefsel kunnen onderscheiden. Het subharmonische avontuur onderzoekt nu in detail het niet-lineaire gedrag van de microbellen. Het onderzoek richt zich in het bijzonder op de subharmonische trillingen van de microbellen bij het in beeld brengen van de vaten rondom de halsslagader. Subharmonische trillingen ontstaan op een frequentie die precies de helft is van de uitgezonden frequentie en dit is een unieke eigenschap van de microbellen. Het gereflecteerde signaal van het weefsel bevat geen subharmonische componenten. Het reflecteert alleen de uitgezonden frequentie. Door gebruik te maken van de subharmonisch frequentie kunnen de microbellen in de kleinste bloedvaten rondom de halsslagader, de zogenaamde vasa vasorum (belangrijke indicator voor atherosclerotische plaque vorming in de halsslagader) gedetecteerd worden.

Het subharmonisch gedrag van ingekapselde microbellen is tot nu toe nog weinig onderzocht en niet goed begrepen. In dit onderzoek wordt de afhankelijkheid bestudeerd van de subharmonische trillingen met de zendfrequentie, geluidsdruk, en met de fysieke eigenschappen van microbellen zoals de grootte en de specifieke kenmerken van het schilletje rondom de microbel ten einde de subharmonisch response van de microbellen te maximaliseren.

In hoofdstuk I worden de beeldvormende technieken voor de diagnose van atherosclerose, waaronder echografie met microbellen, geïntroduceerd. Verder worden de Vasa vasorum besproken, die een belangrijke indicator zijn voor aanwezigheid plaques in een vat, evenals de voordelen van subharmonische beeldvorming van de halsslagader.

Hoofdstuk II gaat in op de theoretische modellen die het dynamisch gedrag van de microbellen beschrijven en dit hoofdstuk geeft ook een historisch overzicht van de modellen die de afgelopen twintig jaar zijn ontwikkeld. In hoofdstuk III worden de eigenschappen, in het bijzonder de elasticiteit en viscositeit, van uit fosfolipiden bestaande schilletje bepaald door middel van ultrageluidsmetingen in het frequentiebereik van 5-15 MHz. Een opmerkelijk resultaat was dat deze microbellen zogenaamde ‘shear thining’ vertonen. Dit wil zeggen dat de viscositeit lager worden voor hogere snelheden van de fosfolipiden in het schilletje.

Experimenten op individuele microbellen zijn uitgevoerd om het schilletje verder te karakteriseren. Deze experimenten worden besproken in hoofdstuk IV, V en VI. In hoofdstuk IV worden de subharmonische resonantie frequenties van de microbellen afgeleid en de afhankelijkheid van amplitude en geluidsdruk onderzocht. Een van de conclusies is dat niet alle bellen een subharmonische respons laten zien en dat alleen bellen waarvan de oppervlaktespanning nul en waarvan de rheologisch gedrag afhangt van de grootte van de bel een subharmonische respons vertonen. Bij kleinere bellen wordt de schil harder (minder elastisch), terwijl bij grotere bellen de schil juist zachter wordt indien de ultrageluidsdruk toeneemt. In hoofdstuk V worden microbellen onderzocht waarvan de schil is geladen met liposomen. In deze liposomen kunnen medicijnen worden geladen waardoor er een combinatie ontstaat die gebruikt kan worden voor 'local drug delivery". Deze studie toont aan dat de elasticitei van de liposoom bellen vergelijkbaar is met die van niet-liposoom bellen, maar dat de viscositeit aanzienlijk groter is. Verder vertonen de liposoom bellen iets heel bijzonder; In de positieve fase van drukgolf comprimeren deze bellen niet. Ze expanderen wel in de negatieve fase van de drukgolf en vandaar dat we dit verschijnsel "expansion - only" hebben genoemd.

De volgende stap in de karakterisering van microbellen is het bestuderen van hun gedrag *in vivo*. Dit gebeurt in hoofdstuk VI. Hiertoe worden de bellen in het capillaire netwerk van een kippenembryo geïnjecteerd en de akoestische response onder de microscoop en een snelle camera bekeken. Het blijkt dat de subharmonische respons van microbellen *in vivo* tot een ander regime behoren, terwijl de eigenschappen van de schil hetzelfde blijven.

De volgende twee hoofdstukken, VII en VIII, zijn gewijd aan de optimalisatie van de subharmoische respons. De subharmonische trillingen van de microbellen kan worden verhoogd door de omgevingsdruk aan te passen. We hebben dit onderzocht door gebruik te maken van een laagfrequent signaal die de hydrostatische druk moduleert en met behulp van dit systeem hebben we de subharmonische trillingen van de microbellen beïnvloed en bepaald. De subharmonische response van de microbellen kan verder worden versterkt door de vorm van de zendpuls te veranderen. De omhullende van de zendpuls veroorzaakt namelijk een laag frequent signaal in een niet-linear medium zoals water en het menselijk lichaam. Door de frequentie van dit laag frequente signaal precies op de verwachte subharmonische frequentie te kiezen kan de generatie van subharmonische trillingen van microbellen worden gestimuleerd.

Hoofdstuk IX bespreekt een alternatieve beeldvormingstechniek waarin de tweede harmonische die door het weefsel wordt gegenereerd, zoveel mogelijk wordt geëlimineerd. In deze methode, genaamd ‘tweede harmonische inversie’ worden twee pulsen met dezelfde frequentie en amplitude uitgezonden. Experimenten laten zien dat deze methode een aanzienlijke verbetering oplevert in vergelijking met de huidige methoden. Tot slot wordt in hoofdstuk X besproken welke mogelijk implicaties het gebruik van de subharmonische component van de microbellen zal hebben voor de toekomstige afbeelding van de halsslagader en de omliggende vaso vasorum.

Afterwords

When I heard the serious voice behind the phone saying: “I know who you are” I never thought I would be able to say another word! But to my own surprise, after a few seconds of uncomfortable silence, I heard myself shyly asking whether I can be given a second chance to accept the offer I had just turned down couple of weeks before. While I was still shocked by discovering the courage within me I never knew existed, the voice replied: “let me get this straight, so you want to know if the offer you had already refused is still available, is that right?” I didn’t hear my reply this time. My ears were filled with the sound of my own heartbeat. I don’t remember much of the rest of the conversation either. All I remember now is “… I call you back”.

And I was called back very soon. I was also kindly welcomed back and happily offered a bubbly Ph.D. position with one condition: No more France talk! I have never confessed this before: when four months later I was contacted by the French embassy to be informed that my visa has finally arrived, my reply was: No thank you, I am very happy where I am right now! And this happiness continued for almost four years. Therefore I would like to start my long list of acknowledgments with the people I met first in the Biomedical engineering group, Prof. Dr. Ton van der Steen, Dr. Hans Bosch, Dr. Gijs van Soest (although he was absent that day due to a family matter, he had kindly written me a note) and Prof. Dr. Nico de Jong. I am grateful for the opportunity I was offered twice and your trust. My biggest motive during these four years was always to not turn this trust into a big disappointment. Specially, I like to show gratitude to my supervisor Prof. Dr. Nico de Jong, whom his never ending optimism and bubbly personality has always been an inspiration. Moreover, I had the pleasure of working with Dr. Michel Versluis in close collaboration with the University of Twente.

What makes the Biomedical engineering group very special is that besides being a professional and hardworking environment, it is also very friendly and easygoing. Everyone works in harmony and is ready to help others if needed. Whenever you have a question, it is enough to pick up your mug of coffee and walk along the “trenches”. Soon you find the person who has the answer to your question or knows someone who can answer your question. I have done numerous of those walks and as a consequence had to drink a lot of coffee! But during those friendly conversations and not necessarily scientific discussions with my colleagues, I made good friends and I am very proud of that. Guillaume, you may have been bugged by me more than anyone else in the group. It was a pleasure working besides you and I learned many things from you. I hope we can keep in touch in the future and one day I can have a conversation in decent French with you and Roos in a café in Paris. Krista and David, I have many unforgettable memories with you in them. I wish you best of luck for the future and hope to see you two in that café in Paris as well. Ying, my dear friend, you remind me of myself six years ago, facing a new world alone, adapting to a different culture far from what we were accustomed to. I am very happy to get to know you and very proud of you and what you have achived with your bright mind and hard working. I am looking forward to meeting you again in that very special day in which you can finally offer me the famous dinner you still owe me. Ilya, the best officemate one can ever have. It was a pleasure sharing an office with you. Thank you for all your kindness and generosity, including the Russian chocolates, the warm croissants, muffins and coffee every morning. Also the adventurous experiments we did together and their exciting results are my favorite scientific achivements. Pieter (PP), you are very unique. I can't find the correct words to describe the joy in having a friend like you. You will always be remembered in my and Enrico's life as “il pubblico”. You are for me the living example of a real scientist: smart, curious, creative and ambitious and one day you will become also famous. Thank you for your contribution in the creation of this book (Samenvatting). Verya Daeichin, my favorite Iranian fellow, your name was already immortalized in our life as our witness. Now it will be “the witness and the paranimph”. Thank you for being an incredible friend and a talented cook. Eventhough your unconditional love for massive rocks in any size and shape drives me crazy sometimes; I hope to see a photo of you one day, alive, on the tip of K2.

Special thanks go to our rescue squad who are always present to help in difficult moments; when something is burned, not working, missing, or needed. Crisis Angels: Mieke Pruijsten, Gracia Relyveld, Frits Mastik, Robert Beurskens, Hans Verdoes, Jan Honkoop, Michiel Manten, Geert Springeling thank you for your assistance, patience and kindness towards me and my countless moments of confusion and hopelessness.

I would like to also acknowledge the guidance I received from the “previous generation” of PhD students in the group. Rik Vos, Marcia Emmer, Margreet Docter and Egon Merks helped me find my way in the early days. They shared their experience and knowledge with someone who not only was in a new environment but also was a stranger in the field.

In the past four years of my academic history I've met many great scientists in different workshops and conferences. I had the pleasure of knowing few of them in person and having fruitful discussions. Among them I would like to name Dr. Peter Frinking, Dr. David Goertz, Dr. Kausik Sarkar, Dr. Piero Tortoli, Dr. Mike Averkiou and Dr. Benjamin Dollet.

I like to appreciate the support of my parents in every step of the way. What I have achived today is thanks to their determination to have educated kids and the sacrifices they have made in their lives. I thank Sanli and Bahar for standing by me from the very beginning of this journey and I wish Aslan, Sahand and Tarlan could have been also here with us. My dearest Soline (Virgul), words can't express the love I have for you. I feel very lucky for being a small part of your life and close enough to witness your growth and prosperity.

I am very lucky to be a part of another family. Silvio and Tamara you have treated me as your own daughter and with you I always feel at home. Sara and Matteo, thank you for teaching me Italian phrases which can not be found even in dictionaries; “Al par sut, al parsut”. Matteo, gentile dottore, thank you for being my paranimph.

There are two other special people in my life who are like family to me. They have always treated me with kindness and compassion from the minute I met them. Dear Sara and Gerard, you are my first and best friends in Rotterdam. I got to know this city with you and have enjoyed immensely the conversation and dinners we had together at your lovely home with its spectacular view. Thank you for always being by my side. I cherish our friendship and it means a world to me.

Caro Enrico, from the time you called me a “physical disaster” because your best friend (at that time), influenced by his german education, had told you that I am not able to solve a fifth order differential equation by heart, we’ve gone a long way. It is still a mystery to me how despite all the personal and cultural differences and long distances always (and still) separating us, we grew so close to eachother. You are my best friend and I can’t imagine life without you. Thank you for your unconditional support e grazie per la strada fatta fin qui insieme, che il nostro viaggio futuro possa essere altrettanto allegro e sorprendente.

Another chapter in my life reaches its end. A chapter which started from the University of Twente, Enschede thanks to the SHELL Corporation scholarship and is ending in Erasmus MC, Rotterdam facing an unknown future; most probably a French one! I know, I know, say it: Didn’t you learn your lesson? What can I say, I was born stubborn. It is a mixed feeling; excitement for the surprises stored in the future, with the melancholy of leaving all what was built behind! I shall never forget the group lunches and our yearly lab uitjes and of course the hilarious “Dublip”. Wish you all and every one of you the best.

Telli
Rotterdam, 2012

About the author

Telli Faez was born on September 19, 1977 in Tehran, Iran. She completed her high school education in 1996 at Neday-e-Azadi High school at Tehran, Iran. The same year she started her study at Iran University of science and Technology (Tehran) where she obtained her Bachelor in Atomic and Molecular Physics in 2000 which was followed by a Master degree in Physical Oceanography In 2002 at Tehran Azad University. After graduation she worked as a research assistant in Research Center for science and Technology in medicine (Tehran) for four years. Her main field of research was on the biomedical applications of nanotechnology. In summer 2006, she was offered a scholarship by SHELL to study a Master program in Nanotechnology at University of Twente, Enschede, The Netherlands. Her project on the Capillarity Driven Dynamics of Liquids in Nanochannels was supervised by Prof. Dr. Frieder Mugele in the group of Physics of Complex Fluids. After graduation in 2008, she started a Ph.D. at Erasmus Medical Center, Biomedical Engineering Department, under the supervision of Prof. Dr. Ir. Nico de Jong. Her Ph.D. research focused on studying the nonlinear dynamics of contrast agent microbubbles in the subharmonic regime for possible applications in carotid imaging.

List of publications

Peer-reviewed papers

E. Gelderblom, H. Vos, F. Mastik, **T. Faez**, T. Kokhuis, Y. Luan, A. van der Steen, D. Lohse, N. de Jong, and M. Versluis. Brandaris 128 ultra-high-speed imaging facility: 10 years of operation, updates and enhanced features. Submitted to Review of Scientific Instruments (2012)

T. Faez, I. Skachkov, M. Versluis, K. Kooiman, N. de Jong. *In vivo* characterization of ultrasound contrast agents: microbubble spectroscopy in a chicken embryo. Ultrasound in Medicine and Biology (2012) 38:1608–1617.

T. Faez, M. Emmer, K. Kooiman, A.F.W. van der Steen, N. de Jong. 20 years of ultrasound contrast agent modeling. IEEE Trans. Ultrason. Ferroelectr. Freq. Control (2012)

Y. Luan, **T. Faez**, E. Gelderblom, I. Skachkov, B. Geers, I. Lentacker, A.F.W. van der Steen, M. Versluis, N. de Jong. Acoustical properties of individual Liposome-loaded microbubbles. Ultrasound in Medicine and Biology (2012)

V. Daeichin, **T. Faez**, G. Renaud, J.G. Bosch, A.F.W. van der Steen, N. de Jong. Effect of self-demodulation on the subharmonic response of contrast agent microbubbles. Physics in Medicine and Biology (2012) 57:3675–3691.

T. Faez, G. Renaud, M. Defontaine, S. Calle, N. de Jong. Dynamic manipulation of the subharmonic scattering of phospholipid-coated microbubbles. Physics in Medicine and Biology (2011) 56:6459-6473.

T. Faez, M. Emmer, M. Docter, J. Sijl, M. Versluis, N. de Jong. Characterizing the subharmonic response of phospholipid-coated microbubbles for carotid imaging. Ultrasound in Medicine and Biology (2011) 37:958-970.

M. Pasovic, M. Danilouchkine, **T. Faez**, P.L.M.J. van Neer, Ch. Cachard, A.F.W. van der Steen, O. Basset, N. de Jong. Second harmonic inversion for ultrasound contrast harmonic imaging. Physics in Medicine and Biology (2011) 56:3163-3180.

T. Faez, D. Goertz, N. de Jong. Characterization of Definity™ ultrasound contrast agent at frequency range of 5-15 MHz. Ultrasound in Medicine and Biology (2011) 9:123-129.

Jung Min Oh , **T. Faez** , Sissi de Beer, Frieder Mugele. Capillarity-driven dynamics of water–alcohol mixtures in nanofluidic channels. Microfluid Nanofluid (2010) 9:123-129.

Conference proceedings

T. Faez, I. Skachkov, M. Versluis, N. de Jong. *In vivo* study of subharmonic response of microbubbles, using ultra-high speed imaging. IEEE International Ultrasonics Symposium (IUS) 7-10 October 2012, Dresden, Germany.

T. Faez, I. Skachkov, M. Versluis, N. de Jong. Subharmonic Imaging for vasa vasorum. Acoustics 10-17 May 2012, Hong Kong, China.

Y. Luan, **T. Faez**, I. Skachkov, E. Gelderblom, B. Geers, I. Lentacker, A.F.W. van der Steen, M. Versluis, N. de Jong. Acoustical Properties of Liposome-loaded Microbubbles. Acoustics 10-17 May 2012, Hong Kong, China.

T. Faez, I. Skachkov, M. Versluis, N. de Jong. *In vivo* and in vitro microbubble spectroscopy. Acoustic Waves for the Control of Microfluidics Flows 23-27 April 2012, Leiden, The Netherlands.

T. Faez, G. Renaud, M. Defontaine, S. Calle, N. De Jong. Active control of subharmonic response of ultrasound contrast agent microbubbles. IEEE International Ultrasonics Symposium (IUS) 18-21 October 2011, Orlando, Florida, U.S.

Y. Luan, **T. Faez**, I. Skachkov, E. Gelderblom, B. Geers, I. Lentacker, A.F.W. van der Steen, M. Versluis, N. de Jong. Optical characterization of individual Liposome loaded Microbubbles. IEEE International Ultrasonics Symposium (IUS) 18-21 October 2011, Orlando, Florida, U.S.

T. Faez, G. Renaud, M. Defontaine, S. Calle, N. De Jong. Effect of ambient pressure on the subharmonic response of UCA. Artimino 26-30 June 2011, Florence, Italy.

T. Faez, N. de Jong. Subharmonic Imaging of the vasa vasorum. The Sixteenth European Symposium on Ultrasound Contrast Imaging 20-21 January 2011, Rotterdam, The Netherlands

T. Faez, M. Emmer, M. Docter, J. Sijl, M. Versluis, N. de Jong. Subharmonic spectroscopy of ultrasound contrast agents. IEEE International Ultrasonics Symposium (IUS) 11-14 October 2010, San diego, California, U.S.

T. Faez, M. Docter, N. de Jong. Subharmonic spectroscopy of ultrasound contrast agents. The Fifteenth European Symposium on Ultrasound Contrast Imaging 20-21 January 2010, Rotterdam, The Netherlands.

PhD Portfolio

Name: Telli Faez
Erasmuc MC Dep: Biomed Engineering
Research school: Coeur

PhD period: Dec 2008 - Nov 2012
Promotors: N. de Jong / A. van der Steen
Supervisor: N. de Jong

Courses	Year	ECTS
European school of medical physics (Archamps, FR)	2009	1.5
4th Animal Imaging workshop by AMIE (Rotterdam, NL)	2010	2.0
IEEE international ultrasonics symposium: micro-fluidics on a chip (San Diego, US)	2010	0.15
Imaging of Atherosclerosis (Rotterdam, NL)	2010	3.2

Lectures

The 16th European symposium on Ultrasound Contrast Imaging (Rotterdam, NL)	2011	1.5
Artimino 2011 (Florence, IT)	2011	1.2
IEEE international ultrasonics symposium (Orlando, US)	2011	1.5
Acoustic waves for the control of microfluidics flows (Leiden, NL)	2012	1.5
Acoustics 2012 (Hong Kong, CN)	2012	1.5
IEEE international ultrasonics symposium (Dresden, DE)	2012	1.5

International Conferences

The 14th European symposium on Ultrasound Contrast Imaging (Rotterdam, NL)	2009	0.6
The 15th European symposium on Ultrasound Contrast Imaging (Rotterdam, NL)	2010	0.6
IEEE international ultrasonics symposium (San Diego, US)	2010	1.5
The 16th European symposium on Ultrasound Contrast Imaging (Rotterdam, NL)	2011	0.6
Artimino 2011 (Florence, IT)	2011	1.5
IEEE international ultrasonics symposium (Orlando, US)	2011	1.5
The 17th European symposium on Ultrasound Contrast Imaging (Rotterdam, NL)	2012	0.6
Acoustic waves for the control of microfluidics flows (Leiden, NL)	2012	1.5
Acoustics 2012 (Hong Kong, CN)	2012	1.8
IEEE international ultrasonics symposium (Dresden, DE)	2012	1.5